EPFL

Thèse n° 7898

Aqueous Redox Flow Batteries Enhanced by Solid Boosters

Présentée le 15 juin 2020

à la Faculté des sciences de base
Laboratoire d'électrochimie physique et analytique
Programme doctoral en chimie et génie chimique

pour l'obtention du grade de Docteur ès Sciences

par

Elena ZANZOLA

Acceptée sur proposition du jury

Dr A.-S. Chauvin, présidente du jury
Prof. H. Girault, directeur de thèse
Prof. G. Wittstock, rapporteur
Dr K. Toghill, rapporteuse
Dr J. Van Herle, rapporteur

École polytechnique fédérale de Lausanne

2020

To Alessandro,

To the world you may be one person, but to one person you may be the world.

Alla mia famiglia,

Mamma, Marchino e alla mia Super nonna, con tutto il mio affetto.

Acknowledgments

This thesis was an amazing path where I had the pleasure to meet great people and count on the support of the Ecole Polytechnique Federale de Lausanne (EPFL) infrastructures.

First of all, I would like to sincerely thank Professor Hubert Girault, who welcomed me in the Laboratory of Physical and Analytical Electrochemistry (LEPA) in 2016 and then who supervised my research for four years. I really appreciated his contributions to my work, the support to keep my motivation high towards new achievements and the opportunities to attend scientific conferences where I could learn from experts in my field.

I would like to thank the jury committee who revised my thesis manuscript, the president of the jury Dr. Anne-Sophie Chauvin from the Ecole Polytechnique Federale de Lausanne (EPFL), Switzerland, and all the experts: Dr. K. Toghill from the University of Lancaster, Great Britain, Prof. G. Wittstock from the University of Oldenburg, Germany and Dr. J. Van Herle from the Ecole Polytechnique Federale de Lausanne (EPFL), Switzerland.

I am very thankful to all the EPFL staff (human resources and doctoral school members) who helped me with administrative procedures, in particular a special thank you goes to Mrs. A. L. Odegaard. Following, I would like to thank the secretaries of the laboratory: Mrs. P. Byron and Mrs. S. Jaussi for their support.

Coming now to the colleagues I shared the laboratory with, first of all I would like to thank all the scientists who more closely assisted me in the research activity: Dr. C. Dennison, Prof. P. Peljo and Dr. S. Gentil. During their supervision I learned new skills and developed my own scientific method. I am extremely grateful for their contributions, support and patience.

Then, a truthful thank you goes to all the people I had the great opportunity to meet in the laboratory all these four years: Dr. V. Amstutz, Dr. M. Jovic, Prof. A. Lesch, Dr. A. Battistel, Dr. H. Vrubel, Dr. J. Riva Soledad, Dr. V. Costa Bassetto, Dr. W. Oliveira Da Silva, Dr. E. Smirnov, Dr. Dr. N. Gasilova, Dr. D. Baster, Dr. A. Olaya, Dr. B. Nagar, Prof. Tzu-En Lin, Dr. Y. Zhu, Dr. L. Rivier, Dr. G. Gschwend, Dr. M. Frossard, Dr. S. Maye, Y. Ligen, D. Reynard, S. Darvishi, J. Piwek, I. Fouzai, C. Xia, T. Omatru, M. Patel, V. Shandra. A special thank you to my bachelor student, P. Sharma who spent a brief time in the laboratory and followed the last part of my research work.

I am also grateful to Dr. C. Roussel and S. Thonney who welcomed me in their laboratory to teach bachelor and master students from the EPFL for three years.

A special acknowledgement to the awesome staff of the EPFL Valais building where I spent my entire research activity for four years, in particular the responsible of the chemical store L. Seydoux and A.

Coquoz, the staff of the mechanical workshop, of the IT service, the responsible of the building management and security and all the scientific staff responsible of the shared facilities.

A genuine acknowledgment to all the coworkers and professors from the other research groups in the EPFL Valais building, in particular to my Italian friend Valeria. To all the colleagues I met during conferences and scientific meetings outside Switzerland, in particular Dr. C. Armstrong and Dr. D. Bryans all my appreciation.

My biggest gratitude is for Alessandro, always supportive and irreplaceable in my life. To my dear Italian family: mamy, Marchino, Superina, Anna, Giorgio, Enri and Roby, all my thankfulness for being there for me even if geographically distant. Nothing is more fabulous than having all of you as my family.

A sincere gratefulness to Prof. P. R. Mussini and Dr. M. Longhi from the University of Milan Italy, where I studied before joining EPFL Switzerland.

Abstract

One of the main challenges for certain energy production technologies (*e.g*. renewables) is the capability to supply energy according to the demand. It follows that storing energy is a possible solution to the inadequacy between energy production and demand. Redox flow batteries (RFB) are largely employed for storing energy, especially in stationary applications. These devices exploit electrochemical reactions of dissolved redox-active species, stored in external reservoirs. In general, RFB are scalable, durable, and robust devices, although, compared to other batteries, they show a significantly poor storage capacity (10-40 $Wh \cdot L^{-1}$), determined by the solubility limit of the redox-active species dissolved in the electrolytes.

In this thesis, a method to overcome capacity issue in RFB is presented, and it consists of adding redox solid-phase materials as primary storage media into the liquid electrolytes. In the present work, these solid materials are called "boosters". These boosters can receive charge from the redox-active species reacting in the flow cell, if the respective Fermi levels are aligned. This concept is denoted as "redox-mediated" charge transfer.

The "redox-mediated" approach of the charge transfer is applied first to an acidic and then to a neutral pH aqueous RFB. Particular attention is dedicated to the choice and synthesis of the solid boosters, ranging from polymers, such as polyaniline and polyimide to intercalation compounds of alkali metal ions, such as Prussian blue analogues. In addition, most of the boosters are designed along with carbonaceous coaters, such as carbon nanotubes and carbon acetylene black to be highly electronically conducting upon battery cycling, increasing the overall cell performances.

In an aqueous RFB at acidic pH in presence of inorganic redox-active species at a concentration of 1 M in the electrolytes, a solid booster made of polyaniline and carbon acetylene black placed in both reservoirs showed a three-fold increase in the volumetric capacity, as compared to the electrolytes alone.

On the positive-side of a neutral pH aqueous RFB, a composite of copper hexacyanoferrate with carbon nanotubes along with an organic redox-active molecule at 10 mM exhibited 10^4 increase in the volumetric capacity. Finally, a new redox-active organic molecule was synthesized as a candidate for the negative-side electrolyte of a neutral pH aqueous RFB, and a solid booster was judiciously paired with it. Its viability was preliminarily tested, and initial measurements to study the electron transfer kinetics at the solid/liquid interface were recorded by scanning electrochemical microscopy.

This work opens a series of future studies of utilizing this approach to enable bulk-phase charge storage in the reservoirs of RFBs. In addition, it looks promising to be utilized in industrial demonstrators.

Key-words: redox flow battery, volumetric capacity, redox solid booster, "redox-mediated" charge transfer, redox mediator, conductivity, carbon nanotubes, intercalation, redox organic molecules.

Riassunto

La domanda di energia é spesso incongruente con la produzione, pertanto risulta importante immagazzinare energia. Le batterie redox a flusso sono un tipo di tecnologia largamente impiegata per immagazzinare energia, specialmente a livello stazionario. Nelle batterie redox a flusso l'energia é immagazzinata all'interno di sostanze redox-attive completamente solubilizzate, contenute in grosse cisterne. In generale, le batterie redox a flusso sono un tipo di tecnologia estremenente robusta e flessibile, tuttavia la loro capacitá di immagazzinare energia é limitata (10-40 Wh L^{-1}), dalla solubilitá delle specie redox-attive.

Questo lavoro di tesi presenta un approccio innovativo per superare la capacitá di immagazzinare carica in batterie redox a flusso, basato sull'aggiunta di materiali in fase solida agli elettroliti liquidi. In questo concetto, i materiali in fase solida sono denominati "boosters". I boosters sono in grado di ricevere carica dalle specie redox in soluzione se il livello di Fermi é allineato con il potenziale standard della coppia redox. Secondo le seguenti definizioni, questo concetto viene definite come trasferimento della carica "redox-mediato".

Particolare attenzione é stata dedicata alla scelta e poi alla sintesi dei booster, secondo questo approccio e talvolta additivi a base carbonio sono stati aggiunti ai booster per aumentare la loro conduttivitá elettronica, riscontrando prestazioni piú elevate. In aggiunta, una vasta gamma di booster é stata considerata, passando da materiali polimerici (come ad esempio polianilina e la polimide) a composti cristallini di intercalazione (come ad esempio derivati del Blu di Prussia).

In particolare, questo approccio é stato testato su due batterie redox a flusso, una in presenza di elettroliti in soluzione acquosa a pH acido e una con elettroliti in soluzione acquosa a pH neutro. Nel primo caso, un materiale composito fatto da polianilina e carbone come booster in entrambe le soluzioni elettrolitiche ha esibito un aumento di densitá volumetrica pari a tre volte quella dell'elettrolita di partenza. Invece, nella batteria redox a flusso a pH neutro, un materiale composito fatto da rame esacianoferrato e nanotubi di carbonio come booster al lato positivo del sistema ha esibito 10^4 volte la capacitá iniziale dell'elettrolita. Infine, una ricerca accurata é stata condotta per il lato negative di una batteria redox a flusso a pH neutro e un nuovo elettrolita é stato sintetizzato. In linea con il concetto di questa tesi, un booster é stato trovato e la sua viabilitá é stata inizialmente testata. In particolare, caratterizzazione elettrochimica é stata effettuata e uno studio iniziale della cinetica della rezione del trasferimento di carica all'interfase liquid/solido utilizzando la microscopia di scanning elettrochimico.

Parole-chiave: batteria redox a flusso, capacitá volumetrica, redox booster, mediazione redox del trasferimento di carica, mediatore redox, conduttivitá, nanotubi di carbonio, intercalazione, molecole organiche redox attive.

List of abbreviations

AEM= anion exchange membrane

AIRFB= aqueous inorganic redox flow batteries

AORFB= aqueous organic redox flow batteries

ARFB= aqueous redox flow batteries

CAB= carbon acetylene black

CB= conduction band

CE=Coulombic efficiency

CE= counter electrode

CNTs= carbon nanotubes

Co-Co-PBA= cobalt Prussian blue analogue

CoFe PBA= cobalt iron Prussian blue analogue

CoHCF= cobalt hexacyanoferrate

CuHCF= copper hexacyanoferrate

CP= carbon paper

CV= cyclic voltammetry

EE= energy efficiency

EESS= electrochemical energy storage systems

ESSs = energy storage systems

FTIR= Fourier-transform infrared spectroscopy

GCE= glassy carbon electrode

IEA= International Energy Agency

IUPAC= international union of pure and applied chemistry

LCOS= levelized costs if storage

LIB= lithium-ion batteries

M= mediator

MnHCF= manganese hexacyanoferrate

MTABT= N-Methyl-N'-(3-trimethylammonioethyl-)-4,4'-bipyridinium tetrachloride

MV= methyl viologen

MWCNTs= multi walled carbon nanotubes

NARFBs= non-aqueous redox flow batteries

NIB= sodium ion batteries

NiO-GO= nickel oxide graphite oxide

NQS=sodium 1,4-dioxonaphtalene 2-sulfonate

OCP and OCV= open circuit potential and open circuit voltage

OECD = organization for the Economic co-Operation and Development

PANI=polyaniline

PANI/CB= polyaniline with carbon black

PANI-EB= polyaniline emeraldine base

PANI-ES= polyaniline emeraldine salt

PANI-LE= polyaniline leucoemeraldine

PANI-PE= polyaniline pernigraniline

PB= Prussian blue

PBAs= Prussian blue analogues

PEC= photo-electrochemical cell

PEDOT= poly(3,4-ethylenedioxythiophene)

PEEK= polyether ether ketone

PNTCDA= polymer of 1,4,5,8-naphthalenete-tracarboxylic dianhydride

Poly-TEMPO= polymer of TEMPO

PPy= polypyrrole

PTFE=polytetrafluoroethylene

RAG= redox active group

RAGEP= redox active group embed polymers

RAPs= redox active polymers

RAPBP= redox active group pendant bearing polymers

RDE= rotating disk electrode

RE= reference elecctrode

RFBs= redox flow batteries

RFLB= redox flow lithium battery

RM= redox mediator

ROM= redox organic molecules

SB= solid booster

SECM= scanning electrochemical microscopy

SEI= solid electrochemical interface

SEM= scanning electron microscopy

SWCNTs= single walled carbon nanotubes

TEMPO= (2,2,6,6-tetramethylpiperidin-1-yl)oxyl

TEMPOL= 4-hydroxy-2,2,6,6-tetramethylpiperidin-1-oxyl

TEMPTMA= N,N,N-2,2,6,6-heptamethylpiperidyloxy-4ammonium chloride

TMAP-TEMPO = 4-[3-(trimethylammonio)propoxy]-2,2,6,6-tetramethylpiperidine-1-oxyl

UME= ultramicroelectrode

VB= valence band

VOx= vanadium oxygen

VRFBs= vanadium redox flow batteries

VOx= vanadium oxygen

WE=working electrode.

Table of Contents

Chapter 1 *General Introduction*

Electricity is at the heart of modern economies and its demand is set to increase further as a result of rising household incomes, with the electrification of transport and heat, and growing request for digital connected devices and air conditioning.[1]

In 2018, as described in the electricity statistics report from the International Energy Agency (IEA)[2], in the countries of the Organization for the Economic co-Operation and Development (OECD, made of thirty-six nations, including most of the Europeans, Switzerland and United States of America), the net electricity production was 10'652 TWh [2]. As shown on ***Figure 1.1***, electricity was principally produced by non-renewable sources in 2018, coming from conventional thermal (*i.e.* sources which produce electricity through combustion of fuels, 6155 TWh) and nuclear with 1870 TWh.[2] The remaining energy was generated by hydro (1484 TWh) and renewable sources (1143TWh).[2]

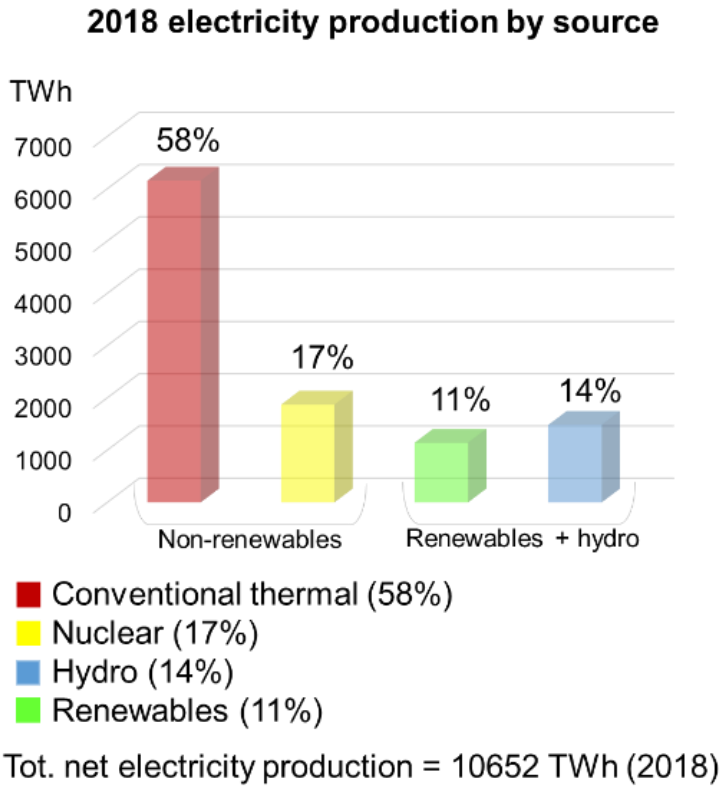

Figure 1.1 Graphical representation of the electricity production in 2018 by source. The legend below the graph shows the different energy sources, distinguishing non-renewables (conventional thermal and nuclear) from renewables and hydro. Above each bar in the chart, the percentage of the electricity produced is reported. [2]

Unfortunately, despite the increase in renewable energy and fall in coal in 2018[1], low-carbon energy sources didn't keep pace with gas growth, resulting in a 0.5% increase in energy-related carbon dioxide

emissions.[1] Therefore, increasing concerns about energy security and environment are driving towards new approaches to decrease energy production from fossil fuels and to stabilize the discontinuous and fluctuating yield between energy demand and supply. Certainly, a decarbonization process of electricity is happening in most of the European countries, especially in the mobility sector where fuels such as hydrogen or synthetic liquid fuels are taking place.[3] Besides encouraging progresses in the decarbonization of the mobility sector stationary energy storage can represent a valid option.

Looking towards stationary energy storage systems, a couple of approaches can be easily identified. First, the surplus energy can be stored when the demand is low and the production is high and later released when the demand is high again.[4] Second, the energy can be stored when it is cheap (*e.g.* during the night) and released upon peak demand periods.[4] On the other hand, storage deployment remains dependent on the supportive policy and market framework: in fact, in countries where incentives are introduced the growth and progression of storage systems is faster. As a result, in the OECD European countries from 2013 to 2016, either grid-scale or "behind the meter" storage systems grew consistently, whereas in 2018, the annual deployment of energy storage systems reached 8 GWh.[1]

Storage systems look already promising options in the current energy scenario, thus, in the following sections of this chapter the main technologies will be described in the context of this thesis. Later, electrochemical energy storage technologies and in particular batteries will be introduced. Among batteries, redox flow batteries (RFB) are the focus of this thesis. A general overview of the working principle will be introduced along with the approach developed to overcome one great limitation in this technology.

[1] IEA (2019), "Tracking Energy Integration", IEA, Paris https://www.iea.org/reports/tracking-energy-integration

1.1 Energy storage systems (ESSs)

Energy storage systems (ESSs) are attracting quite a lot of attention as they represent a valid option moving towards a decarbonization of the energy sectors. In particular, they can be a promising solution to integrate electricity generated from renewables into the whole production. Renewable sources are considered highly intermittent since their power output can change with respect to the degree of availability of the sustainable source, which unfortunately cannot necessarily correspond to the grid's peak demand. [5] Once electricity is produced seasonally from a renewable source it can be stored and released on-demand to balance fluctuations between production and consumption. This situation called peak shaving reduces peak energy demand bringing advantages to the end-consumers by saving on their electricity bills.

Now it is important to define which type of ESSs are available and for which purposes; according to a review from Perron and co-workers[5], there are four main applications of ESSs:

i) Low power in isolated areas

ii) Medium power in isolated areas

iii) Network connection application with peak leveling

iv) Power-quality control

Each application can be categorized as follows (***Table 1.1***):

Table 1.1 Energy storage systems (ESSs) including technologies, main applications and performances. [6 5 7].

ESSs	***Technology***	***Application***[5]	***Performances*** [5]
Mechanical	Flywheels, compressed air (CA), pump hydro (PH)	Low-medium power (flywheels, CA) Large-scale (hydro)	100 MWh 100−130 $kWh \cdot kg^{-1}$ (for flywheels)
Electrical	Capacitors, super-capacitors, superconducting magnetic storage	Low-medium power (capacitors)	5−10 $Wh \cdot kg^{-1}$
Thermal	Low and high temperature energy storage	Large-scale	In the specific temperature range of 120−360°C, 1332 $MJ \cdot m^{-3}$
Chemical	**Electrochemical**, thermo-chemical, chemical storage devices	Small and large-scale (**electrochemical**)	50 $Wh \cdot L^{-1}$ (charge capacity)

A way to compare the technologies in ***Table 1.1*** is considering their levelized cost of storage (LCOS) (*x*-axis ***Figure 1.2***); [8] [5] according to Schmidt *et al*.[8] levelized costs can be described as the total lifetime cost of the investment divided by its cumulative delivered electricity. [8] Levelized costs reflect the internal average price at which electricity can be sold. [8] These definitions can be summarized by the formula in ***eqn. 1.1***:

Eqn. 1.1[8]

$$LCOS\left[\frac{\$}{\text{MWh}}\right] = \frac{IC + \sum_n^N \frac{O\&M\ cost}{(1+r)^n} + \sum_n^N \frac{Charging\ cost}{(1+r)^n} + \frac{End\text{-}of\text{-}life\ cost}{(1+r)^{N+1}}}{\sum_n^N \frac{Electrity\ discharged}{(1+r)^n}}$$

This formula defines all the elements necessary to determine the LCOS of an energy storage technology: the investment cost (IC), the operation and maintenance (O&M), the charging cost and end-of-life cost, divided by electricity discharged during the investment period.[8] Moreover, the equation assumes all investment costs are incurred in the first year and sums ongoing costs in each year (n) up to the system lifetime (N), discounted by the discount rate (r).[8]According to ***eqn. 1.1***, Schmidt *et al*. [8] made a very interesting comparison of some energy storage technologies and a projection up to 2050 (***Figure 1.2***).

In 2015, pumped hydro energy storage (PHES) and compressed air (CA) dominate most applications apart from consumption services and primary response, where size and response time requirements make these technologies unsuitable. [8] In consumption service applications battery systems such as lead acid, sodium sulphur, lithium-ion, and vanadium redox flow compete for least-cost exhibiting the highest probability of lowest LCOS in most applications beyond 2025 (***Figure 1.2***). [8] By 2030, lithium-ion appears to be more cost efficient than vanadium flow batteries, with <4 h discharge and <300 annual cycles. As from 2030, hydrogen with a maximum of ~ 1000 h discharge, can likely become the most cost efficient solution for seasonal storage.[8]

This analysis of LCOS for different energy storage technologies by Schmidt *et al*. [8] was made before the current situation of the virus COVID−19, which largely affected the economies of the countries all over the world, therefore the 2050 projection needs to be reconsidered.

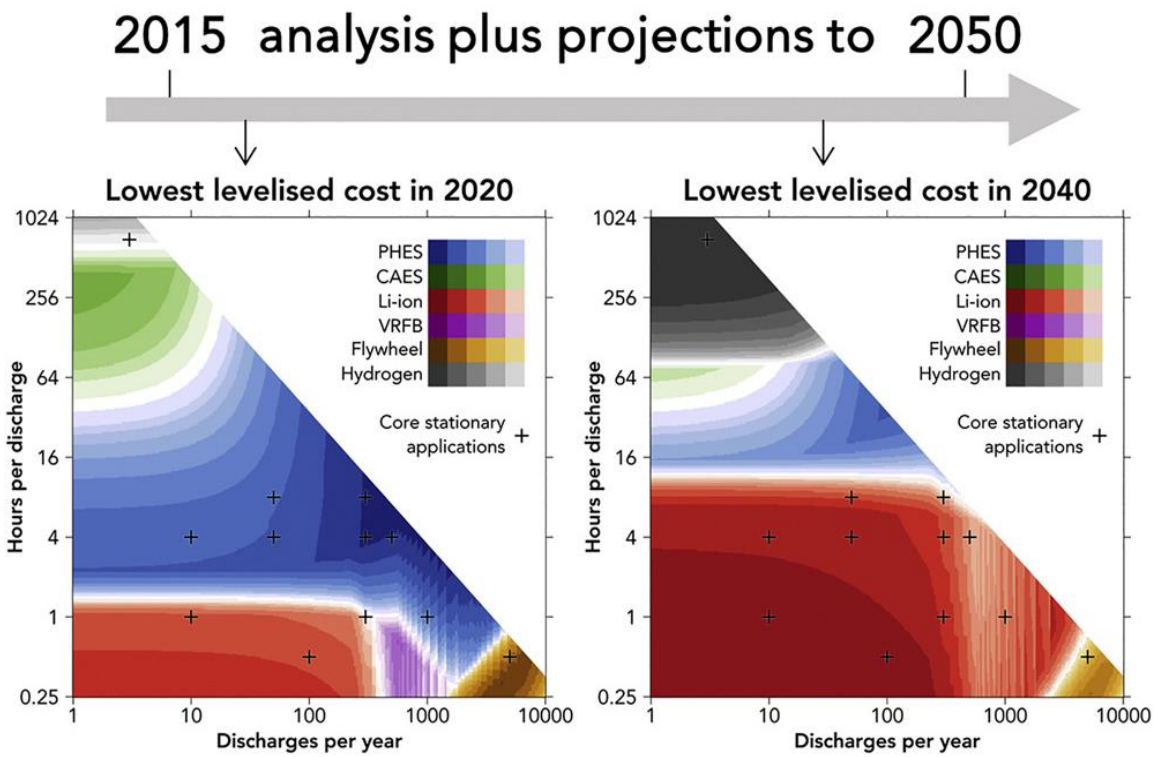

Figure 1.2 A) Levelized costs for some energy storage technologies (on the left side) and projection of levelized cost in the year 2040 (on the right side). This image is reproduced with permission from the work of Schmidt at ref 8. Copyright 2020, Joule, Elsevier.

1.2 Electrochemical energy storage systems (EESs)

Each EESSs offer specific operational characteristics in agreement with the desired application. Among the discussed storage systems, electrochemical energy storage technologies there are different technologies either for low-medium (*i.e.* transport or portable electronics) or large-scale applications (*i.e.* grid-connected and storage).[9] Within mobile applications, one can consider autonomous vehicles (*e.g.* hydrogen electric vehicles, HEV), where the storage system can be placed on the vehicle[9] or portable electronics (*e.g.* LIB). Within stationary applications, stand-alone or grid-connected are the most significant examples (*e.g.* LIB, NIB, electrochemical capacitors and RFB).[9]

1.2.1 Batteries

Batteries are the most popular devices within EESSs: they are able to store electricity in the form of chemical energy and convert it with a specific electrochemical process. The batteries discussed in this section are commonly called "secondary batteries" as they are all rechargeable devices. According to specific characteristics and design features, we can distinguish several operational parameters, such as:

***i*)** System power ratings: total electrical power required for a normal operation of a device.

***ii*)** Discharge time at rated power: discharge current at which the battery will discharge in a certain time.

***iii*)** Volumetric energy density: quantity of energy a system contains in comparison to its volume (expressed in $Wh \cdot L^{-1}$).

***iv*)** Gravimetric energy density: quantity of energy a system contains in comparison to its weight (expressed in $Wh \cdot kg^{-1}$).

Figure 1.3 displays some batteries according to these operational parameters:

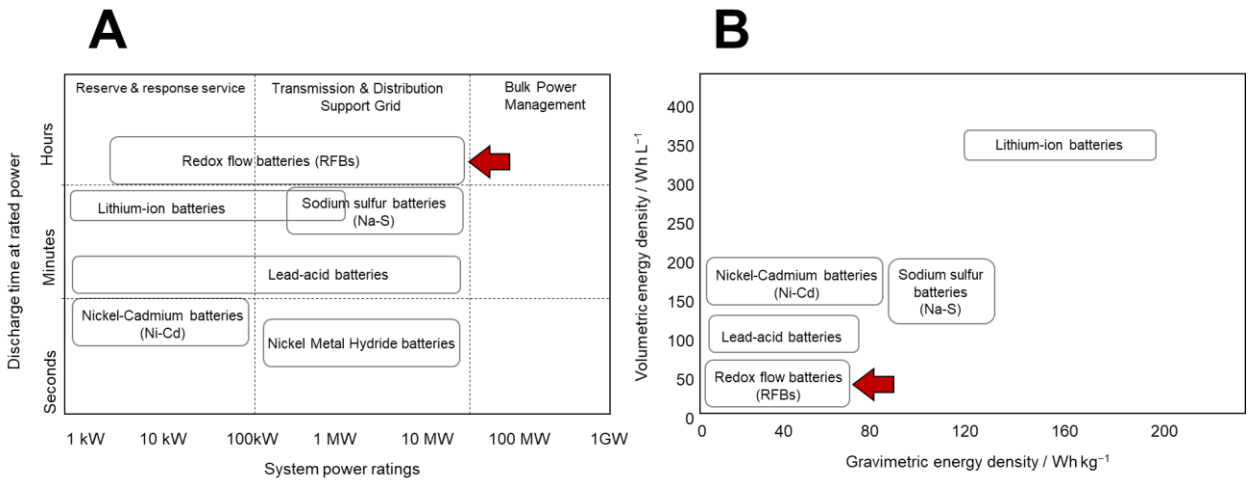

Figure 1.3 A) Schematic of batteries as electrochemical storage technologies according to system power ratings (on the x-axis) and discharge time at rated power (on the y-axis). B) Schematic of the same batteries in A), according to gravimetric energy density (on the x-axis) and to volumetric energy density (on the y-axis).[10] In both schematics the red arrow is pointing redox flow batteries as focus of this thesis.

From ***Figure 1.3B)*** it is possible to discriminate whether the battery is meant to serve in a mobile or in a stationary application. RFB are utilized in stationary applications to support the grid (despite their volumetric capacity is limited). On the contrary, LIB are employed in both mobile and stationary applications, since they are high energy dense devices. ***Table 1.2*** describes different batteries highlighting performances and safety limits.

Table 1.2 Comparison of some rechargeable batteries (RFB, LIB, sodium-sulfur, nickel-cadmium, lead- acid).[10] [11]

	RFB	***LIB***	***Sodium-sulfur***	***nickel-cadmium s***	***lead-acid***
Type of application	Stationary, grid support	Mobile (*e.g.* portable electronics)	Grid support or stand – alone systems	Portable tool devices	Automotive
% Energy efficiency	70-80	90	80−85	70−90	70−80 [6]
Charge capacity	54 $Ah \cdot L^{-1}$	70 $Ah \cdot L^{-1}$	400 kWh (typical unit)[12]	N/A	N/A
Energy density	35 $Wh \cdot L^{-1}$	>200 $Wh \cdot L^{-1}$	120−200 $Wh \cdot L^{-1}$ [13]	150−200 $Wh \cdot L^{-1}$ [13]	150−200 $Wh \cdot L^{-1}$ [13]
Specific energy	31 $Wh \cdot kg^{-1}$	>160 $Wh \cdot kg^{-1}$	>100 $Wh \cdot kg^{-1}$	40−80 $Wh \cdot kg^{-1}$ [13]	~50 $Wh \cdot kg^{-1}$ [13]
Cycle life-time	>10’000	~ 600−1200	~ 2500−4500 [14]	Lifetime > 10 years	~200−300
Discharge time at rate power	hours	Minutes-hours	Minutes-hours	Minutes	Minutes
Safety	Quite safe	Flammable	Not very safe	Toxicity of Ni	Corrosive (H_2SO_4)

1.2.1.1 Lithium-ion batteries (LIB)

In between the 1970s and 1990s, John Goodenough, Stanley Whittingham, Richard Yazami and Akira Yoshino [6] among many others developed the technology of LIB, which just in 2019 was awarded with the Noble Prize in Chemistry by the Royal Swedish Academy of Science. From the early stages of development, in LIB transition metal oxides (TMO) and sulfides were excellent reversible positive-side materials. Later, thanks to the introduction of graphite (*i.e.* crystalline form of the element carbon with its atoms arranged in a hexagonal structure) as negative-side material and lithiated transition metal oxides (LTMO) as positive-side compounds, LIB started to receive greater attention for mobile applications (cellular phones, laptops, digital cameras), due to their high energy density either per unit volume or mass (> 250 $Wh \cdot L^{-1}$ and < 100 or ~180 $Wh \cdot kg^{-1}$). [13]

In LIB there are four main components: *i*) positive-side material, *ii*) negative-side material, *iii*) electrolyte and *iv*) separator (***Figure 1.4***).[15]

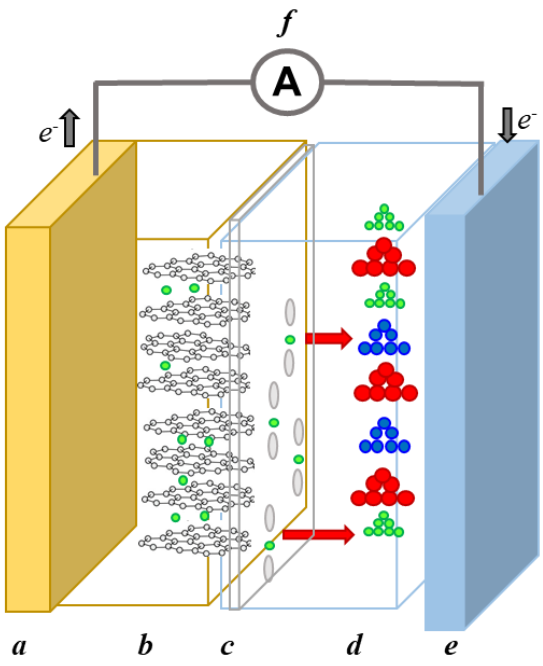

a = Current collector (copper)
b = Negative-half side (graphene and lithium ions as green spheres)
c = Separator and solvent (as gray and green spheres)
d = Positive-half side (lithium metal oxide as red blue and green spheres)
e = Current collector (aluminum)
f = External circuit (current)

Figure 1.4 General schematic of a LIB. All the components are labeled and detailed in the legend below the representation. The electron path is depicted (gray arrows), as well as the lithium one (red arrow).

Upon operation, the first process is a charging reaction, where the positive-side metal oxide species are oxidized (delithiation or extraction of the lithium ion). Then, there is a reduction reaction (lithiation) of the negative-side material (graphite). Unfortunately, this ideal mechanism is often spoiled by the formation of a passivating film on the electrode material known as solid electrochemical interphase (SEI). The SEI layer can grow gradually upon cycling thereby increasing the cell resistance. [16]

Conventional LIB use organic electrolytes, which are a mix of lithium salts and organic solvents.[15] Common lithium salts are lithium hexafluoroposphate ($LiPF_6$), lithium tetrafluoborate ($LiBF_4$) and lithium perchlorate ($LiClO_4$). [15] Then, frequently employed organic solvents are ethylene carbonate (EC), propylene carbonate, dimethyl carbonate (DMC) and diethyl carbonate.[15] Finally, a separator, generally made of polyethylene and polypropylene, is placed between the positive and the negative-side to prevent short circuit by direct contact.[15]

Despite their large usage in common portable electronics, LIB cannot always be considered as fully safe devices. They are quite often involved in accidents sometimes during transportation or due to improper

management. Lithium metal is overall corrosive and it requires special handling. It is a hazard and any contact with moisture leads to the formation of caustic lithium hydroxide (LiOH).

Overcharge is often considered as one of the most severe dangers in LIB,[17] since it can lead to thermal runaway and ultimately to fire and explosion of the devices.[17] In this process, the cell voltage can increase above the designed per-limit and lithium can de-intercalate from the LTMO structure causing irreversible phase transition and collapse.[17] Thermal runaway is also related to temperature rising originating from the external or internal heat generation during the abnormal abuse. [17]

Another critical aspect in LIB is the flammability of the organic electrolyte[17], which usually rises challenges in the manufacturing process. Consequently, the addition of flame-retardant (FR) compounds in the organic electrolyte (*e.g.* phosphate groups) is required to block the chain reactions of hydroxyl radicals during the combustion of the organic electrolytes. [17]

In LIB, energy safety should be the focus for further developments. Many efforts are dedicated to improve operational characteristics and material design to propose less harmful options. Recently researchers have identified sodium-ion batteries (NIB) as a good alternative to LIB.

1.2.1.2 Sodium-ion batteries (NIB)

Researchers started investigating NIB in between the 1970s-1990s, but only twenty years later the research was revitalized. As seen in LIB, NIB are characterized by a positive and a negative-side. One main difference arise from the negative-side though, which is not graphite, as this material cannot store large sodium ions. [18] As a consequence, hard carbon is used as negative-side material and it demonstrates good cycling stability.[18] Other compounds such as sodium titanate phases (*e.g.* $Na_2Ti_3O_7$,[19] and $NaTiO_2$ [20]) are also frequently utilized.

At the positive-side, NIB store sodium ions in TMO *via* intercalation reaction mechanisms. However, from a desire to keep costs low and safety high, significant research is moving towards the replacement of metals in the oxides. Cobalt, vanadium, chromium, nickel and recently iron have been investigated for this purpose (*e.g.* $Na_xMn_yNi_zFe_{0.1}Mg_{0.1}O_2$ from Passerini and co-workers).[21] Recently, Prussian blue analogues (PBAs) have also been proposed as positive-side materials for NIB.[22] [23]

In terms of safety, NIB show more advantages than LIB, such as : *i*) non-dissolution of the negative -side aluminum current collector upon discharge[24] and *ii*) compatibility of hard carbon with organic solvents.

Metal ion batteries are undoubtedly a valid option to store energy, especially looking towards the integration of renewable sources into the whole energy supply. LIB are especially suitable for mobile applications, but their usage as large scale energy storage devices is still under development, mostly due to the safety concerns. Nevertheless, some large scale storage systems are already in operation, as described by a recent report from the International Renewable Energy Agency (IRENA)[2]. In 2016, Low Carbon LIB in Glassenbury UK presented an installation showing 40 MW power, in 2017 AES-SDG&E LIB storage in California USA presented 30 MW and 120 MWh LIB system. [3]. Importantly, long-time prospects for permanent integration at grid-level of LIB are challenged by energy safety and environmental concerns (*e.g*. fire hazards from the organic solvents), as well as cost effective scale-up and battery lifetime and cost (LCOS).[25] In this case, NIB can be considered more promising solutions, mainly in terms of materials safety. Nonetheless, the technology is not mature enough for a large-scale deployment.

1.2.2 Electrochemical capacitors

Among EESSs other systems are electrochemical capacitors (EC) (*i.e*. supercapacitors). In EC, energy is stored in the capacitor of the electric double layer (EDL) that is formed at the interface between the electrolyte (aqueous or non-aqueous) and the electrode.[26] EC have lower energy density compared to lead-acid batteries, but they can cycle tens of thousands of times and they are more powerful than batteries (fast charge and discharge capability). [26]

Supercapacitors typically have high power density, long cyclic stability and high safety, and thus they can be considered as an alternative or complement to rechargeable batteries in applications that require high power delivery or fast energy harvesting.[27] Xia and co-workers[27] compared the charge storage mechanism of supercapacitors with those in batteries and with pseudo-capacitors (with intercalation behavior) (***Figure 1.5***).

[2] IRENA (2019), Innovation landscape brief: utility-scale batteries, International Renewable Energy Agency (IRENA), Abu Dhabi.

3 The Energy Disruption Triangle. D. C. Fessler.

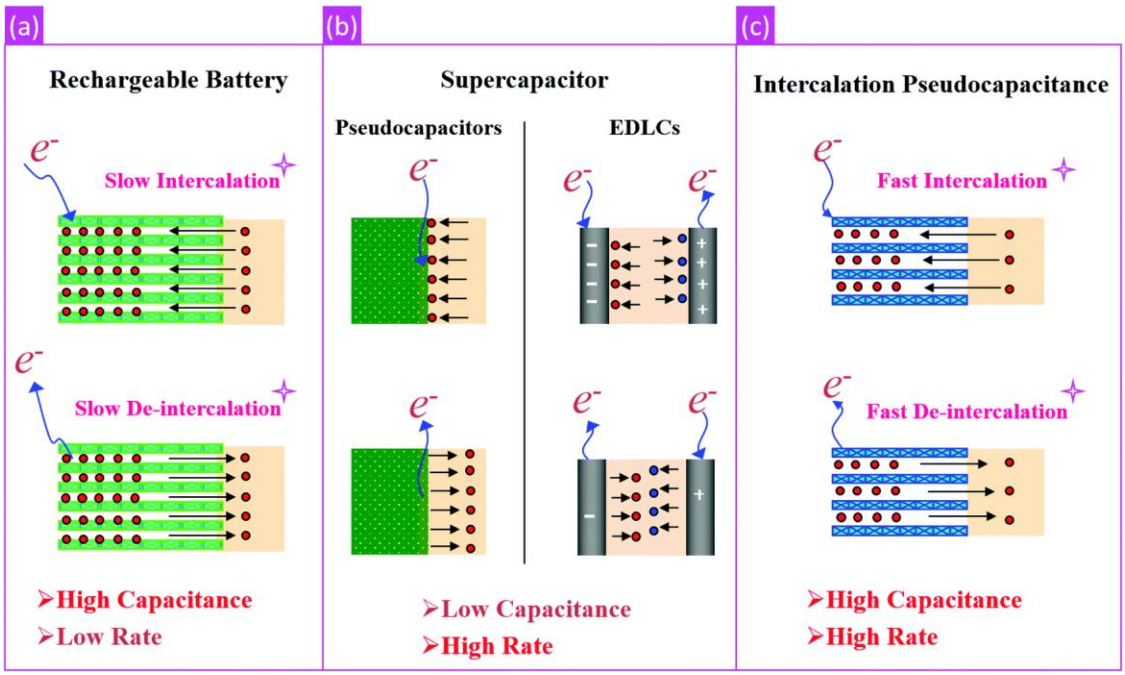

Figure 1.5 Charge storage mechanism in rechargeable batteries (a), supercapacitors (b) and pseudo-capacitors (c). This figure is reproduced with permission from the work of Xia and co-workers at ref. [27], Copyright 2020, Royal Society of Chemistry.

In rechargeable batteries (***Figure 1.5a)***), the capacity depends mainly on the intercalation (and de-intercalation) reactions of cations (H^+ or Li^+) within the crystalline structure of electrode materials, coupled with the redox reactions of metal ions within the crystalline structure. [27] As an example LIB show exactly this electrochemical behavior.

In supercapacitors (***Figure 1.5b)***) the capacitance rises from surface reactions of electrode materials, including electrochemical adsorption/desorption of cations and anions at the electrode/electrolyte interface (*i.e.*, capacitive behavior) and surface faradic redox reactions (*i.e.*, pseudocapacitive behavior).[27] Intercalation pseudocapacitance (***Figure 1.5c)***) relays on the intercalation/de-intercalation of cations (*e.g.* Li^+, Na^+, K^+, and H^+) in the bulk of active materials, but it is not limited by the diffusion of cations within the crystalline framework of active materials. [27] In cation-intercalated pseudocapacitance the advantage of batteries (*i.e.* charge storage in the bulk of the electrode materials) is united with the advantage of supercapacitors (*i.e.* charge storage without diffusion control). [27]

1.3 Redox flow batteries (RFB)

RFB are particularly suitable for energy storage at stationary level because of their decoupled power and energy capacity.[4] The power is determined by the size and number of electrochemical cells and the energy capacity is linked to the volume of the redox liquid electrolytes, where the energy is stored.[4] This unique characteristic makes RFB scalable and flexible as compared to other storage devices.

According to Skyllas-Kazacos[27], early works on redox batteries began in the 1970s, with the development of the iron-chromium battery by NASA.[28] Later, at the University of New South Wales, the group of Skyllas-Kazacos[27], invented the famous vanadium redox flow battery (VRFB), which is the largest type commercialized. The high interest and impact that VRFB are generating can be told by the industrial installations active all around the world (*e.g*. 1996, Sumitomo Electric Industries Japan, VRFB, 450 kW/900 kWh, 2013, Ecole Polytechnique Fédérale de Lausanne (EPFL) Switzerland, VRFB, 200 kW/400 kWh, 2015 Dalian Rongke Power China, VRFB, new generation of 200 MW/800 MWh storage). A general overview on the working principle of the VRFB is shown later in this chapter.

Nonetheless, RFB (and mainly VRFB) still face important challenges, such as:

i) Enhance the energy storage capacity

ii) Minimize the cost of the electrolytes to promote higher commercialization

iii) Find alternatives to vanadium, indeed, although it is stable its price is too volatile and too high on average for globally ubiquitous deployment in large-scale RFB.[25]

As a result research recently focused on the development of RFB where electrolytes can be synthesized from earth abundant elements, including inorganic (*e.g*. Fe and its complexes) and organic (*e.g*. C, N, O, S, *etc*.).

1.3.1 Working principle of a RFB

RFB store energy in liquid electrolytes composed of dissolved redox-active species. The electrolytes are placed in two separated external reservoirs (***Figure 1.6***). When the flow battery is operating, charging and discharging processes occur. Upon charging at the positive electrode, an oxidation reaction is observed, while a reduction reaction occurs at the negative electrode. Upon discharging, the opposite electrochemical reactions take place. Interconversion between stored chemical and electrical energy upon operation is facilitated by pumping the liquid electrolytes through an electrochemical cell.[25] Inside the electrochemical cell, redox reactions take place on the surface of porous electrodes separated by a separator (often an ion-exchange membrane).

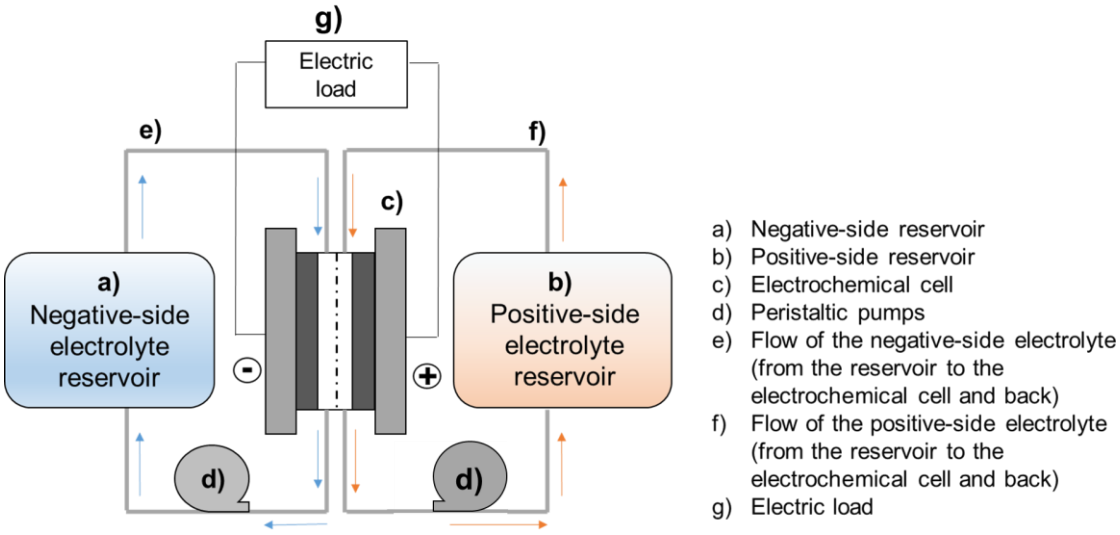

Figure 1.6 Graphical schematic of a RFB. All the components are detailed in the legend beside the figure.

In RFB the theoretical volumetric charge (Q_V) (*i.e.* the amount of electrical charge stored in a volume) can be calculated from the expression in ***eqn. 1.2***:

eqn. 1.2 $$Q_V = n \cdot c \cdot F \cdot V \ \text{(C)}$$

Where, n is the number of electrons involved in the redox reaction, c is the concentration of the electro-active species in the electrolyte (in $mol \cdot L^{-1}$), F is the Faraday constant (96485 $C \cdot mol^{1}$) and V the volume of the electrolyte (in L). The volumetric charge (Q_V) calculated from the expression in ***eqn. 1.2*** is expressed in Coulomb (C), although it is also common to see it in milli-ampere hour (mAh) (1 mAh = 3.6 Coulomb).

The expression in ***eqn. 1.2*** introduces already one important aspect in flow batteries, which is the solubility limit related to the concentration of the electro-active species in the electrolyte. Aqueous RFB

(focus of this thesis) exhibit 25-40 $Wh \cdot L^{-1}$ volumetric energy density, as compared to LIB with an energy density above 250 $Wh \cdot L^{-1}$.

Energy density in RFB (and in particular in aqueous RFB) represents a fundamental issue, which should receive great attention to facilitate the growth of this technology in the storage scenario. This thesis, is proposing a promising approach to enhance energy density in aqueous RFB.

In RFB performances are usually presented in terms of energy efficiency, which correspond to the product of the voltage efficiency and Coulombic efficiency. Their definitions are provided below:

i) *Voltage efficiency* (η_V) is given by the ratio between the charging and discharging voltage. It represents the reversibility of the system. [7] The voltage efficiency, according to Skyllas-Kazacos *et al*.[27] can be defined as (***eqn.1.3***)

eqn. 1.3[27]

$$\eta_v = \frac{\oint V_{dis}\,dt}{\oint V_{ch}\,dt} \times 100$$

The voltage efficiency is strictly related to some losses in the flow battery system, such as ohmic resistances, activation overpotential.[27] In addition, the voltage efficiency can be maximized by reducing the resistance of all the components in the cell, in particular, utilizing electrode materials with high electrical conductivity, good electroactivity and high surface area.[27] An example is the use of porous electrodes to improve the surface area creating flow-fields for the electron transfer reactions.[27]

ii) *Coulombic efficiency* (η_C) is given by the ratio between the amount of electrical charge during charging and discharging. This parameter is ranging with the crossover of electro-active species across the separator and side-reactions (hydrogen or oxygen evolutions).[7] ***Eqn. 1.4*** provides the general formula for the Coulombic efficiency. Coulombic efficiency can be maximized by reducing side-reactions and self-discharge processes in the electrolytes. It usually decreases at both high and low current densities. Indeed, the low current density decrease is associated with greater degree of self-discharge across the membrane at the longer charging and discharging times[27], while the drop-off at high current densities is produced by the greater rate of irreversible side reactions during charging. [27]

eqn. 1.4[27]

$$\eta_C = \frac{\oint I_{dis}\,dt}{\oint I_{ch}\,dt} \times 100$$

iii) *Energy efficiency* (η_E) is the product of these two efficiencies. The energy efficiency is an estimation of the energy recovered from the battery as compared to the amount of energy used to charge the battery. [7] It is as well an indication of the general performance of the flow cell. A general formula for energy efficiency is given in ***eqn. 1.5***. [26]

eqn. 1.5[27]

$$\eta_E = \eta_V \bullet \eta_C$$

In RFB another important definition is the state of charge (SOC), as in ***eqn. 1.6***. The SOC is a measure of the extent to which the half-cell reactions have taken place during charge and discharge cycles.[27] $E_{\text{cell OCP}}$ is the theoretical open circuit potential (OCP) of the cell and $E^0_{\text{cell OCP}}$ is the formal potential or theoretical OCP.[27] For most chemistries, any changes in the oxidation state of the electroactive species in solution will give rise to color changes that can often be used for the qualitative determination of SOC.[27]

eqn. 1.6[27]

$$E_{cellOCP} = E^0{}_{cellOCP} + \frac{RT}{nF}\ln\left(\frac{SOC}{1-SOC}\right)$$

1.3.2 Main components in the electrochemical cell

The process of designing a RFB (even at laboratory-scale) can be challenging since many aspects need to be taken into consideration: for instance, the electrolytes (if aqueous or non-aqueous) and their chemistries (solubility limit, operational pH (if aqueous), temperature, viscosity and conductivity). Consequently, the choice of the components in the electrochemical cell is generally made according to the type of electrolytes. The main components in the electrochemical cell are illustrated in ***Figure 1.7***:

a) a') Negative and positive-side end plates (to close the system)

b) b') Negative and positive side current collectors (usually made of graphite, titanium or copper)

c) c') Gaskets (separators, usually made of silicon or derivatives)

d) d') Porous electrodes (usually made of carbon or graphite, here the redox processes take place)

e) Separator (it avoids the direct mix of the two electrolytes)

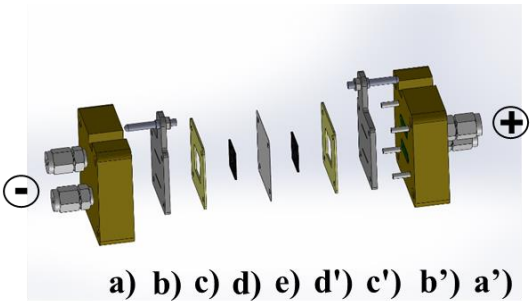

a) a') Negative and positive side end-plates
b) b') Negative and positive side current collectors
c) c') Gaskets
d) d') Porous electrodes
e) Separator

Figure 1.7 Graphical schematic of an electrochemical cell of a RFB. All the components are illustrated and defined in the legend close to the figure.

As displayed in ***Figure 1.6***, the electrochemical cell is directly connected to the storage reservoirs to/from where the liquid electrolytes flow. Among all the components of the electrochemical cell two need to receive greater attention: *i)* electrode materials and *ii)* separators, since they regulate the redox reactions and cross-over of the entire system.

I) <u>Electrode materials</u>

There are some important requirements that an electrode for flow batteries should possess:

i) Porosity

ii) Conductivity towards the charge transfer reaction

iii) Chemical and electrochemical inertness

In particular, considering a general electrode reaction $\mathrm{Ox} + ne^- \rightarrow \mathrm{Red}$, two steps are occurring:

i) Mass transfer of the redox-active species (Ox) from the bulk of the electrolyte solution to the electrode surface.

ii) Electron transfer at the electrode surface: the redox-active species is reduced or oxidized through the transfer of the electron from the electrode surface.

Moreover, secondary reactions like surface reactions (*e.g.* adsorption, desorption, electrodeposition) can take place too, [29] hence, it is important to understand from which step the whole electrochemical mechanism is governed and at least two options are possible:

i) The electrochemical process is diffusion-controlled (*e.g.* controlled by the mass-transfer from/to the bulk/electrode surface)

ii) The electrochemical process is kinetically-controlled (*e.g.* controlled by the electron transfer kinetics between the redox active species and the electrode surface).

Additionally, an electrochemical reaction is defined “reversible” when the rate determining step (*e.g.* the step characterized by the sluggishness velocity in the overall process) is under diffusion control, “quasi-reversible” when the rate of the electron transfer process is in the same order as the rate of the diffusion process and “irreversible” when the rate determining step is under kinetic-control (*e.g.* electron transfer control).[25 26]

Electrodes play a delicate role in the electrochemical conversion of the redox-active species. In general, carbon-based electrodes, such as felts, papers and cloths are widely used in RFB to provide redox-active sites for electro-active species, because of their high electrical conductivity (***Figure 1.8***).[31] These electrodes can be also improved by pre-treating the surface (*i.e*. heat pre-treatment, electrochemical pre-treatment and functionalization with some electrocatalytic materials[4]), especially to remove oxides or other impurities that can affect the kinetics of the main redox reactions and also to be more hydrophilic.

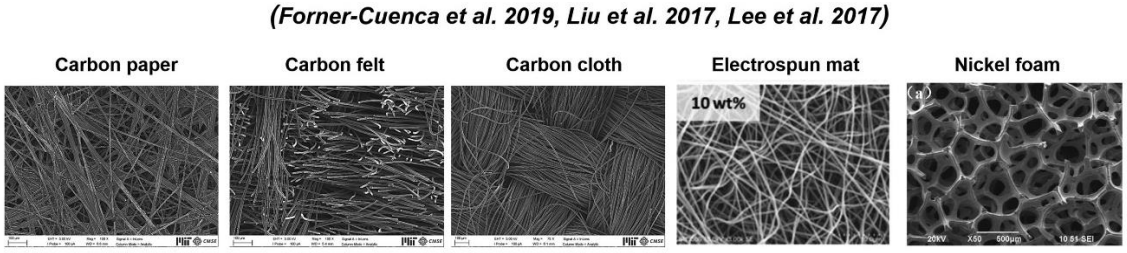

Figure 1.8 A selection of pristine electrode substrates including carbon paper, felt, cloth, electrospun mat, and nickel foam featuring distinct microstructures. This image is reproduced with permission from the work of Brushett at ref. [32] Copyright 2020, Elsevier.

Extensive research on the development of electrodes for RFB began with Skyllas-Kazacos and co-workers[33], with carbon–polymer composite electrodes for VRFB. Recently, Brushett and co-workers[32] summarized recent developments in the design and characterization of porous electrodes for RFB, with a focus on understanding and controlling both the microstructure and surface chemistry, which broadly align with mass transport and reaction kinetics. [32] The authors explain how the manufacturing process may affect the behavior of the flow cell during operation. In particular, the authors believe that engineers must reach a delicate balance between generating high surface areas to maximize reaction kinetics, providing small pores such that diffusion distances are minimized, and simultaneously incorporating large pores to minimize the pressure drop that occurs through the electrode. [32]

II) Separators

Another essential component in RFB is the separator. The presence of a separator is necessary to avoid direct electrolytes mixing, which can affect the life time and the efficiency of the installation. RFB can employ specific membranes as separators between the electrodes.[25] Their general characteristics and requirements are summarized below[34]:

i) Good ion-conductivity to minimize the ohmic drop (*i.e.* or *IR* drop (ΔE_{ohm}) is the resistance of the media during the flow of electrical current through the cell).[35] A significant ohmic drop can affect the cell voltage.

ii) Strong ion-selectivity to avoid electrolyte crossover. The crossover can lead either to short lifetime or to poor efficiency of the battery.

iii) Chemical stability upon cycling. This feature contributes to the battery lifetime.

iv) Rather low cost and high commercial availability.

In RFB, mainly three types of membranes are employed: [36]

i) Ion-exchange (cation and anion)

ii) Non-ionic

iii) Amphoteric

Among ion-exchange, cation-exchange membranes can be generally classified in three categories:

i) Perfluorinated

ii) Partially fluorinated

iii) Non-fluorinated[4 34]

Nafion™ is the most well-known fluorinated cation-exchange membrane (***Figure 1.9***).[4] It constitutes a polymeric chain of polytetrafluoroethylene (Teflon) characterized by highly hydrophobic C−F bonds and by a termination of sulfonic acid (HSO_3^- groups). [4] The proton conductivity in Nafion™ is *ca.* 0.1 $S \cdot cm^{-1}$ at room temperature.[29]

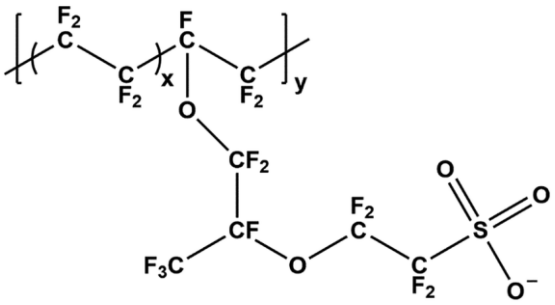

Figure 1.9 Molecular structure of a Nafion membrane. The image is reproduced with permission from the work of Baker at ref.[38], copyright 2020, Royal Society of Chemistry.

Anion-exchange membranes (AEM) contain fixed cationic groups with mobile anions, common cationic head-groups are shown in ***Figure 1.10***.[4 39] AEM repel cations of the solutions and allow anions to be transported.[40] The conductivity in AEM is often improved by increasing the number of ammonium sites, without a consequent increase of cation permeability, since cations are repelled by the ammonium cations.[40]

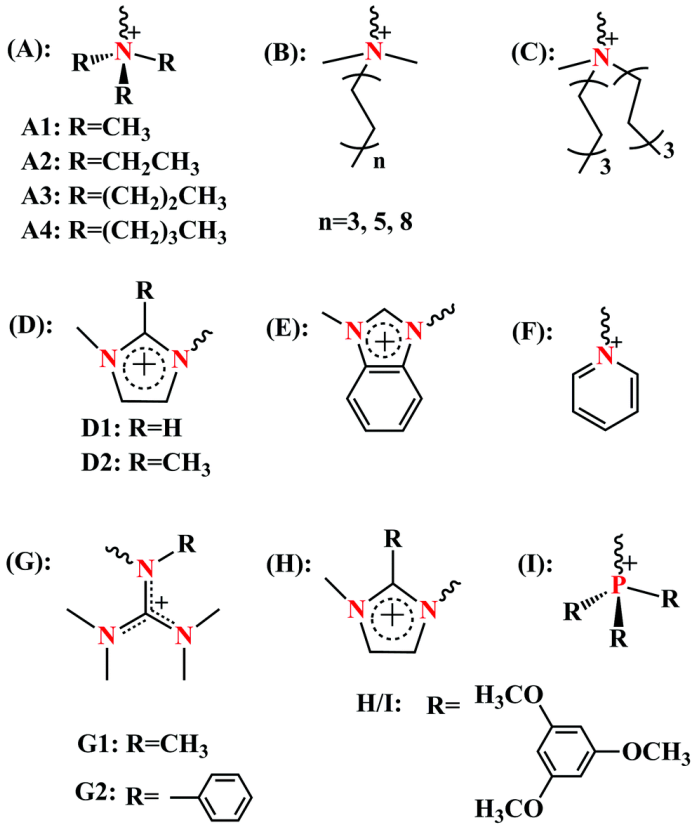

Figure 1.10 Common cationic head-groups for AEM. This image is reproduced with permission from the work of Xu at ref. [39] Copyright 2020, Royal Society of Chemistry (RSC).

1.3.3 Different chemistries in RFB

Two main classes of RFB are distinguished according to the type of supporting electrolyte: *i*) non-aqueous and *ii*) aqueous. In this thesis, only aqueous RFB (ARFB) are studied, therefore, different redox-active species will be introduced later. Among ARFB, two categories can be distinguished according to the nature of the redox-active species dissolved in the supporting electrolyte:

i) Aqueous inorganic RFB (AIRFBs)

ii) Aqueous organic RFBs (AORFB)

AIRFB operate in acidic environment, a table of comparison is provided later (***Table 1.4***). In these systems the concentration of the acidic supporting electrolyte can vary from 1 up to 5 M.[40] The conventional acid is sulfuric, but hydrochloric can also be used, especially when the anodic redox couple can oxidize at a potential lower than the one corresponding to the oxidation of chloride to chlorine[40] (E^0 = 1.36 V *vs.* SHE). [40] Interestingly, as discussed by Amstutz *et al*. [40], the nature of the acid and its concentration may affect the standard reduction potential of some redox couples [40] , as, for instance, in the case of cerium.

1.3.3.1 Aqueous inorganic RFB (AIRFB): VRFB and systems based on VRFB

The most well-known example of AIRFB is the VRFB (***Figure 1.11***), which is based on the four redox states of vanadium. As previously mentioned, VRFB attracted a lot of success over the last 30 years and commercial installations are in operation all over the world.

VRFB performances are summarizes in ***Table 1.3***:

Table 1.3 Main performance and characteristics of VRFB

Characteristic and units	***Value***
Range of power (kW)	10 – 10’000
Range of capacity (kWh)	10-50’000
Lifetime (years/ # of cycles)	10-15/ 10’000-15’000
Volumetric energy density ($Wh \cdot L^{-1}$)	35
Cell voltage (V)	1-2.5
Time of charge/discharge (h)	1-10
Energy efficiency (%)	70-80

A general schematic of the working principle of VRFB is depicted in ***Figure 1.11***.

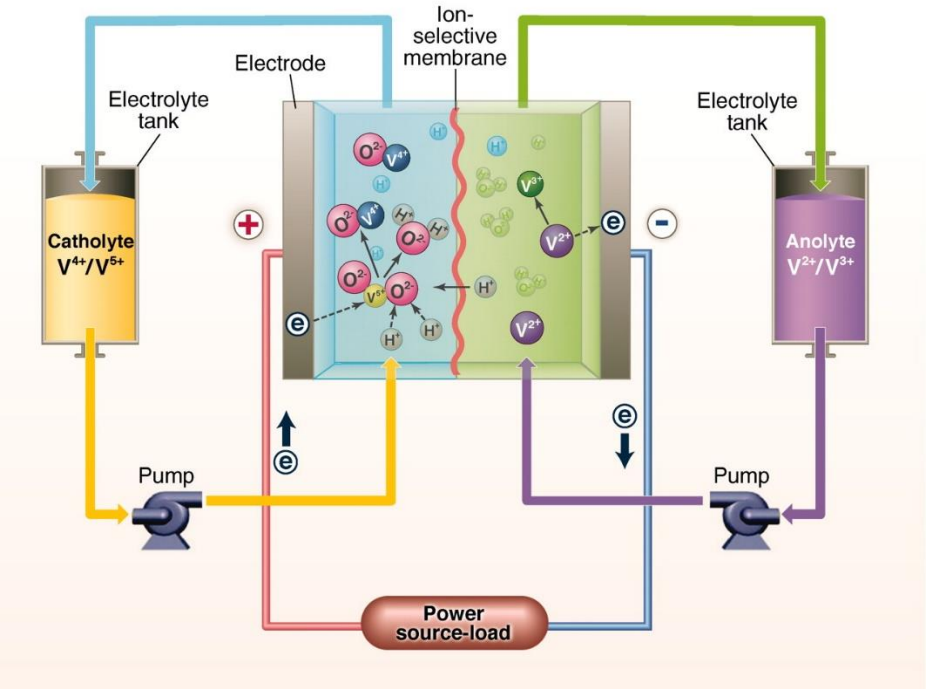

Figure 1.11 Schematic of the working principle of VRFB, where the V^{II}/V^{III} redox couple circulates through the negative compartment (negative-side electrolyte), whereas the V^{IV}/V^{V} redox couple circulates through the positive compartment (positive-side electrolyte). This image is reproduced with permission from the work of Kinter-Meyer at ref. [41], copyright 2020, American Chemical Society (ACS).

The redox reactions of the VO_2^+/VO^{2+} and V^{2+}/V^{3+} redox couples can be described as follows (***eqn. 1.7 and 1.8***)[42]:

eqn. 1.7 (upon charging at the positive-side electrolyte)

$$VO^{2+} + 2H^+ \rightarrow VO_2^+ + H_2O - e^-$$

E^0 = 1.00 V *vs.* SHE

eqn. 1.8 (upon charging at the negative-side electrolyte)

$$V^{3+} + e^- \rightarrow V^{2+}$$

E^0 = −0.26 V *vs.* SHE

The discharge reactions occur in the opposite direction.

A similar system to the VRFB is the vanadium-oxygen (abbreviated as VOx) installation, demonstrated by Piwek *et al* (***Figure 1.12***).[43] The VOx system is proposed to be integrated in the "dual-circuit" RFB by Girault and co-workers[44] with the goal of providing a high rate of conversion while minimizing the energy required. The following reactions take place in the VOx system:

i) V–O_2 cell:

$$2H_2O \rightarrow O_2 + 4H^+ + 4e^- \quad E^0 = 1.23\ \text{V } \textit{vs.}\ \text{SHE}$$ ***eqn. 1.9***

$$VO_2^+ + 2H^+ + e^- \rightarrow VO^{2+} + H_2O \quad E^0 = 1.00\ \text{V } \textit{vs.}\ \text{SHE}$$ ***eqn. 1.10***

ii) VRFB

$$VO^{2+} + H_2O \rightarrow VO_2^+ + 2H^+ + e^- \quad E^0 = 1.00\ \text{V } \textit{vs.}\ \text{SHE}$$ ***eqn. 1.11***

$$V^{3+} + e^- \rightarrow V^{2+} \quad E^0 = -0.26\ \text{V } \textit{vs.}\ \text{SHE}$$ ***eqn. 1.12***

iii) Hydrogen circuit

$$V^{3+} + e^- \rightarrow V^{2+} \quad E^0 = -0.26\ \text{V } \textit{vs.}\ \text{SHE}$$ ***eqn. 1.13***

$$2H^+ + 2e^- \rightarrow H_2 \quad E^0 = 0\ \text{V } \textit{vs.}\ \text{SHE}$$ ***eqn. 1.14***

The VOx system at laboratory-scale reached a total energy efficiency in the range of 42–62%, which is a good result considering the *tandem* efficiency of a VRFB and of an electrolyzer. [43]

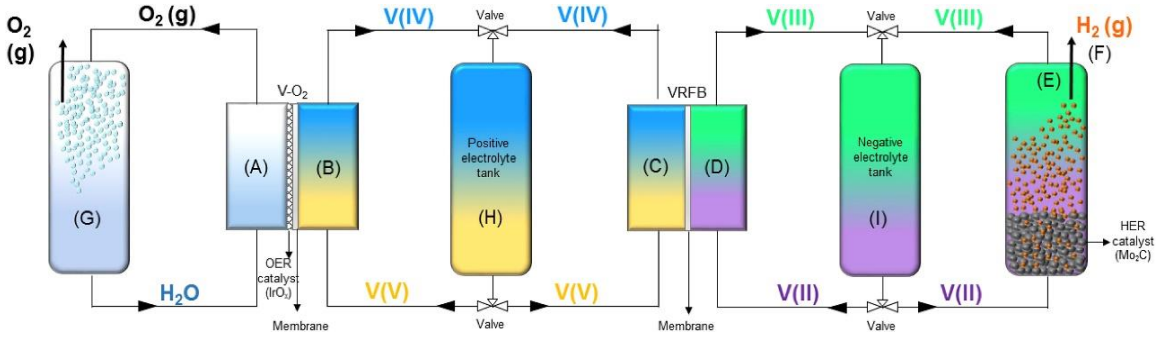

Figure 1.12 Schematic of the VOx system. The image is reproduced with permission from the work of Piwek et al. at ref. [43], copyright 2020, Elsevier.

In the table below some of the most extensively studied AIRFB are summarized:

Table 1.4 Summary of the most extensively studied AIRFB in acidic supporting electrolyte.

Flow battery	*Redox Couples*		*Supporting electrolyte*	*Performances and remarks*	*Ref.*
All-Vanadium	VO_2^+/VO^{2+}	Positive-side	H_2SO_4	• Low electrolyte crossover (all Vanadium) • Low energy density (~10-50 $Wh \cdot L^{-1}$) • 1.6 M operating concentration	[22–25]
	V^{3+}/V^{2+}	Negative-side			
Vanadium-polyhalide	$BrCl_2^-/Cl^-$	Positive-side	HCl	• Cell potential of 1.3 V • CE and VE = 80% • Toxicity of bromine	[26]1
	V^{3+}/V^{2+}	Negative-side			
Vanadium-Cerium	Ce^{4+}/Ce^{3+}	Positive-side	H_2SO_4	• Cell potential of 1.78 V • Toxicity of Cerium	[27]1
	V^{3+}/V^{2+}	Negative-side			
Vanadium-Manganese	Mn^{3+}/Mn^{2+}	Positive-side	H_2SO_4	• Complicated management of Manganese	[28]
	V^{3+}/V^{2+}	Negative-side			
Vanadium-air	H_2O/O_2	Positive-side	H_2SO_4	• Low efficiency • Complicated management	[29-30]
	V^{3+}/V^{2+}	Negative-side			
Iron-Chromium	Fe^{3+}/Fe^{2+}	Positive-side	HCl	• Slow kinetic of Chromium • Toxicity of Chromium • Fast kinetic of Iron	[32]
	Cr^{4+}/Cr^{3+}	Negative-side			
Zinc-Cerium	Ce^{4+}/Ce^{3+}	Positive-side	CH_3SO_3H	• Zinc dendrites • Toxicity of Cerium	[34]
	Zn^{2+}/Zn	Negative-side			

1.3.3.2 Aqueous organic RFB (AORFB): advantages and challenges

Some AIRB, such as those including manganese and cerium redox couples in the electrolyte are particularly difficult to manage, due to corrosion, stability and toxicity concerns. Undeniably, the presence of a strong acid in these systems rises concerns about safety and environmental risks, which recently led researches to consider other options for making less harmful electrolytes. In this case, an alternative can be represented by organic carbon-based redox-active molecules (ROM). Indeed, shifting towards these electrolytes would bring some benefits:

i) Decrease the costs of the electrolyte, counting on the higher abundance of the raw materials and precursors.

ii) Decrease some costs in the design of the electrochemical cell, in particular the usage of expensive separators (for instance Nafion^{TM}), employing affordable membranes.[45] A great example in this case is presented by Janoschka *et al*.[46] showing a RFB system operating with a size-exclusion[46] membrane using polymer electrolytes from organic species in aqueous medium.

Nevertheless, chemical stability can be a great challenge in the development of aqueous organic electrolytes for RFB. Recently, Aziz and co-workers[25] have proposed an interesting review where the chemical stability of organic molecules is deeply discussed also in terms of levelized costs of the storage chemistry. In particular, if the present value of a series of future replacement costs for an AORFB is lower than the capital costs savings from using an organic system rather than a vanadium system, then the lower-cost organic system may be the more economically preferable option. (***Figure 1.13***).[25]

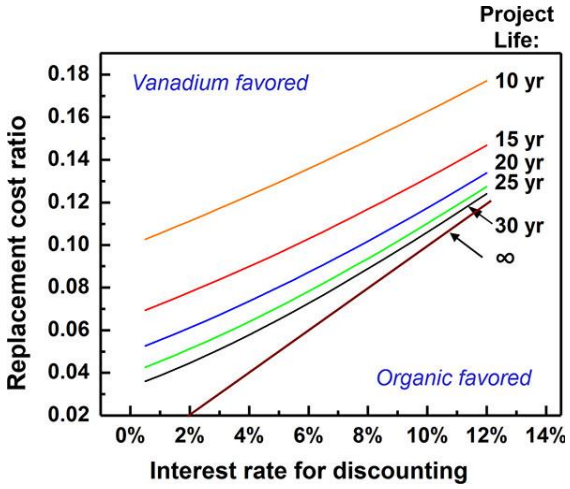

Figure 1.13 Breakvalue of the replacement cost ratio vs. interest rate for discounting, assuming project lifetime as indicated. Adapted with permission from reference [25]. Copyright 2020 American Chemical Society.

A variety of molecular engineering studies can be done to integrate extra moieties and change chemical properties in the redox organic molecules (ROM).[47] For example, introduction of electron-donating groups in the molecular structure (*e.g.* hydroxyl, OH^-) and electron-withdrawing moieties (*e.g.* sulfonate, SO_3^-), can move the redox potential of the molecule (more negative) or (more positive), respectively.[47] Moreover, as observed in many recent works [48] [49] [50] [51] [52] [53] the addition of bulky ammonium groups can increase both solubility and electrochemical rate.[47]

A closer look to some of the ROM for AORFB is provided in ***Figure 1.14***.

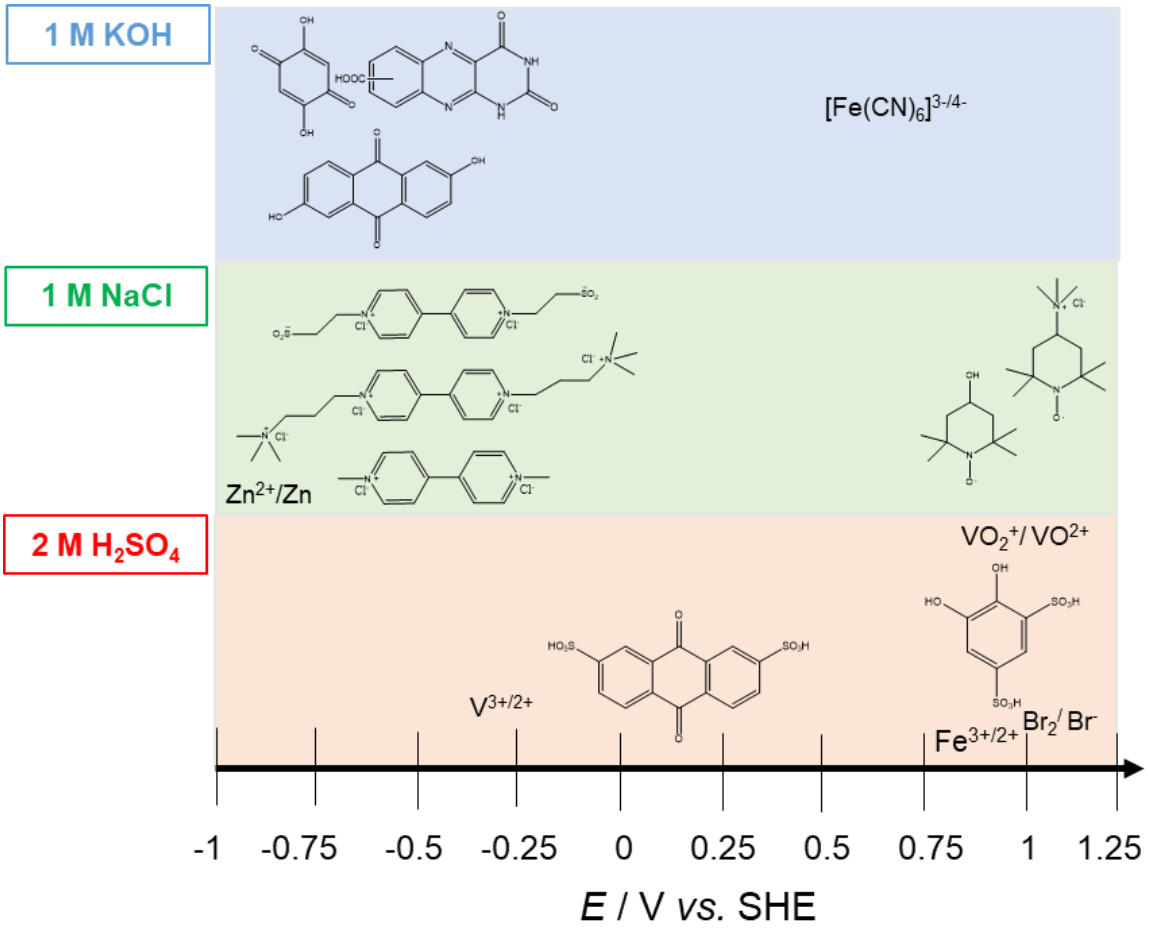

Figure 1.14 Schematic of some common organic and metal-free redox active species in aqueous RFBs. For each material the redox potential is depicted on the x-axis (vs. standard hydrogen electrode – SHE). In the 2 M H_2SO_4 section (from the left) is represented the anthraquinone-2,7-disulfonic acid, and the 1,2-hydroxybenzene-4,6-disulfonic acid. In the 1 M NaCl section (from the top left) are represented: the 1-[3-(trimethylammonio)propyl]-1'-(3-sulfonatopropyl)-4,4'-bipyridinium dibromide, the 1,1'-bis[3-(trimethylammonio)propyl]-4,4'-bipyridinium tetrabromide and the methyl viologen. Then from the top right there are the N,N,N -2,2,6,6-heptamethylpiperidinyl oxy-4-ammonium chloride and the 4-Hydroxy-2,2,6,6-tetramethylpiperidine 1-oxyl. In the 1 M KOH section, from the top left there are the 1,4-Dihydroxycyclohexa-1,4-diene-3,6-dione, the alloxazine carboxylic acid, 2,6-dihydroxy-anthraquinone. This representation is adapted from reference [47].

Anthraquinone and derivatives are quite often employed in AORFB at acidic and alkaline pH. At acidic pH, the sulfonic acid groups imparted hydrophilicity and raised the solubility of AQS and AQDS to ~ 1 M at pH = 0.[54]

Aziz and co-workers[55] compared different anthraquinone derivatives (***Figure 1.15***). The authors investigated four anthraquinone derivatives as negative-side electrolytes for an aqueous quinone-bromide redox flow battery: anthraquinone-2-sulfonic acid (AQS), 1,8-dihydroxyanthraquinone-2,7-disulfonic acid (DHAQDS), alizarin red S (ARS), and 1,4-dihydroxyanthraquinone-2,3-dimethylsulfonic acid (DHAQDMS).[55] The authors discovered that DHAQDS and ARS undergo irreversible reactions on contact with bromine, which excludes their use against bromine, but not necessarily against other electrolytes, [55] however, they successfully demonstrated an AQS-bromide flow cell with higher open circuit potential and peak galvanic power density than the equivalent AQDS-bromide cell. [55] The average energy efficiency 73.5% is better than that of the AQDS cells, which have reported to be equal to 62% at the same current density at room temperature with a nearly identical positive-side electrolyte (3.5 M HBr, 0.5 M Br_2).

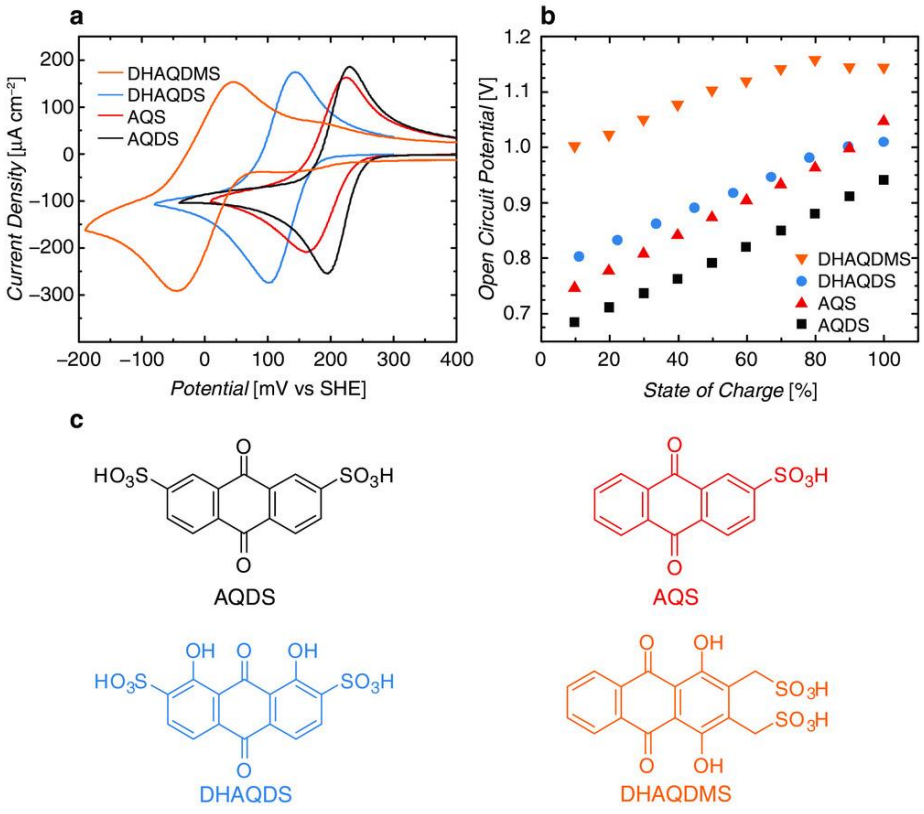

Figure 1.15 a) Cyclic voltammograms of AQDS (black), AQS (red), DHAQDS (blue), and DHAQDMS (orange), showing the decrease in reduction potential through chemical modification. b) Open circuit voltage as a function of state of charge for each quinone in a flow cell paired with the bromine-hydrobromic acid positive-side electrolyte. c) Structures of AQDS, AQS, DHAQDS, and DHAQDMS. This image is reproduced with permission from the work of Aziz and co-workers at ref.[55], copyright 2020, Wiley.

Anthraquinone derivatives look promising candidates even at alkaline pH for AORFB. In particular, at pH 12 Kwabi *et al*.[56] proposed the negative electrolyte material 4,4′-((9,10-anthraquinone-2,6-diyl)dioxy)dibutyrate (2,6-DBEAQ), six times more soluble than 2,6-DHAQ at pH 12 (***Figure 1.16***). The authors demonstrated that by pairing 2,6-DBEAQ with a potassium ferri-/ferrocyanide positive-side electrolyte and utilizing a non-fluorinated membrane, this near-neutral flow battery shows a capacity fade rate that is the lowest of any quinone and rivals the lowest ever reported for any flow battery in the absence of rebalancing processes. [56]

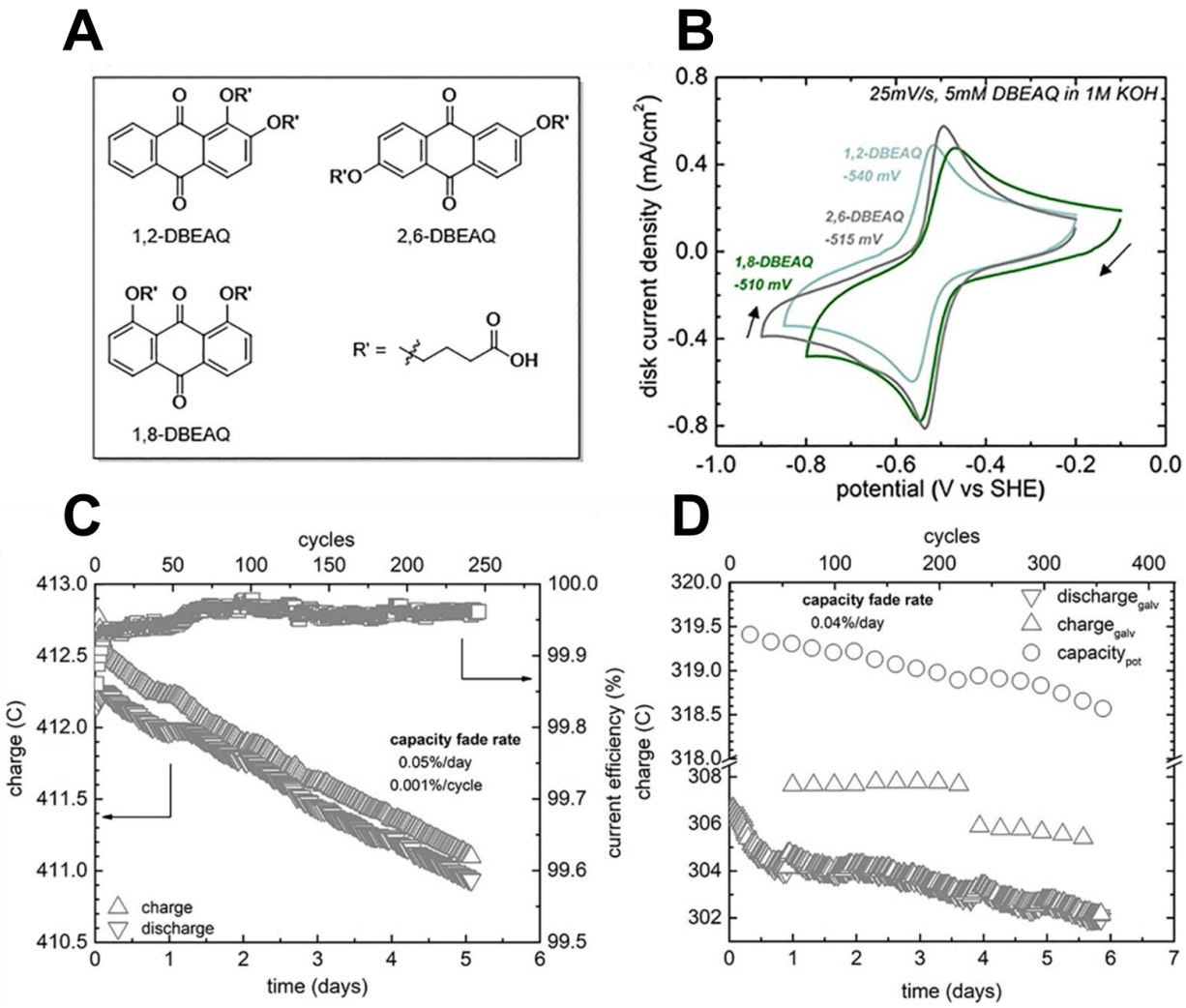

Figure 1.16 A) Chemical structures of 1,2-, 2,6-, and 1,8-DBEAQ. B) Cyclic voltammograms of 1,2- (blue), 2,6-(gray), and 1,8- (green) DBEAQ. The redox potential vs SHE of each isomer is indicated. C) and D) Extended Full Cell Cycling of 2,6-DBEAQ at 0.5 M and pH 12. These image is reproduced with permission from the work of Kwabi et al at ref. [56]Joule.

1.3.3.3. Electrolytes employed in AORFB at neutral pH

Table 1.5 summarizes some of the most well-known electrolytes for the positive and the negative-side of AORFB operating at neutral pH.

Table 1.5 Comparison of electrolytes employed in AORFB at neutral pH. Abbreviations: N,N,N -2,2,6,6-heptamethylpiperidinyl oxy-4-ammonium chloride (TEMPTMA), methyl viologen (MV), 1,1'-Bis[3-(trimethylammonio)propyl]ferrocene dichloride (BTMAP-Fc), bis(3-trimethylammonio)propyl viologen tetrachloride (BTMAP-Viologen), ferrocenylmethyl trimethylammonium chloride (FcNCl), 4-[3-(trimethylammonio)propoxy]-2,2,6,6-tetramethylpiperidine-1-oxyl (TMAP-TEMPO).

Positive-side electrolyte	***Negative-side electrolyte***	***Supporting electrolyte***	***Performances***	***Ref.***
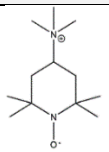 ***TEMPTMA***	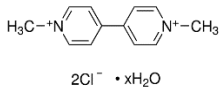 ***MV (hydrated form)***	$NaCl_{aq}$	54 Ah L^{-1} 1.4 V	51
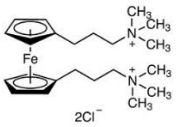 ***BTMAP-Fc***	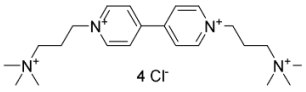 ***BTMAP-Viologen***	$NaCl_{aq}$	99% capacity retention 11% capacity fade/year	57
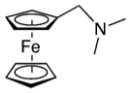 ***FcNCl***	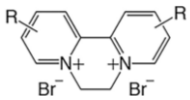 ***Diquat derivative***	$NaCl_{aq}$	99% capacity retention per cycle	58
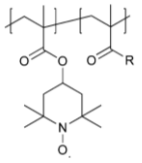 ***Poly-TEMPO***	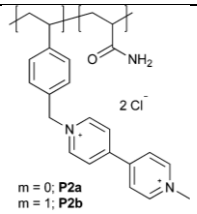 ***Poly-viologen***	$NaCl_{aq}$	1.12 V (inferred from graph in paper)	45
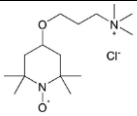 ***TMAP-TEMPO***	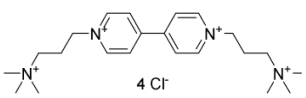 ***BTMAP-Viologen***	$NaCl_{aq}$	500 cycles, 1.12 V (at 50% SOC)	52

I) ROM at the positive-side of AORFB at neutral pH:

Recent works from Aziz[57] and Schubert[51 49 59] have identified two ROM for the positive and the negative-side of an AORFB. For the positive-side: (2,2,6,6-tetramethylpiperidin-1-yl)oxyl (TEMPO) and its own derivatives are quite well known. TEMPO is a highly chemically stable nitroxyl radical as compared to others because of the electron delocalization between the nitrogen and oxygen atoms and the steric protection of radicals from four methyl groups (CH_3). TEMPO is not soluble in water, but the addition of hydroxyl group (OH^-) makes it soluble (2.1 M in water).

Figure 1.17A) gives an overview of all the most extensively studied derivatives of TEMPO, including their solubility limits (***Figure 1.17B)***), along with the redox mechanism (***Figure 1.17C)***).

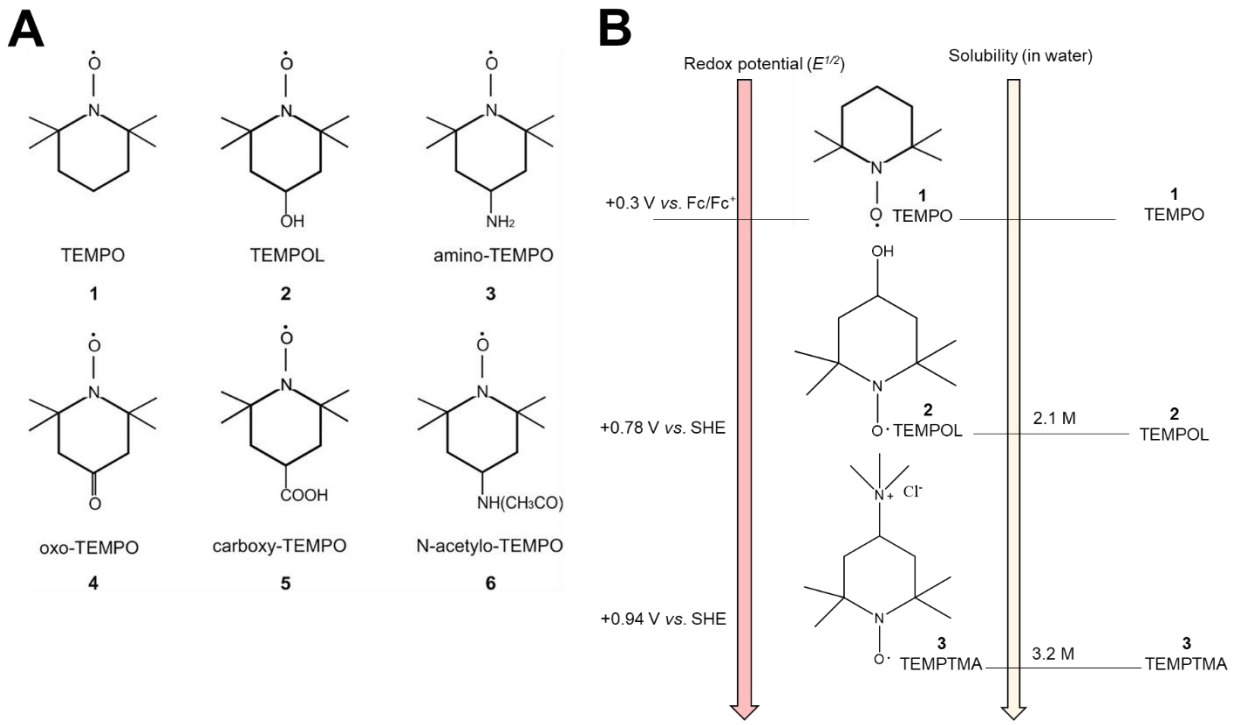

Figure 1.17 A) Different derivatives of TEMPO. B) Two of the most extensively employed derivatives of TEMPO in AORFBs at neutral pH. The molecular structures are reported along with solubility limits and half-wave potentials ($E^{1/2}$).

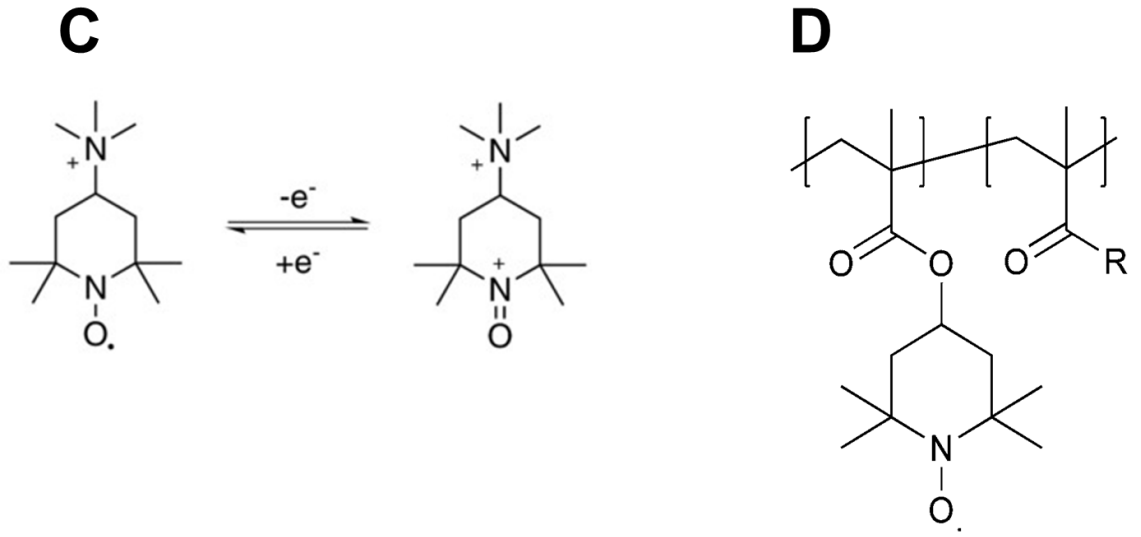

Figure 1.17 C) Redox reactions of TEMPO derivative upon charge (oxidation) and upon discharge (reduction). D) Molecular structure of TEMPO-polymer from the work of Schubert and co-workers. [45]

Schubert and co-workers[51] were recently very active in the functionalization of TEMPO. They synthetized a derivative known as N,N,N-2,2,6,6-heptamethylpiperidinyl oxy-4-ammonium chloride (TEMPTMA), by adding a tetramethylammonium chloride (TMA^+Cl^-) salt to the 4-position of the piperidine ring. The synthetic route is proposed in ***Figure 1.18***.

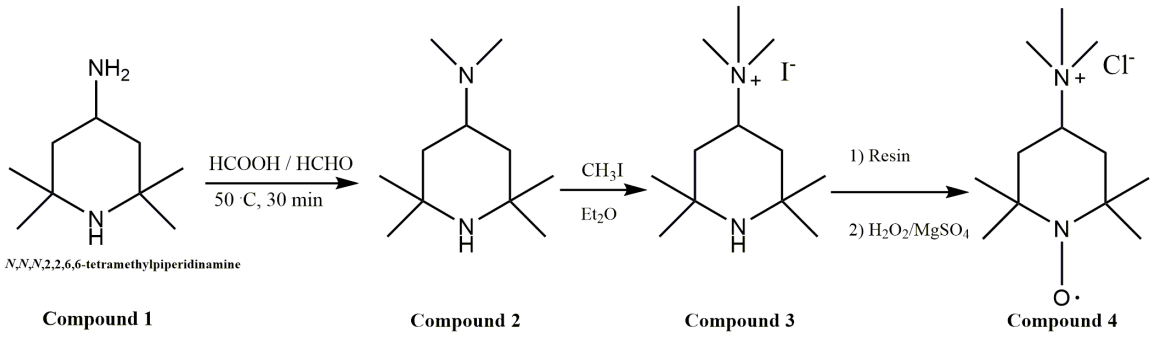

Figure 1.18 Synthetic route of TEMPTMA.

TEMPTMA is a very versatile molecule and it is often chosen for the following properties: *i*) high solubility (3.2 M in water and 2.3 M in 1 M $NaCl_{aq}$), *ii*) high redox potential (+0.944 V *vs*. SHE[59]), and *iii*) good chemical stability. In good agreement, in the present thesis TEMPTMA is used as positive-side electrolyte in an AORFB at neutral pH.

II) ROM at the negative-side of AORFB at neutral pH:

For the negative-side of an AORFB at neutral pH, viologen is often one of the most extensively ROM. The following section gives a brief overview on the chemistry of viologens, describing synthesis methods, redox properties and toxicity. Finally, a summary of the most extensively studied AORFB using viologen electrolytes at the negative-side and TEMPOs at the positive-side will be proposed. Importantly, a more detailed review about the chemical stability of viologens is proposed later in chapter 4, since a derivative from this class of ROM is experimentally used in this thesis.

According to Striepe *et al.*,[60] viologens, di-quaternized 4,4′-bipyridyl salts, have been well studied and published as early as the 1970s.[7] Due to their large investigation, several ways have been developed to synthesize viologens, and in a recent review Ding *et al.*[61] reported the most well-known (***Figure 1.19***).

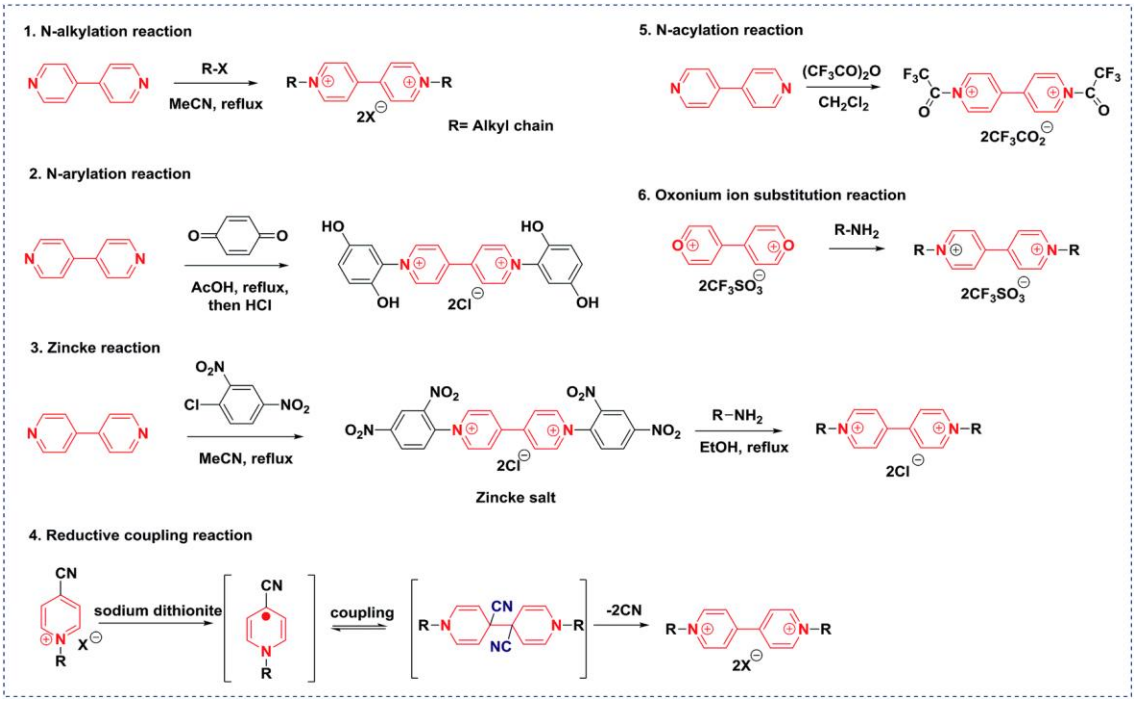

Figure 1.19 Scheme of the synthetic routes of viologen starting from 4,4'-dipyridine. This figure is reproduced with permission from the work of Ding et al. in ref.[61]. Copyright 2020, Royal Society of Chemistry.

The first synthetic route, which is the reaction between the 4,4'-bipyridine and a halogen, is the most common above all for obtaining products in high yield.[61] However, other methods are quite largely used, such as the Zincke reaction.[61] In general, viologens look like versatile candidates for energy storage devices, especially because of the three redox states,[60] the desirable electron-accepting capability, and the tunability of the nitrogen substituents with counter-ion(s).[60] The latter is an important aspect to modulate thermodynamic properties such as solubility and crystallinity in the molecule.[61] The following ***Figure 1.20***

shows the possible combinations of N-substituted groups and counter anions in the synthesis by N-alkylation reaction.[61]

Viologens synthesized with halides (*e.g.* Br^-, Cl^- and I^-) are soluble in protic solvents[61] (*i.e.* any solvent that contains a labile H^+), while viologens synthesized with triflate, PF_6^- or BF_4^- are soluble in aprotic solvents[61] (*i.e.* any solvent with no O–H or N–H bonds). Interestingly, as reported by Pande *et al.*,[62] the PF_6^- group is less hygroscopic (*i.e.* materials able to absorb a moisture), [62] while, the larger non-polar anions, $[TFSI]^-$, typically impart lower basicity and nucleophilicity (*i.e.* the ability of a nucleophile to react at an electron-deficient center)[63] and thus good solubility in polar organic solvents. [62]

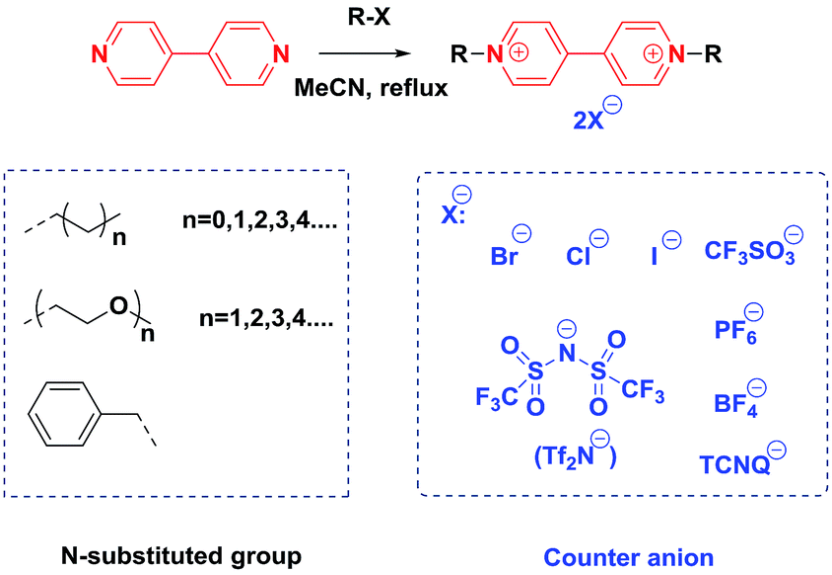

Figure 1.20 Scheme of the different functional groups (N–substituted) and counter anion in viologens. This image is reproduced with permission from the work of Ding et al. in ref 8. Copyright 2020, Royal Society of Chemistry.

Notably, the counter anions have an effect on the electrochromic properties of viologens. In this case, an interesting study was proposed again by Pande *et al.*[62], which shows the spectroelectrochemical transitions of asymmetric viologens in ion gel-based electrochromic devices, in presence of PF_6^- and $[TFSI]^-$ as counter anions, respectively.[62] In particular, the viologen with PF_6^- counter anion showed a color change from colorless to blue at 604 nm, producing an optical contrast of 35.4% and a coloration efficiency of 107.27 $cm^2 \cdot C^{-1}$ [62], consistently with the fact that the PF_6^- ion is chemically inert, small and it can escape from the electrode surface due to faster ion diffusion, which leads to faster bleaching. [62] On the other hand, the viologen functionalized with $[TFSI]^-$ as counter anion exhibited a long optical memory effect (140 min) [62], as compared to the previous one (maximum 35 min) [62] with also a higher coloration efficiency of 120 $cm^2 \cdot C^{-1}$. [62]

Among viologens, methyl viologen (MV) is one of the most largely employed ROM for electrochemical devices. MV is commonly known as paraquat[64] or 1,1′-dimethyl-4,4′-dipyridinium chloride.[9] It consists of a 4,4'-bipyridinium backbone and two methyl functional groups connected to the N atoms. The following ***Figure 1.21*** shows the molecular structure of MV.

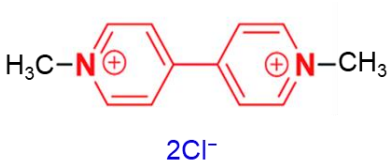

Figure 1.21 Molecular structure of methyl viologen (MV), paraquat or 1,1'-dimethyl-4,4'-dipyridinium chloride.

MV is characterized by three redox states:[60]

- ***i)*** A fully oxidized form (MV^{2+}), known for being relatively stable in air and at room temperature
- ***ii)*** A radical cation ($MV^{\bullet+}$), which corresponds to an intermediate redox state
- ***iii)*** A neutral form (MV), which is the fully reduced one.

The following ***Figure 1.22*** depicts the three redox transitions of MV along with the redox potentials and the corresponding colors.

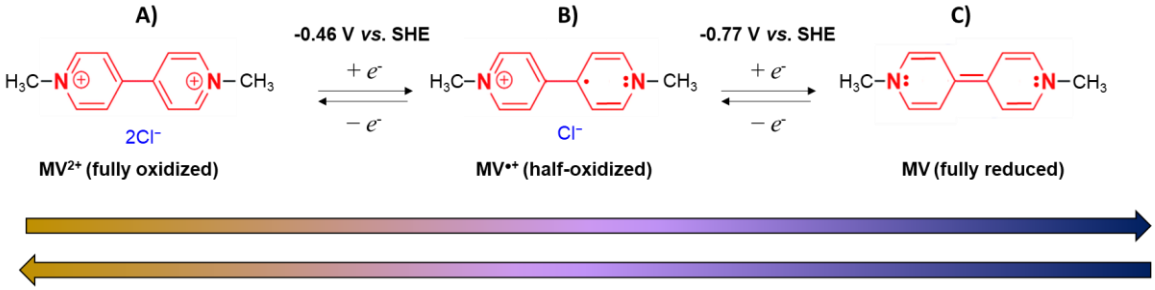

Figure 1.22 Redox states of MV: A) MV di-cation (MV^{2+}) fully oxidized. B) MV radical-cation ($MV^{\bullet+}$) half-oxidized state. C) MV in the fully reduced state (quinoid form). The redox potentials (vs. SHE) for all the transitions are reported. The arrows below the schematic represent the change in color according to the three different oxidation states.

Safety aspects of viologens

An interesting aspect when it comes to the usage of viologens in electrochemical energy storage devices, is the toxicity. According to Tsai *et al*.[65] MV is frequently used as herbicide: its excellent effect within plant cells in crop protection and horticultural[65] use makes it highly utilized. In particular, as described by Zielonka *et al*.[66], MV exercises its herbicidal activity by interfering with the intracellular electron transfer systems in plants through the inhibition of the reduction of nicotinamide coenzymes, $NADP^+$ to NADPH, during photosynthesis and the formation of reactive oxygen species that leads to the destruction of plant organelles.[66] Importantly, MV (but also viologens in general) are known for being toxic to human beings, with, the main affected organs after poisoning from viologens being the lungs and to a lesser extent the liver, kidneys, and heart.[66] The toxicity starts as soon as the fully oxidized form reduces to the radical-cation. This redox reaction involves the enzymatic system, which includes NAD(P)H-cytochrome P450 reductase, NADH-ubiquinone oxidoreductase (complex I), nitric oxide synthase, and xanthine oxidase.[66] The mechanism is represented in ***Figure 1.23***.

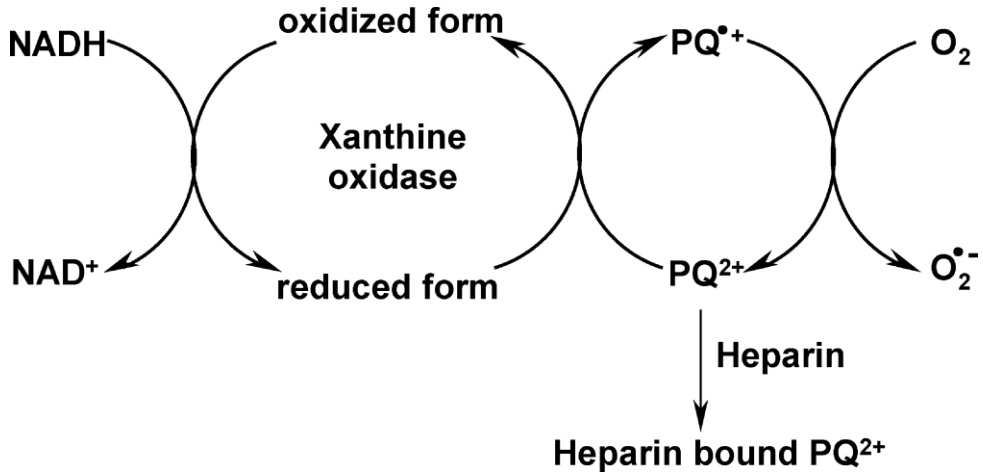

Figure 1.23 Redox reaction of MV (or paraquat, PQ in the schematic) and involvement with the enzymatic system, which includes NAD(P)H. This figure is reproduced with permission from the work of Zielonka et al. in ref. 14. Copyright 2020, American Chemical Society (ACS).

The toxicity of the radical-cation of viologen comes from the reaction with oxygen to produce the superoxide radical anion ($O_2^{\bullet-}$) and subsequently hydrogen peroxide (H_2O_2), as well as hydroxyl and peroxyl radicals.[66] According to Keyer *et al*.[67], the superoxide anion has an implication in the production of oxidative DNA damage. However, Keyer[68] discusses also that the superoxide anion is incapable of damaging DNA directly, but it is believed to do it indirectly by participating in the production of hydroxyl radicals ($OH^{\bullet}$).

1.4 Approaches to enhance the storage capacity in RFB

Storage capability in RFB is a critical problem, requiring large tanks of electrolyte to achieve rather modest energy storage capacities [69]. Much work has been conducted [70–72] proposing some additives to increase the solubility of the redox-active species in the electrolytes [73,74], multiple redox-active species [75] or multi-electron redox-active species [76,77]. The approach of multi-electron redox-active species is quite complicated due to the drawbacks of transferring more than one electron. Recently, $Mn^{7+/6+}$ was proposed as a high energy density positive electrolyte in alkaline media with a solubility of 4 M. [78] Some interesting approaches have been proposed to provide innovative solutions for the energy density issue in RFB.

i) Semi-solid RFB

One of the first approaches considered were systems called semi-solid rechargeable flow batteries, introduced by Duduta *et al*.[79] in 2011.This system is based on making a suspension of energy dense active materials employed to react at the electrode surface. A general scheme of semi-solid rechargeable flow battery is illustrated in ***Figure 1.24***.

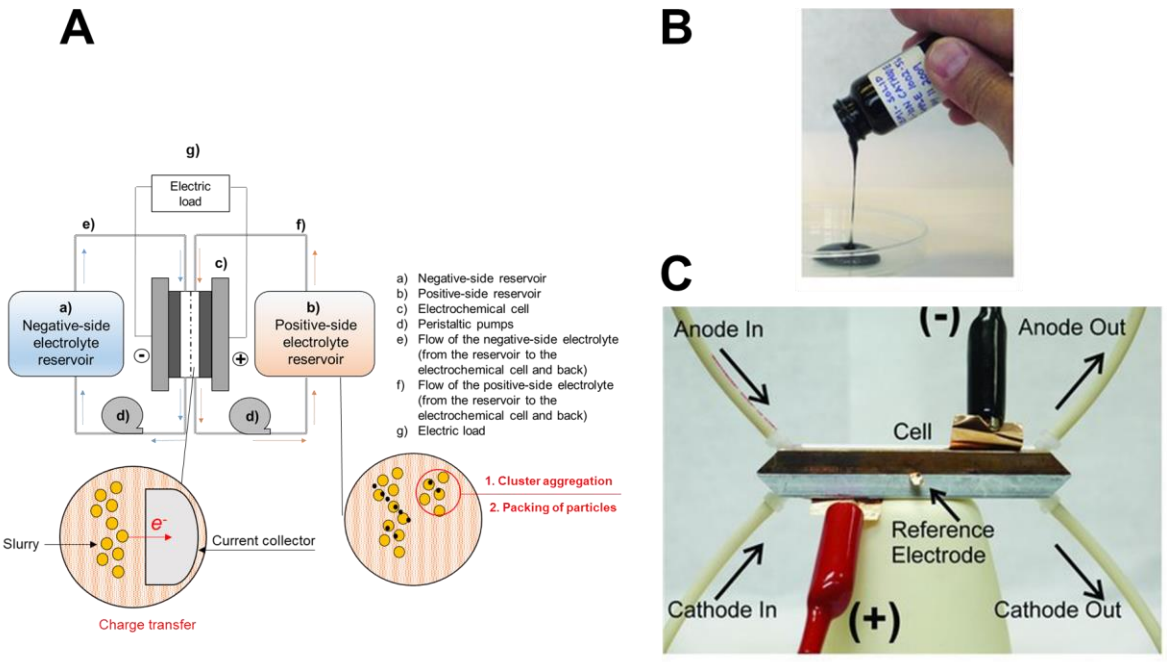

Figure 1.24 A) General scheme of a semi-solid flow battery. B) Semi-solid electrolyte for the semi-solid flow battery. C) Cell configuration in the semi-solid flow battery. Images B) and C) are reproduced with permission from the work of Duduta et al. at ref. [79], copyright 2020, Wiley.

The semi-solid flow battery is able to exploit the inherent advantages of a flow battery architecture increasing the storage capacity by using the suspension of solid active materials that percolate in the liquid electrolytes, as displayed in the close up in ***Figure 1.24***. The particles aggregate according to two steps:

***i*)** A diffusion-limited cluster aggregation to form conductor networks

***ii*)** A volumetrically dense packing of micrometer-scale particles.

The suspension stores and transfers the charge at the current collector. Assuming a solid content of 50% the volumetric capacity of the semi-solid suspensions is 5−20 times higher (*e.g.* 10 to 40 M) that than in ARFBs (1 to 3 M). Another useful advantage of the semi-solid redox flow batteries is that it can operate at low flow rates with low mechanical dissipations [79].

However, in this system some drawbacks are encountered and mainly linked to the particles nature. The charge transfer belongs to the particle-particle aggregation/interaction to form conducting networks, which results in low conductivity values (around 0.1 mS·cm^{-1} [79,80]) (***Figure 1.25***).

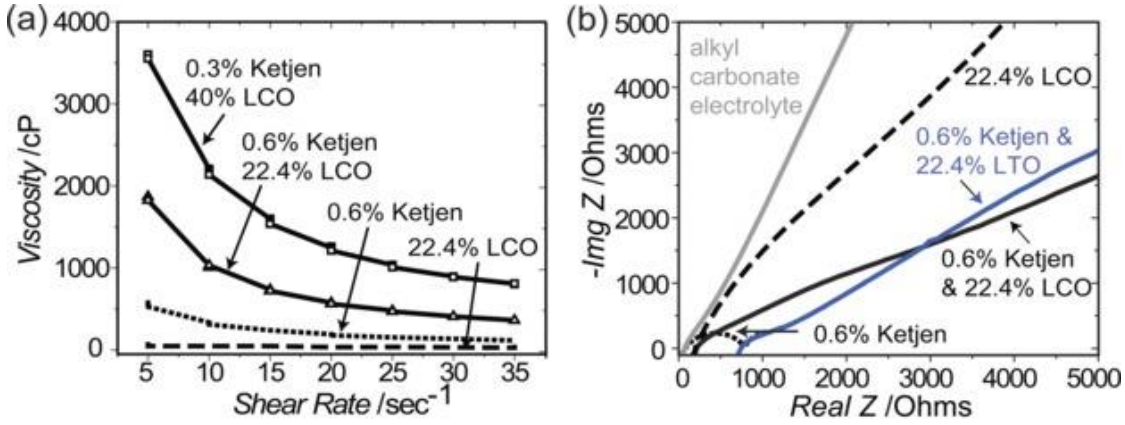

Figure 1.24 a) Viscosity versus shear rate for suspensions of nanoparticulate carbon (Ketjen black) and $LiCoO_2$ (LCO) in alkyl carbonate electrolyte. The suspensions show shear-thinning behavior consistent with the presence of Ketjen networks partially disrupted by shear stress. b) Nyquist plots for the different suspensions and their components. The high frequency intercept on the real axis provides the ionic conductivity, and is the same for the pure alkyl carbonate electrolyte and the 0.6% Ketjen suspension in the same electrolyte (Z = 55 Ω intercept corresponds to 22 mS cm^{-1} ionic conductivity since cell configuration factor = 1.2 cm^{-1}). At higher solids fractions the ionic conductivity decreases, e.g., the slurry containing 22.4% LCO and 0.6% Ketjen has 6 mS cm^{-1} ionic conductivity (Z = 200 Ω). The 22.4% $Li_4Ti_5O_{12}$ (LTO) + 0.6% Ketjen suspension uses dioxolane solvent (1 M $LiPF_6$) and has lower ionic conductivity of 1 mS cm^{-1} (Z = 750 Ω). The electronic conductivity, extrapolated from low frequency data, is about 10^2 lower than the ionic conductivity, being 0.06 and 0.01 mS cm^{-1}, for the LCO + Ketjen and LTO + Ketjen suspensions, respectively. These images are reproduced with permission from the work of Duduta et al at ref. [79] copyright 2020, Wiley.

ii) "Redox-targeting"

In 2006, an innovative approach was proposed by Grätzel and co-workers[81], utilizing solid-phase materials as primary charge storage media in batteries. This concept was denominated "redox-targeting" (***Figure 1.26***).[81]

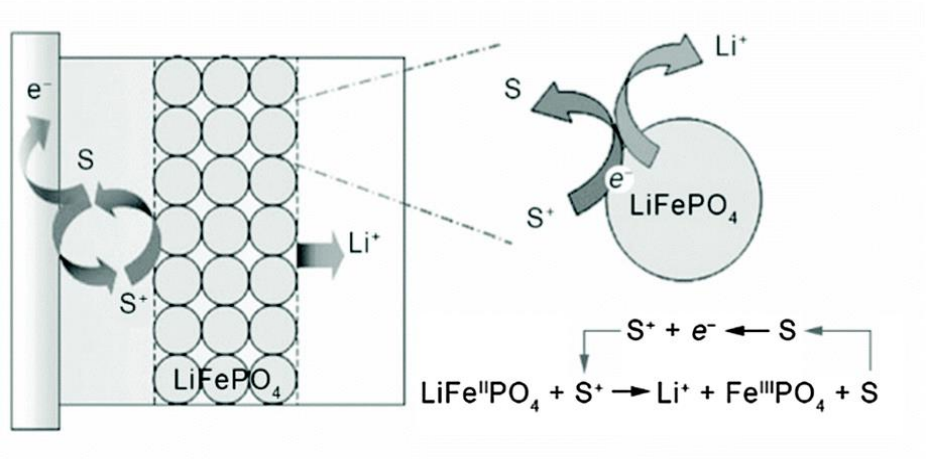

Figure 1.26 Schematic of the "redox-targeting" system proposed by Grätzel and co-workers.[81] This image is reproduced with permission from the work of Zhao et al. at ref. [82]. Copyright 2020, Royal Society of Chemistry.

Interestingly, this concept was proposed first to address the insulation of the commonly employed battery material $LiFePO_4$. [81] According to the concept, a molecular redox shuttle (abbreviated as "S" in the schematic in ***Figure 1.26***) dissolved in the electrolyte oxidizes during charging at the current collector, delivering the charge to the solid material ($LiFePO_4$) by bulk diffusion. [81] Then, the $LiFePO_4$ is indirectly charged/discharged *via* the redox shuttle molecule in the electrolyte, which acts as a mediator for the charge transfer (Li^+ intercalation) (***Figure 1.26***). This last step can occur only because the standard redox potential of the oxidized redox shuttle matches closely the Fermi level of the $LiFePO_4$.[81] Then, the oxidized redox shuttle molecule is reduced back by hole injection into the $LiFePO_4$ particles[81], resulting in the oxidation of Fe^{II} to Fe^{III} and in the release of lithium ions.[81]

The "redox-targeting" approach was believed extremely promising to increase charge capacity in energy storage technologies, such as RFBs. However, it also showed one drawback, in fact, the "indirect" charge/discharge of the $LiFePO_4$ was carried out by a couple of redox shuttle molecules (*i.e.* two different osmium complexes), giving rise to kinetic limitations and eventual energy losses.

Later in 2015, another similar system was proposed by Wang and co-workers.[83] They utilized dibromoferrocene ($FcBr_2$) and ferrocene (Fc), and cobaltocene ($[Co(Cp)_2]$) and bis(pentamethylcyclopentadienyl)cobalt ($[Co(Cp^*)_2]$), for the "redox-targeting" reactions with $LiFePO_4$ and TiO_2 solid materials, respectively (***Figure 1.27***).[83]

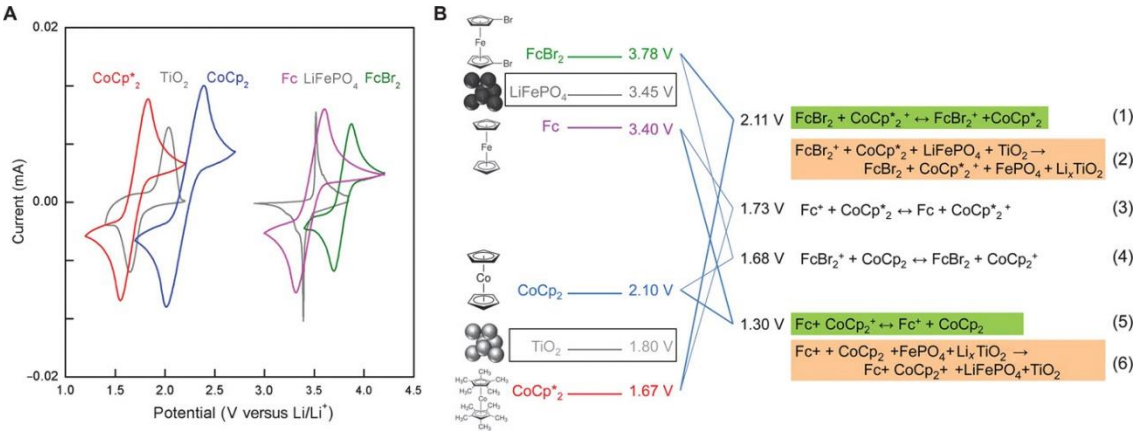

Figure 1.27 A) Cyclic voltammograms of the redox mediators and Li storage materials $LiFePO_4$ and TiO_2. B) A scheme compiling the chemical reactions between the redox mediators and materials in the tanks, as well as the electrochemical reactions of the mediators in the cell at different charging and discharging stages. These images are reproduced with permission from the work of Wang and co-workers at ref[83] . Copyright 2020, Advance Science Mag.

In this work, considering a 50% porosity of the solid materials, the volumetric capacity of the cell could reach up to 500 $Wh \cdot L^{-1}$, which means 10 times the conventional VRFB volumetric capacity (***Figure 1.28***)[83]

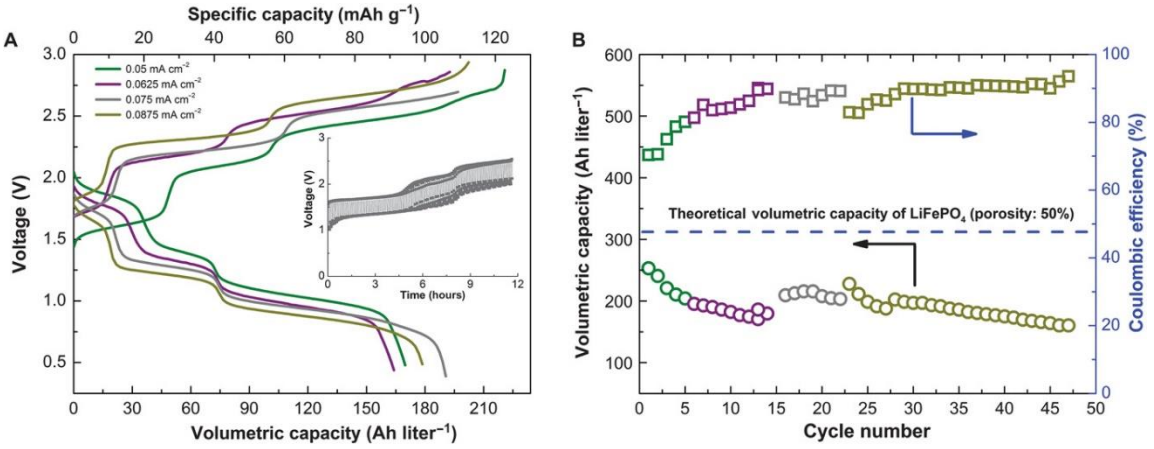

Figure 1.28 A) Typical voltage profiles of the RFLB full cell at different current densities. The inset shows a fraction of the GITT (galvanostatic intermittent titration technique) curve of the cell during the charging process at a current density of 0.05 $mA \cdot cm^{-2}$. B) Volumetric capacity retention and Coulombic efficiency of the cell over cycling at different current densities. These images are reproduced with permission from the work of Wang and co-workers at ref[83] . Copyright 2020, Advance Science Mag.

iii) "Dual circuit RFB"

In 2014, a related approach, where excess electricity is converted to H_2 and O_2 through indirect water electrolysis, was demonstrated by Girault and co-workers [44,84]. This concept is known as "dual circuit redox flow battery" (***Figure 1.29***) and it has been previously mentioned in the general discussion about RFB chemistries. The "dual circuit" system has the advantage of providing a secondary platform to store surplus energy beyond the capacity of the charged electrolytes, in the form of hydrogen.[44] This system represents also a complementary technology allowing renewable electricity that would otherwise be lost when the RFB is at full capacity.[44] Furthermore, the catalytic reactions occur independently of the electrode processes providing the chance to use low-cost, non-precious catalysts to obtain hydrogen. [44]

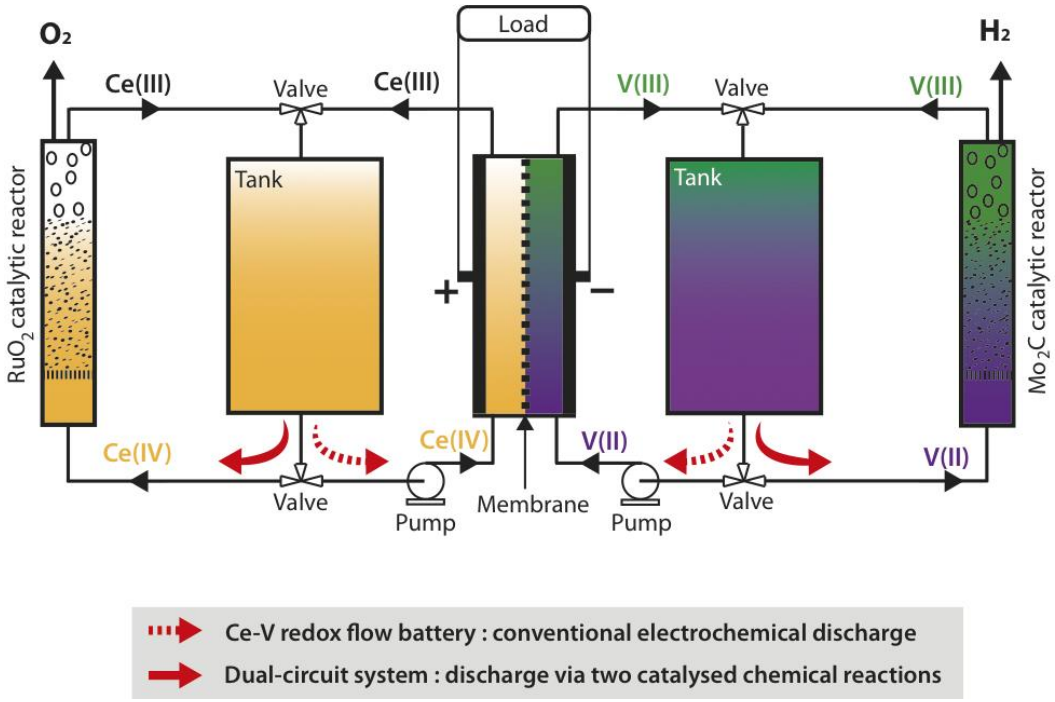

Figure 1.29 Principle of indirect water electrolysis as an alternative discharge process for a V–Ce RFB. Once in the charged state (V(II) and Ce(IV)) both electrolytes may be directed in an external catalytic bed to be chemically regenerated, and then return to the RFB. The catalyzed chemical reactions taking place in the catalytic beds allow the generation of hydrogen from the positive electrolyte (V(II)) and oxygen from the negative electrolyte (Ce(IV)).This image is reproduced with permission from the work of Amstutz et al. at ref [84].

The majority of the studies summarized herein have focused exclusively on Li^+ intercalation in organic electrolytes, while in this work the "redox-mediated" approach of charge transfer is applied to aqueous (acid and neutral pH) electrolytes, as they are typical of current large-scale RFB.

1.5 The approach of the present work: "redox-mediated" charge transfer

1.5.1 Working principle and engineering of the electrolyte reservoir

Unlike hybrid flow batteries, wherein the solid charge storage material resides inside the flow cell and directly accepts/donates electrons from/to the external circuit, [85]in the present thesis a different concept is proposed and called: "redox-mediated" charge transfer.

More specifically, when soluble redox-active species in the electrolyte undergo oxidation/reaction upon cell charging/discharging, the charge output of these redox reactions is carried within the flow cell to solid-phase materials, placed stationary at the bottom of the electrolyte tanks. Indeed, this mechanism is entirely *mediated* by the solubilized redox-active species in the electrolyte, which for this reason are called redox mediators (RM). On the other hand, the solid-phase materials who become the primary charge storage media, are denominated solid boosters (SB).

The schematic in ***Figure 1.30*** depicts how this concept works in the actual RFB. The redox-mediator (RM) flows from the storage reservoir to the electrochemical cell where it reacts on the electrode surface. Then, when it comes back to the reservoirs it encounters the solid booster (SB), stationary placed at the bottom. If (as in the case represented in the schematic below) the Fermi level of the RM is higher than that if the SB, the RM will reduce the booster.

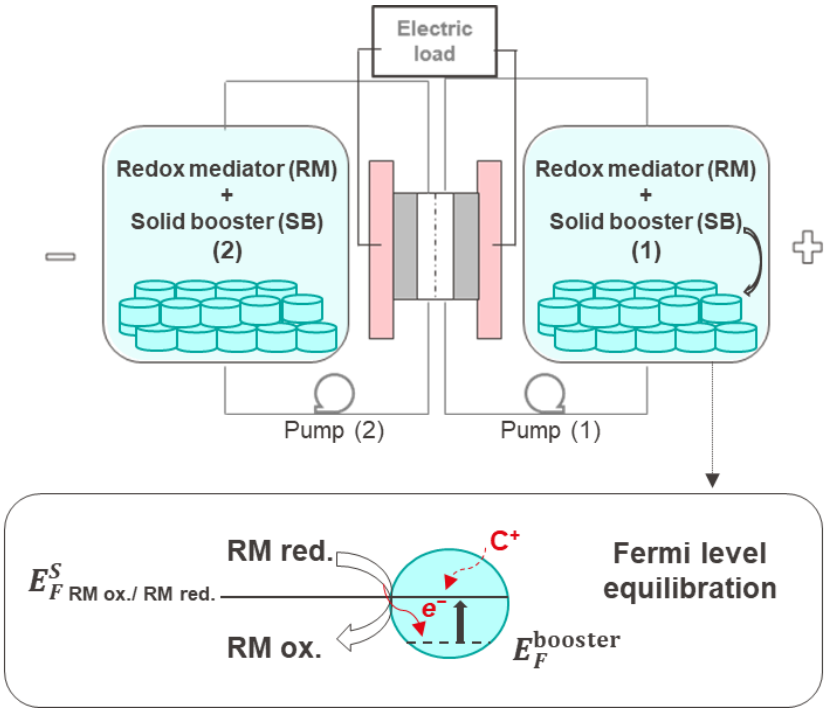

Figure 1.30 Schematic of the "redox-mediated" charge transfer with Fermi level equilibration. In this particular case cation storage is represented since it corresponds to the experimental work.

From the inset in ***Figure 1.31*** it is possible to see how the conventional configuration of the electrolyte storage reservoirs in the RFB has charged since the addition of the solid boosters. Importantly, the SB has to be stationary placed at the bottom of the reservoir during the whole cell cycling, otherwise floating of solid particles into the cell would lead to components failure (electrodes and membrane).

Initially, this is done using a piece of carbon felt having the same diameter of the reservoir's bottom along with a flow regulator and pipes to allow a full percolation of the booster from the electrolyte solution (*design 1* in ***Figure 1.31***). Later, the electrolyte reservoir was completely modified to improve and facilitate the electrolyte flow through the booster particles (*design 2* in ***Figure 1.31***).

An important aspect to take into account during the design of the reservoir with SB is the booster configuration. The booster cannot be flown in the RFB as powder or slurry, since the goal is to have a solid storage (*i.e.* a storage material in the solid-phase) placed in the reservoir while the liquid electrolyte flows constantly. In this work this aspect was addressed according to the booster material, for instance in the case of polymers as SB no particular configuration was needed, however with intercalation compounds with crystalline structure, pellets were made.

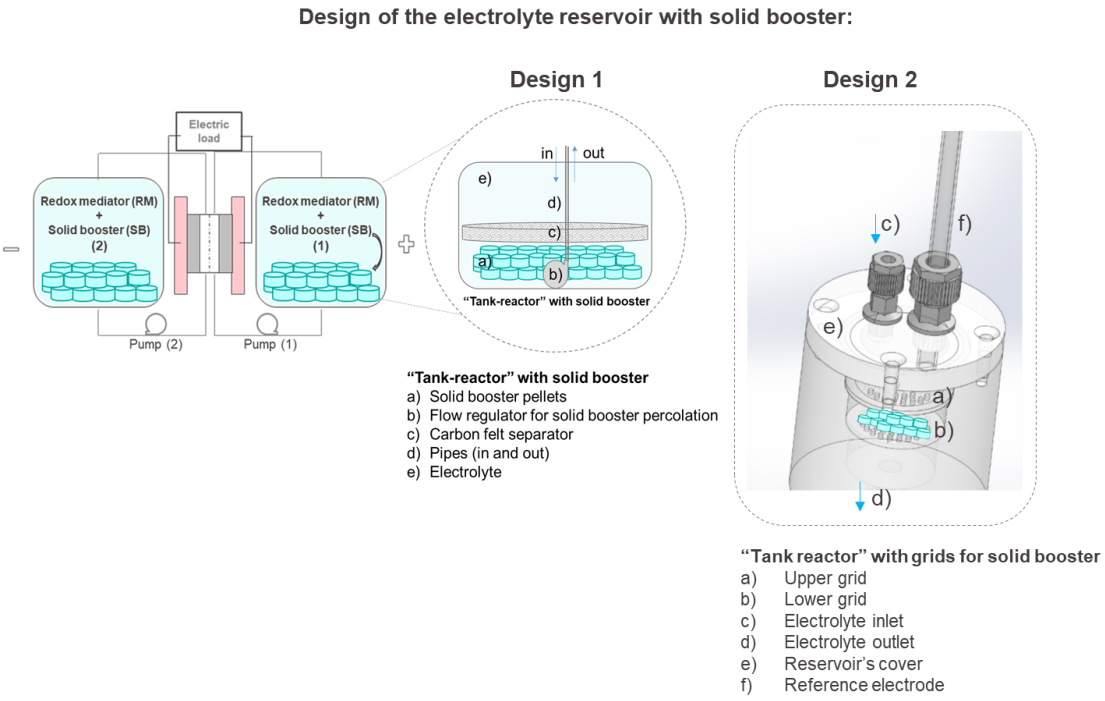

Figure 1.31 Schematic of the "redox-mediated" flow battery with solid boosters in the electrolyte reservoirs. The close up shows how the tank is arranged in presence of the solid booster particles. The legend below the representation explains all the components.

1.5.2 Theoretical aspects of the approach

The concept of "mediated-charge" transfer applied to RFB relies on fundamental theoretical aspects, which are discussed in this paragraph. First, the thermodynamic definition of standard electrochemical potential ($\tilde{\mu}$) of any redox-active species in the solution is given, which suddenly leads to the derivation of the Nernst equation, expressed in terms of electrochemical Gibbs energy and of the activity (*a*) of the species (***eqn. 1.15***). These fundamental definitions are necessary to understand the how species in the solution (*i.e*. liquid electrolytes or solid boosters) characterized by redox activity can react.

Eqn. 1.15[30] shows the situation where a redox reaction occurs, then at the equilibrium the *delta* of the electrochemical Gibbs energy is equal to zero, as well as the electrochemical potential of the species ($\tilde{\mu}$) for the redox reaction proposed. The electrochemical potential of any species *"i"* can be further defined as the sum of the chemical potential (μ_i) of the species *"i"* (*i.e*. this is a chemical term that includes all the short-distance interactions between the ion and its environment, such as ion-dipole interactions, ion-dipole included interactions, dispersion forces, *etc*.)[30], an electrostatic term ($z_iF\chi_i$) (*i.e*. this is an electrostatic term linked to the crossing of the layer of oriented interfacial dipoles) and ($z_iF\psi_i$) (*i.e*. this is an electrostatic term linked to the charge of the phase). In all these expression, *F* is the Faraday constant (96485 C/mol).

Eqn. 1.15[30]

$$Ox^S + ne^- \rightleftharpoons Red^S$$

$$\Delta\tilde{G} = 0$$

$$\tilde{\mu}_{red}^S - (\tilde{\mu}_{ox}^S + \tilde{\mu}_{e^-}^S) = 0$$

$$\tilde{\mu}_i = \mu_i + z_iF\chi_i + z_iF\psi_i$$

Then, from the expression of the electrochemical potential of the species *"i"* ($\tilde{\mu}$) in ***eqn. 1.15***[30], it is possible to carry on with the demonstration of the electrochemical potential and write it as in ***eqn. 1.16***[30]:

Eqn. 1.16[30]

$$\tilde{\mu}_i = \mu_i + z_iF\chi_i + z_iF\psi_i$$

$$\tilde{\mu}_i = \mu_i + RT\ln a_i + z_iF\phi_i$$

$$\phi_i = \chi_i + \psi_i$$

$$\alpha_i = \mu_i + z_iF\chi_i$$

In the expression of the electrochemical potential of the species *"i"* ($\tilde{\mu}$) in ***eqn. 1.16***[30], a new term is introduced, which is ϕ_i. This is the inner potential or Galvani potential of a phase and it is defined as the sum of the surface and the outer potentials. As described by Girault[30], these potentials are really potential

differences, the inner potential of a phase is the potential difference between the bulk of the phase and the vacuum. ***Figure 1.32*** illustrates the radial distribution of potential for a metal of radius *R* carrying a positive charge *Q* with the contributions of the outer potential and the surface potential. The inner potential is constant inside the sphere. [30]

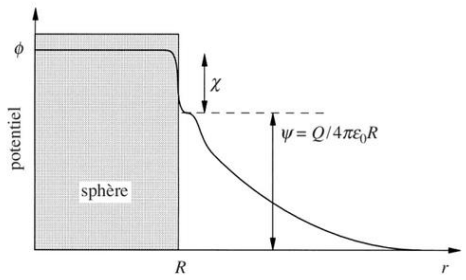

Figure 1.32 Illustration of the radial distribution of potential for a metal of radius R carrying a positive charge Q. This image is reproduced from the textbook of Girault at ref [30].

In the expression of the inner potential, given that ψ can be measured it was proposed to define the real chemical potential (α_i). Thus the electrochemical potential can be defined as the sum of the real chemical potential and an electrostatic term related to the charge of the phase (***eqn. 1.16***). [30]

Finally, coming back to the equilibrium situation where the *delta* of the electrochemical Gibbs energy is equal to zero as the electrochemical potentials of the redox species, it is possible to develop the following ***equation 1.17***[30], which leads to the derivation (according to a thermodynamic approach) of the Nernst equation.

$$Ox^S + ne^- \rightleftharpoons Red^S$$

$$\Delta\tilde{G} = 0$$

$$\tilde{\mu}^S_{red} - (\tilde{\mu}^S_{ox} + \tilde{\mu}^S_{e^-}) = 0$$

eqn. 1.17[30]

$$[\tilde{\mu}^{0S}_{red} + RT\ln a^S{}_{red} + z_{red}F\phi^S{}_{red}] - n[\mu^M_{e^-} - F\phi^M] - [\tilde{\mu}^{0S}_{ox} + RT\ln a^S{}_{ox} + z_{ox}F\phi^S{}_{ox}] = 0$$

$$nF(\phi^M - \phi^S) = (\tilde{\mu}^{0S}_{ox} - \tilde{\mu}^{0S}_{red} + n\mu^M_{e^-}) + RT\ln\left(\frac{a_{ox}{}^S}{a_{red}{}^S}\right)$$

$$= -\Delta G^0 + RT\ln\left(\frac{a_{ox}{}^S}{a_{red}{}^S}\right)$$

In ***eqn. 1.17*** μ_i^0 is the standard chemical potential of the species *"i"* in solution in the molarity scale (or molality). The difference of ϕ is the difference of the Galvani potential between the metal (*M*) and the solution (*S*). The term $nF(\phi^M - \phi^S)$ is the electrical work required to transfer one mole of elementary charges from inside the metal to the bulk of the solution. [30]

Another important theoretical aspect to define for the complete understanding of the "mediated-charge" transfer, is that of Fermi level of electrons in solutions. The definition of Fermi level of electron in solution is based on recent works by Peljo and Girault. [75] [86]

By analogy with the Nernst equation, we can define the standard redox potential on the absolute vacuum scale (AVS) by considering the virtual reduction reaction between an electron at rest in vacuum and the oxidized species in solution (***eqn. 1.18***)[86]:

eqn.1.18[75] [86]

$$-\Delta G_{\text{reduction}} = \tilde{\mu}^{S}_{\text{Ox}} - \tilde{\mu}^{S}_{\text{Red}} = e\left[E_{\text{Ox/Red}} + \phi^{S}\right]^{S}_{\text{AVS}}$$

By definition, the electron at rest in vacuum is the origin of the AVS scale.[86] Then, we can define the electrochemical potential of the electron in solution and consequently a Fermi level for the electron in solution as shown in ***Figure 1.33*** and in the ***eqn. 1.19*** and ***1.20***.

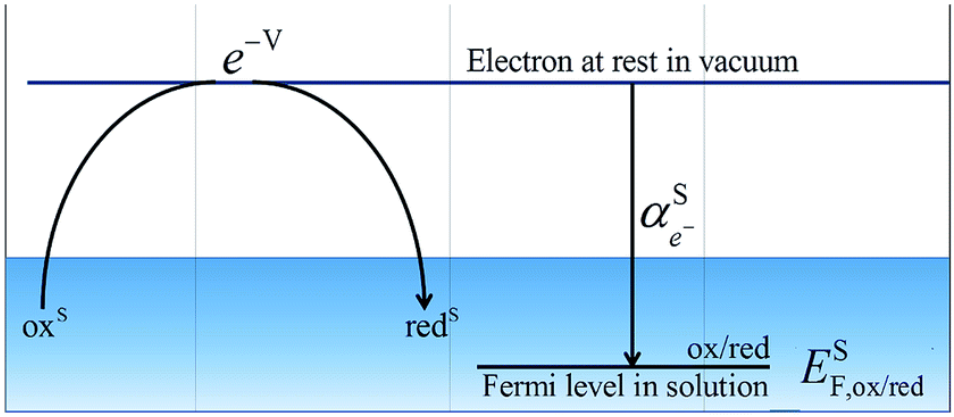

Figure 1.33 Redox reaction for the definition of the absolute redox potential considering electrons at rest in vacuum. This image is reproduced with permission from the work of Girault and co-workers at ref.[86]. Copyright 2020, Royal Society of Chemistry.

eqn.1.19[75] [86]

$$-\tilde{\mu}^{S}_{e^-} = e\left[E_{\text{Ox/Red}} + \phi^{S}\right]^{S}_{\text{AVS}}$$

eqn. 1.20[75]

$$-\alpha^{S}_{e^-} = e\left[E_{\text{Ox/Red}} + \phi^{S}\right]^{S}_{\text{AVS}} = \alpha^{S}_{Ox} - \alpha^{S}_{Red}$$

Additionally, as graphically represented in ***Figure 1.30***, one of the main aspect regarding the "mediated-charge" transfer concept is the Fermi level equilibration between the RM (in the liquid phase)

and the SB (in the solid phase). Girault and co-workers[86] describe it considering the case of a metallic nanoparticle immersed in a solution (***Figure 1.34***). In this case, the nanoparticle in the solution will reach, albeit very slowly, an electrochemical equilibrium with the surrounding solution. [86] If the redox potential in solution is dominated by a single redox couple, ox/red, in excess, then the Fermi level of the electrons in the metallic nanoparticle, E^{NP}_{F}, will change to become equal to the Fermi level of the electrons in solution, $E^{S}_{F,ox/red}$, for this redox couple. [86] This change results in either an electrostatic charging of the metallic nanoparticle accompanied by an oxidation of the redox couple in solution or discharging of the metallic nanoparticles accompanied by a reduction of the redox couple in solution. [86]

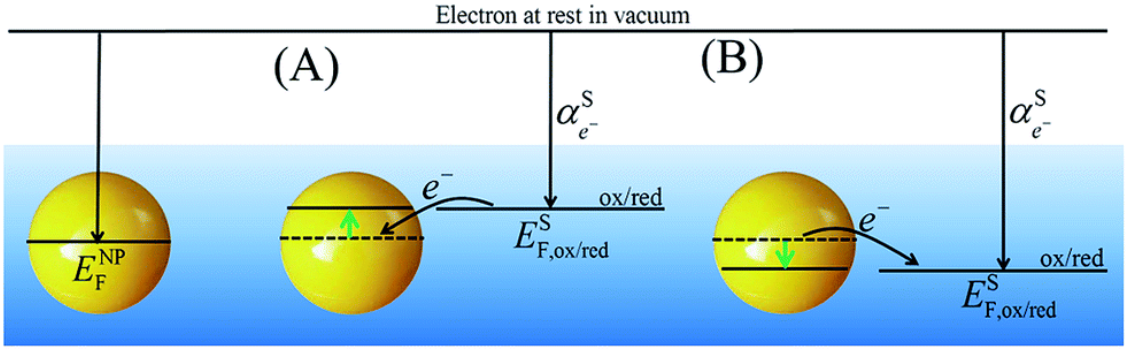

Figure 1.34 Redox equilibria for metallic nanoparticles in solution showing the capabilities of metallic nanoparticles to be (A) charged and (B) discharged upon Fermi level equilibration with an excess of a single dominant redox couple in solution. This image is reproduced with permission from the work of Peljo et al. at ref. [86]. Copyright 2020, Royal Society of Chemistry.

In principle, "redox-mediated" flow batteries should be readily scalable. Flow batteries already exist at reasonably large scales, as do other flow-assisted electrochemical processes. The engineering of heterogenous flow-through reactors is also quite well established, and it's nearly ubiquitous across the chemical industries. Designers of "redox-mediated" flow batteries would benefit directly from the existing knowledge in these fields.

Chapter 2

A "redox-mediated flow battery" at acidic pH with polyaniline as solid booster

Based on the article;

Zanzola, E.; Dennison, C. R.; Battistel, A.; Peljo, P.; Vrubel, H.; Amstutz, V.; Girault, H. H. Redox Solid Energy Boosters for Flow Batteries: Polyaniline as a Case Study. *Electrochimica Acta* **2017**, *235*, 664–671

2.1 General Introduction

Previously, storage technologies were presented as an encouraging option in the current energy scenario, where they can bring some benefits to the overall energy supply, for instance, by integrating renewables as highly intermittent sources. An important aspect while discussing storage technologies is the choice of materials for achieving high performances, especially in terms of storage capability and cycle life-time. In this chapter, redox polymers will be employed in an AIRFB. Indeed, as previously discussed, ARFB suffer from low energy density (25-40 $Wh \cdot L^{-1}$)[7], limited by the concentration of the redox-active species dissolved in the supporting electrolyte. The purpose of this chapter is to implement solid-phase redox boosters in the electrolytes to enhance the whole volumetric capacity. Redox polymers were selected as solid boosters, due their diversity, unique electrochemical properties and cost-effectiveness. In particular, among them polyaniline (PANI) was identified for designing a first aqueous "redox-mediated" flow battery in the presence of acidic electrolytes. The main objective of the present work is to study the booster contribution in a full RFB as proof-of-concept.

2.2 Redox active polymers (RAPs)

RAPs are defined by IUPAC as materials containing groups that can be reversibly reduced or oxidised.[88] Each redox process occurring in the polymer may be associated with changes in the properties of the material, such as chemical, mechanical or optical, making these polymers versatile for many applications. RAPs have been historically classified according to different principles, but due to their large variety there are some exceptions and hybrid forms[89]. According to Kim *et al*.[90] two main groups can be distinguished: *i*) redox active group-embedded polymers (RAGEP) and *ii*) redox active pendant-bearing polymers (RAPBP). A graphical schematic of the classification of RAPs is displayed in ***Figure 2.1***.[90] Furthermore, each of these classes has two subdivisions; in fact, RAGEP consist of conductive polymers (***Figure 2.1a)***, (*e.g*. PANI, PEDOT, PPy PEDOT:PSS) and other polymers (***Figure 2.1b)*** (*e.g*. P-*p*-P, and poly(S-*r*-DIB) copolymer).[90] Then, the category of RAPBP, according to Kim *et al*.[90], is made by polymers with redox –active groups (RAG) (***Figure 2.1c)***, (*e.g*. ferrocene, imide, quinone, viologen, *etc*.) and by polymers with radical group (***Figure 2.1d)***, (*e.g*. nitroxyl and galvinoxyl).

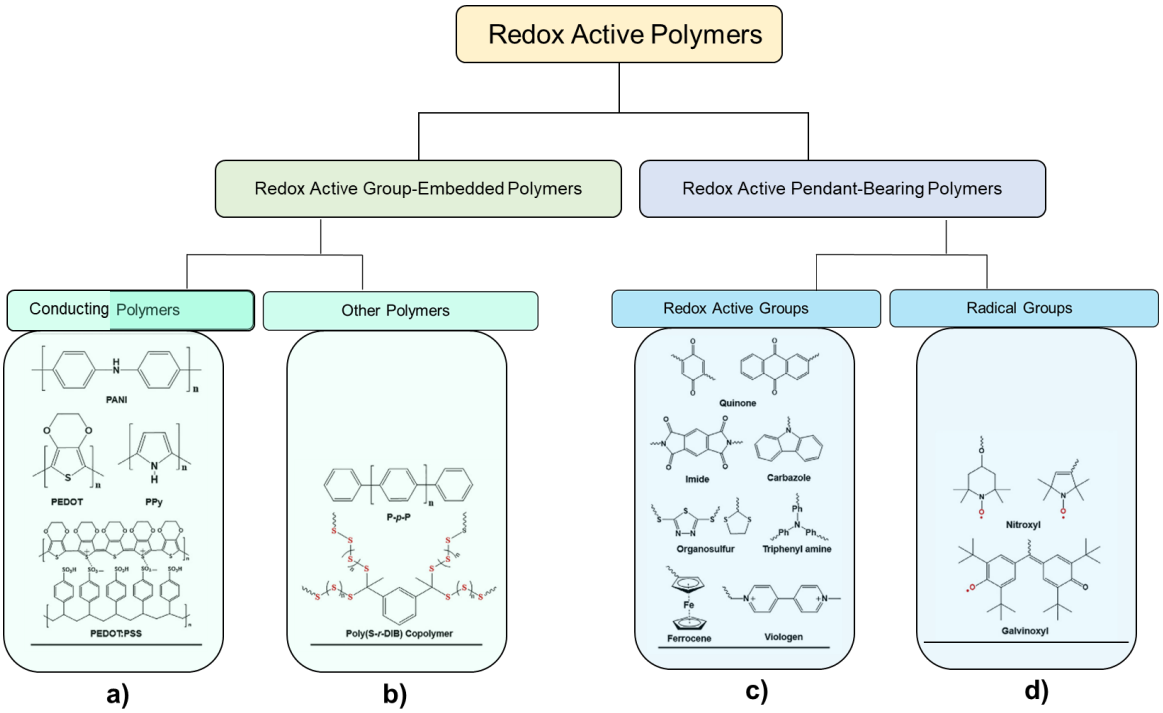

Figure 2.1 Schematic of the classification of RAPs. The main classes are RAGEP and RAPBP. From the first group of RAEBP, conducting polymers (in a)) and other polymers (in b)) can be classified. Then, from the second group of RAPBP, RAG polymers (in c)) and radical group polymers (in d)) can be identified. This figure contains a few examples of each polymers and it was inspired by the work of Kim et al. at ref [90].

2.2.1 Redox active group-embedded polymers (RAGEP)

RAGEP possess an electrochemically active backbone consisting of redox-active monomers.[90] RAGEP (***Figure 2.1a)***), usually undergo electrochemical reactions by doping and de-doping mechanisms and the dopant ion depends on the polymer species. The charge related to this redox process is stored in the conjugated oxidized or reduced states of the polymer.[90] The doping mechanism controls the conductivity, which is an important characteristic considering the application of these polymers in electronic devices.[91] Interestingly, in between 1980s and 1990s, it was discovered that Brønsted acids (*i.e.* any species capable of donating a proton $–H^+$) were responsible for p-doping in many organic conducting and semi-conducting polymers.[91] This doping mechanism proceeds by charge transfer from the valence band (abbreviated as VB) of the semiconductor to the conduction band (abbreviated as CB) of the dopant, introducing a hole on the semiconductor while simultaneously creating a negatively charged dopant anion.[91]

RAGEP polymers are a good option to substitute conventional inorganic materials for the positive and the negative-side of a battery system, due to their competitive performances, good mechanical and thermal stability, low toxicity and safety.[89] Indeed, they fit well in electrochemical storage devices since they can match operational requirements such as: *i*) cell voltage, *ii*) capacity, *iii*) Coulombic efficiency (CE), and *iv*) cycle life-time.[89] An interesting work is proposed by Su *et al*.[92] on the utilization of PPy in the synthesis of a PPy-containing ferrocene positive-side LIB material. This PPy-containing ferrocene material exhibited good cycling performances, and the authors demonstrated that the introduction of ferrocene into PPy improved the capacity from 16.5 $mAh{\cdot}g^{-1}$ of PPy to *ca*. 43 $mAh{\cdot}g^{-1}$. [92]

Furthermore, a variety of works discuss the usage of PANI in LIB, as positive or negative-side battery material. Recently, Luo *et al*.[93] have made a review on the application of PANI in different batteries such as LIB, lithium-sulfur and supercapacitors. In particular, as negative-side material, PANI has been largely used to improve the low capacity in anode materials.[93] In a LIB, Hu *et al*.[94], utilized PANI in the synthesis of a novel hierarchical PMo_{12}/PANI/MWNTs nanocomposite, as negative-side battery material. [94] This nanocomposite based on PANI and MWCNTs shows great cycling performance. The authors claim that it delivers an overall discharge capacity of 1000 $mAh{\cdot}g^{-1}$ for 100 cycles at a current density of 0.5 $mA{\cdot}cm^{-2}$.[94]

A remarkable work which proposes PANI and SWCNTs as negative-side material for LIB is presented by Ge *et al.* (***Figure 2.3A)***).[95] In this work, the authors prepared a SWCNT/PANI nanoribbon hybrid aerogels[95] as free-standing flexible LIB electrodes by micelle-induced self-assembly of aniline monomers, followed by *in-situ* polymerization of PANI within the wet SWCNT gels (***Figure 2.3A)***). [95].

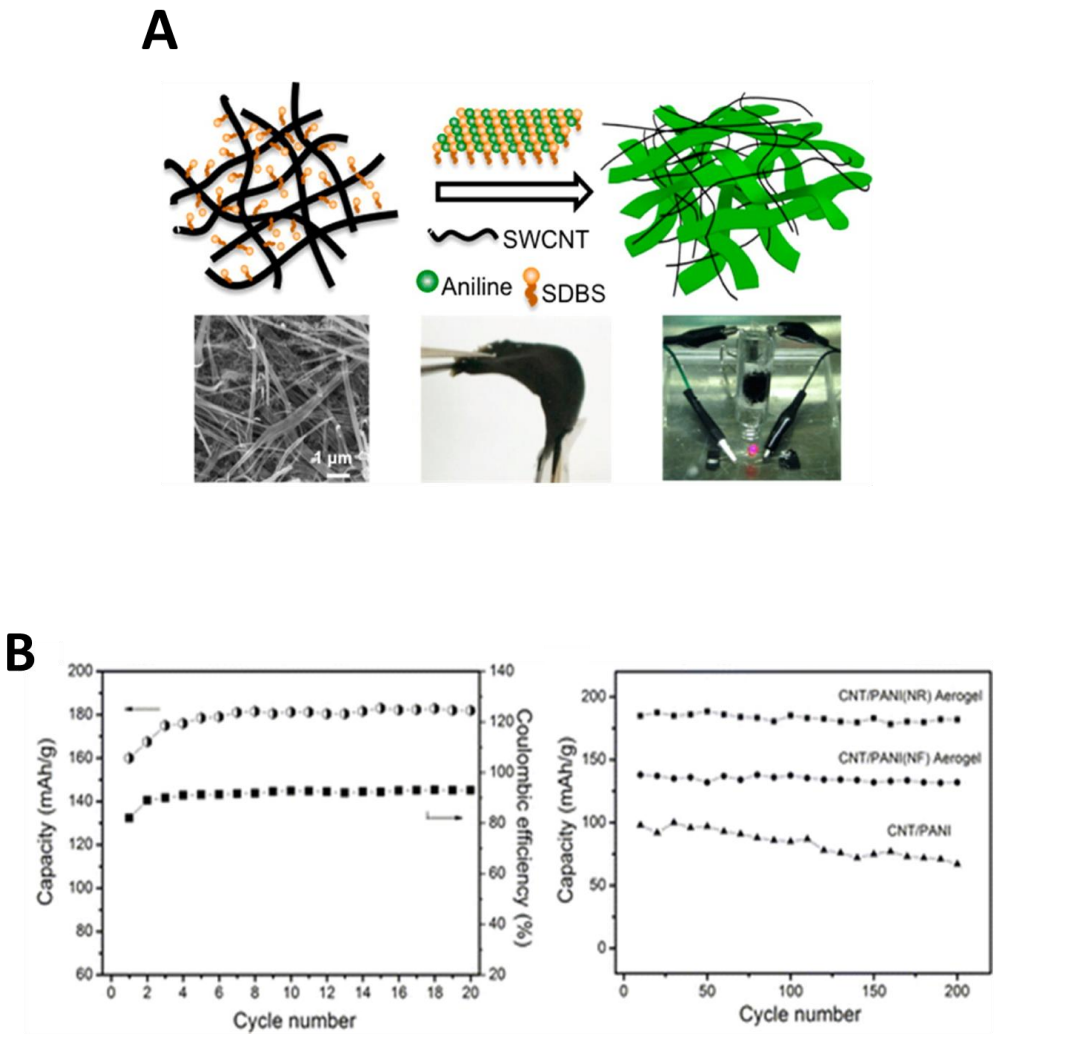

Figure 2.3 A) Schematic of the synthesis process of the SWCNTs/PANI nanoribbon aerogel nanocomposite. B) Capacity and CE of coin cells with SWCNTs/PANI nanoribbon composite aerogel electrode at a current density of 30 mA·g^{-1}. Comparison of lithium storage of different CNTs/PANI composites as electrodes. The composite electrodes all had a CNT content of ~33 wt. % nanoribbon, nanofiber. These images are reproduced with permission from the work of Ge et al. at ref [95]. Copyright 2020, American Chemical society (ACS).

The *in-situ* synthesized SWCNTs/PANI nanoribbon aerogel nanocomposites by Ge *et al.* [95] exhibited 185 mAh·g^{-1} capacity[95] and high cycling stability, with no fading up to 200 cycles. [95] According to Ge *et al.* [95] , the capacity enhancement could be attributed to the interpenetrating aerogel networks of

SWCNTs and PANI nanoribbons for efficient ion/electron transport, and to highly interconnected nanopores in aerogels, which provided highly effective penetration of electrolyte ions.[95]

On the other hand, PANI is also employed as positive-side material in LIB: for example, FeS_2/PANI composite, synthesized *via in-situ* chemical polymerization of the aniline monomer in presence of fine FeS_2 particles in aqueous suspension.[96] This composite exhibits a 767 $mAh \cdot g^{-1}$ gravimetric capacity at 100 $mA \cdot g^{-1}$. [96]

2.2.2 Redox active pendant-bearing polymers (RAPBP)

RAPBP (***Figure 2.1c)***) have electrochemically active groups on their non-conductive polymer backbones, similar to a grafted polymer structure.[90] They usually undergo redox reactions where their doping level can be changed by doping and de-doping mechanisms.[90] RAPBP are frequently employed in many electrochemical storage devices, such as positive or negative-side electrode materials in metal-ion batteries (*i.e*. NIB and LIB, respectively)[89] or as electrolyte RFB materials.[48] [46]

The following ***Figure 2.4*** shows a few examples of RAPBP along with their main performances in electrochemical devices such as NIB or LIB (***Figure 2.4a)*** and ***b)***) or in RFBs (***Figure 2.4c)*** and ***d)***).

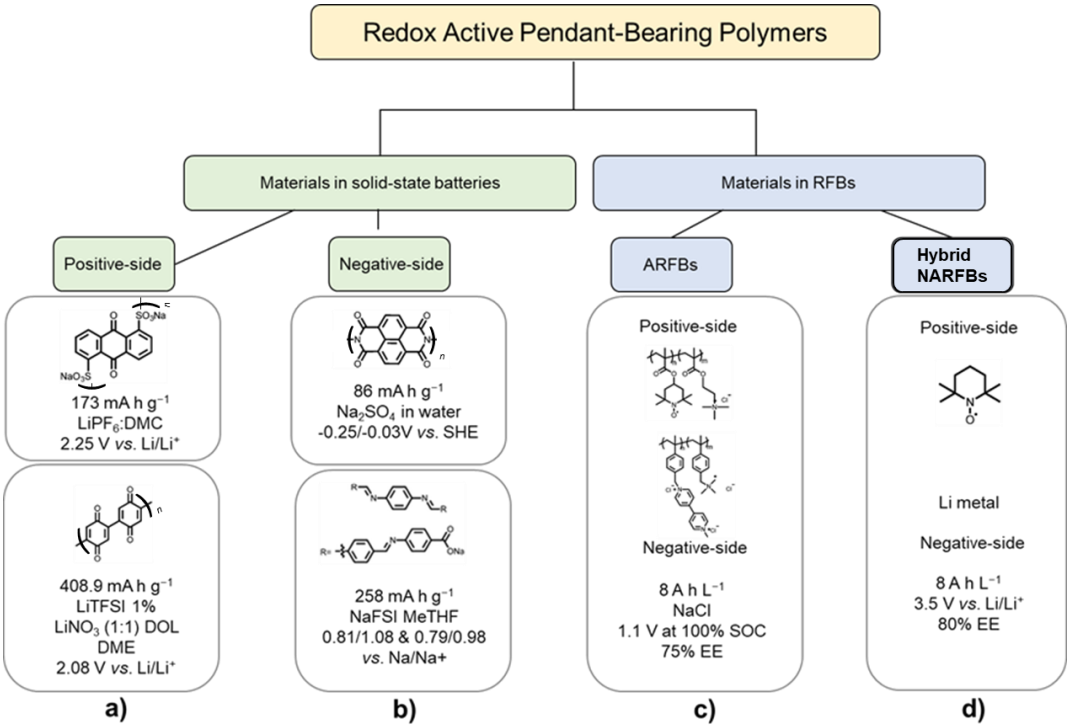

Figure 2.4 RAPBP: a) Polymers employed typically as positive-side materials in LIB or NIB batteries. b) Polymers employed as negative-side materials in LIB or NIB. c) Polymers employed in ARFBs and d) in NARFBs. In the figure the following abbreviations are used: $LiPF_6$ for lithium hexafluoroposphate, DMC for dimethyl carbonate, LiTFSI for lithium bis (trifluoromethane sulfonamide), $LiNO_3$ for lithium nitrate, DOL for dioxolane, DME for dimethyl ether, NaTFSI for sodium

bis (trifluoromethane sulfonamide), MeTHF for 2-Methyltetrahydrofuran, EE for energy efficiency. The contents of this figure are reproduced with the permission from ref [90], Copyright 2020, Royal Chemical Society.

Importantly, in these polymers the insulating backbone could represent an issue for long cycling performances in the electrochemical storage device, requiring the employment of conducting additives (*e.g.* carbon acetylene black (CAB) or MWCNTs) to enhance the whole electronic conductivity. As an example, Shimizu *et al.* [97], studied para- and ortho-quinone derivatives having two carbonyl $-CO_2$ Li groups as positive-side materials in a LIB. These materials were prepared for cycling tests directly with CAB as conducting additive and polytetrafluoroethylene (PTFE) as binder in a ratio (1.5/4.0/1.0 wt. %). In particular, in the case of the 2,6-bis(lithiooxycarbonyl)-9,10-anthraquinone (LCAQ) derivative, the battery showed an initial capacity of 85 mAh·g^{-1} (49% of the theoretical capacity equal to 174 mAh·g^{-1}), which after 20 cycles decreased to 70 mAh·g^{-1}.[97] The work proposed by Shimizu *et al.* [97] exhibited excellent cyclability compared to those using the parent quinones, although still functionalized with carbonaceous additives for enhancing the conductivity in all cycling tests. Furthermore, Lu *et al.*[98] reported the incorporation of sodium 1,4-dioxonaphthalene-2-sulfonate (NQS, in ***Figure 2.5a)***) into the network of MWCNTs, using a dissolution–recrystallization method, which produced a flexible and free-standing hybrid film for LIB applications (***Figure 2.5b)*** and ***d)***). The average discharge capacities of the NQS/MWCNTs hybrid film with an average content of 41 wt. % NQS were 146, 125, 107, and 93 mAh g^{-1} at 0.2, 0.5, 1.0, and 2.0 C, respectively (based on the mass of NQS), which were considerably higher than that of pristine NQS at the same rates.[98]

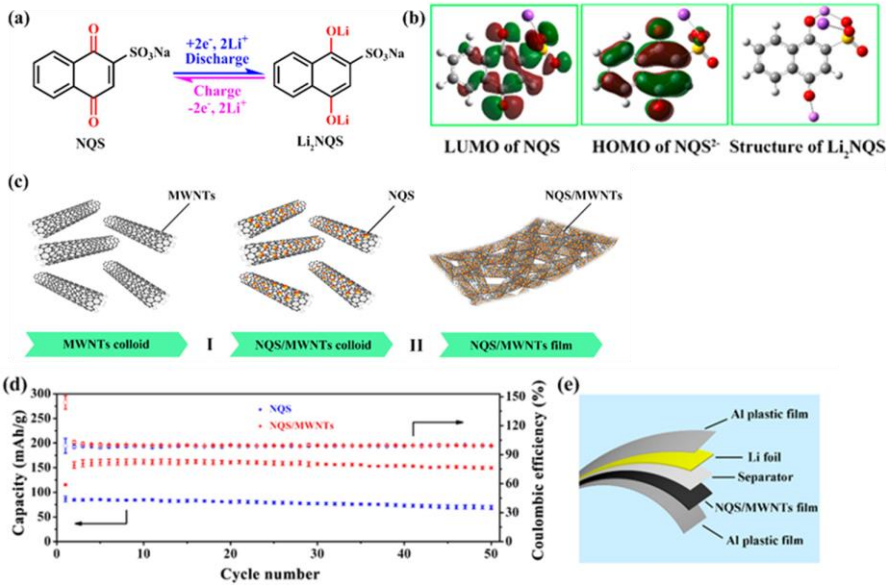

Figure 2.5 a) Structural formula and reversible electrochemical redox mechanism of NQS/Li_2NQS. b) The LUMO plot of NQS molecule, the HOMO plot of NQS^{2-}, and the optimized structure of Li_2NQS. c) Schematic process for preparing

NQS/MWNTs hybrid films by (I) depositing NQS particles on the surface of MWNTs scaffolds; (II) self-assembly of MWNTs with NQS nanoparticles and the formation of NQS/MWNTs hybrid films. d) Cycling performance with Coulombic efficiency of NQS and NQS/MWNTs at 0.2 C. e) Schematic diagram of a flexible soft-packaged lithium battery. This figure is reproduced from ref. .[98], reprinted with permission, copyright 2020, American Chemical Society (ACS).

In the field of RFB, RAPBP are also attracting considerable attention. The ARFB employing TEMPO and viologen polymers as neutral pH electrolytes developed by Schubert and co-workers (depicted in ***Figure 2.6a)*** and ***b)***)[48], exhibits very interesting cycling performances. Indeed, being fully constituted by earth-abundant elements, it is an option to design relatively low-cost systems. TEMPO and viologen polymers are soluble in 2 M $NaCl_{aq}$ supporting electrolyte and have a cell voltage of 1.1 V at 100% SOC. The full ARFB has a volumetric capacity equal to 8.2 $Ah \cdot L^{-1}$ and an energy density of 8.0 $Wh \cdot L^{-1}$. Additionally, due to the macromolecular nature of the polymers, the Nafion™ membrane can be replaced by a dialysis membrane (preventing crossover by size exclusion), contributing to further decrease the overall costs of the installation.[99] In this particular case, the thickness-normalized diffusion coefficient of the dialysis membrane was found to be $(9.3 \pm 0.1) \cdot 10^{-5}$ $cm \cdot s^{-1}$, [48] which lead to a low area resistance in aqueous sodium chloride solution of 1.14 ± 0.03 $\Omega \cdot cm^2$ (in the range of Nafion™ membrane).

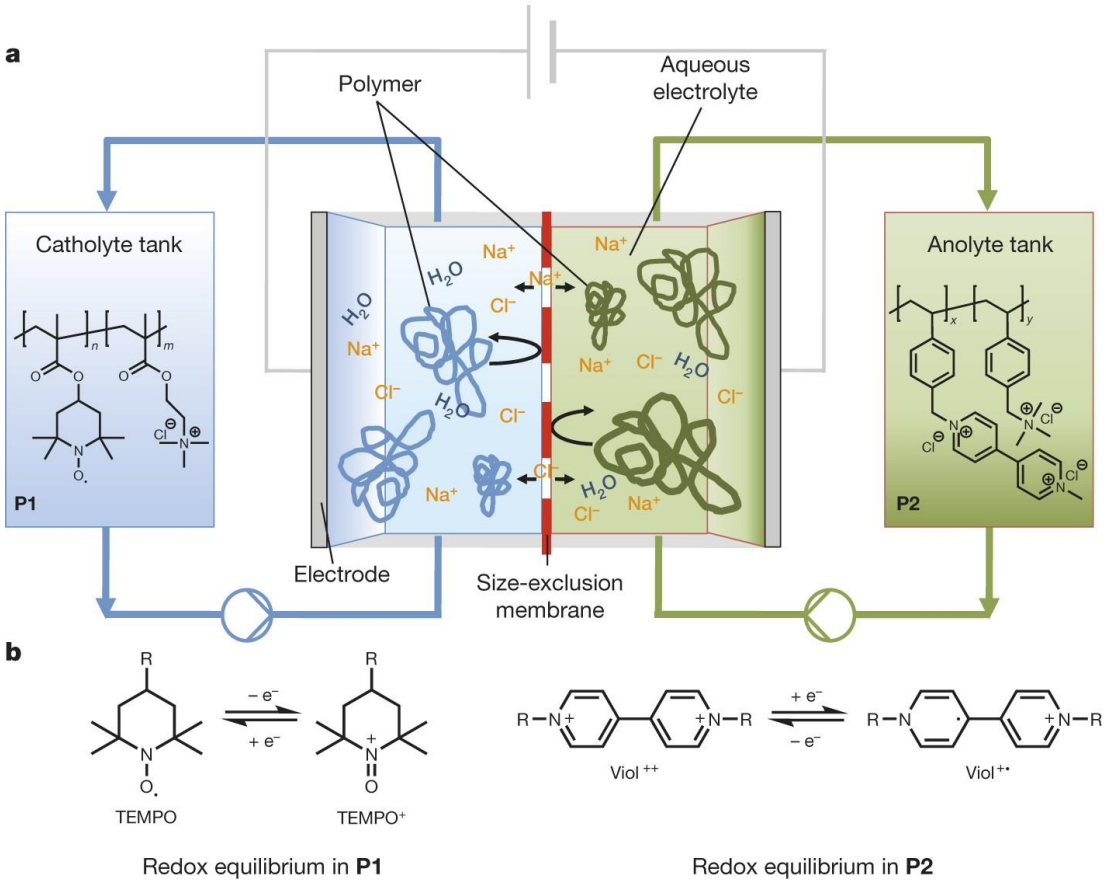

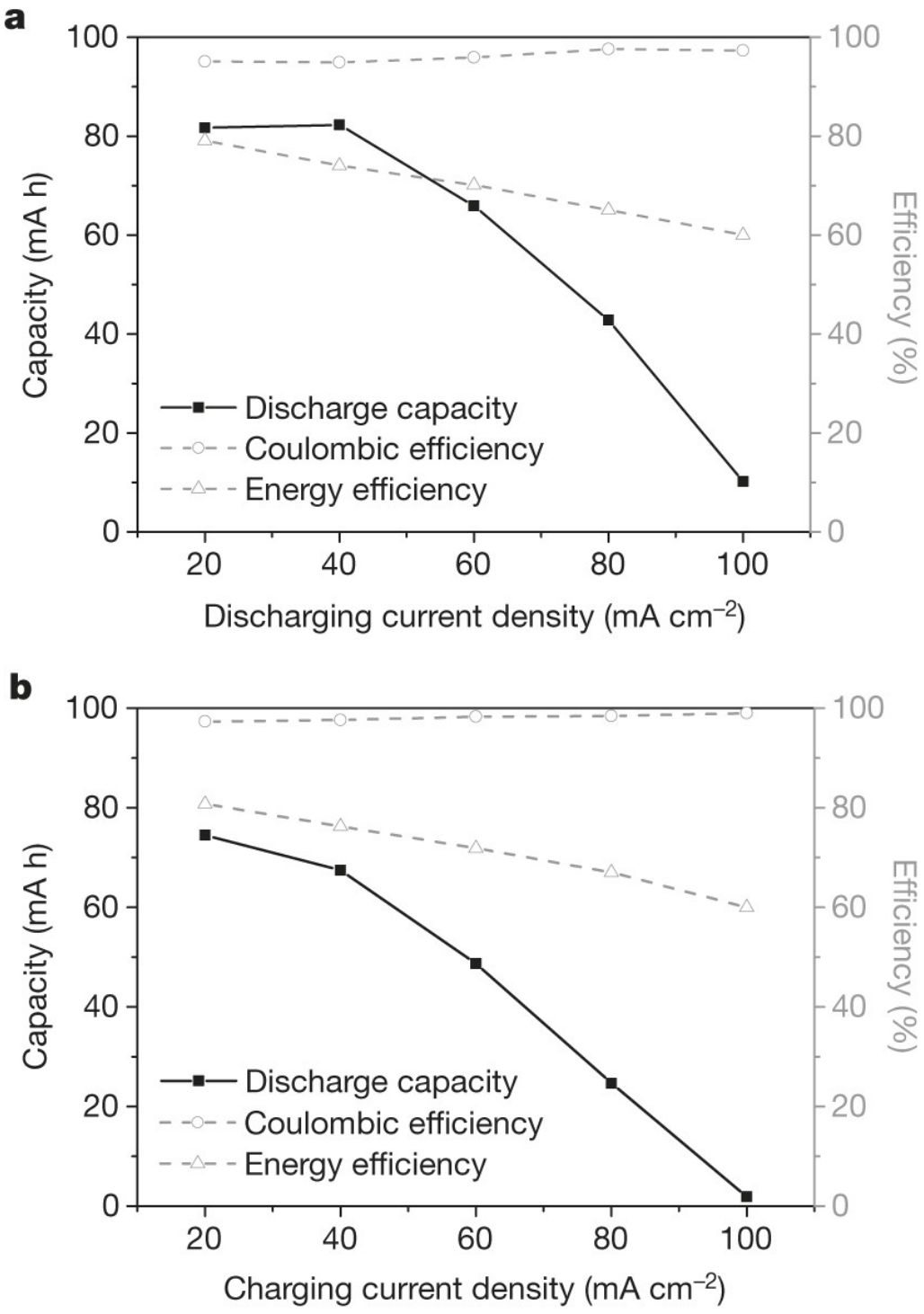

Figure 2.6 a) Schematic of poly-TEMPO and poly-viologen redox flow battery, with redox reactions of TEMPO and viologen derivatives (b) Below (a and b): cycle tests of poly-TEMPO and poly-viologen redox flow battery. These figures are reproduced with permission from ref [48], Copyright 2020, Royal Society of Chemistry.

Additionally, TEMPO and viologen-based RAPBP have also been utilized in NARFBs: in particular, a poly(norbornene)-*g*-poly(4-methacryloyloxy-2,2,6,6-tetramethylpiperidin-1-oxyl) (PNB-*g*-PTMA) was cycled in 0.1 M (n-$C_4H_9)_4NClO_4/CH_3CN$ in ethylene carbonate/diethyl carbonate (1/1 in v/v), and the cell delivered 95% of theoretical capacity.[46]

The synthesis of PNB-*g*-PTMA is shown in ***Figure2.7a)*** and ***b)***: the branch chains containing TEMPO unit were polymerized by living anionic polymerization first, and then the main chain was polymerized by a ring-opening metathesis polymerization (ROMP).[100 101]

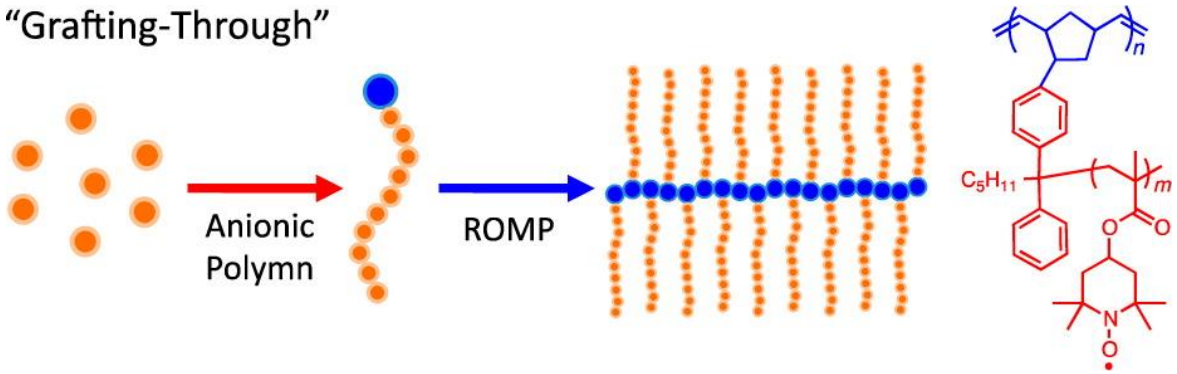

Figure 2.7 Schematic of the synthetic process of PNB-g-PTMA. This image is reproduced with permission from the work of Nishide at ref. [101] copyright 2020, ACS.

A stable redox reaction of TEMPO/$TEMPO^+$ was observed at +0.80 V *vs.* Ag/AgCl in 0.1 M (n-$C_4H_9)_4NClO_4/CH_3CN$ supporting electrolyte. [100] The authors demonstrated a half-cell flow cell with 0.1 M PNB-*g*-PTMA in 0.1 M (n-$C_4H_9)_4NClO_4$ in ethylene carbonate/diethyl carbonate (1/1 in v/v), delivering 95% of theoretical capacity.[100] In addition, Moore and Rodríguez-Lopez's groups[102] investigated the viability of viologen-based RAPs in NARFBs as well. In particular, poly (vinylbenzylethyl viologen) with controlled molecular weight between 21 and 318 kDa was synthesized to study the influence of molecular weight on electrochemical properties and the transportation behavior across the porous membrane. [102] This polymer exhibited high solubility over 2 M in aprotic solvent such as acetonitrile and propylene carbonate, as well as fast redox reactions at a potential of −0.70 V *vs.* Ag/Ag^+.[102] Then, poly(vinylbenzylethyl viologen) with different molecular weights showed high charge accessibility (94–99%) in the controlled potentials bulk electrolysis experiments.[102] In conclusion, Moore and Rodríguez-Lopez [102] demonstrated that viologen-based polymers with high molecular weight could be efficiently blocked by porous membranes.

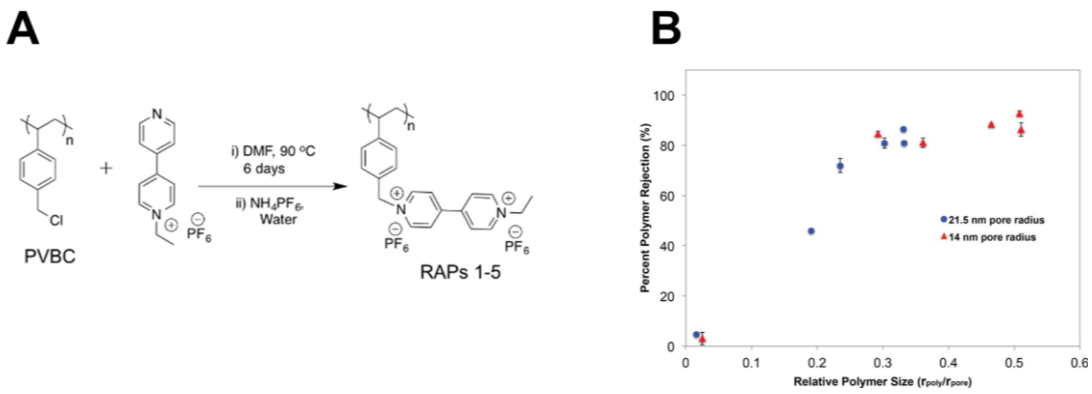

Figure 2.8 A) Synthesis of poly(vinylbenzylethyl viologen). B) Relative polymer size-dependent polymer rejection across COTS porous separators for RAPs. Reproduced with permission from ref [100]. Copyright 2020, American Chemical Society.

In the present work, among RAPs PANI was selected for operating as solid booster in a RFB employing acidic electrolytes. Indeed, PANI is characterized by a facile synthetic procedure with high yield, a well-defined redox activity and a good mechanical stability in strong acidic condition, which is required from the operating environment of the flow cell. In the following sections a general introduction to PANI as RAGEP is provided, focusing the attention on its redox features, electronic conductivity and different synthetic procedures.

2.3 Polyaniline (PANI)

2.3.1 PANI redox states and doping mechanism

PANI was discovered by Runge in 1834.[103] PANI is a mixed oxidation state polymer and it consists of a reduced benzoid and oxidized quinoid units.[103] PANI exhibits three oxidation states: *i*) leucoemeraldine (PANI-LE) as fully reduced, *ii*) emeraldine (PANI-E) as half oxidized and *iii*) pernigraniline (PANI-PE) as fully oxidized (***Figure 2.9***).

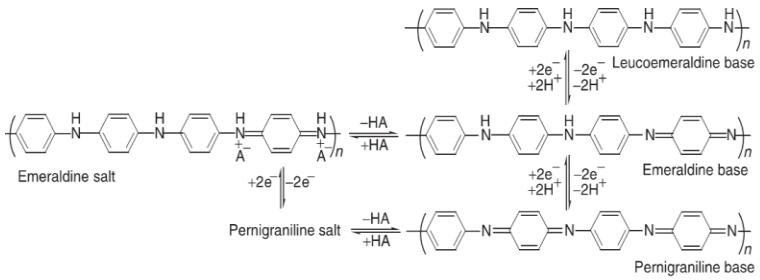

Figure 2.9 PANI chemical structures and oxidation states. Equilibria between PANI base and salts are also represented. In the schematic "HA" represents a general acid, such as hydrochloric (HCl). In addition all the abbreviations for the three different PANI forms are reported beside each molecular structure.

PANI is a conducting polymer and its electronic conductivity changes according to the oxidation states and to the degree of protonation.[103]

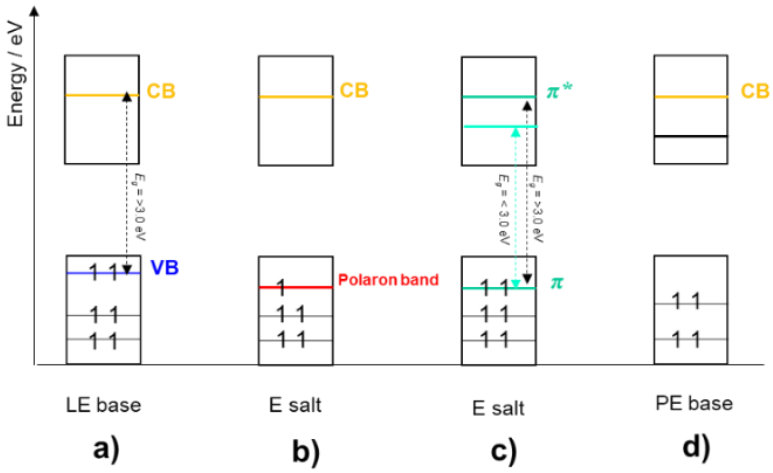

Figure 2.10 Different band gaps in PANI base and salt. This representation is inspired by the work of Molapo et al in ref. [103].

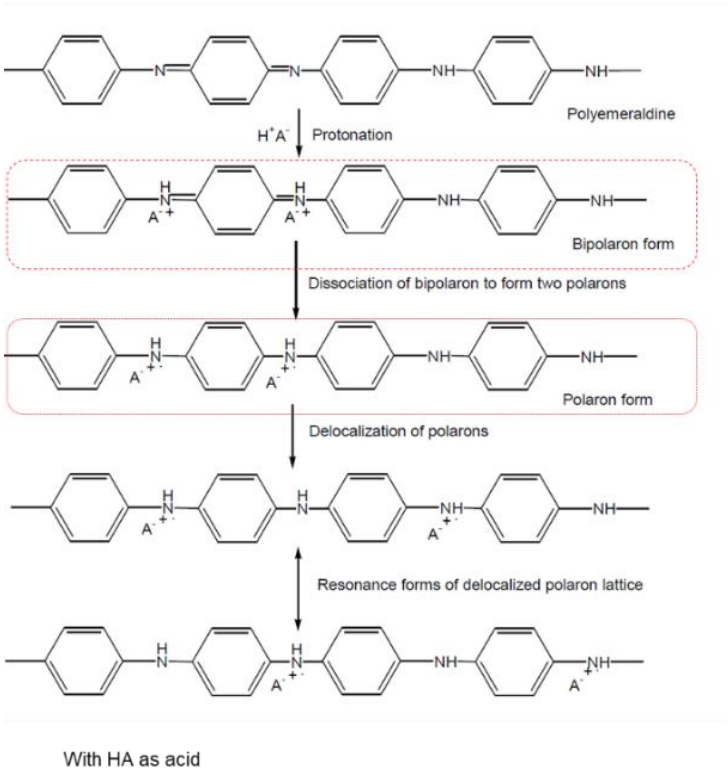

Figure 2.11 Doping mechanism involving polaron structures. These representations are inspired by the work of Molapo et al in ref. [103].

Among the three oxidation states, the intermediate, PANI-E, is the only conducting one.[103] This form of PANI has a structure consisting of an equal amount of amines (−NH−), imines (=N−). By protonic acid (HA) doping the protonated imine sites a structure called "bipolaron" (*i.e*. a di-cation salt) is formed (***Figure 2.11***).[103 104] In this mechanism the anion balances the charge making the system electroneutral.

Importantly, it is believed that an irreversible decrease in the electronic conductivity and redox activity can lead to degradation processes of PANI. In particular, the electronic conductivity degradation foresees a bond breaking in the polymer chains leading to a loss of monomer mass. In addition, any degradation might be due to an inhomogeneity of the oxidation reaction, in fact, the number of the intercalation sites can change affecting the ion transport across the polymer solution/interface increasing the required energy for the counter-ion intercalation [105]. As described by Stafström[104] *et al*. upon protonation of the imine sites, the conductivity increases by a factor of 10^{10}, reaching from 1 to 10^2 S·cm^{-1} (which is many order of magnitude higher than that of common polymers, < 10^{-9} S·cm^{-1}, but lower than that of typical metals, >10^4 S·cm^{-1}),[106 103] despite the unchanged electron concentration. Indeed, the proton ($-H^+$) has been largely used to control the oxidation states of PANI.[90] In particular, this doping chemistry enables PANI to possess both p and n-doped state from protons and metal ions, respectively. [90]

Kim *et al*. [90] describe particularly well the protonation/de-protonation mechanism in PANI and also the n-doping/de-doping process using lithium ion instead of protons (***Figure 2.12***).

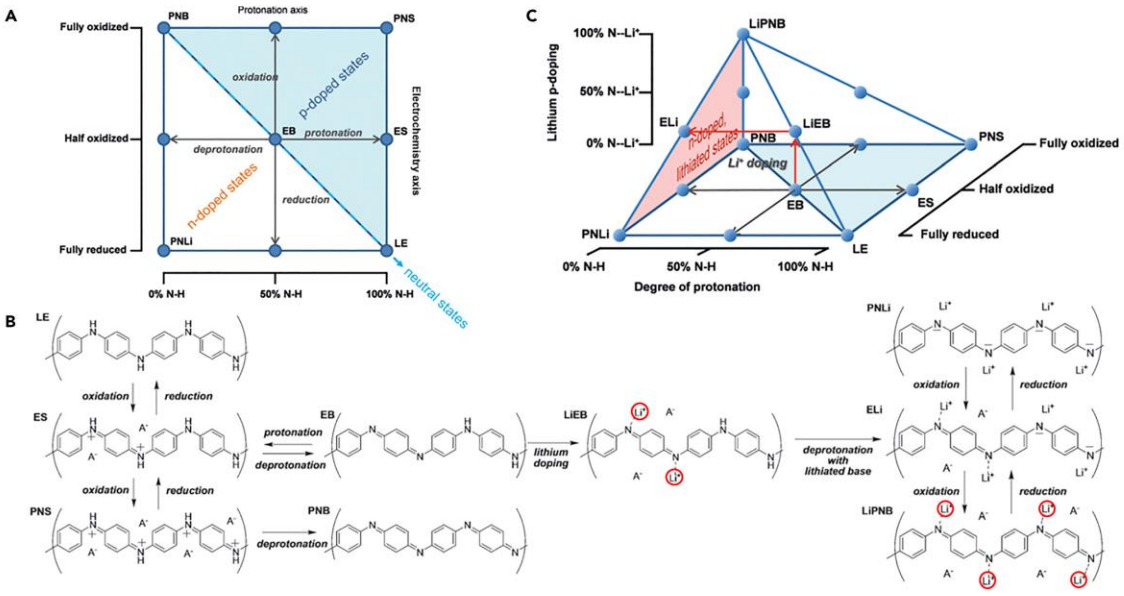

Figure 2.12 Lithium n-doped PANI for LIB. A) Diagram showing the different possible protonation and degrees of oxidation of PANI: the circles show the canonical forms that can be represented with four aniline repeating unit formulas. B) Formulas and reactions of some of the PANI states, including some of the new deprotonated-lithiated states (right). C) Extension in 3D of A) with an axis to include the possible lithium p-doped states. These images are reproduced with permission from the work of Kim et al. at ref [90]. Copyright 2020. Joule.

2.3.2 PANI synthesis

PANI can be synthesized either chemically or electrochemically. The chemical synthesis is a polymerization reaction in presence of an oxidizing agent (*e.g.* ammonium persulfate, $(NH_4)_2S_2O_8$)) in aqueous acidic medium (*e.g.* HCl). As explained by Molapo *et al.*,[103] the polymerization of aniline monomer proceeds *via* a multi-step radical propagation mechanism (***Figure 2.13a)***, ***b)*** and **c)**). Initially, the aniline monomer is oxidized forming a radical cation (***Figure 2.13a)***), where the charge can be redistributed in the aromatic ring allowing two resonance forms. Later, a coupling phenomenon of the radical-cation is observed (involving the para position of the aromatic ring), which suddenly leads to a re-aromatization mechanism accompanied by protons elimination (***Figure 2.13b)***).[103] Finally, chain propagation results from the radical cation of the dimer coupling with an aniline cation (***Figure 2.13c)***).

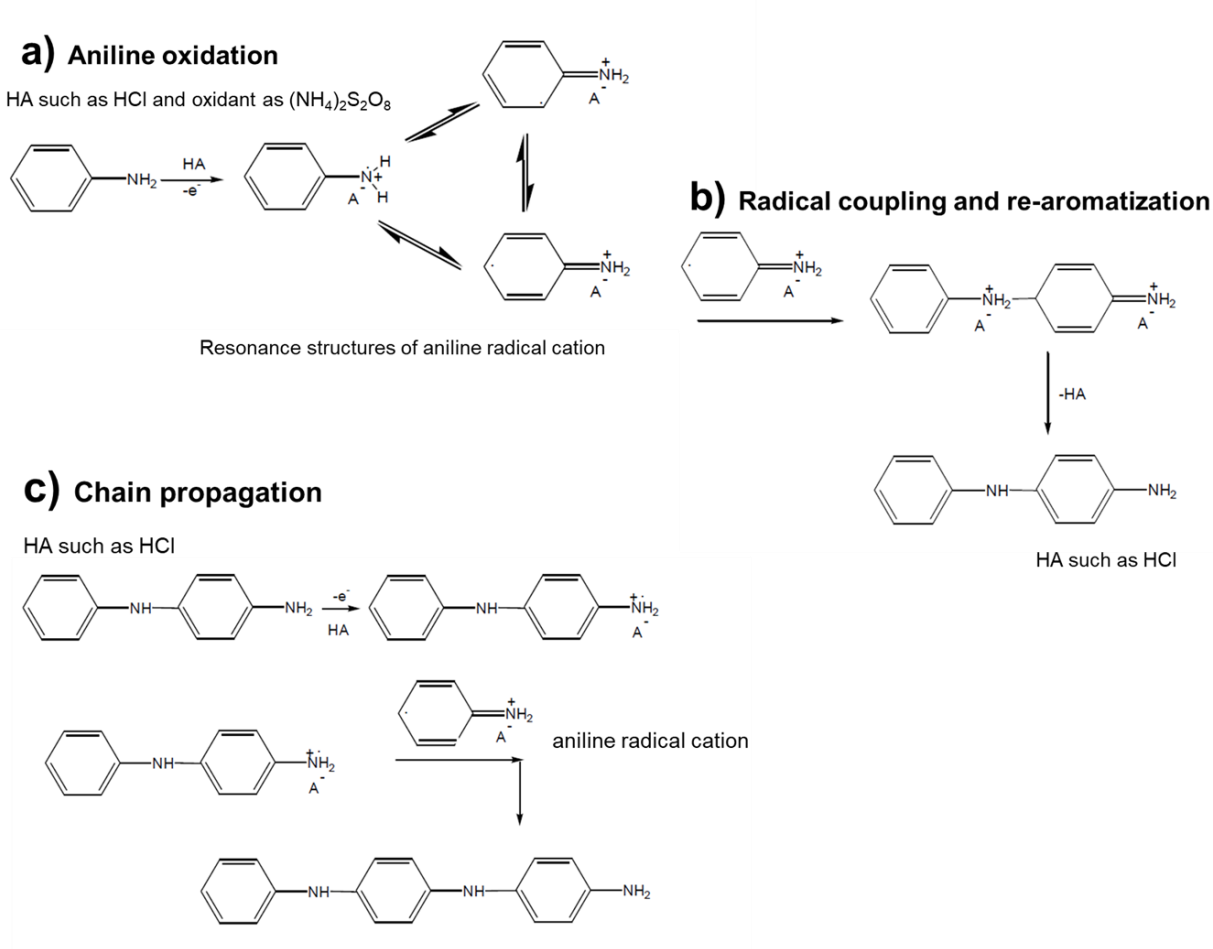

Figure 2.13 Full mechanism of chemical polymerization of aniline into PANI. a) Aniline monomer oxidation step. b) Radical coupling and re-aromatization step. c) Chain propagation step. This representation is inspired by the work of Molapo et al. in ref. [103].

On the other hand, electrochemical synthesis of PANI can also be performed and generally it can be done in a few ways : *i*) potentiostatically (*i.e*. applying a constant potentials and registering the current), *ii*) galvanostatically (*i.e*. applying a constant current and registering the potential, as it will be elucidated in the case of the present work) and *iii*) by cyclic voltammetry.[107]

In general, the polymerization reaction is carried out in aqueous solution of aniline in acidic medium (*e.g*., 1 M HCl, $HClO_4$ and H_2SO_4)[107]. The acidic medium is quite important and the pH of the solution has to be rather low to facilitate the solubilization of the aniline monomer in water and to avoid excessive branching of undesired products, but instead generate the desired emeraldine salt form.[103]

Nowadays PANI is employed in a variety of applications, including automotive, food, chemical, energy (*i.e*. batteries such as LIB)[107] [94], medical and environmental sectors. For instance, Tanguy *et al*.[108] describes it in ammonia sensing and detection, where the combination with metal oxides and carbon nanotubes enables reaching superior performance due the capability of the composites of forming *p-n* nano-junctions resulting in high ammonia selectivity. [108]

2.4 PANI as solid booster

PANI was selected judiciously as redox solid booster in the electrolyte reservoirs of an acidic ARFB. PANI chemically synthesized will be stationary kept at the bottom of the electrolyte tank and the flow of the electrolyte will fully pass through it. Then, upon flow cell operation PANI will be indirectly oxidized/reduced by the redox mediators, consequently storing the electrical charge. The schematic in ***Figure 2.14*** represents the general redox reactions of the synthesized PANI salt upon flow cell operation In addition, the Fermi level equilibration for the materials employed in the RFB is depicted in ***C)***.

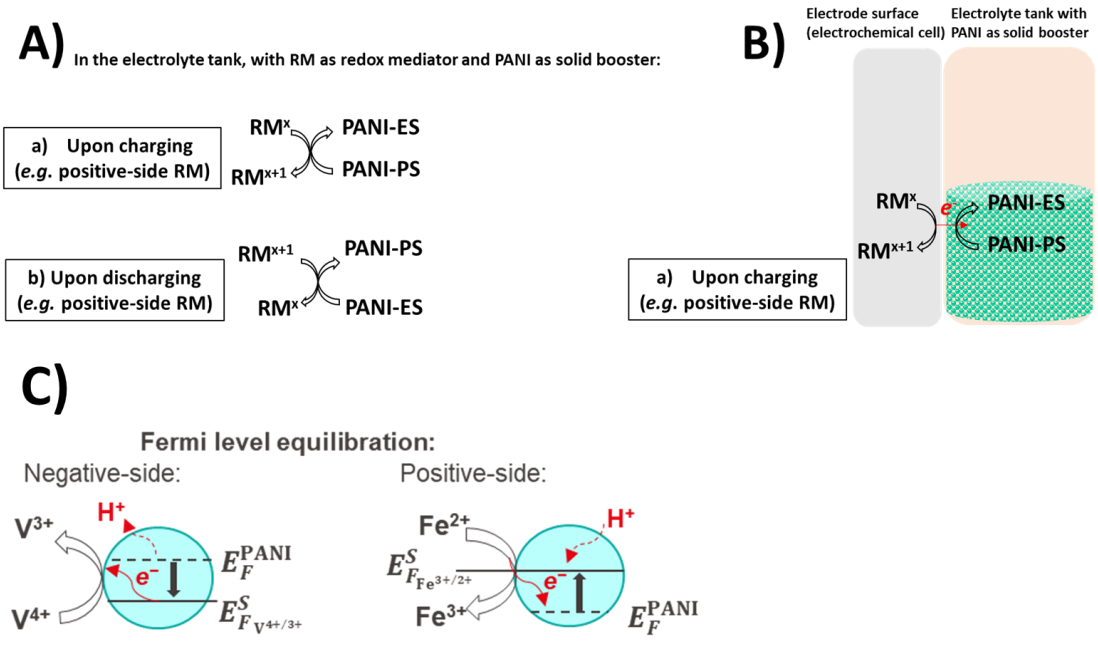

Figure 2.14 A) Redox reactions of PANI solid booster with generic redox mediator (RM) in the tank of the ARFB. In this case, PANI salt is depicted as synthesized for the flow cell cycling tests. B) Schematic of "redox-mediated" charge transfer in the case of PANI when the electrolyte is charging. C) Equilibration of Fermi level between PANI and the actual RM employed experimentally in ARFB. At the negative-side:* V *(IV/III) and at the positive-side* Fe *(III/II).

Furthermore, with a simple calculation it is possible to show how the addition of PANI booster into the electrolyte can increase the volumetric capacity. For example, for an electrolyte with a concentration of 1 M, the volumetric capacity is equal to 26.8 Ah·L^{-1} (considering one electron transfer reaction). The theoretical capacity of PANI is 144 mAh·g^{-1} [109] and its density is 1.3 g·mL$^{-1,}$ thus, the equivalent volumetric capacity is 187 Ah·L^{-1} (which is 7 times the volumetric capacity of the electrolyte alone at 1 M). Then, for a RFB containing 50% of PANI and 50% of 1 M liquid electrolyte, the final volumetric capacity would be 106 Ah·L^{-1}, which corresponds to 4 times the electrolyte capacity alone (26.8 Ah·L^{-1}) (***Figure 2.15***).

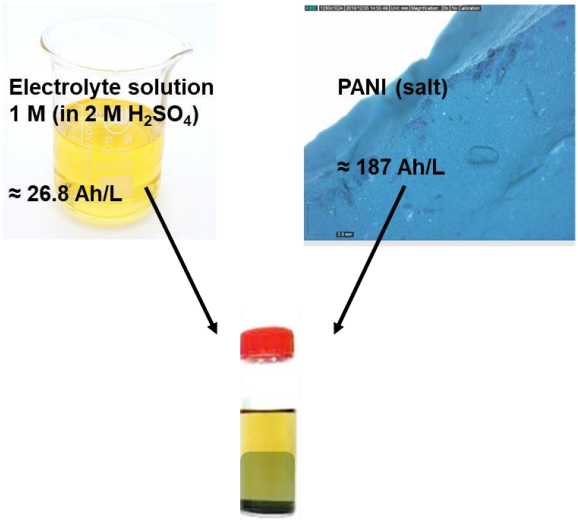

Figure 2.15 Schematic to explain the calculation having a system made of 50% wt. of 1 M electrolyte solution (in 2 M sulfuric acid) and 50% PANI (salt) in the same solution. The respective volumetric capacities are reported in the schematic according to the calculation. The image showing PANI in the vial is adapted from the work of Al-Dulaimi et al. at ref. [110]

It can be observed from this simple calculation that the addition of the booster can potentially quadruplicate the initial volumetric capacity of the electrolyte in a ratio (50:50) %, which is encouraging in the perspective of large-scale ARFB.

In the following sections, the viability of PANI as solid booster is presented: first, a preliminary electrochemical characterization of the polymer in absence of any redox mediator is performed, with the goal of understanding the position of the redox potentials through the cyclic voltammetry. Then, redox mediators will be carefully chosen in order to match the redox features of the PANI according to the "redox-mediated" charge transfer approach.

Subsequently, electrochemical cycling of PANI in the absence and then in the presence of the redox mediators will be recorded to obtain the deliverable gravimetric capacity and see whether the mediators would add some limitations. Finally, a "redox-mediated flow battery" in presence of the PANI booster in both the electrolyte reservoirs will be assembled and cycled to obtain an enhancement in the volumetric capacity of the electrolyte.

2.5 Electrochemical characterization of pristine PANI

2.5.1 Cyclic voltammetry of PANI on carbon paper (PANI/CP)

Electrochemical characterizations of PANI deposited onto carbon paper (herein denoted PANI/CP) after electrodeposition is shown on ***Figure 2.15***. The protocol of the electrodeposition of PANI from aniline monomer in acidic solution is fully described in chapter 5.

For all the electrochemical characterizations shown in this work, PANI deposited on CP served as working electrode and it was always placed as a 8 mm diameter disk in a polyetheretherketone (PEEK) plastic sample holder, equipped with a titanium current collector (***Figure 2.15A)***). The thickness of PANI film after the electrodeposition was not measured, but a first estimation of the electrode surface coverage, was done from the integration of the faradaic currents from the oxidation reaction in the CV in ***Figure 2.15B)***. In this case, the calculation was performed considering the oxidation currents of PANI (***a)*** in ***Figure 2.15B)***) and taking into account the CV at 50 $mV \cdot s^{-1}$ as scan rate. Thus, knowing the geometric surface area of the CP electrode (0.502 cm^2), a surface coverage of $1.03 \cdot 10^{-8}$ $mol \cdot cm^{-2}$ was found. In addition, a measurement of the PANI mass on the CP (subtracting the mass of a disk in same size of bare CP) after the electrodeposition was taken and for six samples it was (0.38±0.14) mg.

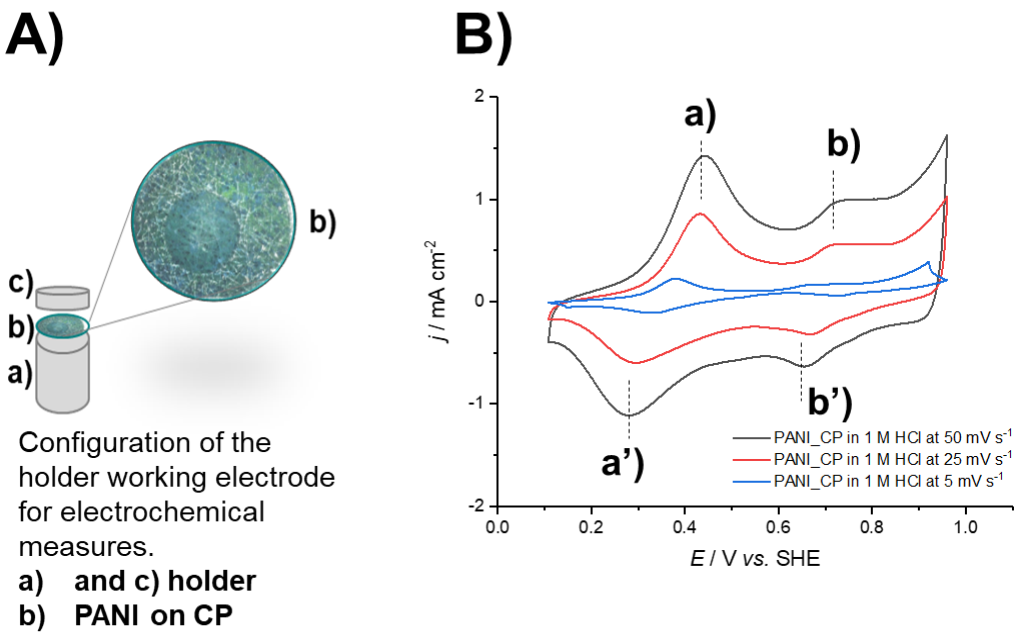

Figure 2.15 A) Sample holder used to fix the electrodeposited PANI/CP disk employed as working electrode (8 mm diameter, 0.502 cm^2 geometric area). B) Cyclic voltammetry of PANI/CP performed in 1 M HCl at 5, 25 and 50 $mV \cdot s^{-1}$. The redox transition of PANI are labeled a) and a') for the emeraldine to leucoemeraldine (PANI-E/ PANI-LE) transition and b) and b') for the emeraldine to pernigraniline (PANI-E/ PANI-PE) transition. The CV measurement was recorded without iR compensation.

In ***Figure 2.15B)***, the oxidation peak at +0.72 V *vs.* SHE corresponding to the transition from PANI-EB to PANI-PE, is quite broad. The increase of current at very positive potentials (> +0.85 V *vs.* SHE) was attributed to oxidative degradation of the polymer, as reported in other works.[111,112]

Further studies were made to investigate this point. In particular, PANI/CP was electrochemically cycled with different oxidation potentials to determine the onset for oxidative degradation. Specifically, the PANI/CP was oxidized from +0.75 V to +1.05 V *vs.* SHE (50 mV steps), always followed by a reduction at +0.60 V *vs.* SHE. Oxidative degradation resulted in an irreversible charge transfer during oxidation, which in turn should lower the Coulombic efficiency for each cycle. The Coulombic efficiency for different oxidation potentials is plotted in ***Figure 2.16*** below:

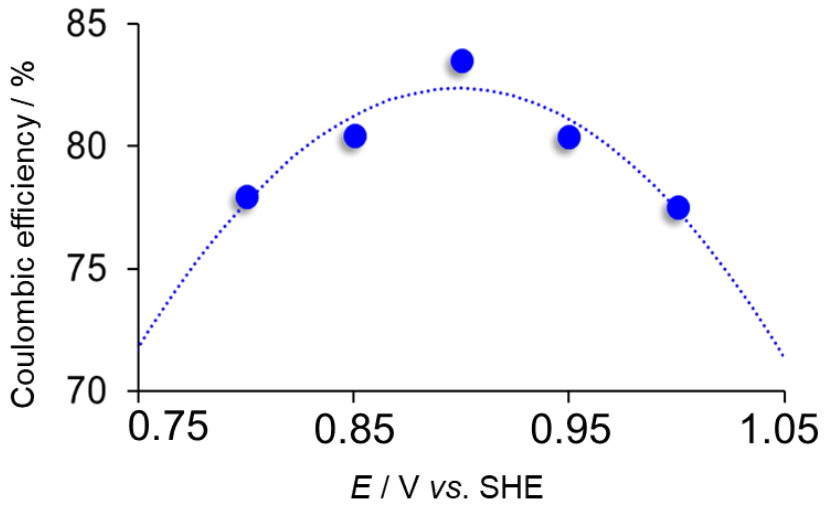

Figure 2.16 Coulombic efficiency (%) as a function of oxidation potential for PANI/CP in 1 M HCl.

The gradual decrease of Coulombic efficiency after *ca.* +0.85 V *vs.* SHE, indicates the onset of oxidative degradation. This was consistent with CV results presented in ***Figure 2.14B)***. The overoxidation and degradation of PANI was largely investigated [113] [114] and in particular, Tang *et al.*[115] measured the relative loss in the capacity of PANI films between -0.15 V and +0.80 V *vs.* Ag/AgCl saturated as reference electrode. They could conclude that the degradation of the PANI film was influenced from the anion present in the solution for the oxidation reaction. [115] In particular, from their experimental tests they found that the degradation of PANI was following the order H_2SO_4 > HCl > $HClO_4$ ≈ H_2SO_4 + $HClO_4$. [115]

2.5.2 Pairing of the redox transitions of PANI with the mediators in the solution

The CV of PANI in ***Figure 2.14B)*** allowed identifying two redox-active couples to pair. At the positive-side, iron ($Fe^{3+/2+}$) was selected to target the transition PANI-PE, and at the negative-side vanadium ($V^{4+/3+}$) for the transition PANI-LE. Indeed, according to the "redox-mediated" approach of charge transfer, the Fermi level of the PANI has to match the standard electrochemical potential of the RM ($V^{4+/3+}$ and $Fe^{3+/2+}$). ***Figure 2.15*** graphically represents this aspect, along with the equilibration of the Fermi level booster and mediator.

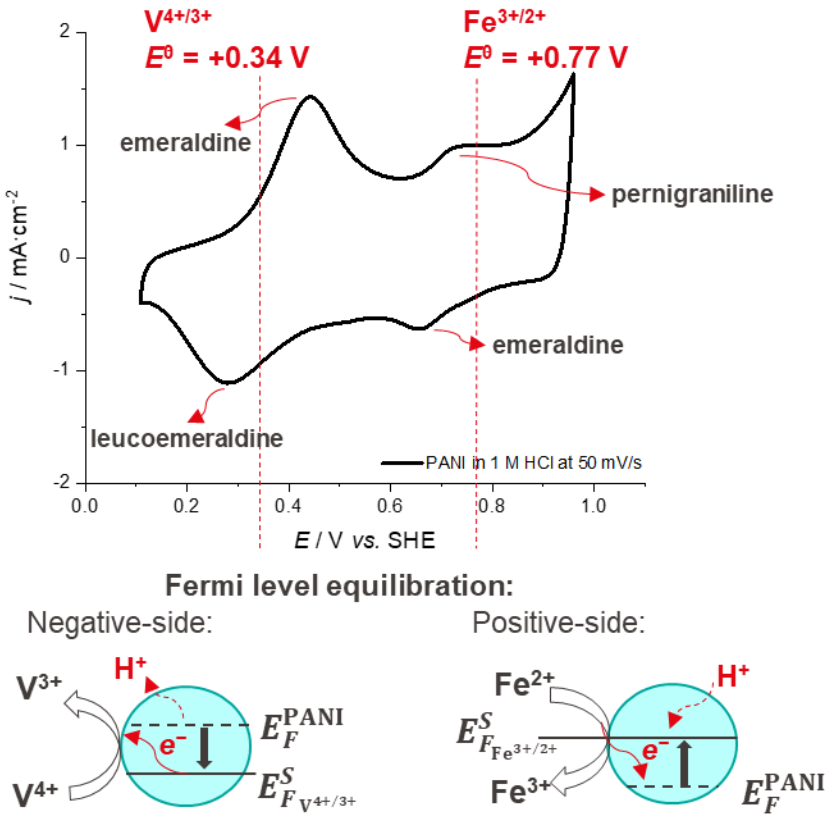

Figure 2.15 Pairing of the redox transitions of PANI from its CV on carbon paper with the redox mediators in the solution for the positive and the negative-side. Below the CV, Fermi level equilibration is represented for both the couple of paired materials in the same medium.

On the negative-side, the thermodynamic reduction potential of $V^{4+/3+}$ (E^{θ} = +0.337 V *vs.* SHE) overlaps quite well with the PANI ES-LE, while at the positive-side, the PANI ES-PE is *ca.* 60 mV more negative than the standard potential of $Fe^{3+/2+}$ (E^{θ} = +0.771 V *vs.* SHE), suggesting that $Fe^{3+/2+}$may only facilitate the oxidation of PANI.

However, according to the Nernst equation, a solution of predominantly Fe^{2+} (*e.g.* 99% of total iron concentration) can target also the reduction of PANI. Thus, when iron is sufficiently reduced it is thermodynamically possible to drive the reduction of PANI. Importantly, $Fe^{3+/2+}$ should also avoid the onset oxidative degradation, as seen from ***Figure 2.16***.

Table 2.1 Redox potentials of the system PANI-mediators. The potentials of oxidation and reduction E_{ox} and E_{red} are reported vs. SHE and they are taken from the CV in Figure 2.14B). For the two mediators Fe and V, the standard redox potential is reported (E^{θ}).

	E_{ox} / V *vs*. SHE	E_{red} / V *vs*. SHE	E^{θ} V *vs*. SHE
Mediator $Fe^{3+/2+}$	+0.880	+0.650	+0.771
Solid booster PANI-PE	+0.720	+0.620	
Mediator $V^{4+/3+}$	+0.450	0.230	+0.337
Solid booster PANI-PE	+0.400	+0.260	

Additionally, it should be noted that this configuration of redox pairs (*i.e*. PANI ES-LE/$V^{4+/3+}$ and PANI ES-PE/ $Fe^{3+/2+}$) offers the advantage of using PANI at both sides of the "redox-mediated flow battery".

2.5.2 Electrochemical cycling of pristine PANI on carbon paper in 1 M HCl

Once the RM were selected, PANI/CP was cycled potentiostatically in 1 M HCl solution in the thermodynamic potential window of mediator. ***Figure 2.17*** displays a potentiostatic cycle for PANI in the chosen potential ranges for $Fe^{3+/2+}$ (***a)*** (positive-side mediator) and of $V^{4+/3+}$.(***b)*** (negative-side mediator). These electrochemical cycling experiments allowed obtaining the practical gravimetric capacity of PANI in the thermodynamic potential window of the selected mediators. In both cases, PANI experimental gravimetric capacity was found *ca*. 31 $mAh{\cdot}g^{-1}$ (31.7 $mAh{\cdot}g^{-1}$ when PANI was paired with $Fe^{3+/2+}$ and 30.6 $mAh{\cdot}g^{-1}$ when PANI was paired with $V^{4+/3+}$). These values are much lower as compared to the theoretical capacity (*ca*. 22%) of the pristine polymer (144 $mAh{\cdot}g^{-1}$).[109]

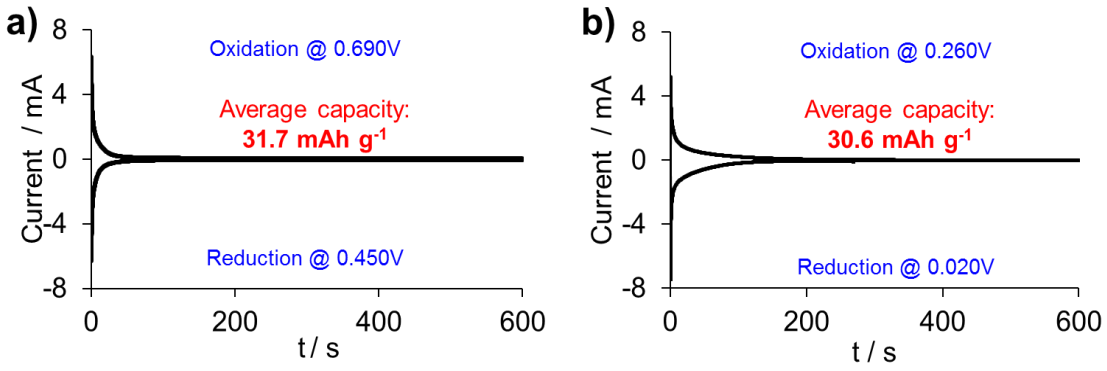

Figure 2.18 Potentiostatic cycling of PANI/CP in 1 M HCl in the potential range corresponding to a) $Fe^{3+/2+}$ and b) $V^{4+/3+}$. The measurements were performed in a three-electrode electrochemical cell assembled with a holder working electrode containing a disk of 8 mm diameter of PANI/CP, a 6 cm coiled platinum wire as counter electrode and an Ag/AgCl in 3 M KCl as reference electrode. The standard potentials given in the inset of the figures are reported according to the Ag/AgCl in 3 M KCl reference electrode. For completeness, a) for $Fe^{3+/2+}$ the oxidation potential is +0.88 V and the reduction potential is +0.65 V vs. SHE. For b) $V^{4+/3+}$, the oxidation potential is +0.23 V and the reduction potential is +0.45 V vs. SHE.

The reason behind these lower experimental values of PANI capacity as compared to theoretical value was not fully understood, however, it was supposed that the ion diffusion within the film could have had an influence in the charge transfer process or as well that as soon as the PANI was fully oxidized or fully reduced, the overall conductivity of the film decreased. Indeed, as it was discussed in the paragraphs above, the conductivity of PANI is related to the oxidation state and the only form known for being conducting is the PANI-E.[103]

Furthermore, just as preliminary study, Cottrell plots were elaborated for both the potentiostatic cycling of PANI/CP in the thermodynamic potential window of $Fe^{3+/2+}$ and $V^{4+/3+}$ mediators. The results are reported in ***Figure 2.19.***

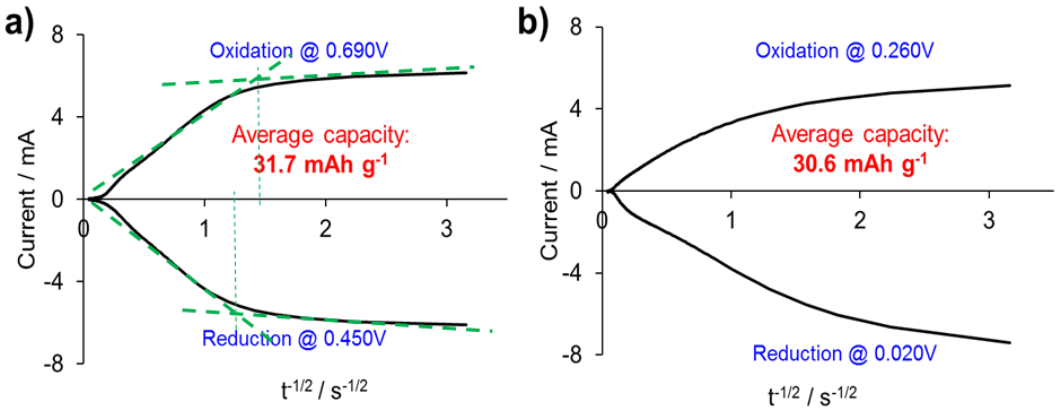

Figure 2.19 Cottrell plots representing the potentiostatic cycling of PANI/CP in 1 M HCl in the potential range corresponding to a) $Fe^{3+/2+}$ and b) $V^{4+/3+}$.

For the potential range corresponding to $Fe^{3+/2+}$ (oxidation potential equal to +0.69 V *vs*. Ag/AgCl in 3 M KCl_{aq} or +0.90 V *vs*. SHE and reduction potential equal to +0.450 V *vs*. Ag/AgCl in 3 M KCl_{aq} or +0.660 V *vs*. SHE, in ***Figure 2.20a)***), two distinct linear regions appear, as represented by the dashed lines on the plot. The exact cause of this behavior is not clear, but it suggests that the system is sequentially controlled by two different transport processes (*e.g.* diffusion of cations in the bulk electrolyte followed by diffusion of cations within the polymer structure). This behavior was not observed in the potential window corresponding to $V^{4+/3+}$ (***Figure 2.20b)***), but even in this case the exact mode was not fully understood.

2.5.3 Electrochemical cycling of pristine PANI on carbon paper with $Fe^{3+/2+}$ and $V^{4+/3+}$

The capacity values obtained in the previous section are representative of the direct reduction/oxidation activity of PANI in the thermodynamic potential window of $Fe^{3+/2}$ and $V^{4+/3+}$ in 1 M HCl supporting electrolyte solution. However, in the current system, PANI would be charged/discharged chemically *via* an actual solution of the RM. Thus, the RM may impose additional limitations on the achievable capacity.

To quantify the practical capacity under "redox-mediated" charging/discharging conditions, PANI/CP was cycled in an oxidizing and reducing solution of $Fe^{3+/2+}$ or $V^{4+/3+}$ (see chapter 5 for the experimental protocol). Initially, PANI/CP was cycled between solutions of Fe^{3+} and Fe^{2+} and the resulting specific capacity along with % CE trend is presented in ***Figure 2.21*** over 25 cycles. The average capacity is around 45 $mAh \cdot g^{-1}$ with high and stable CE (98%). This capacity value is slightly higher (1.4 times) than that in absence of the mediator (31.7 mA g^{-1}). A couple of reasons can explain this experimental result: first, the experimental time in this case was longer than in the previous electrochemical cycling in 1 M HCl solution, second, this can be an effect of the RM and a first experimental proof of the "redox-mediated" charge transfer approach.

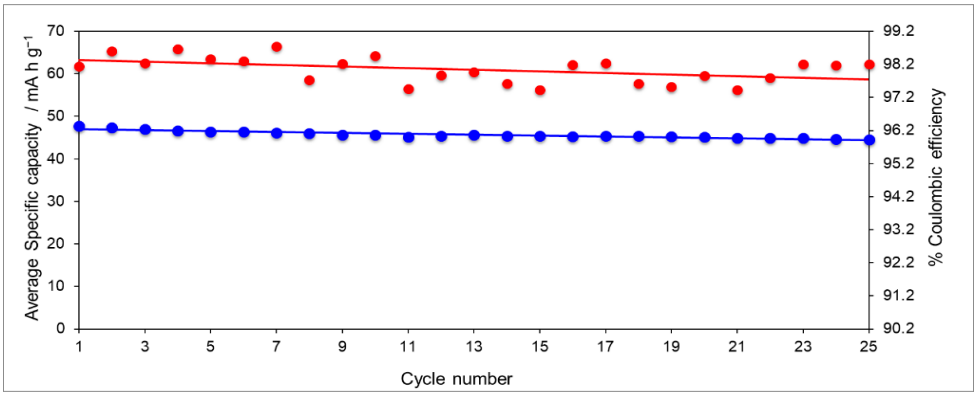

Figure 2.21 Specific capacity (in blue dots) and %CE (in red dots) obtained by cycling of PANI/CP in 0.3 M solutions of Fe^{3+} and Fe^{2+}.

Later, this "mediated" cycling experiment was repeated on three different samples of PANI/CP in order to see the trend of the capacity and % CE in just more than one single sample. The results are summarized in ***Table 2.2*** below.

Table 2.2 Specific capacity and Coulombic efficiency obtained by cycling three samples of PANI/CP in 0.3 M solutions of Fe^{3+} and Fe^{2+}.

"$Fe^{3+/2+}$ / PANI ES-PE	*Mass / mg*	*Specific capacity mAh g^{-1}*	*% CE*	*No of cycles*
PANI/CP sample a)	0.37	47.50	97	25
PANI/CP sample b)	0.27	43.69	98	25
PANI/CP sample c)	0.47	45.67	98	25

Subsequently, PANI/CP was also chemically cycled using solutions of V^{3+} and VO^{2+} as the reductant and oxidant, respectively (***Figure 2.22***). Despite the good specific capacity obtained by electrochemical cycling in 1 M HCl solution (30.6 mAh·g^{-1} experimental gravimetric capacity), in this cycling test the PANI capacity was very poor (*ca*. 5.6 mAh·g^{-1} over 25 cycles). This was preliminarily attributed to the relatively poor kinetics of the $V^{4+/3+}$ couple, suggesting that VO^{2+} is more readily reduced directly to V^{2+}, and similarly V^{3+} is more readily oxidized to VO^{2+} leading to unfavorable electron transfer to PANI.[33] Probably the mediator undergoes two electron transfer mechanisms rather than only one.

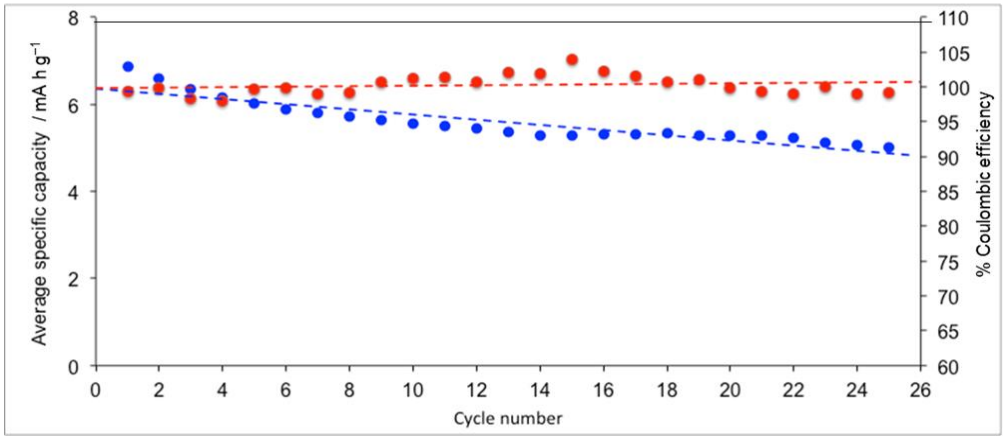

Figure 2.22 Specific capacity (in blue dots) and Coulombic efficiency (in red dots) obtained by cycling of PANI/CP in 0.3 M solutions of V^{3+} and VO^{2+}.

As in the case of iron, this "mediated" cycling test was repeated on three different samples of PANI/CP and the results can be found in ***Table 2.3*** below:

Table 2.3 Specific capacity and Coulombic efficiency obtained by cycling three samples of PANI/CP in 0.3 M solutions of V^{4+} and V^{3+}.

"$V^{4+/3+}$ / PANI ES-LE	***Mass / mg***	***Specific capacity mAh g^{-1}***	***% CE***	***No of cycles***
PANI/CP sample a)	0.17	5.60	97	25
PANI/CP sample b)	0.37	6.12	97	25
PANI/CP sample c)	0.27	5.85	98	25

The "redox-mediated" cycling of PANI on CP shown in this section provides a first estimation of the practical gravimetric capacity and % CE of PANI in presence of the real solutions of the RM (oxidant and reductant, respectively). The goal of these tests was really to see if the RM could add some limitations to the PANI/CP, as observed in the case of $V^{4+/3+}$.

In the next section, the viability of pristine synthesized PANI in an ARFB employing acidic solutions of iron (at the positive-side) and vanadium (at the negative-side) is presented. As it will be seen, during these experiments a few challenges in terms of the chemical reactivity of the PANI in the actual RFB were experienced, but addressed to propose a final system with enhanced volumetric capacity.

2.6 An acidic RFB using $Fe^{3+/2+}$ and $V^{4+/3+}$ electrolytes

The redox flow battery was composed of 1 M $FeSO_4$ (40 mL in 2 M H_2SO_4) at the positive-side and 1 M $VOSO_4$ (40 mL in 2 M H_2SO_4) at the negative-side. The complete schematic of the electrochemical cell as well as of the full RFB setup can be found in chapter 5. The RFB was cycled at 200 mA (15.4 $mA \cdot cm^{-2}$) and the total charge was found equal to 3467 C, *ca*. 90% of the theoretical (3859 C), after 2 just two cycles (***Figure 2.24***).The theoretical capacity (herein denoted as $Q_{th.}$) was calculated according to the following expression ***ii)***.

$$Q_{th.} = c \cdot V \cdot n \cdot F \qquad \textbf{ii)}$$

Where *c* is the concentration of the electrolyte in $mol \cdot L^{-1}$ (or M), *V* the volume of the electrolyte in the tank (in L), *n* the number of electrons involved in the redox reaction and *F* the Faraday constant (95485 $C \cdot mol^{-1}$). The theoretical charge is expressed in Coulomb. For the present $Fe^{3+/2+}$ and $V^{4+/3+}$ RFB, the theoretical performance is reported in ***Table 2.4***, followed by the experimental one in ***Table 2.5***.

Table 2.4 Theoretical performance of the Fe-V flow battery at 200 mA/cm² (40 mL of electrolytes on each side).

***I* /mA**	***j* /mA·cm^{-2}**	**$Q_{th.}$/ C**	**$Q_{th.}$ /mAh**	**$Qv_{th.}$ /Ah·L^{-1}**	**E_{cell} / V**
200	15.40	3859	1072	27	0.43

Table 2.5 Experimental performances of the Fe-V flow battery at 200 mA/cm² (40 mL of electrolytes on each side).

***I* /mA**	***j* /mA·cm^{-2}**	**$Q_{exp.}$/ C**	**$Q_{exp.}$ /mAh**	**Qv_{exp} /Ah·L^{-1}**
200	15.40	3467	963	24

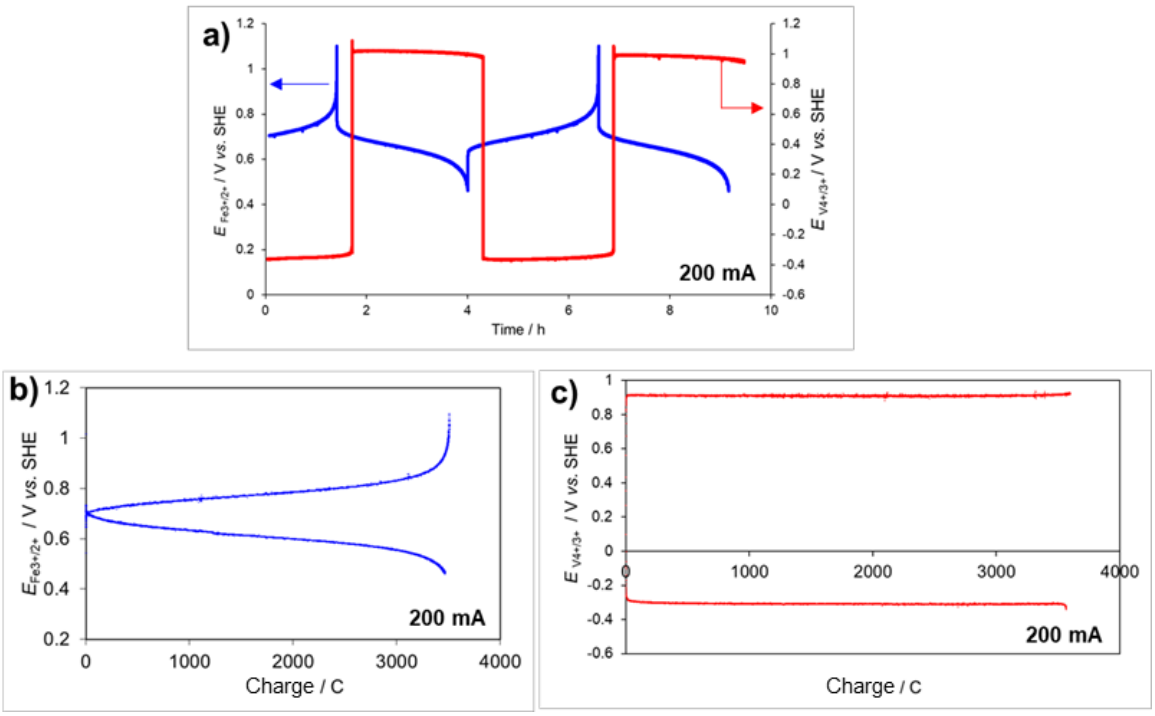

Figure 2.23 a) Potential vs. time for the cycling of 1 M $Fe^{3+/2+}$ (in blue) and $V^{4+/3+}$ (in red) at 200 mA (15.40 mA·cm^{-2}) in the full system. b) Potential of 1 M $Fe^{3+/2+}$ vs. capacity at 200 mA (15.40 mA·cm^{-2}). c) Potential of 1 M $V^{4+/3+}$ vs. capacity at 200 mA (15.40 mA·cm^{-2}). The supporting electrolyte is 2 M H_2SO_4.

Figure 2.23a) b) and ***c)*** shows the cycling performance of the iron and vanadium electrolytes in the ARFB in acidic pH. It can be noticed that the iron redox couple at the positive-side (***Figure 2.24a)*** and ***b)***), performed reasonably well at 200 mA, achieving almost 90% of the theoretical charge (3859 C). On the other hand, this cannot be said unfortunately for the vanadium couple at the negative-side. As it can be observed (***Figure 2.23c)***) the overpotential to sustain the applied current is huge (*ca.*1000 mV), which means that probably the membrane was giving high resistance during the cycling. In case, the flow battery was set in a three-electrode configuration, with the reference electrode (Ag/AgCl in 3 M KCl) placed in the tank of the iron (positive-side). Thus, perhaps, switching the configuration could have been interesting to see whether vanadium would have given a better performance. Additionally, it should be mentioned that just a preliminary investigation of the $Fe^{3+/2+}$ and $V^{4+/3+}$ cyclability at 200 mA was accomplished to obtain the practical charge of the full system in the absence of the PANI. No further investigation tests on the electrolytes cyclability were performed later. As from this point, the vanadium couple at the negative-side of the system is considered as a sort of "sacrificial" electrolyte and the viability of the PANI booster is evaluated only on the iron side, although measurements were actively recorded on both compartments of the cell.

2.7 An acidic "redox-mediated" FB in the presence of pristine PANI

Knowing the theoretical capacity of the redox couple in the electrolyte (1072 mAh, for 1 M and 40 mL) and assuming the specific capacity of the booster from the electrochemical cycling tests on CP (31 mAh g^{-1}) as the maximum achievable in presence of the RM, the amount of solid booster to add into the RFB tanks was calculated. This amount was found equal to 6.9 g, which was added to both tanks of the flow cell prior removal of 5.3 mL of electrolyte, in order to keep balance in the electrolyte volume (40 mL), as compared to the precedent cycling tests without any booster. To place the synthesized PANI salt particles (a few mm in size) at the bottom of the electrolyte tank, a new design of the reservoir was created, named *vertical-bed-packed-reactor* (***Figure 2.24***).

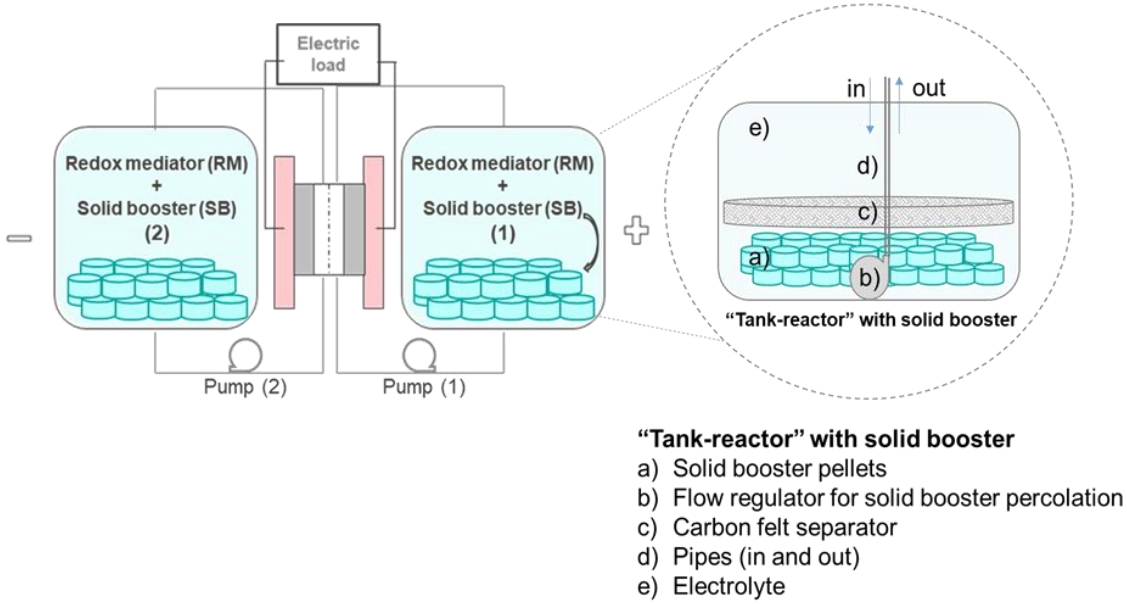

Figure 2.24 "Redox-mediated" flow battery with illustration of the "vertical-bed' packed-reactor" at both sides of the system.

In practice, a bed of PANI was disposed stationary at the bottom of the tank using a piece of carbon felt having the same diameter of the tank. The *tank-reactor* was then filled up by the RM solution and the whole flow from/to the electrochemical cell/tank was adjusted appropriately to guarantee a full percolation of the booster upon cycling. Upon cycling the cell at 200 mA (15.4 mA·cm^{-2}), the electrolyte charge was found to be only 3024 C, an overall *reduction* of 12.8% as compared to the $Fe^{3+/2+}$ alone (3467 C) (***Figure 2.25***).

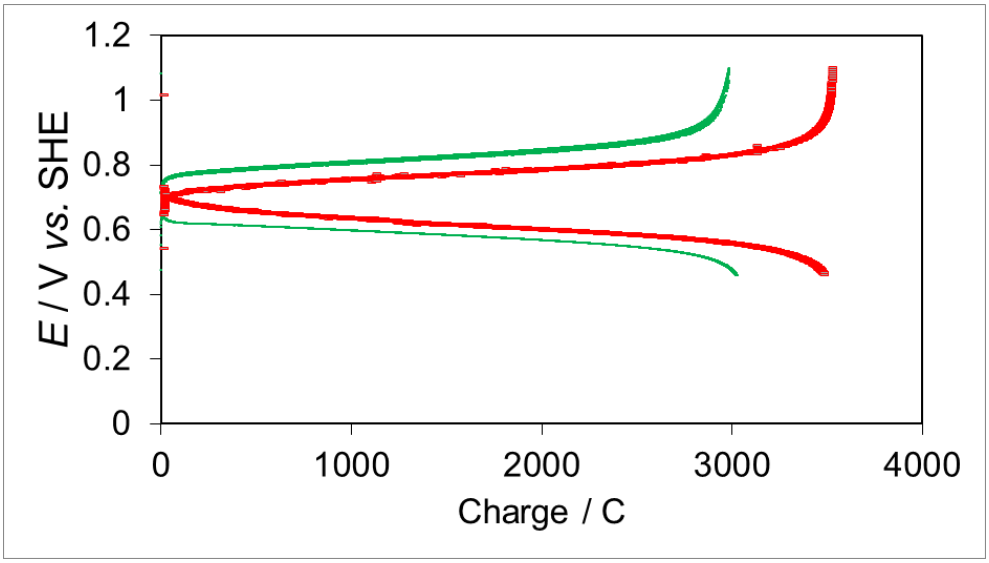

Figure 2.25 "Redox-mediated flow battery" cycling tests at 200 mA (15.40 mA·cm^{-2}): in red, potential of 1 M $Fe^{3+/2+}$ vs. charge and in green potential of 1 M $Fe^{3+/2+}$ + 6.9 g of pristine PANI vs. charge. The supporting electrolyte is 2 M H_2SO_4.

This decrease in the overall charge was first hypothesized to be due to a passivation of the exterior surface of the PANI particles upon the flow cell cycling. Indeed, as aforementioned, only the emeraldine form of PANI (PANI-E) is a good electronic conductor, while when PANI is in the fully oxidized or reduced state (PE and LE, respectively), it is an insulator[116–119] (***Figure 2.27B)***). Consequently, any charge transfer to the interior of the PANI particle would become increasingly difficult as the exterior surface is becoming insulating upon charging/discharging. Certainly, after the exterior of the particle reacted, oxidation/reduction of the interior would only be possible by diffusion of the RM within the pore structure of the particle, imposing a significant rate-limitation.

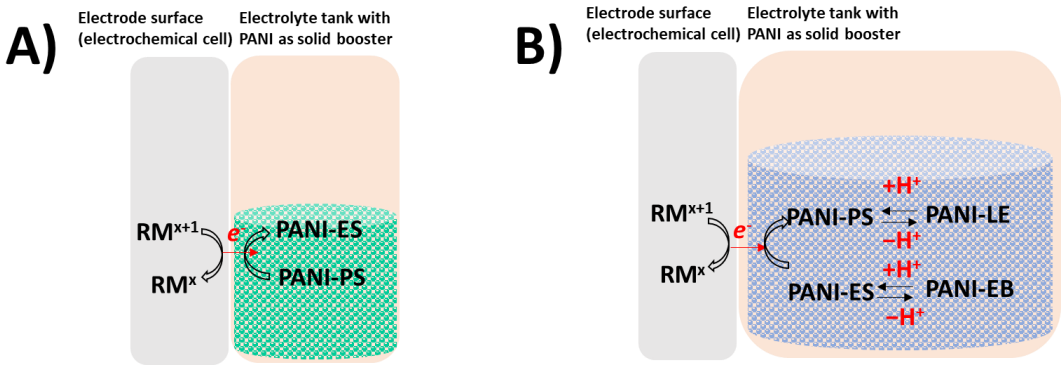

Figure 2.27 A) Redox reaction of the synthesized PANI salt (from emeraldine to pernigraniline) upon battery cycling, coupled with redox reactions of the mediator (RM). B) Equilibria of protonation/ deprotonation in the acidic medium of the flow cell: the conducting emeraldine salt can switch to emeraldine base and become insulating as soon as it reaches the pernigraniline state.

In addition, it was thought that this decrease in the capacity was due to the kinetics of the RM, which could have changed significantly with the oxidation states of the PANI. In such a case, the exterior surface of the particle would be essentially kinetically-passivated. Again, after passivation further oxidation/reduction of the interior of the particle would only be possible by diffusion of the RM into the PANI particle. This insulating effect could have led to a lower measured charge in the flow cell. Furthermore, an additional loss in the flow battery may be due to a portion of the RM ions entering the pore structure and leaving the circulating electrolyte, thus becoming inaccessible during cycling.

To prevent the passivation effect, a composite of PANI with CAB in a weight ratio (80:20) % (herein denoted as PANI/CB) was synthesized and tested in the same "redox-mediated" flow battery configuration. The performance is shown in the following section.

2.8 An acidic "redox-mediated" FB in the presence of PANI/CB

A conductive composite of PANI and CB was synthesized incorporating CAB in the polymerization reaction of the aniline monomer (see chapter 5). CAB was added to increase the electronic conductivity of PANI upon charging/discharging and to provide alternative reaction sites for the RM at the surface of the particle. In this way, the CAB network should enable the RM to react immediately at the surface rather than needing to diffuse into the solid particle. In this case, a comparison of the measured electronic conductivity of pristine PANI and PANI/CB is given in ***Table 2.6***. The electronic conductivity of synthesized pristine and functionalized with CAB PANI was measured by a four-point conductivity test (see chapter 5). All samples were immersed in solutions of $Fe^{3+/2+}$ and in $V^{4+/3+}$ to obtain the LE (fully reduced) and PE (fully oxidized) forms of the polymer, and then washed with 1 M H_2SO_4 and dried thoroughly before analysis.

Table2.6. Summary of dry conductivity values for PANI and PANI/CB.

	PANI-E	***PANI-PE***
PANI	1.55±0.03 $S \cdot cm^{-1}$	1.30±0.16 $S \cdot cm^{-1}$
PANI/CB	6.22±0.86 $S \cdot cm^{-1}$	6.14±0.65 $S \cdot cm^{-1}$

Incorporating CAB into the PANI structure increased the electronic conductivity more than four-fold. Therefore, satisfied with this improvement in conductivity, 9.87 g of PANI/CB was added to each electrolyte tank of the battery. This amount of PANI/CB mass was added following the same procedure as for the pristine PANI explained in the previous paragraph. The battery was again cycled at 200 mA (15.40

mA·cm^{-2}), and a charge of 5159 C (or 1433.0 mAh) was observed. This charge represents an improvement of 49% as compared to the battery without solid booster over the $Fe^{3+/2+}$ alone, at the same current.

When the flow cell was cycled at the higher current of 500 mA (38.5 mA·cm^{-2}), a total charge of 4449 C (or 1235.8 mAh) was obtained leading to an improvement of 64% as compared to the $Fe^{3+/2+}$ alone. This suggests that PANI/CB provides good rate-stability in this "redox-mediated" configuration, allowing the cell to be cycled at high power. The equivalent volumetric capacity of PANI/CB (with a density of 1.3 g·mL^{-1} for pristine PANI) was found *ca*. 84.2 Ah·L^{-1} at 500 mA, which is a three-fold increase *versus* that of electrolyte alone (26.8 Ah·L^{-1}). Importantly, this enhancement was obtained using a single booster and a RM, although in principle it is possible to use two or more to broaden the chemical potential window applied to the solid booster or in another scenario a booster with a different redox potential. ***Figure 2.28A)***, ***B)*** and ***C)*** show the performance of $Fe^{3+/2+}$ RM with PANI/CB at the positive-side at 200 and 500 mA. For completeness, $V^{4+/3+}$ performance in presence of PANI/CB at 500 mA is reported as well (***Figure 2.29***).

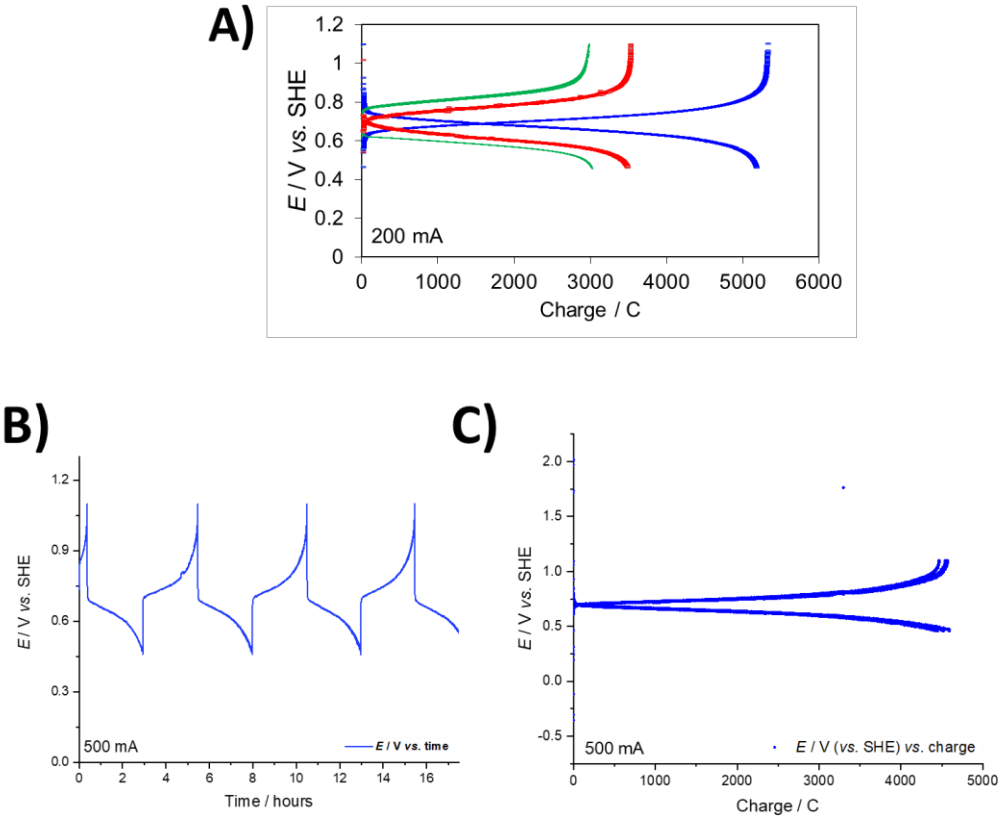

Figure 2.28 A) "Redox-mediated flow battery" cycling tests at 200 mA (14.50 mA·cm^{-2}). A) Potential vs. charge: potential of $Fe^{3+/2+}$ (red line) of $Fe^{3+/2+}$ + pristine PANI (green line) and of $Fe^{3+/2+}$ + PANI/CB (blue line). B) "Redox-mediated flow battery" cycling tests at 500 mA (38.50 mA·cm^{-2}) for the positive-side $Fe^{3+/2+}$: potential vs. time. In case of PANI/CB, the PANI in the composite was 14% and the $Fe^{3+/2+}$ 86% of the electrolyte. C) Potential vs. charge: potential of $Fe^{3+/2+}$ + PANI/CB (blue line).

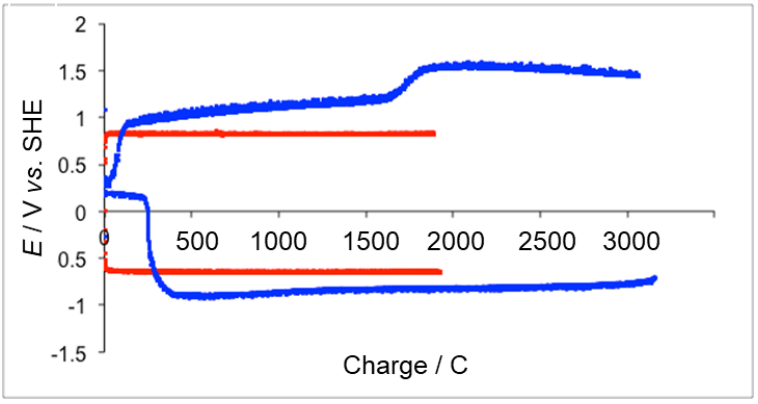

Figure 2.29 "Redox-mediated flow battery" cycling at 500 mA (38.50 mA·cm^{-2}) for the negative-side $V^{4+/3}$. Potential vs. charge: red line $V^{4+/3+}$ and blue line $V^{4+/3+}$ + PANI-CB.

Finally, a preliminary assessment of the cycling stability of PANI/CB was performed at 200 mA to determine if any degradation of the material was occurring (***Figure 2.30***).

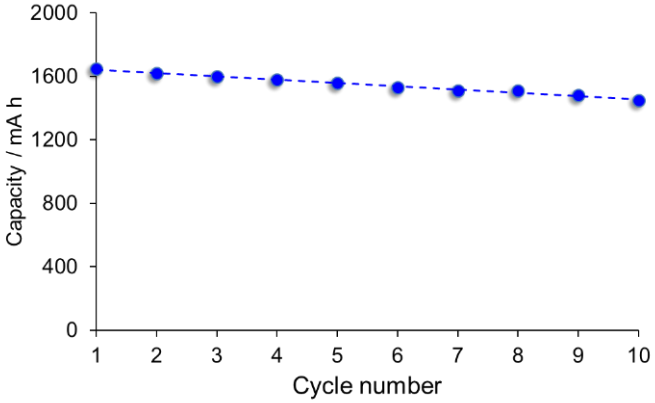

Figure 2.30 Cycling stability data for PANI/CB at 200 mA. A 12% decrease in capacity is observed. The results correspond to the cycling of only the electrolyte $Fe^{3+/2+}$.

It should be noted that these stability measurements were performed after the PANI/CB had been exposed to the RM solutions for nearly two months. As seen in ***Figure 2.30***, a decrease in charge (*ca*. 720 C, or 12% of the initial capacity) is observed after 10 cycles, suggesting some degradation of the booster PANI/CB. Interestingly, however, all of the measured capacity values were larger than previous measurements. This may be the result of improved percolation of the PANI/CB by the redox mediator solutions, due to the long-term exposure of the booster to the electrolyte.

2.9 Conclusions and perspectives

In this chapter, RAPs were described as flexible and versatile materials for energy storage in many electrochemical devices. Among organic redox active polymers, PANI was selected to enhance the volumetric capacity in an ARFB with acidic electrolytes. The capacity enhancement calculated for a system 50% PANI and 50% electrolyte (with 1 M concentration) was equal to four-fold, while in the present system, using a composite with CAB a three-fold improvement was reached. PANI was paired with $Fe^{3+/2+}$and $V^{4+/3+}$ at the positive and at the negative-side of the ARFB, respectively. PANI electrodeposited on carbon paper (PANI/CP) delivered (31.70±7.15) $mAh \cdot g^{-1}$ specific capacity with 81% CE (average values from six samples) when electrochemically cycled in the thermodynamic potential window of $Fe^{3+/2+}$ (+0.90 V *vs*. SHE as oxidation potential and +0.66 V *vs*. SHE as reduction potential). Then, in the thermodynamic potential window of $V^{4+/3+}$, similar results were obtained (30.56±5.17) $mAh \cdot g^{-1}$ with 73% CE (average values from six samples). A cycling method was developed and used to investigate the charging/discharging of the polymer in the actual solutions of the redox mediators. In presence of $Fe^{3+/2+}$*ca*. 45 $mAh \cdot g^{-1}$ experimental specific capacity was found with 98% stable CE over 25 cycles. In presence of $V^{4+/3+}$ charging/discharging performance of PANI was very poor (*ca*. 6 mAh g^{-1} and *ca*. 98% CE over 25 cycles), likely due to the sluggish kinetics of this redox couple $V^{4+/3+}$, suggesting that VO^{2+} is more readily reduced directly to V^{2+}, and similarly V^{3+} is more readily oxidized to VO_2^+ limiting the electron transfer to PANI.[33]

Subsequently, a 1 M $Fe^{3+/2+}$ and $V^{4+/3+}$ in 2 M sulfuric acid RFB was assembled and cycled at 200 mA (15.4 $mA \cdot cm^{-2}$), reaching an experimental charge of 3467 C (90% of the theoretical, 3859 C), while the redox couple $V^{4+/3+}$ (at the negative-side of the setup) did not perform well. High overpotential was observed (*ca*. higher than 700 mV) at 200 mA and for this reason it was deemed unsuitable for the present application. The viability of pristine chemically-synthesized PANI emeraldine salt was tested in 1 M $Fe^{3+/2+}$ and $V^{4+/3+}$ RFB. For these cycling tests a new design of the electrolyte tank was made and PANI was assembled stationary at the bottom of the tank as a bed of particles. The first cycling test at 200 mA in presence of 6.9 g of pristine PANI in both tanks exhibited a lower charge (3024 C) as compared to the $Fe^{3+/2+}$ (3467 C) at the same current. This was likely was attributed to changes in the electronic conductivity of PANI during oxidation/reduction. To mitigate this issue, a composite of PANI and CAB (PANI/CB) (80−20) wt. %, was chemically synthesized and observed to exhibit significantly improved electronic conductivity (6.22±0.86 $S \cdot cm^{-1}$ *vs*. 1.55±0.03 $S \cdot cm^{-1}$ in the pristine PANI emeraldine form), which is almost four-fold higher as compared to the pristine.

The flow cell with PANI/CB (9.8 g added to both tanks) was cycled at 200 mA (15.4 $mA \cdot cm^{-2}$) and also at 500 mA (38.5 $mA \cdot cm^{-2}$). At 500 mA, the $Fe^{3+/2+}$ and PANI/CB exhibited a volumetric capacity

of 84.2 $Ah \cdot L^{-1}$, considering the PANI alone, which represents a three-fold improvement when compared to $Fe^{3+/2}$ solution alone (28.6 $Ah \cdot L^{-1}$).

A preliminary assessment of the cycling stability of PANI/CB was performed at 200 mA to determine if any degradation of the material was occurring. As result, a capacity decrease (*ca*. 720 C, or 12% of the initial capacity) was observed after 10 cycles, suggesting some degradation of the booster PANI/CB, but considering that the booster was exposed to the mediator solution for a couple of months.

In this work, the chemical stability of the booster was a considerable issue, especially in terms of electronic conductivity. However, as proof-of-concept, it was particularly inspiring, and it helps to mature new perspectives to explore the potential of this approach for different ARFB.

As a new goal, the present concept was extended to neutral pH ARFBs. This new environment is favorable as compared to acidic or alkaline because it offers the possibility to investigate either new solid boosters or mediators operating in milder experimental conditions. For new redox mediators, ROM are selected as high soluble materials having a redox potentials able to guarantee a respectable cell voltage in the thermodynamic potential window of water (*e.g.* > 1 V)[57] [51]. For new solid boosters, the search was focused on materials with good chemical stability and high specific capacity. In this case, battery materials frequently used in NIB and LIB were targeted. The work conducted on the ARFB at neutral pH with design and development of solid boosters is fully described in the next two chapters of this manuscript.

Chapter 3

Copper hexacyanoferrate as solid booster for aqueous flow batteries at neutral pH

Based on the article:

Zanzola E.; Gentil S., Gschwend G., Reynard D., Smirnov E., Dennison C.R., Girault H. H. and Peljo P., *Electrochimica Acta*, **2019**, 321,*134704.*

3.1 General Introduction

Earlier the validity of the "redox-mediated" approach of charge transfer for volumetric capacity enhancement in an acidic ARFB was demonstrated. In that system, PANI/CB solid booster was primarily employed as charge storage medium, and at 500 mA in presence of $Fe^{3+/2+}$ as RM, the resulting electrolyte showed a respectable 3-fold volumetric capacity improvement (84.2 $Ah{\cdot}L^{-1}$) as compared to the mediator alone (26.8 $Ah{\cdot}L^{-1}$). However, the PANI "redox-mediated" flow battery was heavily limited at the negative-side, where the kinetics of the mediator $V^{4+/3+}$ affected the electron transfer and charge storage into the solid booster. Additionally, upon charging/discharging, cycles conductivity issues from the pristine PANI were experienced, which perturbed the "mediated" charge transfer since the booster was intrinsically passivated. Furthermore, the acidic environment of the flow cell represented a reason of concern. Subsequently, the primary new goal was to design a system based on earth abundant, safe and relatively cheap electrolyte materials. In the present chapter, a new pair of RM and solid booster is presented as an encouraging candidate for the positive-side of a neutral pH ARFB.

Recently, Aziz[120 121 122 123 124]and Schubert[125 49 48 46] have demonstrated that ROM (*e.g*. ferrocene, viologen, TEMPO, alloxazine, quinones and derivatives), are promising electrolytes for ARFBs. In good agreement, in the present work, TEMPTMA[125 126 46 127 128], a derivative of TEMPO, is employed as RM at the positive-side of an ARFB at neutral pH and it was chosen because of:

- ***i)*** Synthesis from low-cost commodity products at kiloton scale[125] (*i.e*. 4-oxo-2,2,6,6-tetramethylpiperidine)
- ***ii)*** Great solubility limit in aqueous media (practical concentration up to 2 M in aqueous supporting electrolyte)[125]
- ***iii)*** High standard redox potential in the water thermodynamic potential window (+0.94 V *vs*. SHE)

iv) Molecular engineering (*e.g.* poly-TEMPO[46], TEMPOL[126], TMAP-TEMPO[127]).

However, despite these advantages, AORFB electrolytes might be not highly chemically stable and most of all they show a rather a low volumetric capacity. As an example, the system proposed by Schubert and co-workers[48], known as TEMPTMA-MV[48], exhibited only 54 $Ah \cdot L^{-1}$ with 2 M electrolytes concentration, which is quite close to the value in VRFB. Therefore, the addition of solid boosters appears to be highly desirable to improve the volumetric capacity and potentially realize large-scale stationary storage systems operating at milder conditions.

In this work, based on the judicious alignment of the redox potentials, TEMPTMA is paired with CuHCF, a K^+-intercalation compound from the Prussian blue analogues (PBAs), as solid booster. PBAs are battery materials usually employed in electrochemical devices such as solid-state batteries[129] [130], electrochemical sensors, electrocatalysis, photocatalysis, and electrochromism[131] for their high rate capability and good stability.[132–134] Interestingly, PBAs are also gaining attention in large-scale energy storage applications, such as NIB, LIB and KIB. Especially for NIB, PBAs offer a wide abundance and a relatively low cost of the starting materials (*e.g.* according to Wang *et al.*[135], the price for Na carbonate is 0.07-0.37 $€ \cdot kg^{-1}$ *vs.* 4.11-4.49 $€ \cdot kg^{-1}$ of Li carbonate for battery grade 99.9% and the abundance of Na is ca. 2.3% as compared to 20 ppm of Li) [135] and environmental low risk.

PBAs were selected for two important reasons: first, for the stable capacity performance, in fact, the open-framework structure with large interstitial sites can guarantee a fast and reversible ion diffusion. [135] This is an advantage as compared to NIB materials, where a narrow storage capacity and a poor rate capability is frequently experienced, due the limited diffusion into the oxide lattices, resulting from the Na^+ *s*-bonding with the O-2*p* orbital, [135] Second, the synthesis routes for PBAs are usually environmentally friendly and easy to scale-up, as compared to the high-temperature methods frequently needed for layered oxides or poly-anionic compounds for NIBs. These significant aspects make PBAs highly preferable for large-scale energy storage applications as well as for the present study. In the following sections, a general introduction to PBAs is provided.

3.2 PBAs storage materials

3.2.1 General working principle and performances

As described by Wang *et al.*[135] PB was first produced in the laboratory of Johann Conrad Dippel by mistake, and later between the 18th and the 19th century it was largely employed as a pigment.[135] At that time, PB was involved in many applications, for instance, in hydrogen storage as documented by Xu *et al.*[136], for biosensing as explained by Karyakin *et al.*[137], in cancer therapy as discussed by Jia *et al.*[138], for seawater desalinization[107] and sewage treatment.[139] According to Wang *et al.*[135] PBAs can be generically written as $A_xM_{Ay}[M_B\ (CN)_6]_z \cdot nH_2O$, where M_A and M_B are transition metals (*e.g.* Mn, Fe Co, Ni, Cu, or Zn), A is an alkali or alkali earth metal (*e.g.* Li, Na, or K) and *-y* represents the number of vacancies. The center metals in the structure are octahedrally coordinated to six cyanide groups *via* the nitrogen and the carbon atoms.

PBAs possess a face-centered cubic geometry with space group symmetry *Fm-3m.*[135] Additionally, they have an open-framework lattice (***Figure 3.1A)***), where, during the electrochemical reactions, the insertion of alkali and alkali metal ions occur as the metal center changes oxidation state (***Figure 3.1A)d)***). In the crystalline structure the transition metals can also be the same and just distinguished according to their valence states (***Figure 3.1B)***).[135]

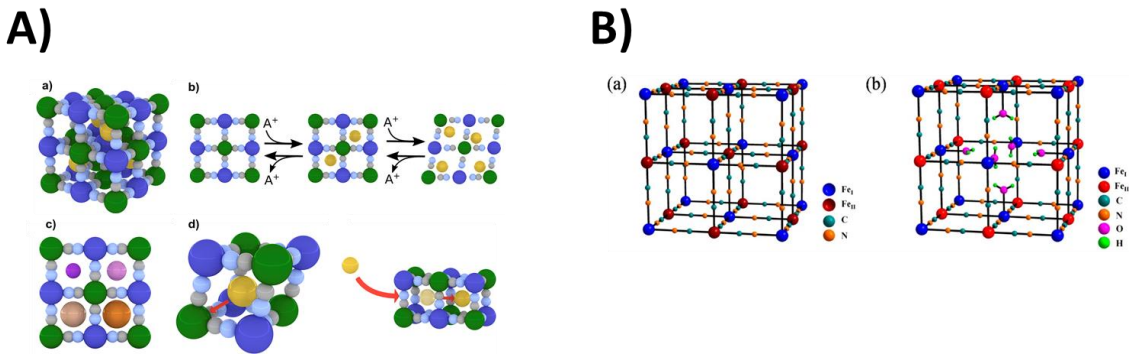

Figure 3.1 A) a) and b) Crystal structure of PBAs (face-centered cubic geometry): the green and dark-blue atoms are TM ions at the M_A site and M_B site, respectively. The yellow atoms are inserting ions. Gray atoms are carbon and light-blue atoms are nitrogen. c) Alkali-metals ions insert into the sub-cubes of the lattice as the TM ions change oxidation state. The relative sizes of (clockwise from top left) lithium, sodium, rubidium, and potassium are shown. d) Concentration of lithium or sodium which can induce a cubic-to-rhombohedral phase change in PBAs as the inserting ion displaces toward the corner of the sub-.cube. These images are reproduced with permission from the work of Pasta and co-workers at ref. [135]Copyright 2020, Joule, Elsevier. B) (a, b) Schematic of PBA: a) unit cell of PBA. b) Unit cell showing water coordination. Fe^{I} stands for Fe^{3+} and Fe^{II} for Fe^{2+}. Reprinted with permission from the work of Wu et al. in ref. [140]. Copyright 2020, American Chemical Society (ACS).

In PBAs, the intercalation reaction of alkali and alkali earth metal ions along with the corresponding redox reaction of the transition center metal is responsible of the charge storage mechanism. The expression ***i)*** below describes the general mechanism of redox reaction in PBAs:

$$A_x M^A[M^B(CN)_6]^{1-y} \cdot nH_2O + A^+ + e^- \rightarrow A_{x+1} M^A[M^{B-1}(CN)_6]^{1-y} \cdot nH_2O \qquad \textbf{\textit{i)}}$$

Where, A denotes the alkali metal ion, M^A and M^B the transition metal ions, and the value *-y* represents the fraction of vacancies of the hexacyanoferrate complex ion. In this expression, water is also taken into account as coordinated. The redox activity of PBAs depends also on the inserting ion's radius, which determines the free energy of the insertion reaction. In particular, the insertion potential for the monovalent ions follows the order $K^+ > Na^+ > Li^+$ in copper hexacyanoferrate, and similarly, $Cs^+ > Rb^+ > K^+ > Na^+ > Li^+$ in nickel hexacyanoferrate, in aqueous electrolytes.[141] Importantly, vacancies, defects and water content in the crystalline structure have an influence on the electrochemical behavior of PBAs too, affecting capacity and cyclability. [29] Thus, many efforts are dedicated to developing synthetic routes where it is possible to control defects and water content. Recently, Wu *et al.*[140] presented a facile hydrolytic precipitation method to obtain low-defects $FeFe(CN)_6$ nanocubes. Accordingly, $FeFe(CN)_6$ nanocubes presented a nearly structural perfection (***Figure 3.2A)b)***). The authors synthesized a 2-Li insertion reaction material with a remarkable Li-storage capacity of 160 $mAh \cdot g^{-1}$ (***Figure 3.2B)b)***), a strong rate performance at 24 C (1 C = 160 $mA \cdot g^{-1}$) (***Figure 3.2B)c)***), and an outstanding cycle stability of ~90% capacity retention after 300 cycles (***Figure 3.2B)d)***).

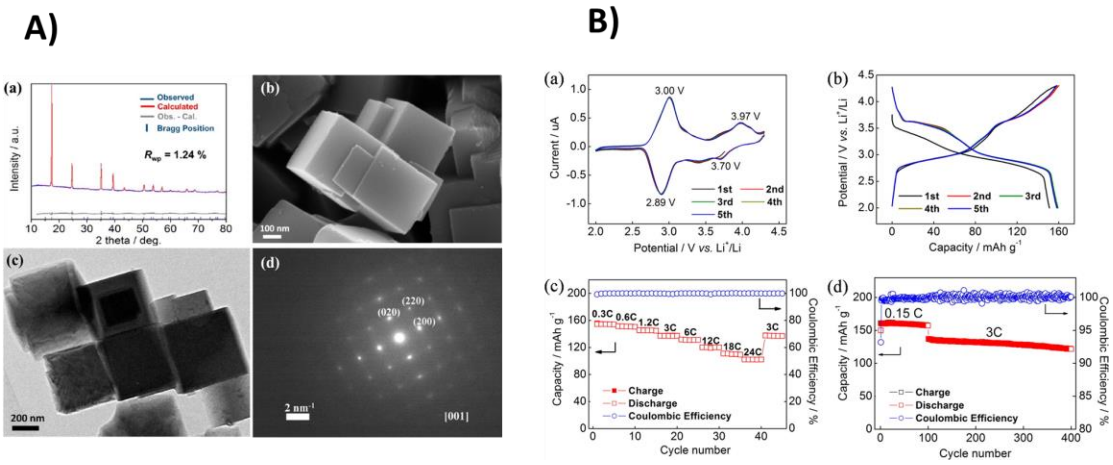

Figure 3.2 A) a) Physical characterizations of $FeFe(CN)_6$: a) XRD pattern and Rietveld refinements of $FeFe(CN)_6$, experimental data (blue line), calculated pattern (red line), difference curve (gray line), and Bragg positions (blue markers). b) SEM images. c) TEM images. d) Selected area electron diffraction (SAED) pattern of a single $FeFe(CN)_6$ particle. B) Electrochemical characterizations of $FeFe(CN)_6$ electrode: a) CV curves measured at a scan rate of 0.1 mV s^{-1}. b) Galvanostatic charge/discharge experiments at a 0.15 C rate (1 C = 160 $mAh \cdot g^{-1}$). c) Rate performance from 0.3 to 24 C. d) Long-term cycle

performance at various currents of 0.15 and 3 C rates. All the cells were tested in the potential range of 2.0–4.3 V vs. Li^+/Li. These images are reproduced with permission from the work of Wu et al. at ref. [140], Copyright 2020, American Chemical Society (ACS).

PBAs can be easily functionalized by different transition metals or having the same in the crystal structure. Additionally, by choosing different transitional elements, structures and properties of PBAs can be adjusted while maintaining their open framework.[135] Among PBAs, mono-metal hexacyanoferrate are commonly employed in electrochemical energy storage devices (LIB, KIB and NIB) and the most known are MnHCF, NiHCF, CuHCF, FeHCF and CoHCF.[135] ***Table 3.1*** summarizes the theoretical specific capacities of these PBAs.

Table 3.1 Comparison of the theoretical specific capacities of some mono-metal hexacyanoferrate (expressed in $mAh \cdot g^{-1}$). The contents of this table are reproduced with permission from the work of Wang et al. in ref [135]. Copyright 2020. iScience, Cell Press.

Ion	CuHCF	MnHCF	NiHCF	FeHCF	CoHCF
Li^+	92.6	190.8	94.5	190.1	188.7
Na^+	83.4	171.3	84.9	170.7	169.6
K^+	62.0	155.3	77.0	154.8	153.9

Mono-metal hexacyanoferrates such as the materials displayed in ***Table 3.1*** are promising candidates for the positive –side of a battery system. For example, Pasta and co-workers[142] investigated the K^+-intercalating CuHCF for grid-scale energy storage applications, because of its *i*) ultra-long cycle life (83% capacity retention after 40,000 cycles), *ii*) high power (67% capacity at 80 C), *iii*) high energy efficiency and *iv*) low cost. Additionally, mono-metal hexacyanoferrate can be synthetically functionalized to become *multi*-metal hexacyanoferrate materials, where the redox properties and performances are enhanced as compared to the single-metal. In this case, an interesting work was proposed by Huang *et al*.[143], where a series of ternary $K_2Ni_xCo_{1-x}Fe(CN)_6$ with various Co/Ni ratios were synthesized for a KIB. In this work, by optimizing the PBA with Ni and Co connected to the N atom end, the resulting material, $K_2Ni_{0.36}Co_{0.64}Fe(CN)_6$, exhibited much higher performance than the corresponding binary.[143] In particular, $K_2Ni_{0.36}Co_{0.64}Fe(CN)_6$ delivered an initial capacity of 86 $mAh \cdot g^{-1}$ with a retention of 98% after 50 cycles. In addition, capacity retention remained up to 88% after 300 cycles, indicating the excellent stability of this material.[143]

One advantage of PBAs is their facile synthesis that can benefit from the abundance of the raw materials and their relative low hazardless. These aspects are particularly interesting when it comes to develop electrolytes for large-scale flow battery installations. In the following section, the main synthetic methods of PBAs are briefly revised along with interesting examples to show their versatility.

3.2.2 Common synthetic routes of PBAs

According to Li *et al.*[144], three main approaches are commonly used for PBAs synthesis: *i*) precipitation, *ii*) hydrothermal and *iii*) electrochemical.

i) Precipitation method

The first synthesis method is the so-called precipitation (or sometimes co-precipitation) and it's one of the most extensively employed.[144] Generally, a solution containing metal-ion salts is mixed with a solution of ferrocyanide ligands to produce the PBA. Following the precipitation method, Yang *et al.*[145] synthesized Co-Co PBA nanocubes (***Figure 3.3A)***). More specifically, they made a first aqueous solution dissolving cobalt acetate and sodium citrate precursors and a second one with hexacyanocobaltate (III). Finally, these were mixed together and Co-Co PBA nanocubes precipitated. Later, Co-Co PBA was used as precursor and, by a simple solution-phase method, mesoporous $Co(OH)_2$ nanocubes was obtained *via* reacting of Co-Co PBA with a NaOH solution. [145] As another example, Kumar *et al.*[146] obtained the NiFe-PBA porous structure by a slightly modified precipitation method, reported in ***Figure 3.3B)***.

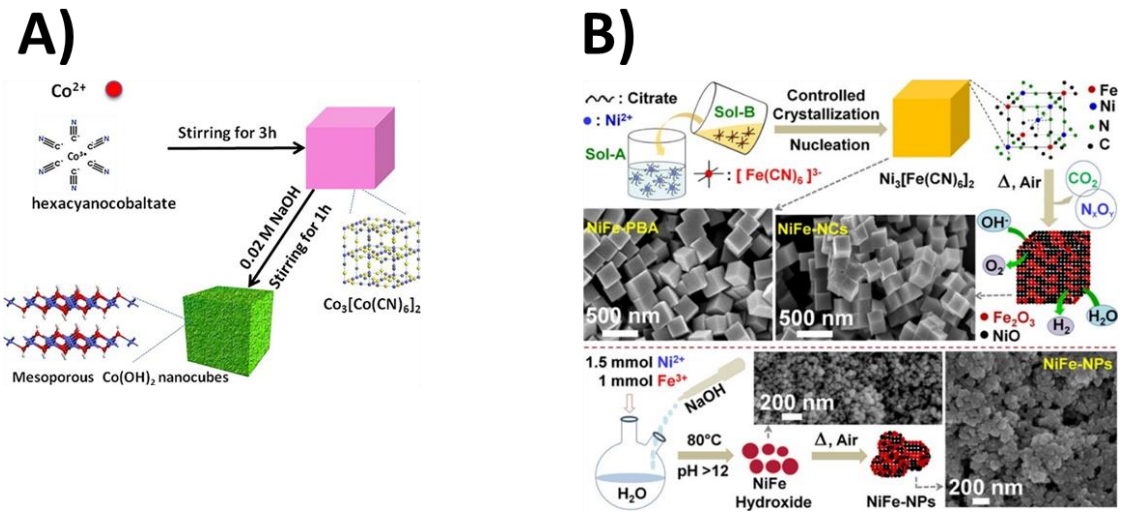

Figure 3.3 Scheme of the precipitation method of Co-Co-PBA from the work of Yang et al. at ref. [145]. This figure is reproduced with permission from ref. [145]. Copyright 2020, Elsevier. B) Schematic of the formation of NiFe-PBA-derived porous NiFe-NCs and NiFe-NPs via co-precipitation method. This figure is reproduced form the work of Kumar et al. in ref, [145], Copyright 2020 with permission of the American Chemical Society (ACS).

In particular, the authors mixed a trisodium citrate solution of Ni(II) with a solution of potassium hexacyanoferrate[146]. Sodium citrate acted as chelating agent and it coordinated with Ni(II), in this way the nucleation rate and crystal growth of the material were regulated (***Figure 3.3B)***). [146] Interestingly, when PBAs are synthesized by precipitation method, the morphology is related to the reaction between the ligand and the metal-ion, and it can be controlled during the synthesis. Accordingly, Durand *et al*.[147] reported a fully controlled precipitation method of PBA (***Figure 3.4A)***). The synthetic process consisted in one-pot synthesis of Co^{2+}containing ordered mesoporous silica monoliths, followed by the impregnation with a potassium hexacyanoferrate solution to precipitate the CoFe-PBA inside the pores.[147] In addition, coordination agents can be used to regulate the morphology of PBAs, slowing down the reaction kinetics. [144] An interesting work using this strategy was proposed by Zakaria *et al*.[148], employing sodium citrate dehydrate as coordination agent in the synthesis of 2 D $Ni[Ni(CN)_4]$ nanoflakes.

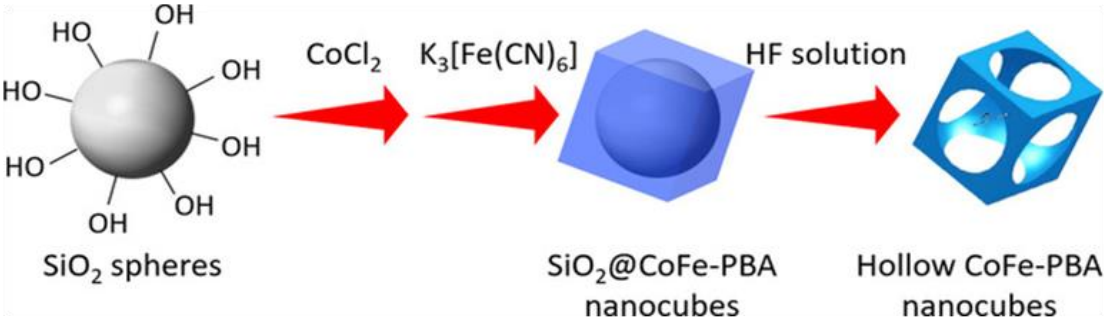

Figure 3.4 A) Schematic of the formation of hollow CoFe–PBA using silica spheres as sacrificial templates. This image is reproduced with permission from the work of Durand et al. in ref. [147] Copyright 2020, Wiley.

One last remarkable aspect in precipitation methods is the possibility of involving acids to assist the dissolution of the MO. Accordingly, Zhang's group[149] reported an acid-assisted precipitation synthesis to prepare the PB@stainless-steel mesh (PB@SSM).[149] In this procedure, the metal oxide/ hydroxide was dissolved into Fe, Ni, or Cr ions with the assistance of an acid, which were immediately precipitated with ferricyanide ions to form the PBA. In particular, Zhang and co-workers[149] prepared the metal oxide/hydroxide through immersing stainless-steel meshes in aqueous ammonia solution under hydrothermal condition.[149] Then, the metal oxide/hydroxide was immersed into a potassium ferrocyanide solution containing dilute hydrochloric acid. [149]

ii) Hydrothermal method

According to Li *et al*.[144], hydrothermal is the second most employed method to prepare PBAs (and especially microparticles of PBA), where the decomposition of $Fe(CN)_6^{4-}$ into Fe^{3+}/Fe^{2+} in acid solution is utilized to react with the residual $Fe(CN)_6$ to form the PBA.

When PBAs are synthesized by hydrothermal method, the crystal growth process is an interesting aspect to investigate. Accordingly, a remarkable work was reported by Zheng *et al.*[150], where $KFe^{II}Fe^{III}(CN)_6 \cdot 3H_2O$ PBA was prepared by a simple hydrothermal route based on the reaction between $K_3Fe(CN)_6$ and the reductant $C_6H_{12}O_6$. In particular, $Fe(CN)_6^{3-}$ was reduced to $Fe(CN)_6^{4-}$ by $C_6H_{12}O_6$, and at the same time it released the Fe^{3+} finally forming the PBA. Under this synthesis condition, Zheng *et al.*[150] investigated the crystal growth of $KFe^{II}Fe^{III}(CN)_6 \cdot 3H_2O$ with different time-dependent experiments. In particular, they performed high-resolution TEM images, which showed that the cube-shaped nanoparticles were crystalline, sharing the same structure as larger particles grown for a longer reaction time.[150] ***Figure 3.5A)*** and ***B)*** depict the experimental results obtained from Zheng *et al.*[150] in the study of crystal growth during hydrothermal method of $KFe^{II}Fe^{III}(CN)_6 \cdot 3H_2O$.

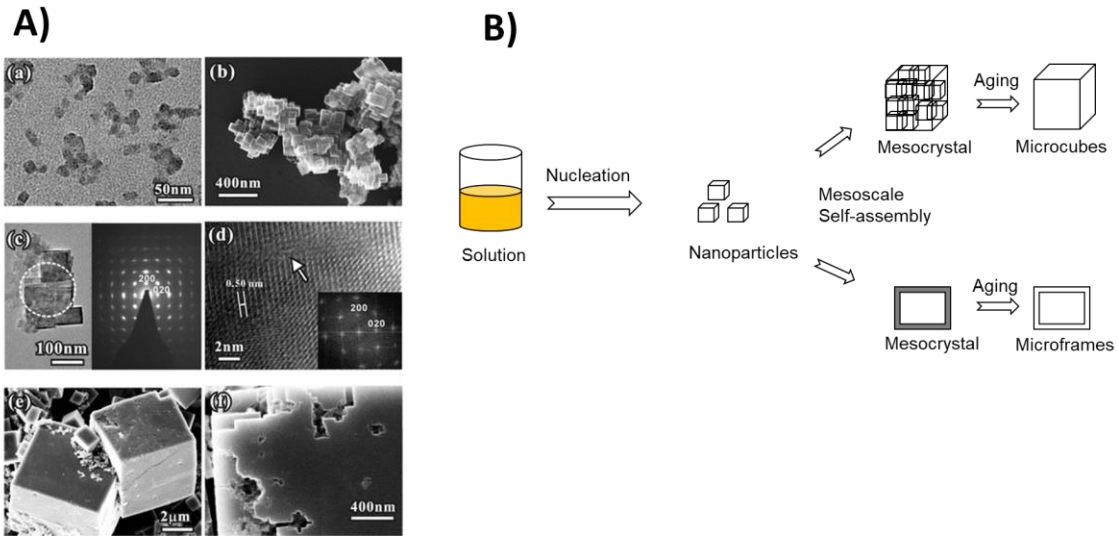

Figure 3.5 A) Typical EM images of PB grown at different growth stages: a) 40 min (TEM) and b) 1.5 h (SEM). c) TEM image of the products of 1.5 h and the corresponding electron diffraction pattern. High-resolution TEM image of the products of d) 1.5 and e) 2.5 h (SEM). f) Enlarged SEM image of the microcube of the products of 2.5 h. B) Proposed mechanism for growth of PB microparticles. These figures are reproduces with the permission of ref [150], Copyright 2020, American Chemical Society (ACS).

iii) Electrochemical method

According to Wang *et al.*[135], the first researcher who proposed an electrochemical synthesis of PB was Neff[134], depositing directly the PB by electrochemical reaction on a 1 cm platinum foil electrode, with platinum lead encased in Teflon. The procedure was performed galvanostatically for 1 h at 1 mA in a 1 M HCl solution. Later, the electrode was placed in a ferric ferricyanide solution and after several minutes a blue film was formed on the surface.[35]

In other approaches, $Fe_4[Fe(CN)_6]_3.xH_2O$ nanowires were electrodeposited on a polycarbonate membrane *via* chronoamperometry under the potential of +0.3 V (*vs*. SCE), by immersing the working electrode in a fresh solution containing $FeCl_3$, $K_3Fe(CN)_6$, H_3BO_4, and KCl. [135] As it was observed, PBAs can be easily synthesized by different methods, which also allow to tune some morphological properties or to investigate the crystal growth under particular conditions. Certainly, due to their encouraging performance in electrochemical devices, PBAs are investigated from many researchers[151] [139] [135]. One interesting work was recently proposed by Girault and co-workers[152], which presented the synthesis of a PBA by oxidative print light synthesis (PLS) (***Figure 3.6***).[152]

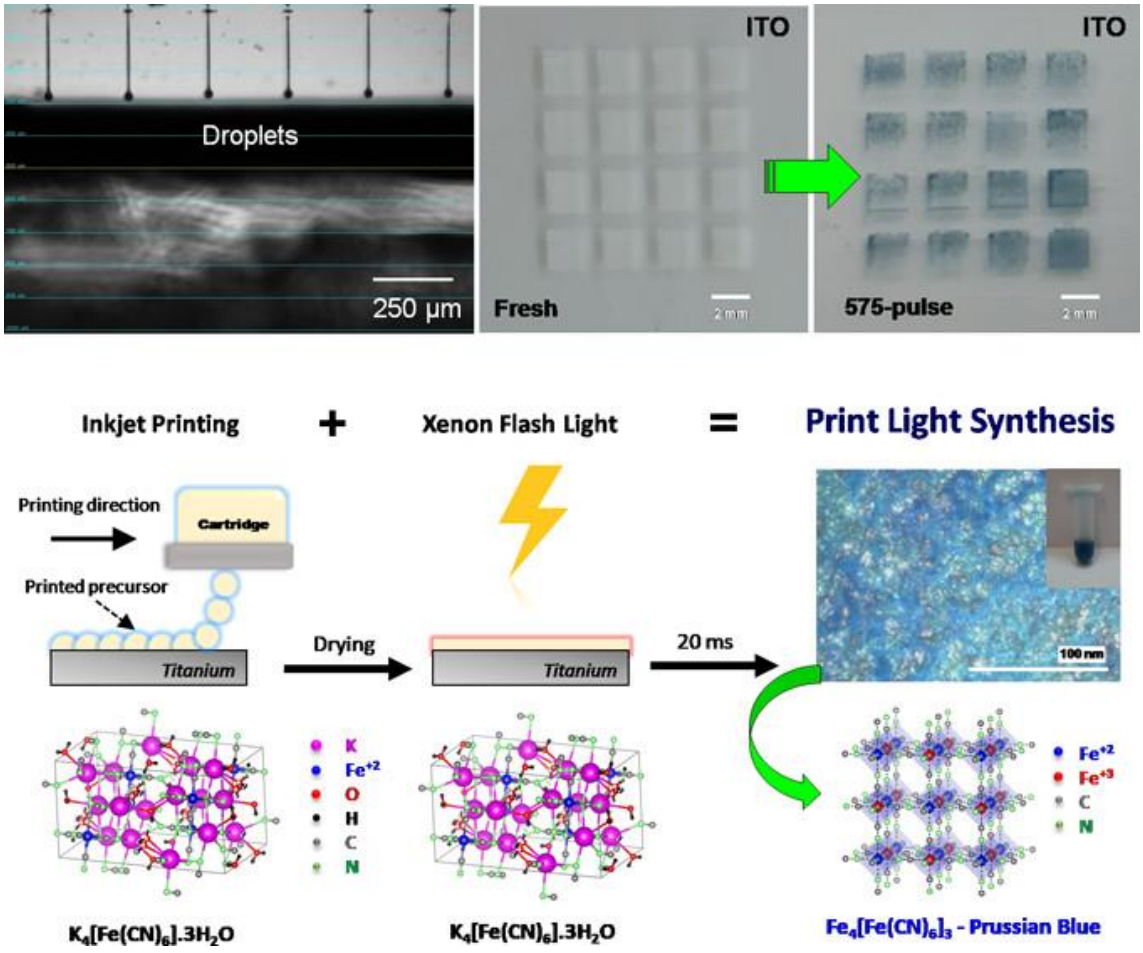

Figure 3.6 A) Schematic of the print light synthesis process to fabricate a PB: a) droplets formation of the precursor ink in six parallel nozzles. b) Printed precursor iron salt before photonic curing (9 squares of 4 mm^2). c) PB patterns obtained after photonic curing. d) Scheme of the complete PLS process on a titanium substrate. This figure is reproduced with permission from the work of Baster et al. at ref [152]. Copyright 2020, American Chemical Society (ACS).

3.3 PBAs in RFBs

It was seen that PBAs are versatile materials for solid state batteries, such as LIB, NIB and KIB, however recently they gained attention even in RFBs. In particular, Wang and co-workers[153] have proposed a very interesting work where they employed $Fe^{III}_4[Fe^{II}(CN)_6 \cdot H_2O]_3$ and $(Cr^{II})_4[Cr^{III}(CN)_6OH]_2$ PBA materials to facilitate the reactions of vanadium ions and to inhibit the side reactions, respectively. In particular, in their system they used VO^{2+}/VO_2^+ at the positive and V^{2+}/V^{3+}at the negative-side (***Figure 3.7a)***). The redox reactions between VO^{2+}/VO_2^+ and $Fe^{III}_4[Fe^{II}(CN)_6 \cdot H_2O]$ and of V^{2+}/V^{3+} and $Cr^{II}_4[Cr^{III}(CN)_6OH]_2$ (in ***Figure 3.7b)***) were inspected with various electrochemical and spectroscopic techniques. The PBA-modified electrodes demonstrated considerably enhanced electrochemical activity towards vanadium species.[153]

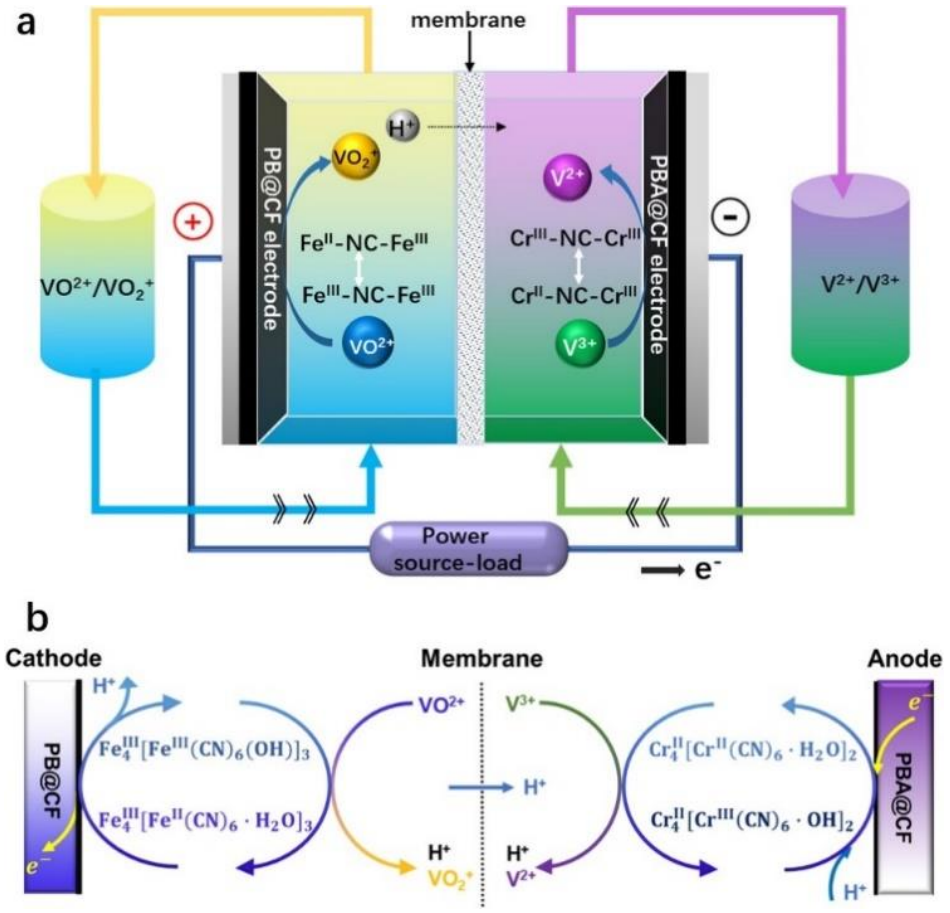

Figure 3.7 a) Schematic illustration of VRB operating upon surface immobilized redox catalysis during charge process. The carbon felt electrodes are grafted with PB and PBA for catalyzed reactions of vanadium species in the respective compartment. (b) Scheme of the targeted redox catalytic reactions of VO^{2+}/VO_2^+ and $Fe^{III}_4[Fe^{II}(CN)_6 \cdot H_2O]_3$ on the positive-side, and that of V^{2+}/V^{3+} and $Cr^{II}_4[Cr^{III}(CN)_6OH]_2$ on the anode during charge process. The above processes reverse upon discharge. These figures are reproduced with permission from ref. [153], Copyright 2020, Elsevier.

To test the influence of the surface-immobilized redox catalysts on the flow battery performance, a RFB single cell with the modified electrodes was assembled. This cell was potentiostatically tested to investigate the inhibiting effects of the modified-electrodes towards the deteriorating oxygen and hydrogen evolutions upon overcharging.[153] ***Figure 3.8*** shows the full performance of the system in terms of capacity (***Figure 3.8a)***) and energy efficiencies (***Figure 3.8b)***).

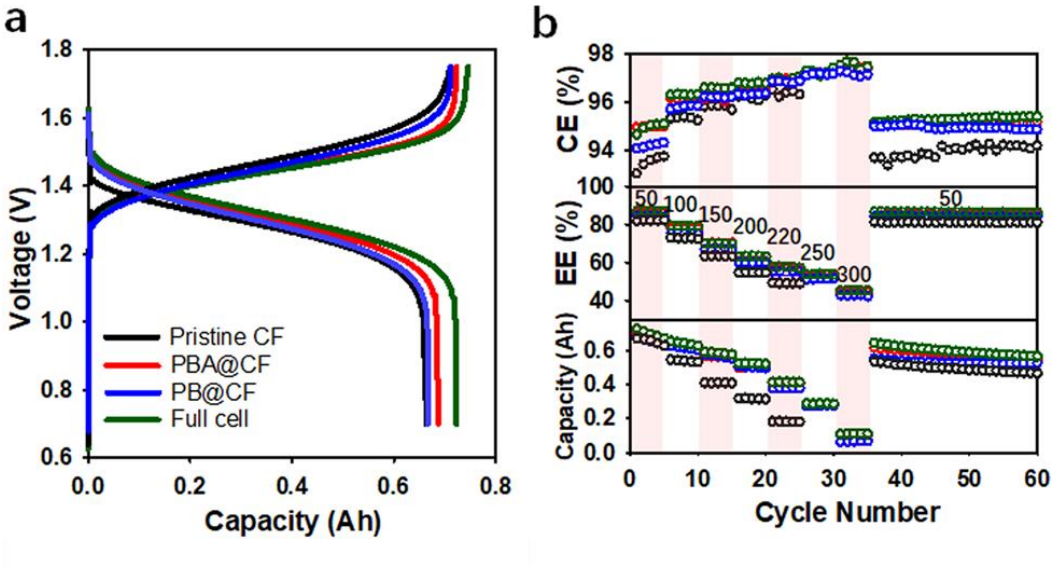

Figure 3.8 Cycling performance of the RFB assembled with modified electrodes. a) Voltage profiles of the various VRBs at a current density of 50 mA·cm^{-2}. b) Discharge capacity, Coulombic (CE) and energy efficiencies (EE) of VRBs at different current densities. This figure is reproduced from the work of Wang and co-workers in ref. [153] with permission. Copyright 2020, Elsevier.

In ***Figure 3.8a)*** the RFB cycled with both electrodes grafted with PBAs showed the lowest overpotential and consequently the highest charge and discharge capacities.[153] Accordingly, the RFB with modified electrodes showed much sharper voltage profile as compared to the cell voltage in the pristine cell, which is largely a result of the parasitic H_2 or O_2 evolutions.[153] Eventually, the pristine RFB without PBA grafted electrodes exhibited an average CE equal to 93.5% at 50 mA·cm^{-2}, which increased to 95.0% for the PBA-RFB, respectively. [153] Hence, as a result of reduced overpotential and parasitic reactions, the energy efficiency (EE) of the PBA-RFB cell was superior to the pristine cell. [153]

Interestingly, Wang and co-workers[154] proposed another promising approach of integrating RFLB into a PEC cell, using a PB material. In particular, the PB material was chosen as a low-cost and environmentally benign Li^+-storage compound, to enhance the energy density of the battery unit.[154] In particular, the PB was loaded in the tank of the RFLB, where the redox molecule ethyl viologen diiodide (abbreviated as EVI_2) was dissolved.

In the resulting system, EVI_2 bridged a dye-sensitized photoelectrode for integrated solar charging. [154] The PB regenerated the redox species and stabilized their concentration in the operation of a photoelectrode. [154] The schematic of the system is proposed in ***Figure 3.9 top***.

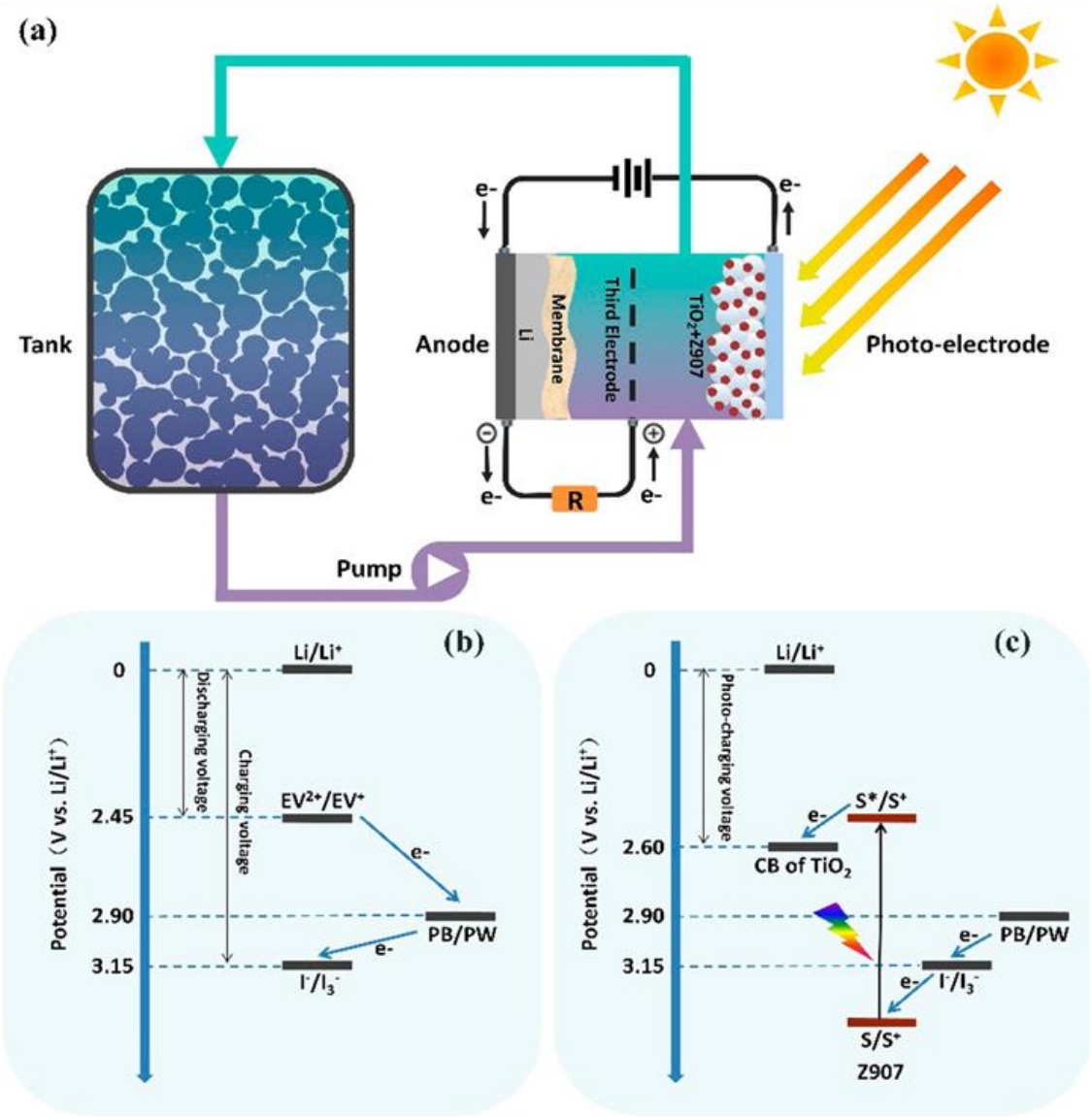

Figure 3.9 top a) Illustration of a solar rechargeable PB-based RFLB. b) Energy diagram of the "redox-targeting" reactions in the energy tank. c) Energy diagram of the photo-assisted charging process.

The overall performance of the PB-based RFLB system realized by Wang and co-workers[154] is reported in ***Figure 3.9 bottom***. In particular, the system presented > 90% of capacity retention, > 80% of CE, and > 66.4% EE over 30 cycles (***Figure 3.9 bottom a)***), with a reversible chemical lithiation/delithiation of $Fe_4[Fe(CN)_6]_3$, showing an energy density of around 117 $Wh \cdot L^{-1}$.[154] In addition, the utilization ratio of the PB material in the energy tank reached 66.8%.[154]

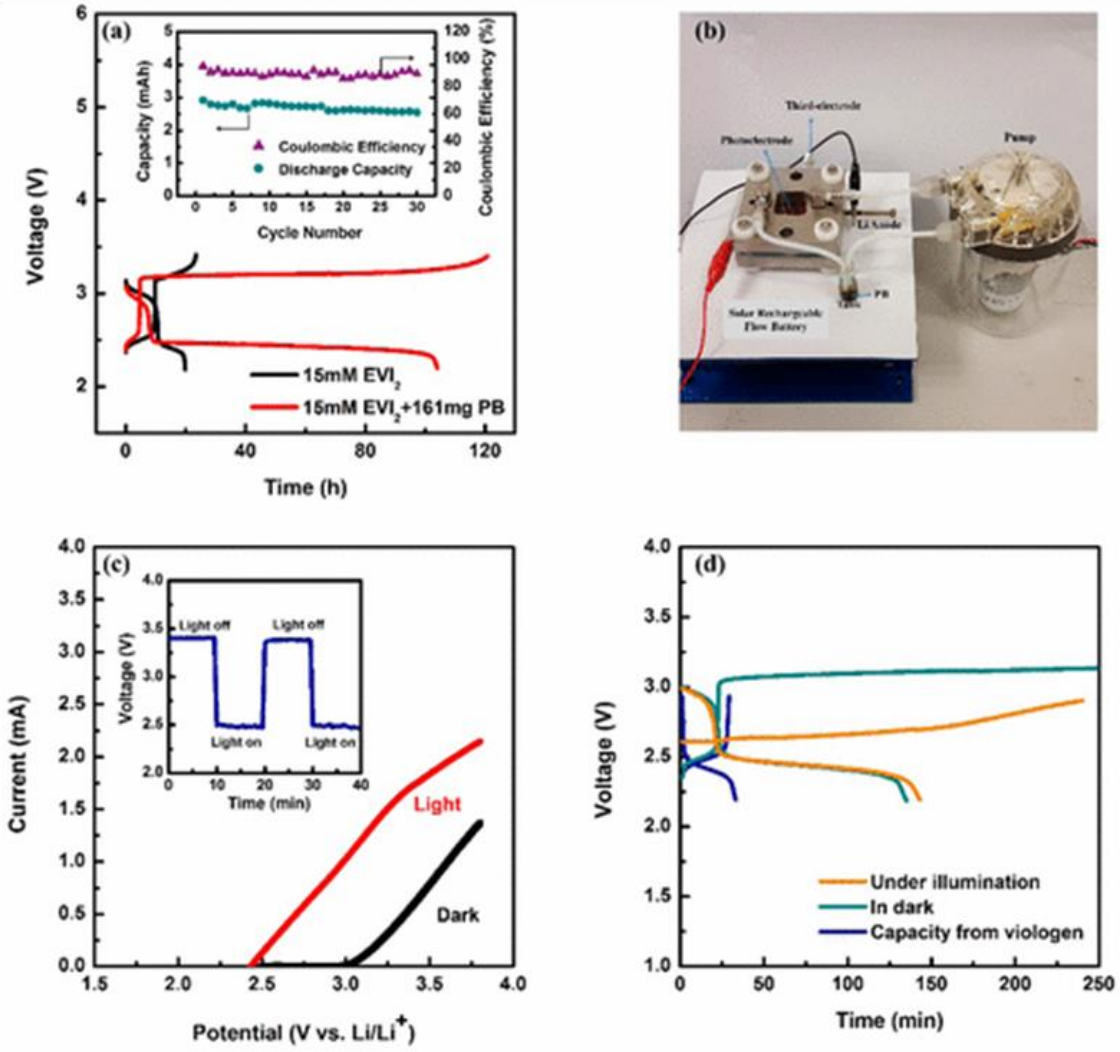

Figure 3.9 bottom: a) Charge/discharge curves of a Li-EVI_2 RFLB cell containing 15 mM EVI_2 without/with 161 mg PB loaded in the energy tank at a current density of 0.025 $mA \cdot cm^{-2}$. The inset shows the capacity retention and Coulombic efficiency of the PB-based RFLB cell cycled at a current density of 0.05 $mA \cdot cm^{-2}$. b) Photograph of a prototype SRFB by integrating Z907-sensitized TiO_2 electrode with a PB-based RFLB. c) Linear sweep voltammetry curves of a SRFB under illumination and in dark at a scan rate of 50 mV/s. The inset is the light response of the cell voltage. d) Charge/discharge voltage profiles of a static solar battery with PW. Light source: 30 W, 2400 LM white LED floodlight (CREE XML-L2, 0.45 sun). These figures are reproduced with permission from the work of Wang and co-workers at ref. [154]. Copyright 2020, American Chemical Society (ACS).

In summary, this system seems an encouraging solution for a low-cost and high-density energy storage installation and it might lead to a reliable way for the development of integrated solar energy conversion and storage device for grid-scale applications.

3.4 CuHCF as solid booster in the present approach

According to the "redox-mediated" approach of charge transfer and volumetric capacity enhancement in ARFBs, in the present work a couple of solid boosters, *i*) pristine CuHCF and *ii*) CuHCF functionalized by CNTs, were alternatively employed along with TEMPTMA as RM at the positive-side of the flow cell. A complete scheme of the redox reactions *in tandem* of these materials is reported in ***Figure 3.10***. First, TEMPTMA reversibly reacts at the surface of a porous electrode in the electrochemical cell, and then the charge output of this reaction shuttles within the flow cell reaching the storage reservoir, where CuHCF is stationary placed. In the present case, a reversible one electron-transfer oxidation of $TEMPTMA^{+}$ into $TEMPTMA^{2+}$ occurs at +0.91 V *vs.* SHE and it's well aligned with the redox potential of CuHCF (+0.97 V *vs.* SHE). The low overpotential (*ca*. 60 mV) is encouraging for the charge transfer process.

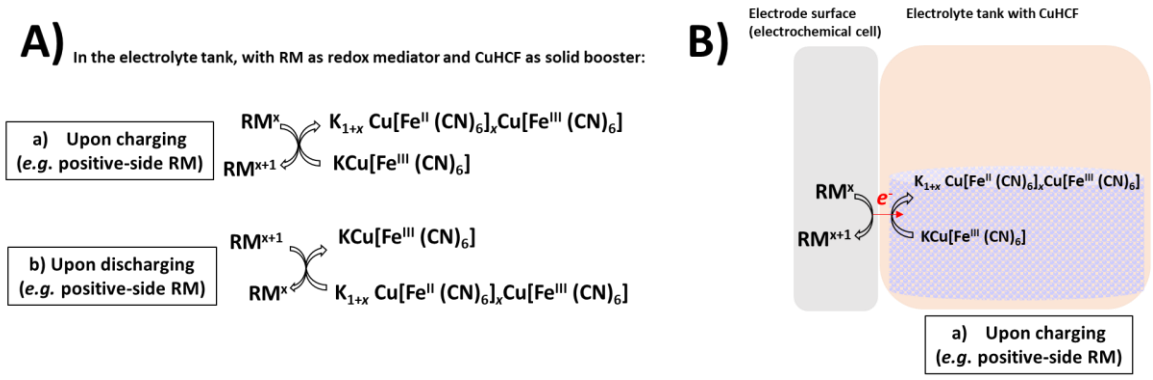

Figure 3.10 "Redox mediated" charge transfer in the AORFBs at neutral pH with TEMPTMA as RM in the schematic and CuHCF. B) Schematic of the approach with RM as TEMPTMA at the positive-side of the system and CuHCF as solid booster.

In the "redox-mediated" charge transfer, the equilibration of the Fermi levels between the flow battery electrode, TEMPTMA, and the booster CuHCF governs the charge storage mechanism. As TEMPTMA is constantly recirculated through the flow battery cell, its redox potential is considered to be in equilibrium with the electrode and upon electrical contact with the CuHCF, it equilibrates its redox potential with that of CuHCF. Additionally, if the Fermi level of electrons in the TEMPTMA species is higher than the Fermi level of the booster, TEMPTMA will reduce the CuHCF until equilibrium is reached (***Figure 3.11b)-top***). On the contrary, in the case where the Fermi level of the booster is initially higher than the Fermi level of electrons in TEMPTMA in solution, electrons will transfer to the TEMPTMA

species until equilibrium is reached (***Figure 3.11b)-bottom***). For CuHCF solid booster, the equilibrium of the Fermi level requires modification of the $Fe^{3+/}Fe^{2+}$ ratio as well as the accompanying intercalation/deintercalation of K^+.

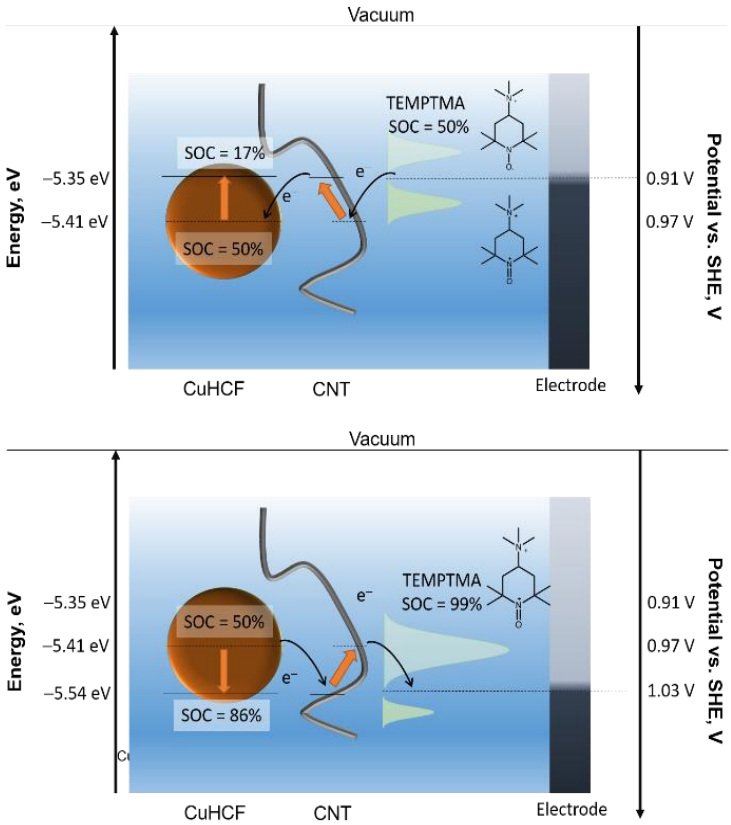

Figure 3.11 Fermi level equilibration of CNT-CuHCF composite as solid booster with TEMPTMA species in solution, when oxidation state of TEMPTMA is fixed by the flow battery electrode, at state of charge of 50% and 99%.

Finally, an assumption can be made to show the benefit of CuHCF to enhance the volumetric capacity of TEMPTMA in the reservoir of an ARFB. In particular, the volumetric capacity of TEMPTMA (with a concentration of 1 M) is equal to 26.8 $Ah \cdot L^{-1}$ and the addition of CuHCF (having a theoretical specific capacity of 62 $mAh \cdot g^{-1}$ and density of 1.33 $g \cdot mL^{-1}$) would improve it by three times (82 $Ah \cdot L^{-1}$). Furthermore, for an electrolyte where 50% is TEMPTMA and 50% is CuHCF, the final volumetric capacity will be 54 $Ah \cdot L^{-1}$, which is almost twice the volumetric capacity of the TEMPTMA alone. In the following sections, the experimental work on this candidate pair of materials is fully detailed leading to the final demonstration of an aqueous battery with enhanced volumetric capacity.

3.5 Experimental results pristine and C-coated CuHCF booster

3.5.1 Characterization of pristine and C-coated CuHCF

CuHCF was synthetized by a precipitation method.[155] The characterization of the pristine material by X-ray powder diffraction suggested a pure face-centered-cubic cell with a space group of *Fm-3m* and a lattice parameter of 10.2 Å (***Figure 3.12A)***)

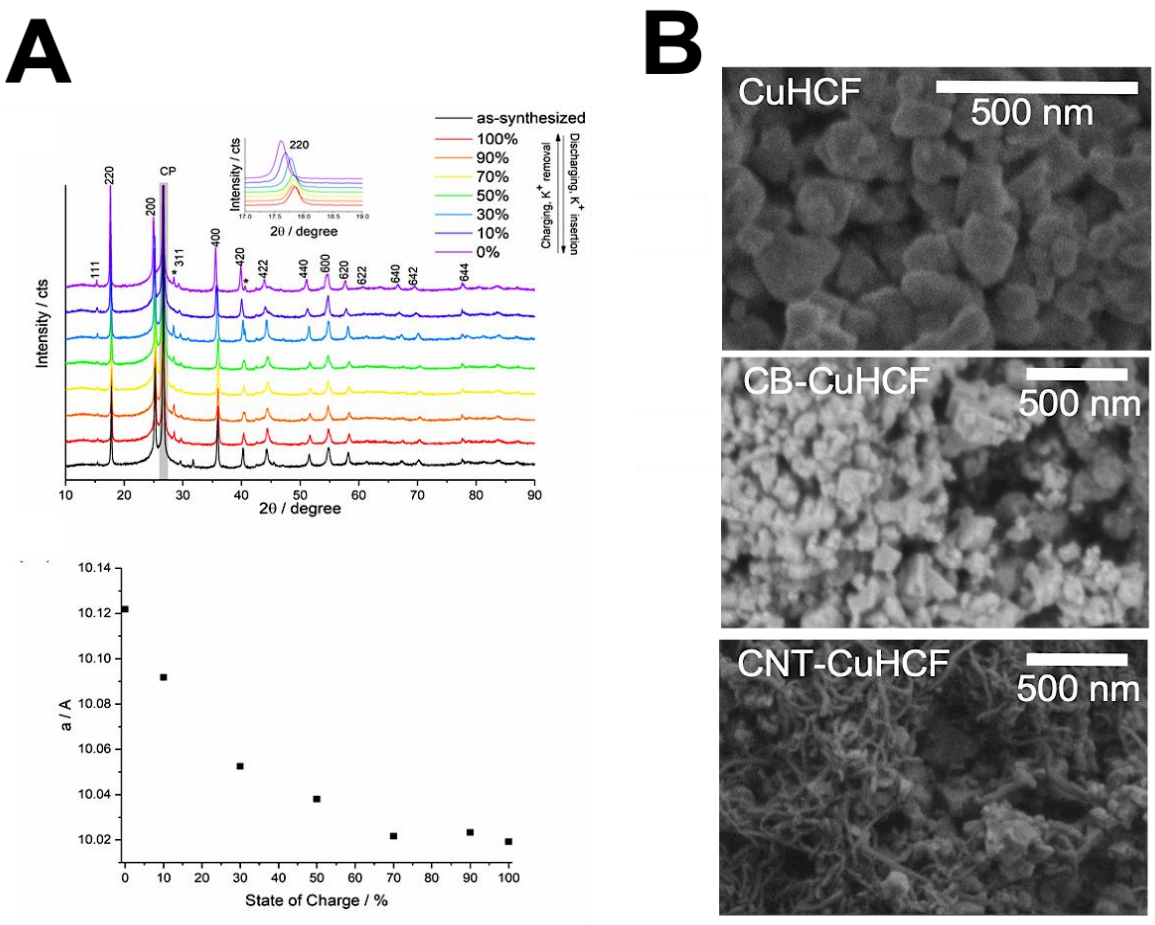

Figure 3.12 A) Top: Obtained PXRD patterns of as-synthesized materials as well as after charging and discharging in chronopotentiometry mode modeling real cell behavior. Peaks marked with a star were attributed to residuals of KCl. Insert: a magnified view of 220 peak. Bottom: Lattice parameter of cubic Fm-3m structure of Prussian blue (a) vs State of Charge. The calculated errors bars for a are smaller than the dots. B) SEM picture of the CuHCF (top), CB-CuHCF (middle) and CNT-CuHCF (bottom) obtained without any conductive coating layer (in-lens detector, 1 kV, 1.6 pA).

The latter decreased linearly only after 30% reduction of Fe^{3+}, which is in good agreement with recently reported 20% by Svensson *et al.*[156] Such inflating of the lattice parameter associated with reduction of Fe^{3+} to Fe^{2+} and insertion of K^+ can be used to monitor the state-of-charge of the solid material during

cycling in the RFB (***Figure 3.12A)*** bottom). Later, scanning electron microscopy (SEM) images of the pristine and carbon-coated CuHCF materials recorded with in-lens detector are presented in ***Figure 3.B12)***. The pristine material showed nanoparticles with size ranging from 50-100 nm. The grape-like shape of the CB is responsible for the aggregation of the CuHCF particle as compared to the CNT in which Prussian blue analogue is well-dispersed over the surface.

3.5.2 Electrochemical characterization of pristine and C-coated CuHCF in 1 M KCl_{aq}.

Cyclic voltammetries of pristine CuHCF, CB-CuHCF and CNT-CuHCF were performed after drop casting the inks onto a glassy carbon electrode (***Figure 3.13B)***).

In all the cases, the oxidation and reduction peaks were attributed to a single electron transfer mechanism for the reduction of Fe^{3+} to Fe^{2+} at a half-wave potential of +0.97 V *vs.* SHE, in good agreement with what was described by Engel and Grabner.[157] The faradaic current increased with the addition of carbon material (while keeping the amount of CuHCF constant), indicating that the amount of active CuHCF increases upon addition of the carbon materials. The surface concentrations of CuHCF, CB-CuHCF and CNT-CuHCF calculated based on the charge passed upon oxidation during the CV were equal to 40, 62 and 73 $nmol \cdot cm^{-2}$, respectively. Therefore, the addition of CNTs increased the amount of active CuHCF by 46% as compared to the pristine material. In CuHCF (***Figure 3.13B)***) and CB-CuHCF (***Figure 3.13B)***) oxidative and reductive peak currents depend linearly with the square root of the scan rate at high scan rates, meaning that the process was limited by the transport of potassium in the solid particle.[157–160]

On the contrary, in CNT-CuHCF films oxidative and reductive peak currents exhibited two kinetics (***Figure 3.13B)***): at low scan rates (< 50 $mV \cdot s^{-1}$), a sweep rate dependency over peak currents was observed, while at higher scan rates (50 – 100 $mV \cdot s^{-1}$), the dependence of the peak current over square root of the scan rate fitted a linear trend, meaning the electrochemical process was controlled by diffusion of K^+ inside the film. The mechanism changes from a surface controlled process to a solution diffusion-limited process, as previously reported.[157,161]

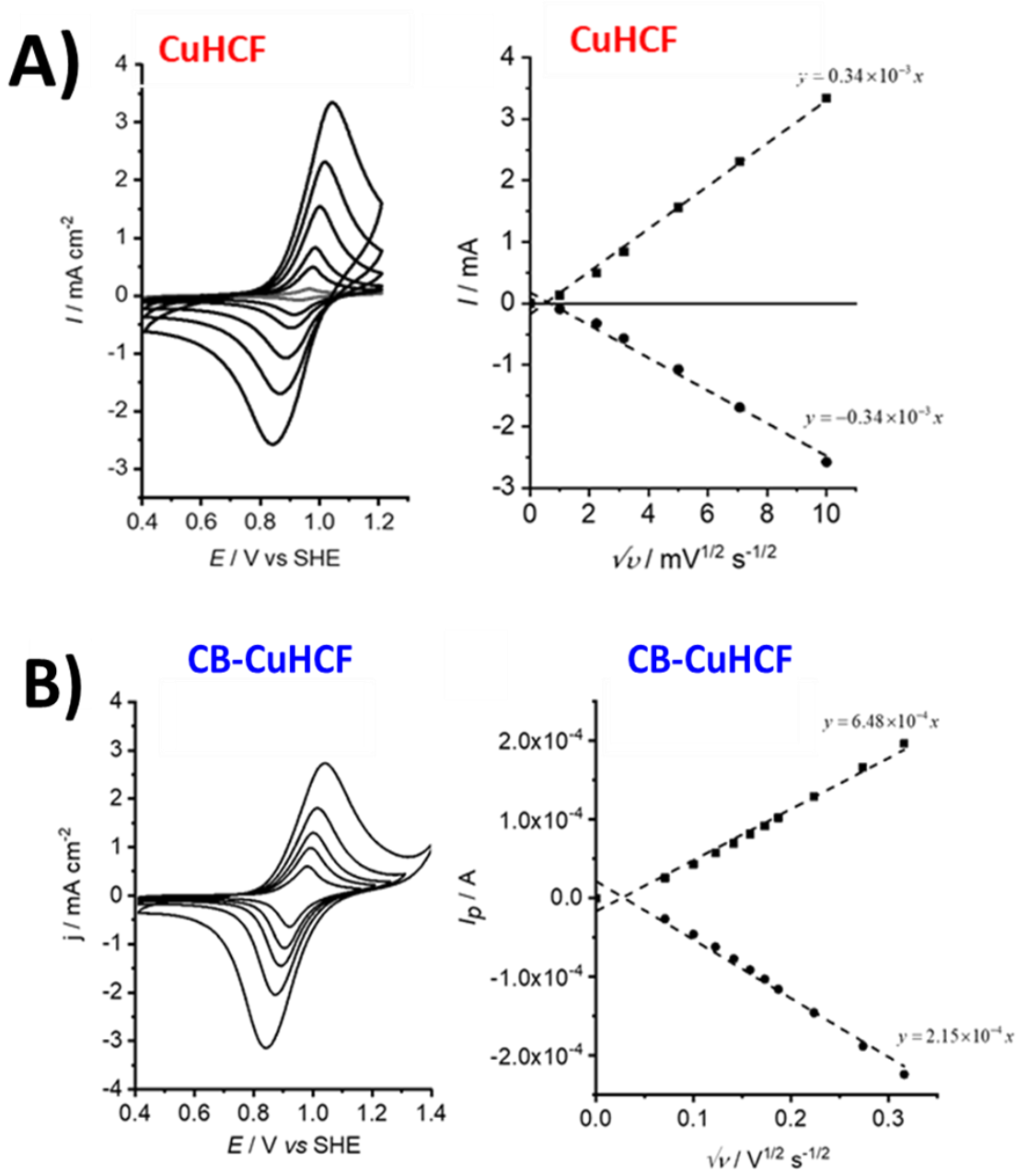

Figure 3.13. A) On the left: CV of the CuHCF drop-casted onto GCE at 5, 10, 25, 50, 75, 100 mV·s^{-1} in 1 M KCl$_{aq}$. All curves normalized by the geometric surface area of the electrode (0.071 cm^2). The CV were recorded without iR drop compensation. On the right: peak current vs. square root of the scan rate dependency. B) On the left: CV of the CB-CuHCF drop-casted onto GCE at 5, 10, 25, 50, 75, 100 mV·s^{-1} in 1 M KCl$_{aq}$. All curves normalized by the geometric surface area of the electrode (0.071 cm^2). The CV were recorded without iR drop compensation. On the right: corresponding peak current vs. square root of the scan rate dependency.

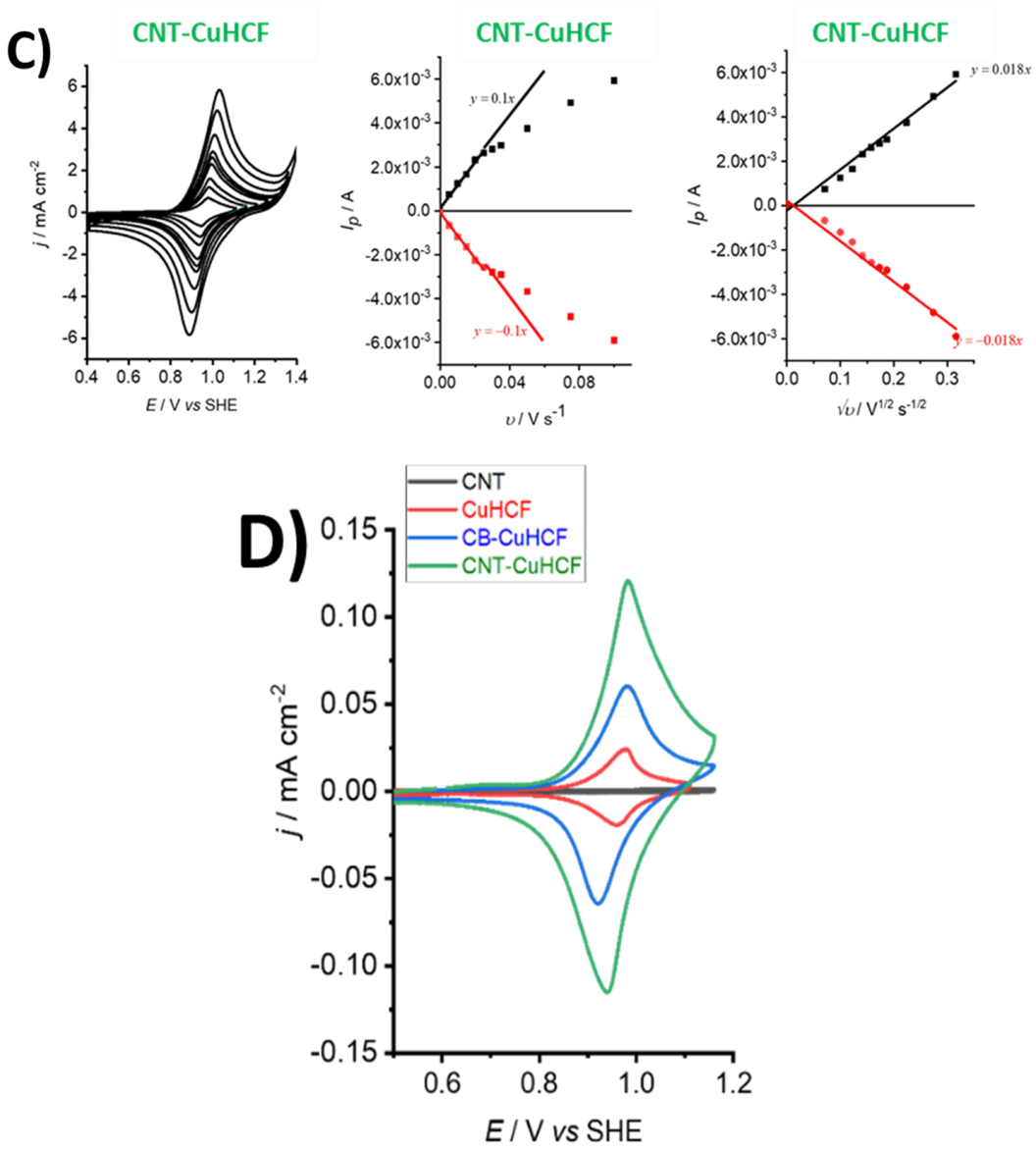

Figure 3.13 C) On the left: CV of the CNT-CuHCF drop-casted onto GCE at 5, 10, 15, 20, 25, 30, 35, 50, 75, 100 mV·s^{-1} in 1 M KCl$_{aq}$. All curves normalized by the geometric surface area of the electrode (0.071 cm^2). The CV were recorded without iR drop compensation. On the right: corresponding peak current vs. scan rate dependency. D) CV comparison at 10 mV s^{-1} in 1 M KCl$_{aq}$ of all CuHCF-based materials on GCE.

3.5.3 Simulation of the electrochemical properties of pristine and C-coated CuHCF booster

The mechanism of intercalation of K^+ inside the CuHCF crystal can be written in the following way:

$$KCu\left[Fe^{III}(CN)_6\right] + e^- + K^+ \rightleftharpoons K_2Cu\left[Fe^{II}(CN)_6\right]$$

Its influence upon the electronic properties was studied by DFT calculations: bond lengths and optimized geometries of KCuHCF and K_2CuHCF are shown in ***Figure 3.14B)***. It appears that the carbon nitrogen bond of the cyanide group is only slightly affected by the redox state of the metal centers (Fe and Cu) and from the insertion of the potassium cations. In contrast, there is clear shortening of the iron carbon bond and lengthening of the copper nitrogen bond upon the two-electron reduction of the compound. This is the opposite of what is seen in solution for the reduction of the ferricyanide to ferrocyanide. These results suggest that the copper nitrogen bond acquires a significant anti-bonding character when Cu^{2+} is reduced to Cu^+. Nevertheless, the overall electronic properties of CuHCF are not changed significantly by reduction or oxidation. Subsequently, the density of states for KCuHCF and K_2CuHCF were calculated (***Figure 3.14C) and D)***). It can be observed also that the reduction of the metal center and insertion of the potassium cations do not significantly alter the electronic states near the Fermi level, suggesting as well similar conductivity between the two materials. Moreover, it appears that free electronic states are placed near the Fermi level, implying that both KCuHCF and K_2CuHCF have metallic character and they could exhibit good electronic conductivity.

However, by spin polarized calculations, Targholi *et al*.[163] demonstrated that the density of states depends on the spin state of the electrons in the material. Indeed, it was found that KCuHCF and K_2CuHCF were just half-metals, suggesting insulating or conducting properties according to the considered spin state. In the present case, all calculations were not spin polarized, therefore it was not possible to see differences in the electronic conductivity properties. Nevertheless, using the Kubo-Greenwood electronic conductivity code (KGEC) and the Kubo-Greenwood formula,[164] it was possible to estimate the electronic conductivity of the oxidized and reduced form of CuHCF.

A

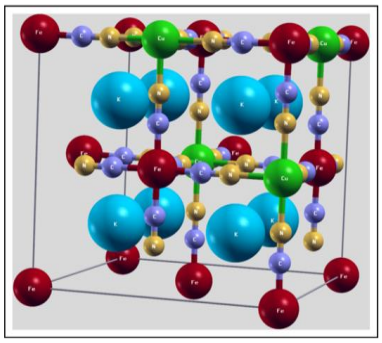

B

	$KFeCu(CN)_6$	$K_2FeCu(CN)_6$
CN	1.17 Å	1.19 Å
FeC	1.98 Å	1.89 Å
CuN	2.01 Å	2.11 Å

C D

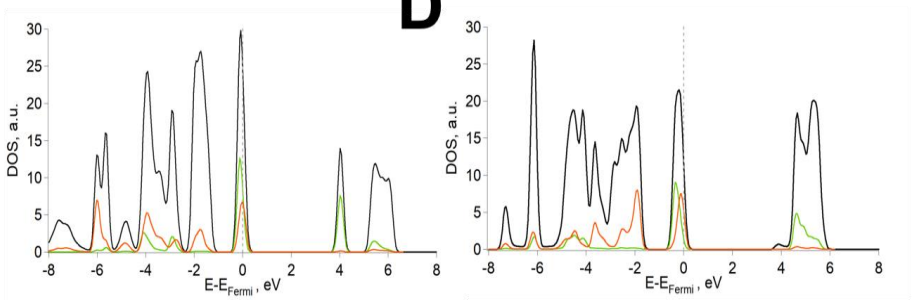

Figure 3.14 A) Unit cell schematic of the CuHCF. Fe atom is reported in red, Cu in green, C in purple, N in yellow and K in blue. B) Bonds lengths and optimized geometries for K^+-deintercalated and intercalated CuHCF forms.

Total and partial computed densities of state (DOS) of $KFeCu(CN)_6$ (in C) and $K_2FeCu(CN)_6$ (in D)). DOS for carbon (green line), copper (orange line) and total DOS (black).

The electronic conductivity of the oxidized and reduced forms of CuHCF were calculated as $2.0 \cdot 10^{-4}$ $S \cdot cm^{-1}$ and $2.6 \cdot 10^{-4}$ $S \cdot cm^{-1}$, respectively. These results are consistent with those proposed by Targholi *et al.*[163] and confirm that CuHCF does not perform as a metal, but rather than as a semi-metal and this behavior is almost independent from the redox state of the compound. The theoretical conductivity value are one order of magnitude below the conductivity of $LiFePO_4$ (10^{-3} $S \cdot cm^{-1}$),[165] which are usually synthetized *in-situ* with carbon black and a polymer linker. The poor electronic conductivity of this material suggests that the combination of the CuHCF with carbon materials is desirable for any electrochemical storage application. A COMSOL simulation of K^+-diffusion inside a porous electrode was performed (***Figure 3.14***). The simulation was done in 1 D considering 25 μm thick porous electrode with a porosity of 0.3. Particle radius was chosen as 1.5 μm. The other parameters are listed in the table below:

Table 3.2 Parameters for the simulation of K+- diffusion inside a porous electrode.

Parameter	*Value*	*Observations*
Electrode thickness	25 μm	
Electrolyte volume fraction	0.3	
Electrode volume fraction	0.5	
Charge transfer coefficients	0.5	
Reference exchange current density	20 A m^{-2}	
Electrolyte concentration c_{l0}	1 M	
Temperature	298 K	
Diffusion coefficient of electrolyte	3.75 10^{-6} $cm^2 \cdot s^{-1}$	Value for 1 M KOH
Electrolyte conductivity	215 $mS \cdot cm^{-1}$	Value for 1 M KOH
Electrode conductivity	1000, 100, 10 $mS \cdot cm^{-1}$	
Diffusion coefficient of K^+ in solid	1 10^{-9} $cm^2 \cdot s^{-1}$	Ref. [158]
Charge carrier concentration in solid	6.65 M	Ref. [158]

The equations from "Battery with binary electrolyte" interface of the COMSOL Multiphysics v. 5.4 were used (from ***a)*** to ***e)***).

$$\frac{\partial c_l}{\partial t} + \nabla \cdot \mathbf{N}_l = R_l \qquad \textbf{a)}$$

$$\nabla \cdot i_l = Q_l \qquad \textbf{b)}$$

$$\nabla \cdot i_s = Q_s, \quad \mathbf{i_s} = -\sigma_s \nabla \phi_s \qquad \textbf{c)}$$

$$\mathbf{i}_l = -\sigma_l \nabla \phi_l - \frac{2\sigma_l RT}{F} \ln\left(1 + \frac{\partial \ln f}{\partial \ln c_l}\right)\left(t_+ + \frac{c_l}{c_0}\right) \nabla \ln c_l \qquad \textbf{d)}$$

$$\mathbf{N}_l = -D_l \nabla c_l + \frac{\mathbf{i}_l t_+}{F} \qquad \textbf{e)}$$

Where, c_l is the KCl concentration in electrolyte, $\mathbf{N}_l$, is the flux of KCl, R is reaction term (here = 0), and Q is the current source. i is current, σ is the conductivity, ϕ is potential, D_l is the diffusion coefficient of KCl, f = 2, t_+ is the transport number of K^+ = 0.22. Subscripts s and l refer to solid and liquid phases,

respectively. The electrode is located from x = 0 to x = 25 μm. Boundary conditions for ***Eqn. a)*** are zero flux at x = 0, and concentration boundary condition $c_l = c_{l0}$. Boundary conditions for ***Eqn. c)*** is applied potential at x = 0, and electric insulation at x = 25 μm. For the electrolyte (***Eqn. d)***) the conditions are zero potential at x = 2000 μm and electric insulation x = 0.

In the porous electrode (x = 0 to 25 μm) Bruggeman corrections were used for the diffusion coefficients and for the conductivities, and the expression ***a)*** becomes:

$$\frac{\partial \varepsilon_l c_l}{\partial t} + \nabla \cdot \mathbf{N}_l = R_l \qquad \textbf{f)}$$

The reaction term expression ***f)*** is:

$$R_l = \frac{S_a j_{loc}}{F} \qquad \textbf{g)}$$

Where S_a is the specific surface area and j_{loc} is the local current density. $Q_l = -Q_s = S_a j_{loc}$.

The mass balance of K^+ in the spherical solid phase is governed by radial diffusion:

$$\frac{\partial c_K}{\partial t} + \frac{1}{r^2}\frac{\partial}{\partial r}\left(-r^2 D_K \frac{\partial c_K}{\partial r}\right) = 0 \qquad \textbf{h)}$$

(Fick's law in spherical coordinates, for the intercalation of the potassium in the solid. Potassium according to the model goes further into the lattice structure by diffusion).

With the following boundary conditions:

$$\frac{\partial c_K}{\partial r} = 0,\ r = 0 \qquad \textbf{j)}$$

$$-D_K \frac{\partial c_K}{\partial r} = j_{loc},\ r = r_p \qquad \textbf{k)}$$

The kinetics of the electrode reaction was realized with insertion reaction –node, with Butler-Volmer type expressions:

$$S_a j_{loc} = i_0 \left[\exp\left(\frac{0.5F\left(\phi_s - \phi_l - E_{eq}\right)}{RT} \right) - \exp\left(\frac{-0.5F\left(\phi_s - \phi_l - E_{eq}\right)}{RT} \right) \right] \qquad \textbf{l)}$$

$$i_0 = i_{0,\mathrm{ref}} \left(\frac{c_K}{c_{K,\mathrm{ref}}} \right)^{0.5} \left(\frac{c_{K,\max} - c_K}{c_{K,\max} - c_{K,\mathrm{ref}}} \right)^{0.5} \left(\frac{c_l}{c_{l,\mathrm{ref}}} \right)^{0.5} \left(\frac{c_0}{c_{0,\mathrm{ref}}} \right)^{0.5} \qquad \textbf{m)}$$

Notably, many of the model parameters were taken from an alkaline Ni-metal hydride battery, as they are not known for the current system. Therefore, the model results are not quantitatively correct, but they are able to evaluate and explain the observed trends.

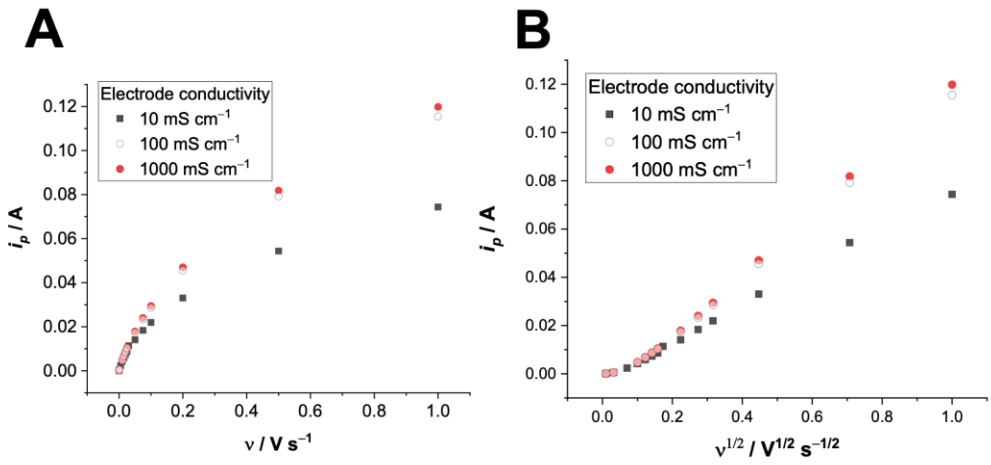

Figure 3.15 A) Simulated peak currents vs. scan rate and B) Square root of the scan rate for different electrode conductivities, with the electrolyte conductivity of 215 mS·cm^{-1}.

The present model can reproduce the transition from linear (***Figure 3.15A)***) to square root dependence of scan rate (***Figure 3.15B)***). At slow scan rates (< 50 mV·s^{-1}), the whole solid particles are reactive (in this case the response resembles that of a surface confined reaction), but at higher scan rates (50-100 mV·s^{-1}), the potassium ion concentration in the solid particle varies significantly between the surface and the center of the particle (a radial diffusion-controlled reaction). Remarkably, as the rates of diffusion and electron-transfer in solid material coupled, it is not possible to evaluate them separately. However, earlier electrochemical impedance spectroscopy results showed an electron-transfer rate of 0.1 cm^2·s^{-1}, meaning the rate of charge propagation in solid is limited by the movement of K^+ in a solid lattice with a rate from 10^{-10} to 10^{-9} cm^2·s^{-1}.[158]

The model shows that the slope of the peak current *vs.* square root of the scan rate plot (***Figure 3.15B)***) highly depends on the conductivity of the porous composite electrode. In the simulations, the ionic conductivity of the 1 M KCl_{aq} electrolyte was taken as 215 mS·cm^{-1} and when the ionic conductivity of the electrode was significantly below this value, only the part of the electrode close to the current collector was active. On the contrary, for a more conductive electrode, the whole surface is equally active. Additionally, the secondary current distribution within the porous electrode is significantly affected by the electronic conductivity of the solid material; in fact, if the solid-phase conductivity is poor, the large ohmic drop in the electrode leads to a situation where the charge transport takes place preferably by ionic conduction in the electrolyte phase, and much of the porous electrode is inactive. In this case, the current distribution is

mainly influenced by the resistance of the solid. However, if the conductivity in the porous electrode is similar or better than in the electrolyte, the current distribution is controlled by electrochemical reactivity, and the whole electrode is uniformly active. The following schematic in ***Figure 3.16A)*** and ***B)*** shows the diffusion process inside a poor or an electronically conducting film of CuHCF.

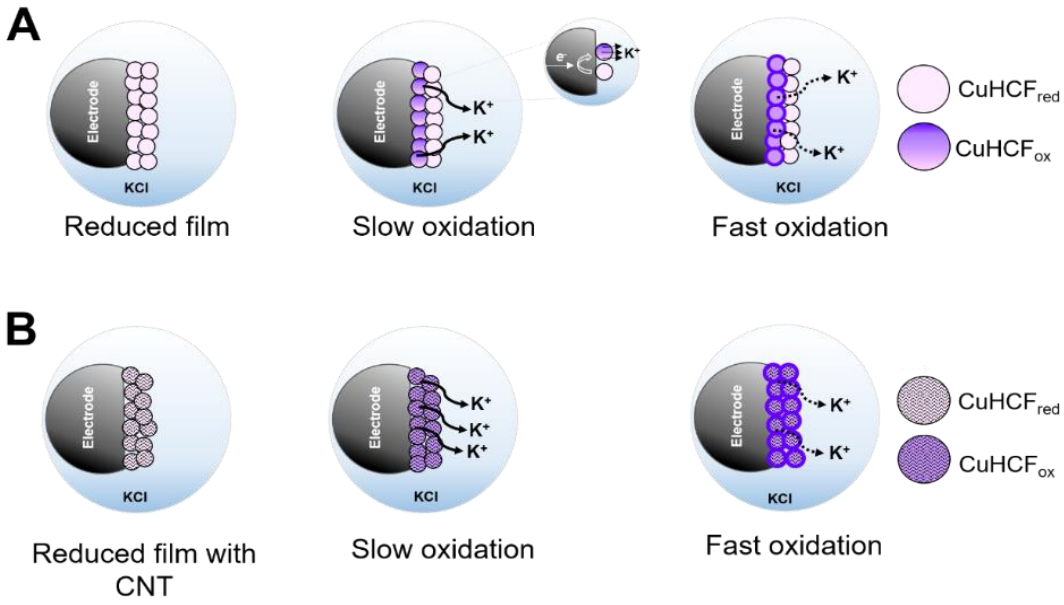

Figure 3.16 A) Scheme of the diffusion process inside a poor electronic conductive film of CuHCF, where only the first layer is electrochemically active. At slow oxidation (slow scan rate), the radial K^+ diffusion is fast enough to allow uniform oxidation of the CuHCF particles. When the oxidation is fast (high scan rate), the radial K^+ diffusion inside the particles becomes limiting and only surfaces of the CuHCF particles are fully oxidized. B) Schematic of the diffusion process inside a highly electronic conductive film of fully active CNT-CuHCF The process is the same as in A), but the overall electrode is active and more particles are oxidized.

3.5.4 Electrochemical cycling of pristine and C-coated CuHCF booster in 1 M KCl_{aq}

To confirm the simulated mechanism of K^+ diffusion in the CuHCF booster, galvanostatic cycling of GC electrodes modified with CuHCF, at 120 $\mu A \cdot cm^{-2}$ as current density in the presence of 1 M KCl_{aq} on glassy carbon electrode with 0.071 cm^2 geometric area. (***Figure 3.17***).

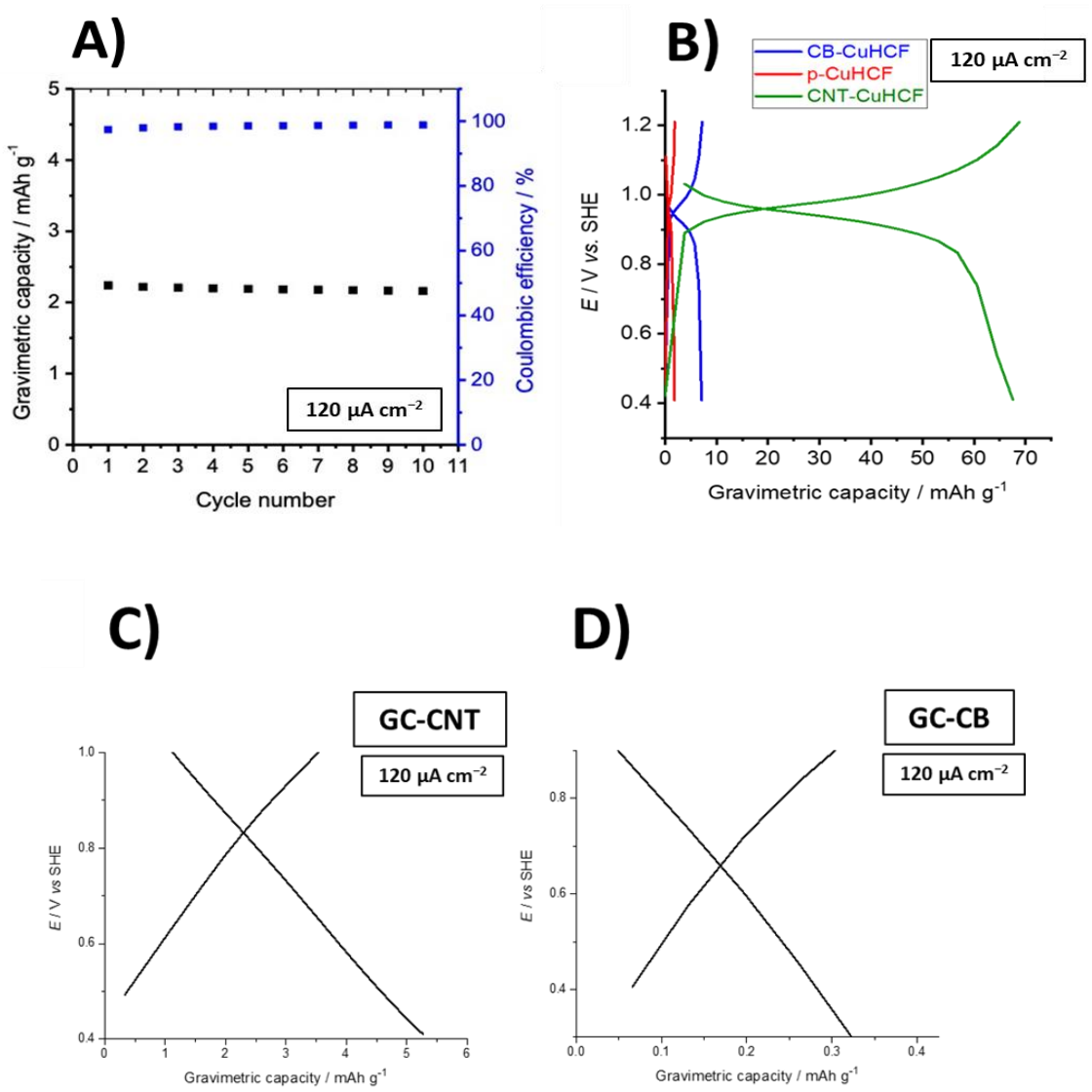

Figure 3.17 A) Galvanostatic cycling of CuHCF drop-casted onto GCE performed at 120 µA·cm^{-2} with cutoff potentials of +0.40 and + 1.20 V vs. SHE in 1 M KCl$_{aq}$. The CE is reported on the secondary y-axis. B) Galvanostatic cycling comparison of different CuHCF-based drop-casted on GCE at 120 µA·cm^{-2}. C) Galvanostatic cycling of a single CNT layer (1 layer of 10 µL from a 5 mg·mL^{-1} dispersion) drop-casted on GCE at 120 µA·cm^{-2} in 1 M KCl$_{aq}$. D) Galvanostatic cycling of a single layer of CAB (1 layer of 10 µL from a 5 mg·mL^{-1} dispersion) drop-casted on GCE at 120 µA·cm^{-2} in 1 M KCl$_{aq}$.

The theoretical specific capacity of anhydrous CuHCF is 85 mAh·g^{-1}. Some previous studies demonstrated that 3.7 molecules of water are present in the crystal lattice leading to a theoretical specific capacity of 62 mAh·g^{-1}.[142]

CuHCF exhibited average experimental gravimetric capacity of *ca*. 2 mAh·g^{-1} at 120 µA·cm^{-2} obtained after 10 cycles in 1 M KCl$_{aq}$ (***Figure 3.17A)***). The latter number was calculated taking into account

the whole amount of CuHCF deposited onto the electrode surface (24 μg). Such a small capacity is explained by the poor electronic conductivity of the material. An estimation of the active surface area from the integration of the faradaic current of oxidation on the CV gave mass of 0.96 μg, meaning that only 4% of the whole deposited material is active. This observation is in good agreement with the COMSOL simulations presented above. In order to guarantee good electron transfer rate between the particles upon cycling, CAB and CNTs were used to boost the overall bulk electronic conductivity of the film. In this case, the deposited total mass of CuHCF was 17 μg based on CuHCF concentration in the ink. Hence, gravimetric capacities of CB-CuHCF and CNT-CuHCF were found to be 7 $mAh \cdot g^{-1}$ (***Figure 3.17B)***) and 70 $mAh \cdot g^{-1}$ (***Figure 3.17B)***), respectively. The contribution of the carbon-based materials on the whole gravimetric capacity is about 4%. For completeness, galvanostatic cycling of GC electrode coated by bare CAB and CNTs in 1 M KCl_{aq} at the same current density were performed (***Figure 3.17C)*** and ***Figure 3.17D)***). As the obtained capacities CNT-CuHCF are already higher than evaluated for the hydrated material, this indicates that the whole electrode is electrochemically active during galvanostatic cycling.

Further, the role of CNTs in the charge storage mechanism of CuHCF booster was investigated. A fixed concentration of CNTs dispersion (5 $mg \cdot mL^{-1}$) was mixed with different loadings of CuHCF (***Figure 3.18***). In the case of the highest loading, an increase of the surface concentration of CuHCF equal to 340 nmol cm^{-2} was achieved. A maximal gravimetric capacity of 85 $mAh \cdot g^{-1}$ was obtained, showing a fully-covered CNTs sidewall.

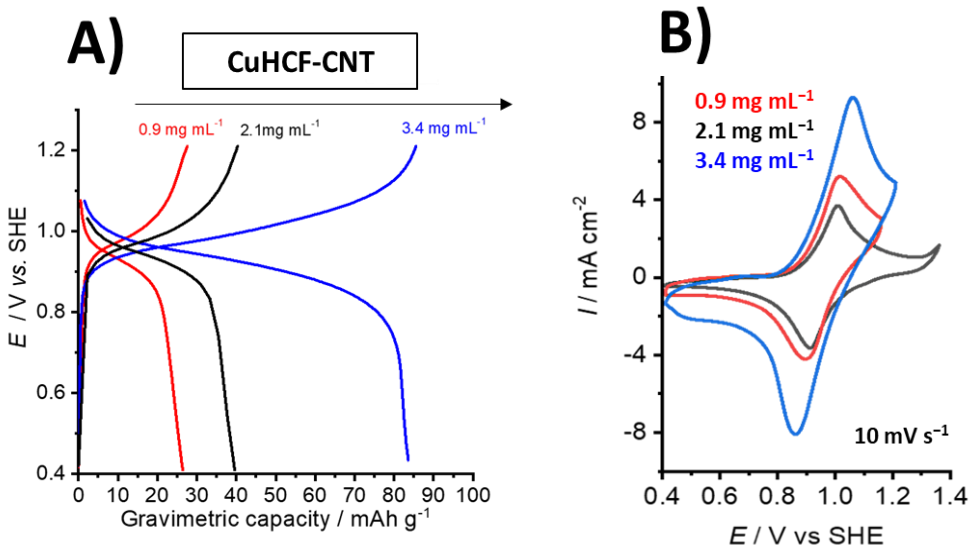

Figure 3.18 A) Galvanostatic cycling of CNT-CuHCF inks on GCE: comparison of increasing concentrations of CuHCF at 0.9 $mg \cdot mL^{-1}$ (red), 2.1 $mg \cdot mL^{-1}$ (black), 3.4 $mg \cdot mL^{-1}$ (blue) keeping the concentration of CNTs (5 $mg \cdot mL^{-1}$) constant. All curves are normalized by the geometric surface area of the electrode (0.071 cm^2).

B) Cyclic voltammetry at 10 mV·s^{-1} of CNT-CuHCF inks on GCE: comparison of increasing concentrations of CuHCF at 0.9 mg·mL^{-1} (red), 2.1 mg·mL^{-1} (black), 3.4 mg·mL^{-1} (blue) keeping the concentration of CNTs (5 mg·mL^{-1}) constant. All curves are normalized by the geometric surface area of the electrode (0.071 cm^2). The CV were recorded without iR drop compensation.

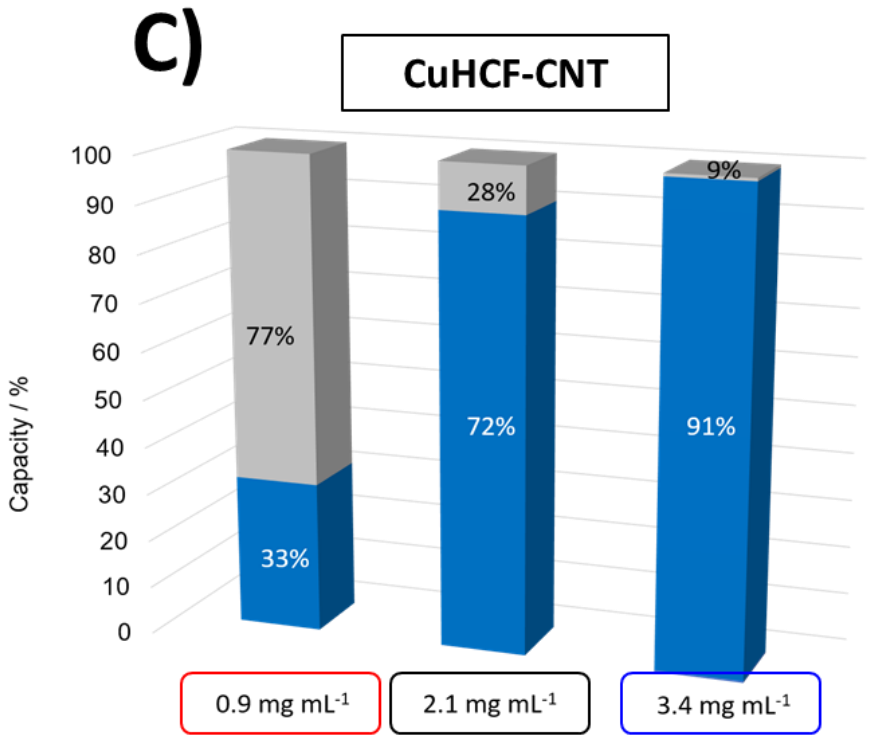

Figure 3.18 C) Bar-chart of CNTs contribution in the different CNT-CuHCF inks in terms of capacity %.

CNTs were employed since they offer many advantages (*e.g.* flexibility, high young modulus, high specific surface area)[166] and therefore they are considered particularly interesting for large electronic conductivity enhancement. However, due to their morphology, they might also enhance non-faradaic capacitive storage[167] as already observed by Sathiya and co-workers.[168,169]

In the present electrochemical characterization of CNT-CuHCF booster, the CNTs pseudo-capacitance on the whole capacity was estimated to be less than 9%, when the concentration of CuHCF was about 3.4 mg·mL^{-1} in the ink.

For completeness, the final CNT-CuHCF booster was characterized by XPS (***Figure 3.19***). Pristine CNTs appear without any metallic impurities of Fe, usually observed owing to their synthetic route. The composite exhibits typical binding energies of 2*p* orbitals for Cu and Fe and 1*s* orbital for N, demonstrating the successful functionalization of the CNTs sidewall by CuHCF.

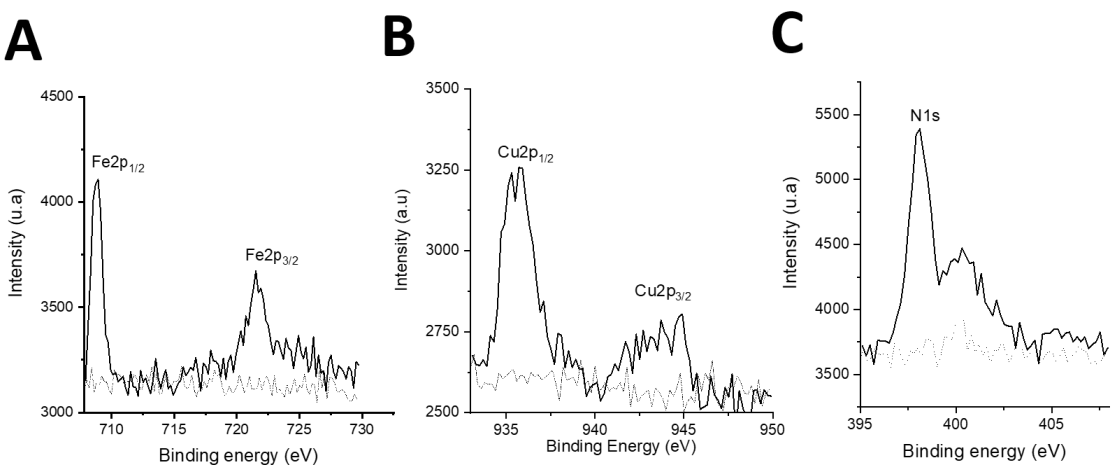

Figure 3.19 A) X-ray photoelectron spectroscopy (XPS) spectrum of pristine CNTs (grey line) and CNT-CuHCF (black line) for Fe 2p orbitals (A), Cu 2p orbitals B) and N 1s orbitals.

3.5.5 TEMPTMA redox mediator and charge transfer to CuHCF or C-coated CuHCF

As previously mentioned, TEMPTMA was chosen as redox mediator for the present approach. TEMPTMA was synthesized from the procedure described by Janoschka *et al.*[170] reported in chapter 5.

Electrochemical characterization of the synthesized TEMPTMA was performed rotating disk electrode (***Figure 3.01 A)***), finding a diffusion coefficient D equal to $0.49 \cdot 10^{-5}$ $cm^2 \cdot s^{-1}$ and an electron-transfer rate constant k^0 of $3.09 \cdot 10^{-3}$ $cm \cdot \cdot s^{-1}$ for the oxidation of TEMPTMA 1 M KCl_{aq}. These values are in good agreement with the literature for this molecule.[170] In particular, the D was found from the Levich equation:

$$I_{lim.} = (0.620) n F A D^{2/3} \omega^{1/2} \nu^{-1/6} C \qquad \textbf{n)}$$

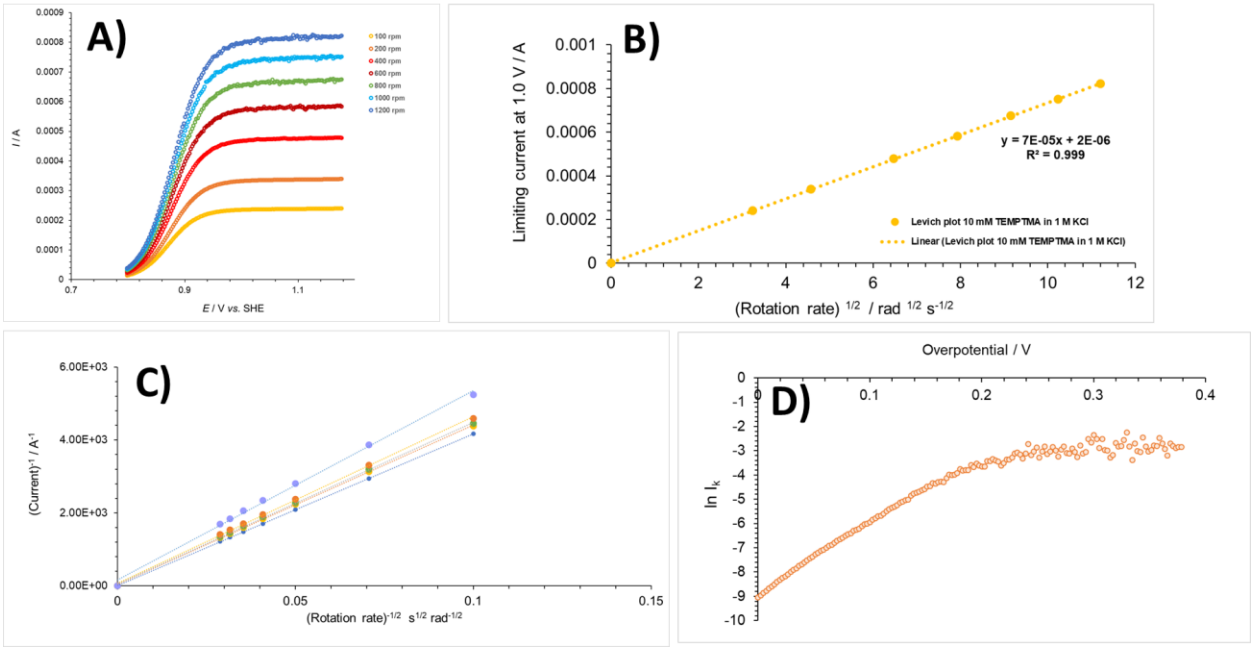

Figure 3.20 Electrochemical characterization by RDE of the synthesized redox mediator TEMPTMA.

A) RDE voltammogram of $1 \cdot 10^{-5}$ $mol \cdot cm^{-3}$ TEMPTMA in 1 M KCl_{aq} on GC RDE at different rotations (rpm). B) Levich plot corresponding of $1 \cdot 10^{-5}$ $mol \cdot cm^{-3}$ TEMPTMA in 1 M KCl_{aq} on GCE RDE. C) Koutecky-Levich plots (potentials, from top: 0.38 V, 0.16 V, 0.15 V, 0.14 V, 0.11 V vs. SHE). D) Tafel plot.

For completeness, a summary of the electrochemical characterization of TEMPTMA by RDE is proposed in the following ***Table 3.3***.

Table 3.3 Summary of TEMPTMA electrochemical characterization by RDE.

$E^{1/2}$ *vs.* SHE	Solubility / M	Diffusion coefficient / $cm^2 \cdot s^{-1}$	k^0 / $cm \cdot s^{-1}$	α
+0.88	2.1	$1.49 \cdot 10^{-5}$	$3.09\ 10^{-3}$	0.50

The reversible one electron-transfer oxidation of $TEMPTMA^+$ into $TEMPTMA^{2+}$ occurs at + 0.91 V *vs.* SHE and it's well aligned with the oxidation potential of CuHCF (+ 0.97 V *vs* SHE) (***Figure 3.21A)***). The 60 mV potential difference in between the formal potentials is small enough to ensure the electron transfer between TEMPTMA and pristine CuHCF. For completeness to the CV, the redox reactions of the mediator and of the booster are reported below the plot.

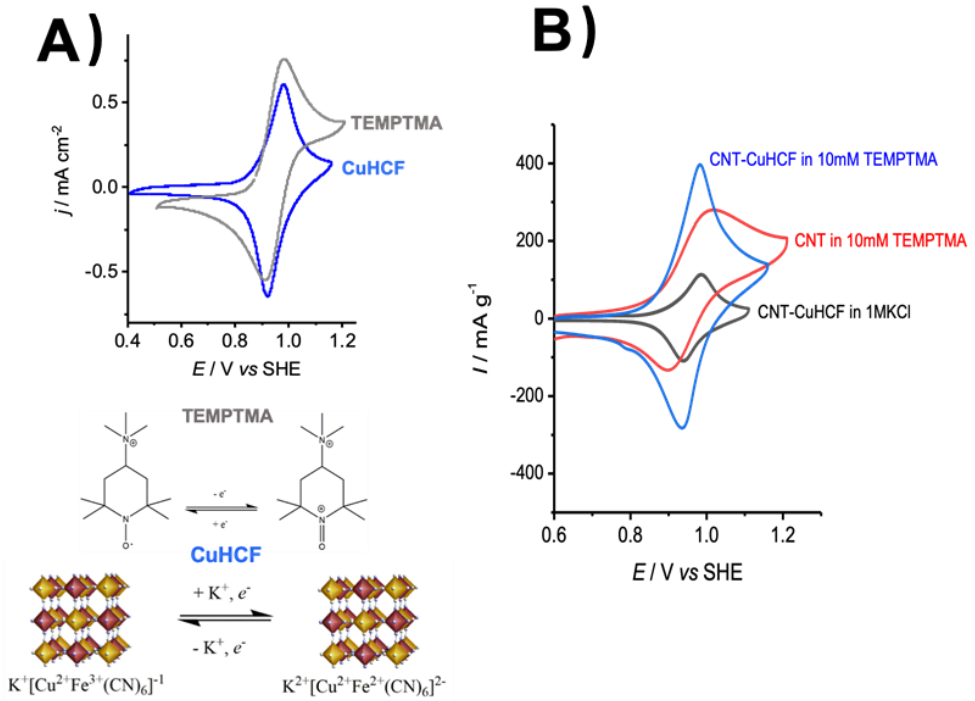

Figure 3.21 A) CV at 10 $mV \cdot s^{-1}$ of TEMPTMA (10 mM in 1 M KCl_{aq}) (in grey) and of a CuHCF drop-casted on GCE in 1 M KCl_{aq} (in blue). For completeness, the redox reactions of CuHCF booster and of TEMPTMA mediator are reported below the CV.B) CV comparison of CNT-CuHCF in 1 M KCl_{aq} drop-casted on GCE (black line), in 10 mM in 1 M KCl_{aq} TEMPTMA (blue line) and single layer of CNTs in 10 mM TEMPTMA (red line). All the CVs are performed at 10 $mV \cdot s^{-1}$ as scan rate and they were recorded without iR drop compensation.

A good alignment of the redox potentials can be seen even in the case of CuHCF functionalized with CNTs and TEMPTMA (***Figure 3.21B)***). Interestingly, as shown in this CV in ***Figure 3.21B)***, for a

modified CNT-CuHCF electrode in presence of TEMPTMA almost 3-fold enhancement of the maximum oxidative and reductive peak current can be noticed and a similar trend was observed with carbon black (***Figure 3.22A-top)***) as well.

Therefore, in order to study the semi-infinite diffusion of TEMPTMA inside the different layers of CB-CuHCF (***Figure 3.22B-top)*** and of CNT-CuHCF (***Figure 3.22B-bottom)***, CV was performed at different scan rates (5-100 mV··s^{-1}). Two distinct kinetics were observed for both CB-CuHCF and CNT-CuHCF, ranging from a surface confined- at low scan rates to a diffusion-limited process at high scan rates. This behavior might be due to TEMPT·'s oxidation inside the porous layers of the carbonaceous coaters, as well as to the oxidation of the CuHCF. In addition, peak-to-peak separation in the presence and absence of TEMPTMA for all the modified GC electrodes was evaluated (***Table 3.4***).

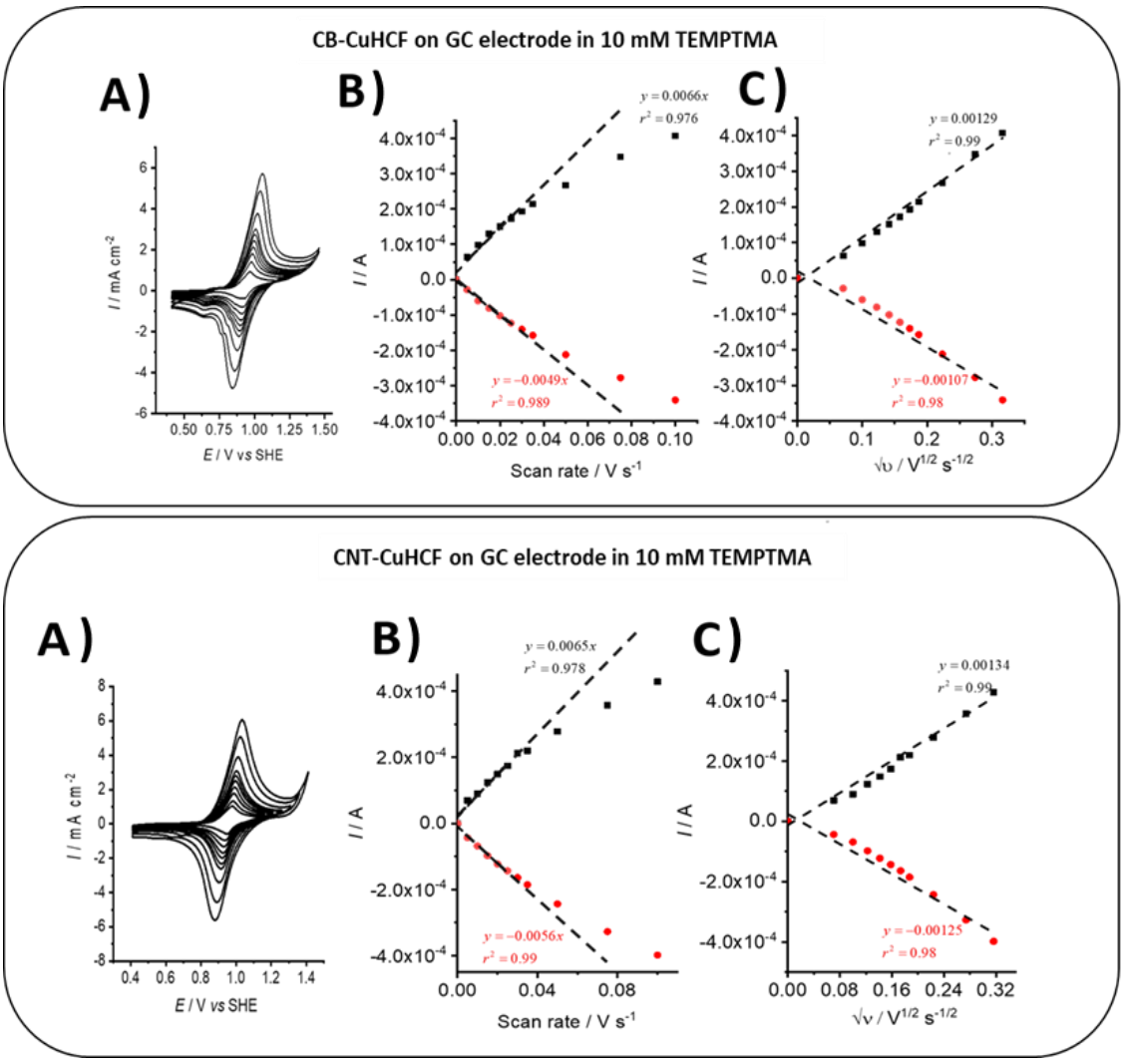

Figure 3.22 top A) CV of CB-CuHCF drop-casted on GCE in 10 mM TEMPTMA performed at 5, 10, 15, 20, 25, 30, 35, 50, 75, 100 mV·s^{-1}. All curves are normalized by the geometric surface area of the electrode (0.071 cm^2) and recorded without iR drop compensation. B) Peak current vs. scan rate of A). C) Square root for the scan rate dependency of A). Peak currents

range linearly with the scan rate below 40 mV·s^{-1} and with the square root of the scan rate from 40 to 100 mV·s^{-1}. Figure 3.23 bottom A) CV of CNT-CuHCF drop-casted on GCE in 10 mM TEMPTMA performed at 5, 10, 15, 20, 25, 30, 35, 50, 75, 100 mV·s^{-1}. All curves are normalized by the geometric surface area of the electrode (0.071 cm^2) and recorded without iR drop compensation. B) Peak current vs. scan rate of A). C) Square root for the scan rate dependency of A). Peak currents range linearly with the scan rate below 40 mV·s^{-1} and with the square root of the scan rate from 40 to 100 mV·s^{-1}.

Peak-to-peak separation from planar GC electrode to the CNTs ranges from 60 to 140 mV for the oxidation of 10 mM TEMPTMA in 1 M KCl_{aq}, highlighting the increase of the electrode thickness and porosity. As studied by Streeter *et al.*[171], the porous surface of the CNTs film entraps pockets of TEMPTMA solution and the electrode can be considered as a thin layer cell.

Table3.4 Peak-to-peak separation for the different types of modified electrode in the absence and presence of redox mediators in solution at 10 mV·s^{-1} scan rate.

Electrodes	***ΔE in 1 M $KCl_{aq.}$ / mV***	***ΔE in 10 mM TEMPTMA / mV***
GC		60
CB		79
CNT		140
CuHCF	22	53
CB-CuHCF	60	58
CNT-CuHCF	50	40

3.5.6 Galvanostatic cycling of CuHCF boosters in 100 mM TEMPTMA in 1 M KCl solution

In order to understand the enhancement in the volumetric capacity brought by the addition of the solid booster, two separate cycling tests were performed in a H-cell battery equipped by:

- ***i)*** Porous frit (2 cm^2 area) as separator
- ***ii)*** 25 mL of electrolytes (10 mM TEMPTMA at the positive-side and 50 mM $ZnCl_2$ at the negative-side, respectively),
- ***iii)*** 6 cm long RVC electrodes and
- ***iv)*** Ag/AgCl in 3 M KCl_{aq} as reference electrode in the TEMPTMA's tank.

A complete schematic of the battery design is presented in chapter 5.

Chronoamperometries of 10 mM TEMPTMA in the absence and presence CuHCF booster were performed, under vigorous stirring and continuous bubbling of nitrogen (***Figure 3.24A)*** and ***B)***). In particular the following boosters were tested:

- ***i)*** 100 mg of pristine CuHCF
- ***ii)*** 100 mg of *ex-situ* composite CNT-CuHCF (90-10) wt. % (the synthesis protocol of the composite is reported in chapter 5).

During the discharge of the battery, the oxidation of $TEMPTMA^+$ into $TEMPTMA^{2+}$ at the RVC electrode surface is balanced with the oxidation of the solid booster (CuHCF) from Fe^{2+} to Fe^{3+}, leading to the de-intercalation of K^+ inside the composite. $TEMPTMA^+$ is then recycled to $TEMPTMA^{2+}$ at the solid-liquid interface, thanks to the driving force existing in between the booster and the RM. At the negative side, Zn(II) is reduced to Zn.

During the oxidation at +1.10 V *vs.* SHE, a charge of 27 C was obtained for the TEMPTMA, 1.125 times higher than the theoretical capacity of 24 C (for 10 mM TEMPTMA in 25 mL of 1 M KCl_{aq}). The reduction at +0.41 V *vs.* SHE gave an apparent discharge capacity of 27 C.

Subsequently, when 100 mg of pristine CuHCF powder was added in the TEMPTMA solution, an apparent charge and discharge of 45 C were obtained, 98% of the theoretical one (46 C, calculated as the sum of the theoretical charge of TEMPTMA (24 C) and the theoretical charge for 100 mg CuHCF (22 C from 62 $mAh \cdot g^{-1}$ theoretical value for the hydrated form).

Finally, the CNT-CuHCF *ex-situ* composite (90-10) wt. % was tested in the same condition and charge and discharge capacities of 59 and 60 C were obtained, respectively.

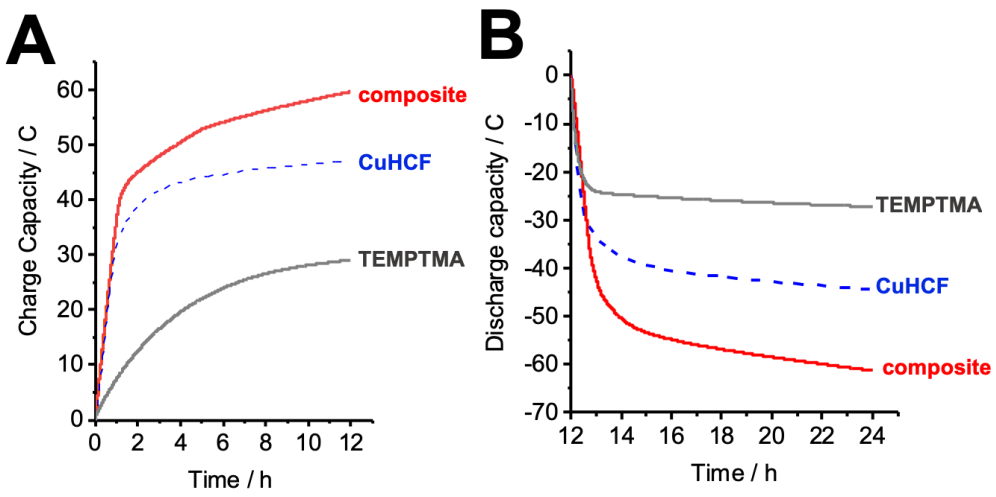

Figure 3.23 A) Charge capacity and B) discharge capacity obtained for 10 mM TEMPTMA without solid material (grey), with 100 mg CuHCF (dashed blue line) and with 100 mg of ex-situ composite CuHCF-CNT (90-10) wt. % (red line) performed at + 1.10 V vs. SHE and + 0.41 V vs. SHE.

The theoretical charge of the composite in the presence of TEMPTMA was found to be 51 C (27 C for the CNT-CuHCF composite and 24 C for the TEMPTMA). Again, it can be noticed that the experimental capacity is 1.16 higher than the theoretical value (51 C). This is not likely due to side reactions (*e.g.* OER), since the capacity values look reversible, but more probably to the π-stacking of the TEMPTMA on the CNTs sidewall, leading to inner surface side-reactions. [172]

Importantly, apparent gravimetric densities for CuHCF and *ex-situ* composite were found equal to be equal to 1.33 (± 0.1) $g \cdot mL^{-1}$ and 1.41 (± 0.1) $g \cdot mL^{-1}$, respectively. Therefore, equivalent volumes of solid boosters are 0.075 mL for CuHCF and 0.071 mL for the *ex-situ* composite, respectively.

Therefore, 100 mg CuHCF booster alone has 298 $C \cdot mL^{-1}$ volumetric capacity (considering 100 mg of mass, 62 $mAh \cdot g^{-1}$ theoretical gravimetric capacity for the hydrated form of CuHCF and 0.075 mL volume of CuHCF calculated using the gravimetric density of the material) and similarly the *ex-situ* composite 310 $C \cdot mL^{-1}$. Importantly, these values have to be considered as related to such small volumes.

3.5.7 An aqueous battery with ex-situ composite CNT-CuHCF and TEMPTMA

Subsequently, due to the encouraging cycling performance of the *ex-situ* composite CNT-CuHCF in the TEMPTMA electrolyte, another battery experiment (configuration as in the previous cycling tests) was performed to check the long-term stability of the booster in the TEMPTMA electrolyte. In particular, the battery was composed of 10 mM TEMPTMA in 1 M KCl_{aq} (25 mL) with 100 mg CNT-CuHCF *ex-situ* composite at the positive-side and 0.5 M zinc chloride in the negative-side (25 mL).

Galvanostatic cycling of the TEMPTMA with the *ex-situ* composite was performed at 2.5 $mA \cdot cm^{-2}$ for 25 cycles (***Figure 3.24B)***). In the absence of solid booster, a CE of only *ca*. 70% was obtained for 10 mM TEMPTMA, probably due to cross-over through the glass frit. Interestingly, the addition of composite solid booster increased the CE up to 95%, because the kinetics of charge transfer is faster in this case being TEMTPMA recycled at the CNT-interface, (***Figure 3.24A)***).

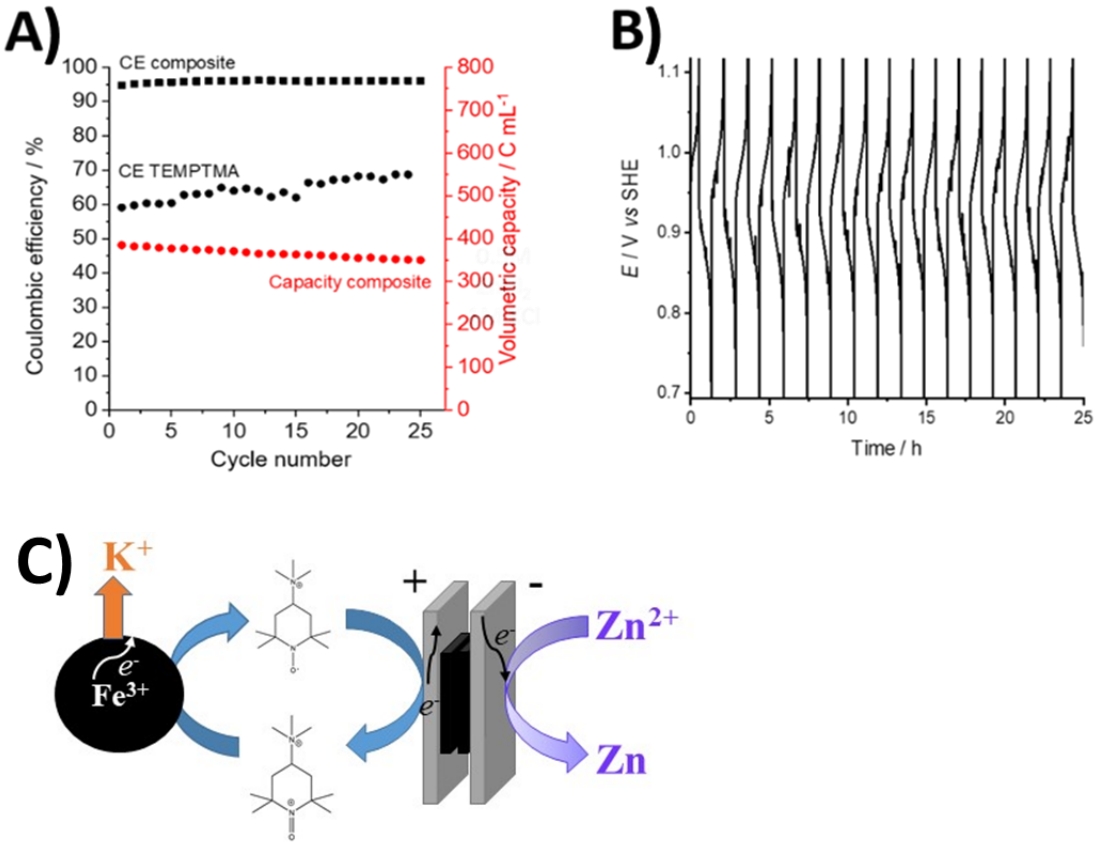

Figure 3.24 A) Coulombic efficiencies in the absence (black circles) and in the presence of the composite (black squares) as a function of the number of cycles. The volumetric capacity in the presence of composite over number of cycle is plotted along the secondary y-axis (red dots). B) Positive electrolyte potential as a function of charge and discharge times. Conditions: Galvanostatic cycling at 2.5 $mA \cdot cm^{-2}$ with charge and discharge cutoff potentials of +1.10 and +0.60V vs. SHE, respectively. The cycling test was performed for 25 cycles in the presence of 100 mg composite and 10 mM TEMPTMA at the

positive side and 0.5 M $ZnCl_2$ in 1 M KCl_{aq} at the negative side. C) Graphical schematic of the redox reactions between the mediator (TEMPTMA) and the booster (CuHCF)

However, 25% of capacity fading (as compared to the theoretical volumetric capacity of 460 $C \cdot mL^{-1}$) might be explained by the slow percolation of the redox mediator through the glass frit. Overall, a 10^4-fold increase of capacity was achieved with the addition of the CNT-CuHCF *ex-situ* composite in the TEMPTMA solution, compared to the capacity of the TEMPTMA alone (***Figure 3.25A)*** and ***B)***). Such enhancement in the storage capacity makes this candidate couple promising for large-scale flow battery installations.

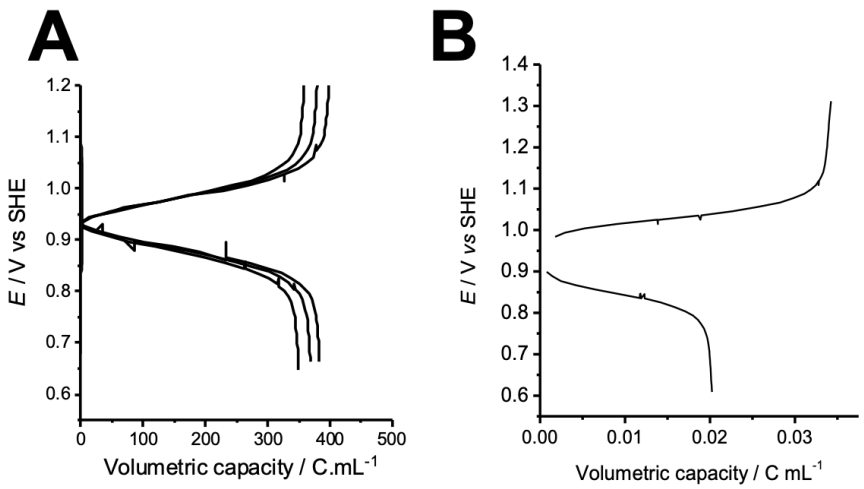

Figure 3.25 A) Galvanostatic cycling performed at 2.5 $mA \cdot cm^{-2}$ in the presence of 100 mg composite and 10 mM TEMPTMA. B) Galvanostatic cycling performed at 2.5 $mA \cdot cm^{-2}$ of 10 mM TEMPTMA.

3.6 Conclusions and perspectives

A solid electrochemical storage strategy was developed for redox flow batteries operating with TEMPTMA and CuHCF at the positive-side of an ARFB at neutral pH.

The redox potentials of TEMPTMA and CuHCF of +0.90 and +0.97 V *vs.* SHE in 1 M KCl_{aq} are close enough to allow the electron transfer at the solid-liquid interface. This property was confirmed by calculating the Fermi level of the CuHCF depending on the state of charge of TEMPTMA.

CuHCF solid booster was electrochemically characterized and successfully functionalized with CNTs to propose a new composite for battery cycling. This composite benefits from the high electronic conductivity of the CNTs and it looks desirable for long flow cell cycling tests. More specifically, the addition of less than 10% CNT to the CuHCF promotes the charge transfer and leads to a gravimetric capacity of 80 $mAh \cdot g^{-1}$. Cycling behavior of CNT-CuHCF-TEMPTMA/Zn aqueous battery was investigated: an excellent CE up to 95% was achieved after 25 cycles with a 10^4-fold increase in the volumetric capacity with relative low concentration of the RM in the electrolyte (only 10 mM). However, for the first time, a composite including CNTs has been cycled according to the "redox-mediated" charge transfer approach along with a relatively safe ROM in the electrolyte.

An encouraging perspective opened up at the conclusion of this work, which consisted in the addition of the second-half of the battery system, still operating at neutral pH. In this case, PBAs are not extremely promising candidates. [129] The PBA Cr^{II}—N≡C—$Mn^{II/I}$ from Pasta and co-workers[129] for aqueous batteries at neutral pH, shows a challenging synthetic route due to the tendency of the Cr^{2+} to hydrolyze and Mn^{3+} to disproportionate.[129] Additionally, Cr is not a safe material. Alternatively, the same authors identified also manganese hexacyanomanganate PBA, but for NIB in organic electrolytes, showing high specific capacity equal to 209 $mAh \cdot g^{-1}$.[173] However, this is not really promising for an aqueous flow battery, hence, other materials have to be considered. As it will be extensively described in the next chapter, the objective is design a pair of solid booster and RM from earth abundant precursors, environmentally safe and easy to scale-up for stationary RFB installations.

Chapter 4

Booster based-negative side electrolyte: a viologen derivative as redox mediator and a polyimide as solid booster

4.1 General Introduction

In the previous chapter, a promising pair of solid booster and RM was proposed and tested at the positive-side of an aqueous redox battery. The resulting system performed well showing a 400-fold increase in the volumetric capacity, as compared to the RM solution alone. In addition, for the first time an optimized booster functionalized with CNTs exhibited a stable cycling performance over time (25 hours) with good capacity retention of 90% after 25 cycles. In particular, this composite benefitted from the interlacing action of the CNTs to connect booster particles and make the whole material more electronically conducting.

After this work, the aim was to complete the battery system always in presence of a solid booster in the electrolyte. Indeed, being satisfied from the cycling performance of the TEMPTMA and keeping the neutral pH as preferable operating medium for the flow cell, another class of ROM was identified for the negative-side. As it was discussed in the previous chapters, ROM are gaining attention in ARFBs, because they can be easily synthesized from earth abundant elements and thus they can potentially represent an interesting option when it comes to propose and design new electrolytes keeping low manufacturing costs.

Especially in a neutral pH ARFB, TEMPO derivatives (*e.g.* TEMPTMA[125], TEMPOL[126] and poly-TEMPTMA[50]) and ferrocene derivatives (FcNCl, FcN_2Br_2) [174] are considered quite promising electrolytes for the positive-side, as it was also discussed and demonstrated in the previous chapter. Frequently, these electrolytes are coupled with viologen derivatives at the negative-side. For instance, Hu *et al.*[174] recently proposed an AORFB system with FcNCl at the positive-side and MV at the negative-side, respectively. [174] The resulting electrolyte (in the concentration of 0.7 M) delivered a good and stable performance with 9.9 Wh L^{-1} and 81% EE after 500 cycles (99.96% for a single charge/discharge cycle). [174] As another example, Janoschka *et al.*[125] proposed again MV along with TEMPTMA as aqueous electrolytes in a neutral pH RFB. The resulting system (with 2 M concentration of the electrolytes) exhibited an energy density of 38 Wh L^{-1}.[125]

Viologen is frequently employed as negative-side material in AORFBs at neutral pH, because among other electrolytes it is a two-electron storage material.[175] Indeed, as described by DeBruler *et al*.,[175] these two-electron storage electrolytes exhibit volumetric capacities up to 96.5 Ah L^{-1} in H_2O (or 75.0 Wh L^{-1} in 2 M $NaCl_{aq}$.) [175] and redox potentials as low as −0.77 V *vs*. SHE, among the highest values of the reduction potentials and charge capacity that have been obtained in aqueous electrolytes. [175] The usage of viologen electrolytes for neutral pH ARFBs is encouraging, especially when combined with positive-side electrolytes such as TEMPO and Fc derivative. The resulting systems can provide a cell voltage up to 1.4 V[125] [175] and an energy efficiency of up to 65%,[175] with capacity retention above 90% for each cycle.[175] Finally, the mild and safe operating environment (*e.g*. KCl_{aq}. or $NaCl_{aq}$.) makes the choice of these electrolytes highly preferable.

For the present thesis, in good agreement with the literature,[125] [175] [176] [174] a new derivative of viologen electrolyte was synthesized with two main objectives:

i) Perform some preliminary cycling tests in an AORFB in presence of TEMPTMA at the positive-side, mainly to understand the chemical stability

ii) Find a candidate solid booster that could feasibly be paired with it.

In the following sections of this chapter, a few examples of AORFB employing viologen electrolytes are discussed, considering especially their stability upon long cycling experiments. The latter is an important requirement to achieve when it comes to designing electrolytes for long-lasting energy storage systems at grid-scale.

4.2 Viologens

4.2.1 Examples of viologens employed in AORFBs

Among other organic electrolytes, 4,4′-dipyridinium (precursor of MV) can be functionalized quite easily to obtain derivatives with usually enhanced properties as compared to MV, especially in terms of solubility and redox potential for electrochemical devices. This has convinced many researchers to design new viologens which could be promising candidates for energy storage applications, such as RFBs.

Recently, Liu and co-workers[176] have proposed a sulfonate-functionalized viologen for AORFBs at neutral pH, in presence of a cation-exchange membrane. According to the authors, the first synthesis attempt of this viologen was quite unsuccessful. The reaction was accomplished at elevated temperature (140°C) over 8 hours in DMSO, where the 2-sulfonatoethyl bromide was added to the precursor 4,4' bipyridine, but after 48 hours the yield was just 15%. [176] On the contrary, the second synthesis trial was successful and the 1,1′-bis[2-sulfonatopropyl]-4,4′-bipyridinium was obtained by an alkylation of 4,4′-bipyridine with 2 equivalents of propane sultone, conducted in refluxed toluene for 3 hours with a final yield of 98%. [176] Indeed, in the first synthetic route the precursor 2-sulfonatoethyl bromide was not enough electrophile (*i.e*. an electron pair acceptor) to react with the 4,4' bipyridine.

The resulting sulfonate-functionalized viologen was tested in an AORFB at neutral pH, in presence of potassium iodide (I_3^-/I^-) at the positive-side, with a Nafion 212 membrane in the electrochemical cell (***Figure 4.1A***).

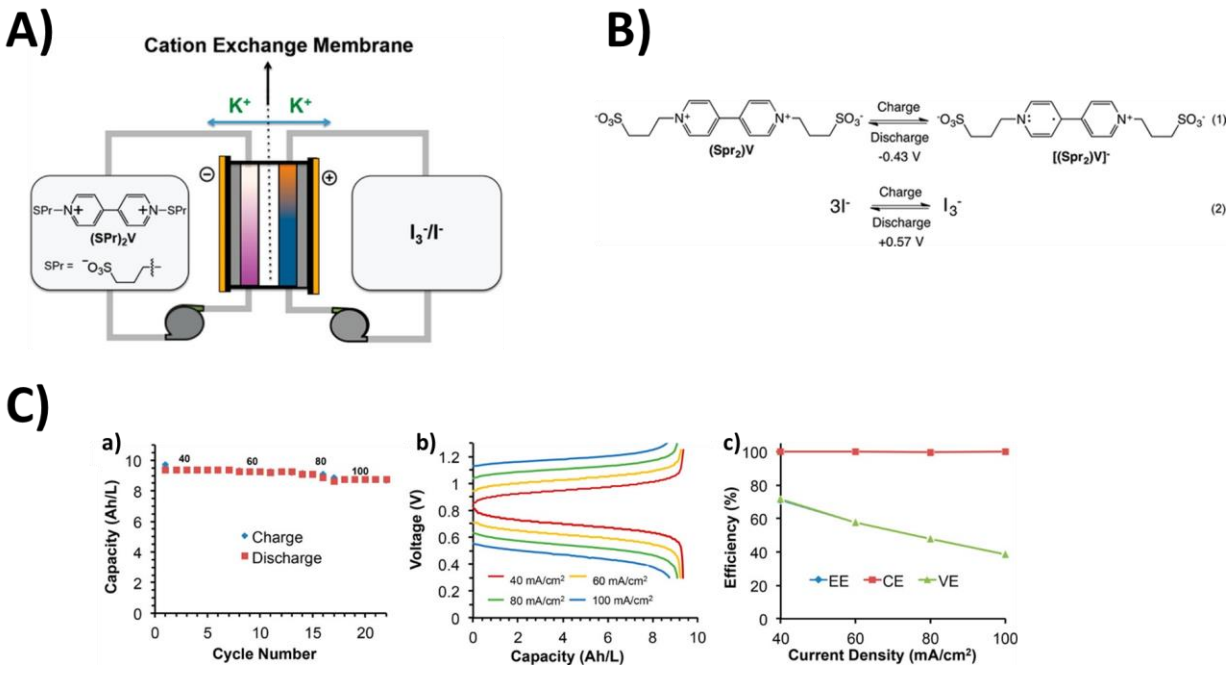

Figure 4.1 A) General scheme of the AORFB system proposed by Liu and co-workers[176].

B) Representation of the redox reactions occurring upon charge and discharge of the RFB.

C) a) Plot of battery capacity vs. cycling numbers of the sulfonate-viologen/KI AORFB 2 at current densities from 40 mA·cm^{-2} to 100 mA·cm^{-2}. b) Charge and discharge curves at current densities from 40 to 100 mA·cm^{-2}. c) Plots of average CE, EE, and VE at different operational current densities. For all the tests, the sulfonate-viologen was employed at 0.5 M in 2.0 M KCl_{aq}., while KI at 2.0 M KI in 2.0 M KCl_{aq}. All the images are reproduced with permission from the work of Liu and co-workers at ref. [176]. Copyright 2020, American Chemical Society.

In particular, the AORFB (as depicted in ***Figure 4.1A)***) showed *ca*. 9.5 Ah L^{-1} volumetric capacity at 40 mA·cm^{-2}, with almost 100% CE at each current density.[176] In addition, the good rate performance and energy efficiencies were in agreement with the high conductivities of the electrolytes (103.2 mS·cm^{-1} and 234.2 mS·cm^{-1}, for the negative and the positive electrolyte, respectively). [176] Another great example is represented by the work of Luo *et al*.,[177], which proposed a new synthetic strategy to obtain a highly water-soluble π-conjugation extended viologen: the 4,4′-(thiazolo[5,4-d]thiazole-2,5-diyl)bis(1-(3-(trimethylammonio)propyl)pyridin-1-ium) tetrachloride, $[(NPr)_2TTz]Cl_4$ .This molecule was suggested as novel two-electron storage negative-side electrolyte for AORFBs. [177] The authors found high solubility in water (1.3 M, 69.7 Ah L^{-1}) [177] and as well in $NaCl_{aq}$ (1.1 M in 2.0 M $NaCl_{aq}$, 60.0Ah L^{-1}). [177] In an AORFB assembled with TEMPTMA at the positive-side, $[(NPr)_2TTz]Cl_4$ delivered 1.44 V battery voltage and 53.7 Wh ·L^{-1} energy density, 70 % EE and 99.97 % capacity retention per cycle.[177] Recently, Liu *et al*.[127], proposed a very stable AORFB based on derivatives of TEMPO and viologen at neutral pH. The negative-side electrolyte was the bis(3-trimethylammonio)propyl viologen tetrachloride and the positive-side the 4-[3-(trimethylammonio)propoxy]-2,2,6,6-tetramethylpiperidine-1-oxyl, synthesized from the TEMPOL by adding Coulombic repulsion to suppress bimolecular interactions that could lead to molecular decomposition.[127] The equivalent system showed 1.1 V[127] OCP and it is considered above all the AORFBs studied at neutral pH the most stable, since it exhibits an extremely high capacity retention rate, at 99.993% per cycle over 1,000 consecutive cycles, with the temporal capacity fade rate of 0.026% per h (independent from the concentration).[127]

4.2.2 Chemical stability of viologens in AORFBs and strategies to improve it

The focus of this thesis is ARFBs and in particular AORFBs, hence, it is extremely important to understand electrolytes stability to ensure long-lasting performances. Recently, Aziz and co-workers[178] have reviewed cycling performances in terms of capacity fade rate of all the AORFBs at neutral pH employing viologens at the negative-side and they are summarized in the following ***Table 4.1***.

Table 4.1 Summary of results of AORFBs containing viologens negative-side electrolyte. This table is reproduced with permission from the work of Kwabi et al. at ref [178]. Copyright 2020, American Chemical Society (ACS).

		capacity fade rate				
name	author/year	%/cycle	%/day	electron conc. (M)	redox potential (V vs SHE)	pH
Diquat 5/FcNCl	Huang/2018[128]	0.2	0.8	0.5	−0.51/0.61	7
MV/4-HO-TEMPO	Liu/2015[62]	0.1	27.5	0.5	−0.45/0.80	7
$(NPr)_2$TTZ/N^{Me}-TEMPO	Luo/2018[122]	0.03	2.25	0.1	−0.44/1.00	7
MV/TEMPO polymer	Janoschka/2015[120]	0.25	7.5	0.37	**−0.45**/0.90	7
MV/TEMPTMA	Janoschka/2016[121]	0.026	0.27	2	−0.45/1.00	7
$(SPr)_2$V/KI	DeBruler/2018[127]	0.01	0.45	0.5	**−0.43**/0.57	7
BTMAP-Vi/BTMAP-Fc	Beh/2017[90]	**0.0057**	**0.1**	1.3	−0.36/0.39	7
BTMAP-Vi/**BTMAP-Fc**		**0.0011**	**0.033**	1.0	−0.36/0.39	7
$(NPr)_2$V/FcNCl	DeBruler/2017[129]	0.01	0.5	0.5	(−0.35,−0.72)/0.61	7
$(NPr)_2$V/N-Me-TEMPO	Hu/2018[130]	0.005	0.2	0.5	−0.38/1.00	7
[(Me)(NPr)V]Cl_3/FcNCl	DeBruler/2017[129]	0.18	8.8	0.5	(−0.39,-0.78)/0.61	7
MV/FcNCl	Hu/2017[125]	0.01	0.22	0.5	−0.45/0.61	7
Phenazine-TEMPO combimolecule	Winsberg/2016[119]	0.011	0.62	0.01	−0.39/0.81	7
Zn^{2+}/**g+-TEMPO**	Chang/2017[117]	0.046	0.7	0.2	−0.69/**0.81**	7
BTMAP-Vi/**TMAP-TEMPO**	Liu/2019[118]	0.007	0.6	0.1	−0.38/**0.81**	7
		0.015	0.55	1.5	−0.38/**0.81**	7
Zn^{2+}/**SO_4-TEMPO**	Winsberg/2017[124]	0.0058	1.38	0.035	−0.87/**0.82**	7
Zn^{2+}/**Im-TEMPO**	Chang/2019[123]	0.11	21.2	0.4	−0.69/**0.95**	7

As it can be seen from the table, since the early experimental works in 2015-2016 where the system capacity fade was quite remarkable (*e.g.* MV/4-OH-TEMPO from Liu *et al.*[126]), the stability of the electrolytes and especially of the viologen at the negative-side largely improved. More precisely, in viologen electrolytes the stability is strictly related to the substituents of the 4,4′-dipyridinium backbone.[127] Indeed, many great works have been proposed showing derivatives of viologens exhibiting high capacity retention (>90% per cycle) for a considerable amount of cycles (from 50 to 500). In addition, as also confirmed by Liu *et al.*[127], viologen and derivatives cannot be adopted to either acidic or alkaline aqueous solutions, because of the attack of ammonium by OH^-, resulting in dealkylation and the annihilation of reduced MV by H^+.[127]

According to recent studies from Liu[127] and Aziz[178], during flow battery cycling, viologen and derivatives essentially can undergo two decomposition mechanisms. The first decomposition path involves molecular oxygen. Upon battery charging, viologen reduces to the radical-cation form ($V^{\bullet+}$), which can be readily oxidized back from molecular oxygen, forming a superoxide anion ($O_2^{-\bullet}$) (***step a*** in ***Figure 4.2***). Hayyan *et al*.[67] suggested that the presence of H^+ in the solution can induce a chemical reaction of the superoxide anion ($O_2^{-\bullet}$) with generation of $HO_2^{\bullet}$ and A^- (***step b*** in ***Figure 4.2***). Then, the $HO_2^{\bullet}$ can react once again with $O_2^{-\bullet}$and generate O_2 and HO_2^- or alternatively with another molecule of $HO_2^{\bullet}$ and form O_2 and H_2O_2.[67]

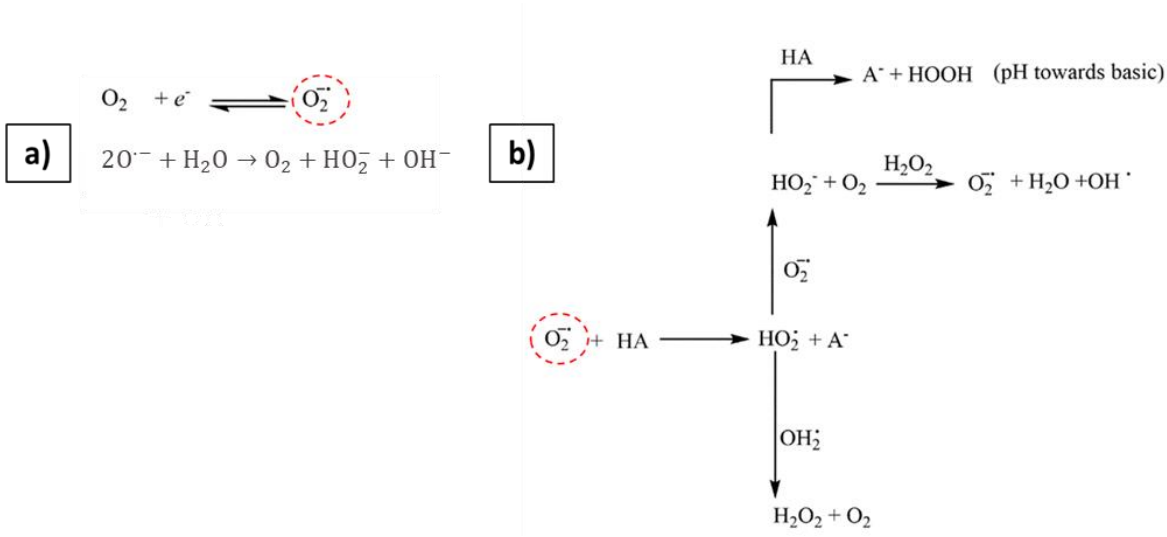

Figure 4.2 Mechanism of the superoxide anion once generated in the solution. This mechanism is inspired from the work of Hayyan et al at ref. [67].

Furthermore, it is assumed[127] that when $V^{\bullet+}$encounters the $O_2^{-\bullet}$, this would lead to an accumulation of OH^- in the solution, which would cause decomposition.[127] Another possible scenario could be that H_2O_2 generated from the $O_2^{-\bullet}$ in presence of acid (HA) can react with the $V^{\bullet+}$ (***Figure 4.3***):

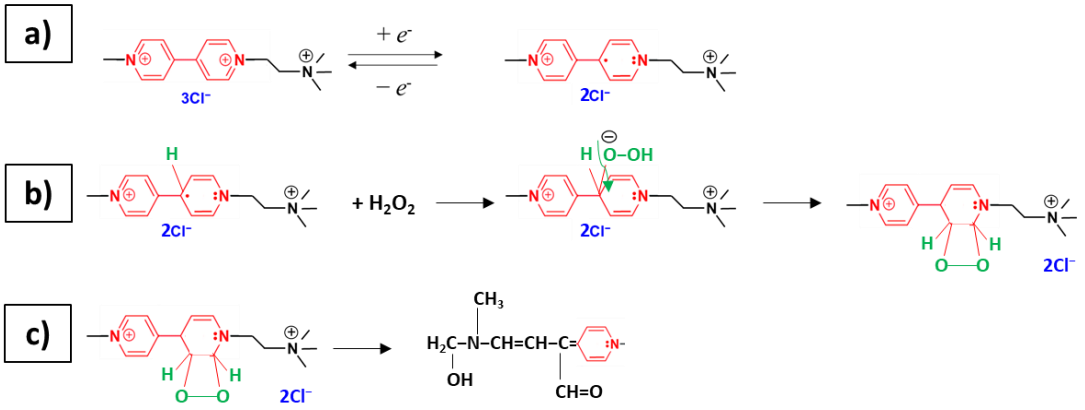

Figure 4.3 Possible mechanism of reaction between $V^{\bullet+}$and hydrogen peroxide (in this case it is represented the viologen derivative synthesized in the present work).

In the first step, as soon as the $V^{\bullet+}$ is generated from the fully oxidized form (V^{2+}) (***step a*** in ***Figure 4.3***), it reacts with H_2O_2 from the previous mechanism involving the $O_2^{-\bullet}$ (***Figure 4.2***). This reaction leads to the formation of an unstable adduct (***step b*** in ***Figure 4.3***), which suddenly by internal re-arrangement of the charge brings to a complete modification of the original molecular structure, generating a final product with an aldehyde bonded to the bypiridinium ring (***step c*** in ***Figure 4.3***). Furthermore, another mechanism of decomposition of viologens does not require the presence of molecular oxygen; in fact, it is believed that the $V^{\bullet+}$can undergo a dimerization process and form a stable dimer in the solution (***step a*** in ***Figure 4.4***).[127]

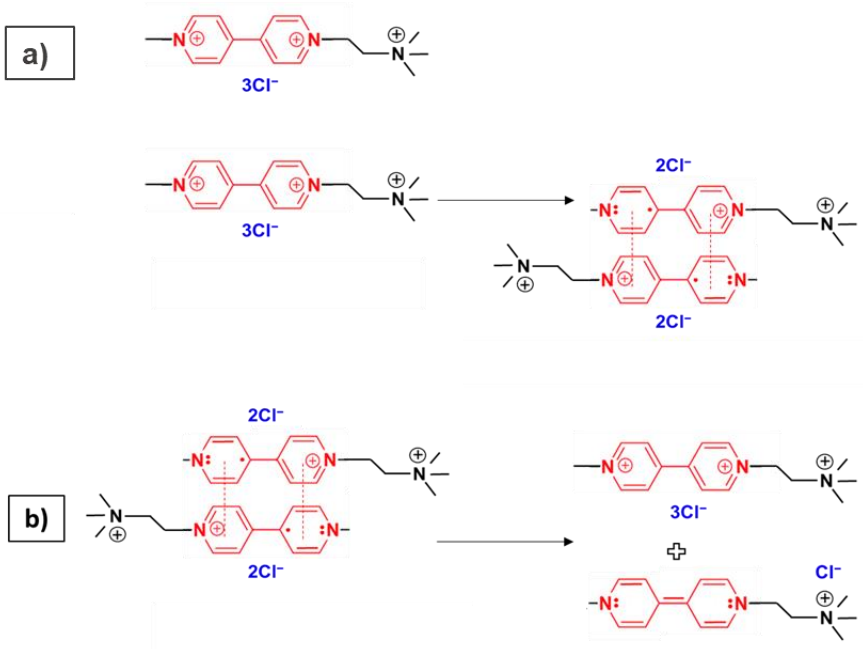

Figure 4.4 Dimerization mechanism of viologen wrote considering the synthesized viologen of the present work.

Subsequently, the dimer can undergo disproportionation resulting in the V^{2+} and fully reduced forms (V) of the viologen (***step b*** in ***Figure 4.4***) [127]. The formation of the stable dimer which suddenly disproportionates can be a possible reason of capacity losses in the battery cycling.[178] Interestingly, Aziz and co-workers[178] reported that, in comparison to much of the AORFB literature involving quinones, in the systems with nitroxyl-radicals and viologen derivatives, the electrolyte fading is less understood. [178] According to Aziz[178], it is not possible to discern the exact reason behind the capacity fade of these electrolytes (nitroxyl-radical and viologens), since not enough information are provided in the experimental results from the literature. However, it is interesting to observe how capacity losses are definitely lower once the nitroxyl-radical or its derivatives are replaced by ferrocene and derivatives at the positive-side. [178] As great example, Aziz [120] proposed a systems using the bis(3-trimethylammonio)propyl viologen tetrachloride at the negative-side and the bis((3-trimethylammonio)propyl)ferrocene dichloride at the positive-side, respectively (***Figure 4.5***)

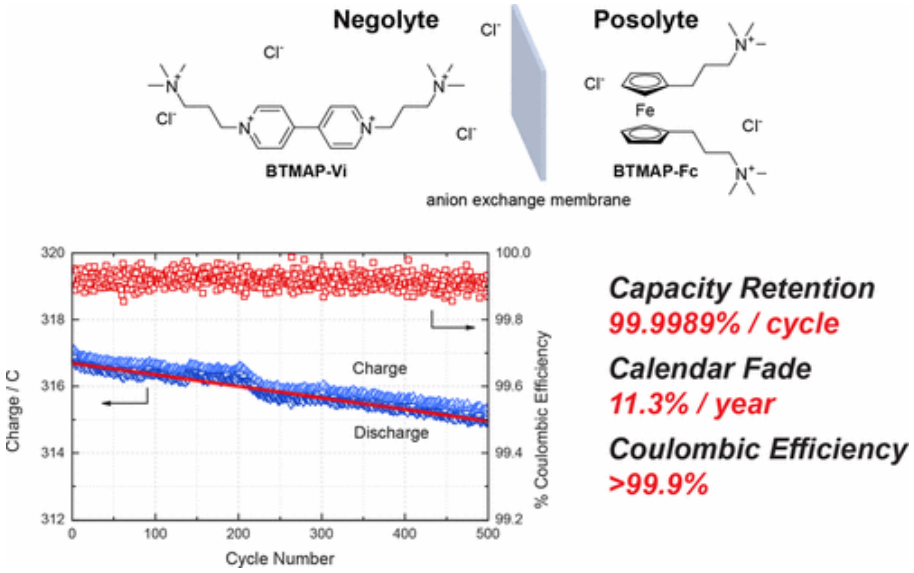

Figure 4.5 Representation of the AORFBs at neutral pH from Aziz and co-workers[120], reproduced with permission from ref. [120]. Copyright 2020, American Chemical Society (ACS).

This system showed outstanding cycling stability, with capacity retention of 99.9943%/cycle and 99.90%/day at a 1.3 M reactant concentration, increasing to 99.9989%/cycle and 99.967%/day at 0.75–1.00 M.[120] In this work, the authors also discussed that viologens and of nitroxyl-radicals can likely start to decompose at relatively high concentration (*i.e.* >50 mM) presumably as bimolecular reactions of the reactants with themselves.[57] Notably, this work proposes also an interesting way of monitoring the permeation of oxygen on capacity retention and to demonstrate it the authors decided to place the RFB installation in a plastic glovebag. At first, the bag was not inflated and the flow cell was cycled in presence

of molecular oxygen. Then, after *ca*. 50 cycles they inflated the bag with nitrogen and the capacity did not fade anymore as before. The corresponded measurement is reported in ***Figure 4.6***.

As appears from the plot in ***Figure 4.6*** the initial charge is around 400 C and after 10 cycles it rapidly decreases to *ca*. 300 C and finally to *ca*. 250 after 50 cycles. The % CE behaves accordingly. This test shows the importance of cycling the electrolytes (and especially the viologen at the negative-side) under inter atmosphere to avoid decomposition and side-reactions.

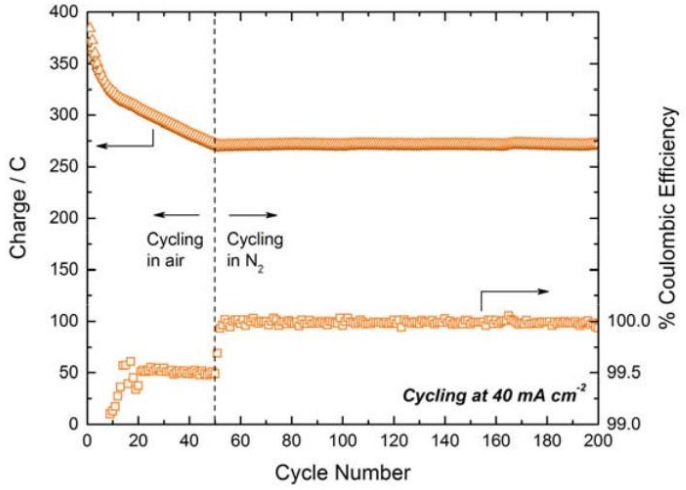

Figure 4.6 Cycling test of the system proposed by Aziz and co-workers at ref [120], employing a nitrogen filled glovebag to monitor oxygen permeation on capacity retention. The images is reproduced with permission. Copyright 2020, American Chemical Society (ACS).

Another interesting strategy to improve the stability of viologens in AORFBs was proposed by Hu *et al*.[179], where the viologen was functionalized to obtain the 1,1′-bis[3-(trimethylammonio)propyl]-4,4′-bipyridinium tetrachloride derivative. [179] This molecule, coupled with the 4-trimethylammonium-TEMPO chloride, enabled the flow battery achieving 97.48% capacity retention for 500 cycles and a power density of 128.2 mW cm^{-2} (***Figure 4.7***).[179]

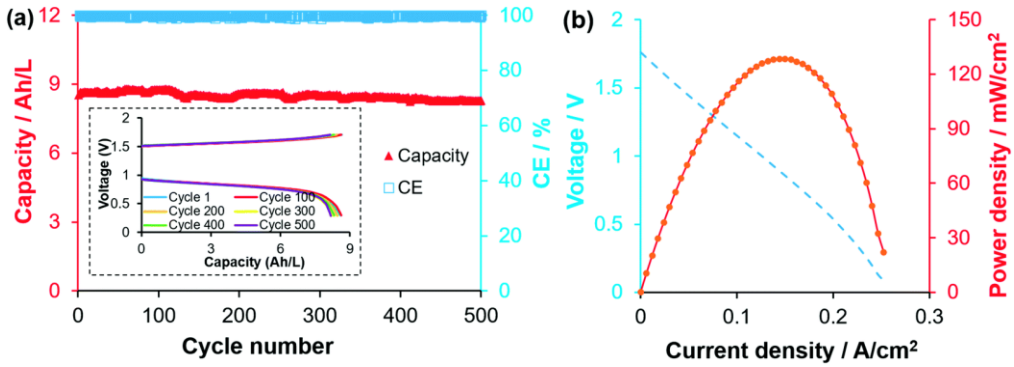

Figure 4.7 Battery performance of 0.5 M electrolytes. a) Capacity and CE vs. cycle number for 500 cycles. The inset shows the representative charge/discharge profiles. The battery was cycled at 60 mA·cm^{-2}. b) Polarization and power density

curves of the AORFB at 100% SOC. These images are reproduced with permission from the work of Hu et al. in ref. [179] . Copyright 2020, Royal Society of Chemistry.

In particular, Hu *et al*. [179] compared the cycling performance of the conventional MV (along with TEMPTMA at the positive-side), with those of the 1,1′-bis[3-(trimethylammonio)propyl]-4,4′-bipyridinium tetrachloride viologen derivative.

They proved by UV/Visible spectroscopy that the radical-cation of the 1,1′-bis[3-(trimethylammonio)propyl]-4,4′-bipyridinium tetrachloride viologen is more stable than that of the MV.[179]

In a glove box, they performed UV/Visible spectroscopy tests of both the viologens in aqueous solutions every 2 hours and they observed that after 48 hours a slight decrease in the main absorption peak at 605 nm corresponded to the formation of the radical-cation in case of the MV (***Figure 4.8a)***).[179]

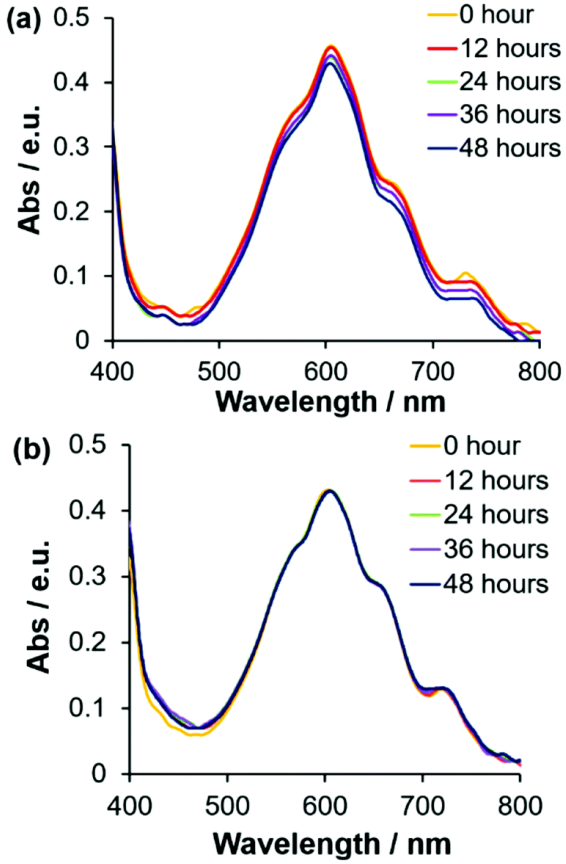

Figure 4.8 UV-vis spectra of (a) $(MV)^{\bullet+}$ and (b) $[(NPr)2V]^{\bullet+}$ in 2 M NaCl aqueous solution over 48 hours. This image is reproduced from the work of Hu et al. in ref. [179] . Copyright 2020, Royal Society of Chemistry.

The authors discussed that in aqueous media the $MV^{\bullet+}$ likely undergoes a dimerization process (***Figure 4.4***), which seems not favored in their own viologen derivative (the 1,1′-bis[3-(trimethylammonio)propyl]-4,4′-bipyridinium tetrachloride viologen), due to the increased charge repulsion by two additional positively charged propyl ammonium pendent arms.[179]

4.3 Results and discussion about TEMPTMA/MTABT AORFB

4.3.1 Characterization of N-Methyl-N'-(3-trimethylammonioethyl-)-4,4'-bipyridinium tetrachloride

N-Methyl-N'-(3-trimethylammonioethyl-)-4,4'-bipyridinium tetrachloride (abbreviated as MTABT) was synthesized following the procedure reported in chapter 5 of this manuscript. Once synthesized, the molecule was characterized by ^{1}H-NMR (in D_2O) and ^{13}C NMR (D_2O) and the spectra are displayed in ***Figure 4.9A)*** and ***B)***.

^{1}H-NMR confirmed the molecular structure of MTABT, where the first chemical shift (δ, ~3.5 ppm) belongs to the protons of the quaternary amine group. The chemical shift around 4 and 5 ppm to the ethyl chain connected to the quaternary ammine group and that around 9 and 9.5 ppm to the protons of the aromatic ring of the 4,4'-bipyridinium. The chemical shift of the solvent D_2O is located at ~4.8 ppm. The complete description of the spectrum is provided in the caption below the NMR spectrum.

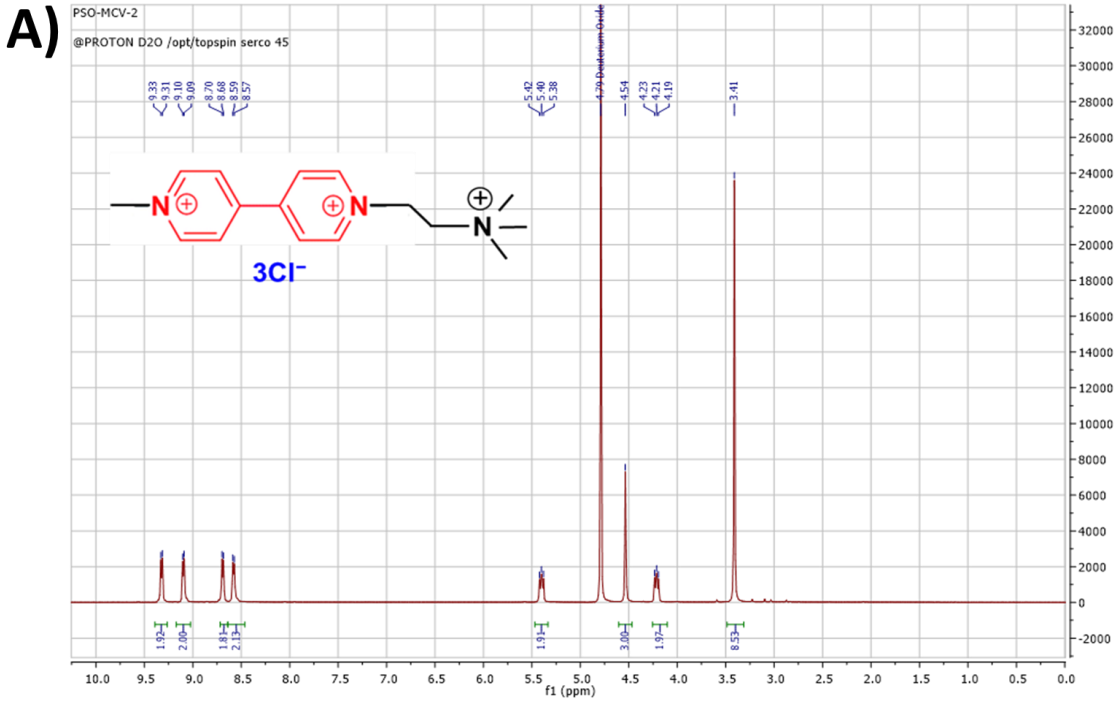

Figure 4.9A) ^{1}H-NMR spectrum of MTABT. The NMR solvent is D_2O. B) ^{13}C-NMR spectrum of MTABT. The NMR solvent is D_2O. ^{1}H NMR (D_2O, 400 MHz): δ3.41 ppm (s, 9 H), 4.21 ppm (m, 2 H), 4.25 ppm (s, 3 H), 5.40 ppm (m, 2 H), .8.59 ppm (m, 2 H), 8.68 ppm (m, 2 H), 9.10 ppm (m, 2 H) and 9.31 ppm (m, 2 H).

^{13}C NMR spectrum confirmed as well the molecular structure of the MTABT. The chemical shift at 125-150 ppm can be attributed to the C atoms of the aromatic rings and those located at high field region (50-70 ppm) to the C−H saturated alkane and to the C atom bonded to the quaternary amine.

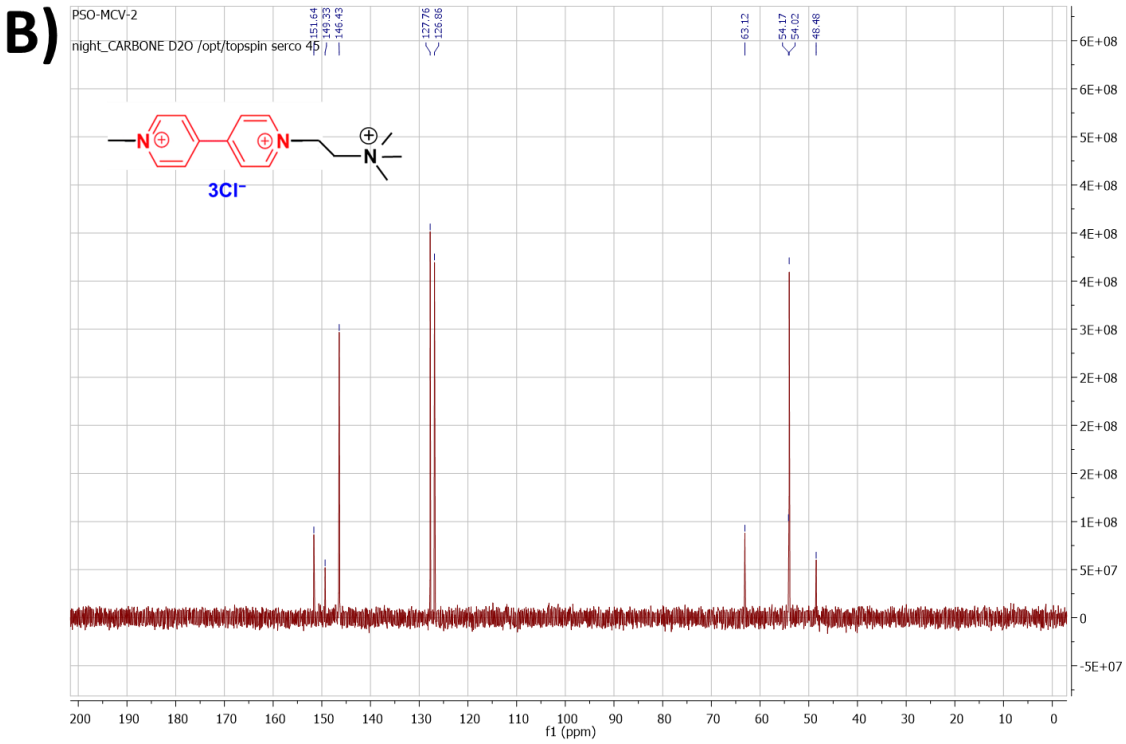

Figure 4.9 B) ^{13}C NMR (D_2O, 400 MHz) of MTABT.

Furthermore, UV/Visible spectroscopy (***Figure 4.10***) was employed to determine the solubility limit of the synthesized MTABT. From a calibration curve (slope giving an extinction molar coefficient of 0.0574 (M^{-1} cm^{-1}) with four standard solutions of MTABT in 1 M KCl_{aq}. (from 2 to 14 µM concentration), the solubility limit was determined as 1.86 ± 0.2 M, obtained after three measurements. This value looks a bit lower than the one from the common MV proposed by Janoschka *et al*.[125] (2.4 M in 1.5 M $NaCl_{aq.}$).

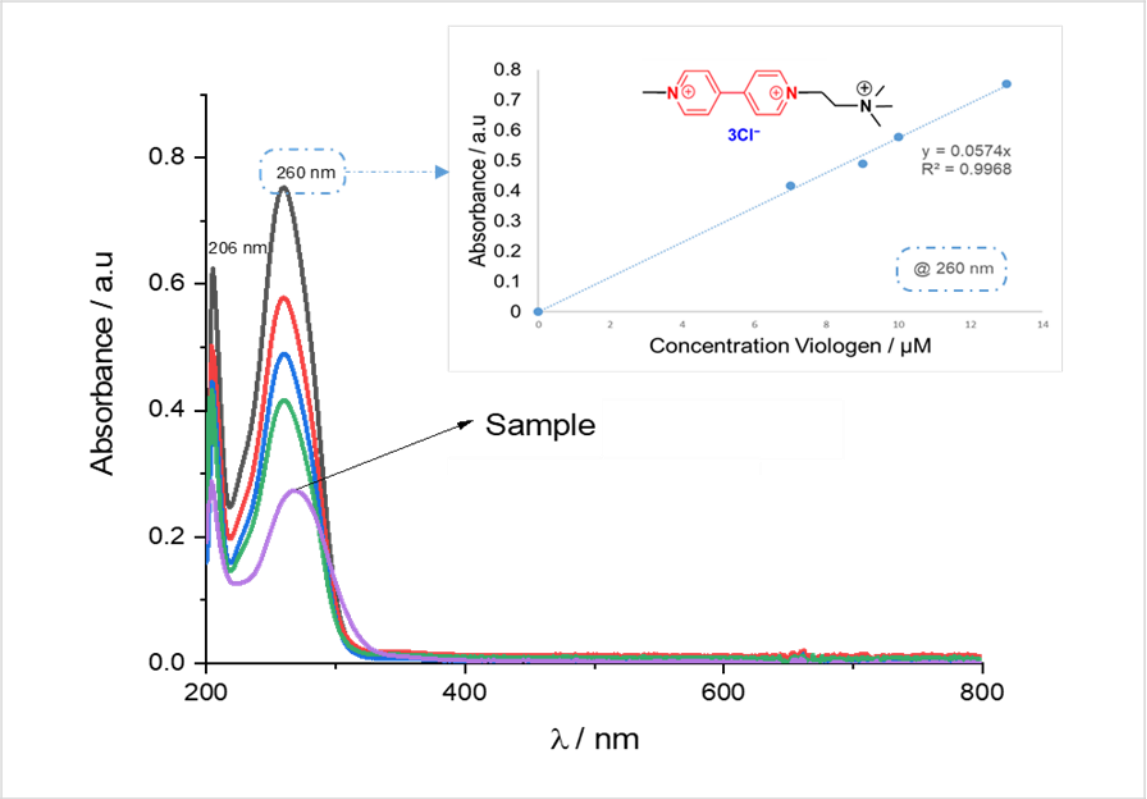

Figure 4.10 Determination of the solubility limit of MTABT by UV/Visible spectroscopy, (the calibration plot according to the Lambert Beer Law, is depicted in the inset of the UV/Visible spectrum and it was recorded at 260 nm).

Interestingly, ***Figure 4.11*** shows (in good agreement with the literature) how MTABT changes its color according to the oxidation state. Indeed, in the fully oxidized state looks yellowish (***Figure 4.11a)***), (at relatively low concentration values) and once it is reduced to the half state it turns bluish/violet (***Figure 4.11a')***).

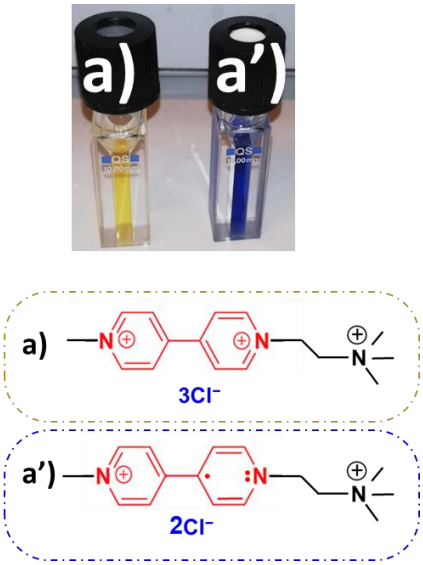

Figure 4.11 Colors of MTABT: a) is the fully oxidized state and a') is the half-oxidized state.

4.3.2 Electrochemical characterizations of MTABT

i) Cyclic voltammetry

Initially, electrochemical characterization was performed by CV on GCE, testing a solution of 10 mM MTABT in 1 M KCl_{aq} (purged with nitrogen for 1 hour before the measurement). ***Figure 4.12A)*** shows the voltammogram of MTABT at different sweep rates. The plot of the anodic peak currents and cathodic peak currents (***Figure 4.12B)***) fits linearly with the square root of the scan rate, meaning that the process is diffusion controlled (according to the Randles-Sevcik equation).

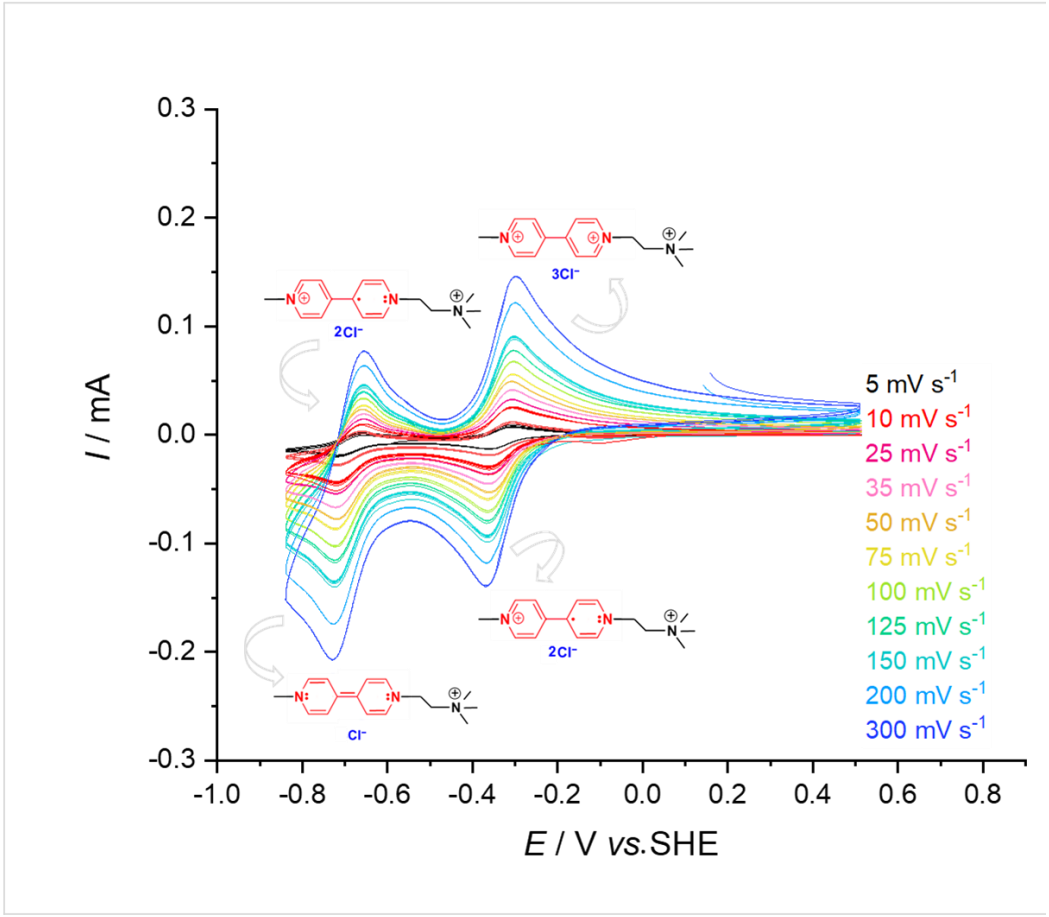

Figure 4.12 A) CV of MTABT (10 mM in 0. 1 M KCl_{aq}.) on GCE (0.071 cm^2 geometric area). The solution was purged for 1 hour with nitrogen before the measurement). All the scan rates are depicted in the legend beside the voltammogram.

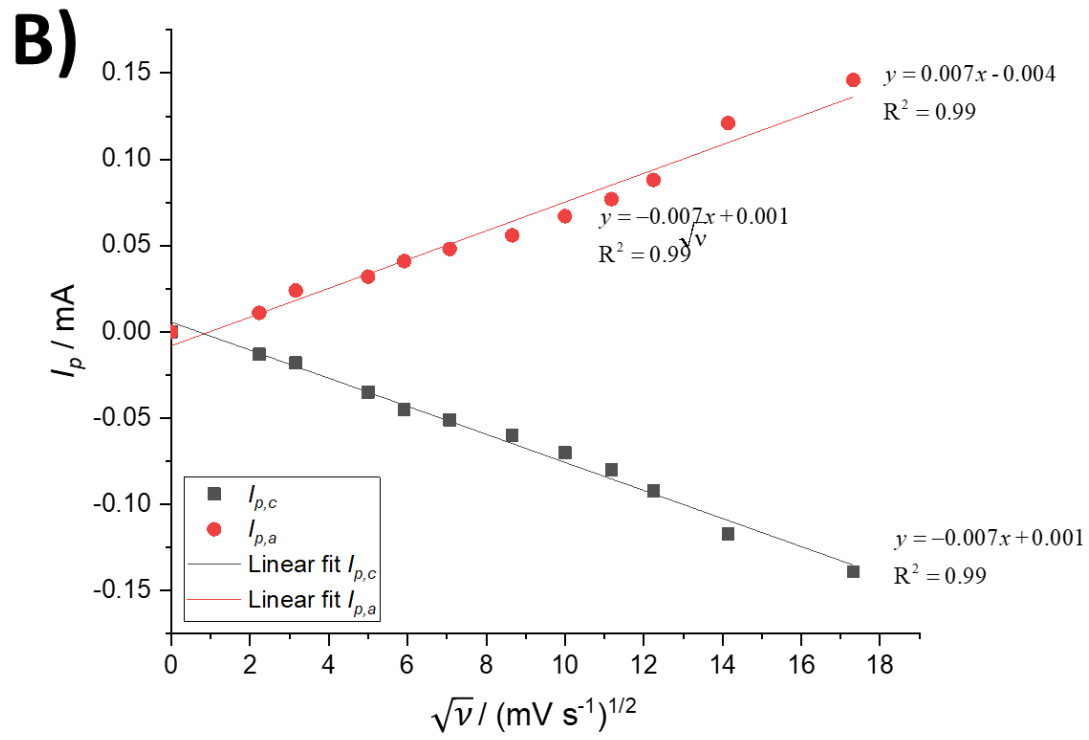

Figure 4.12 B) Plot of the square root of the scan rate vs. the peak current, for both anodic (red dots) and cathodic (black dots) peak currents. The respective equations are reported on the plot.

ii) Rotating disk electrode (RDE)

Later, RDE characterization was accomplished using a GCE (5 mm diameter, Metrohm) in a three electrochemical cell. A solution of 10 mM MTABT in 0.1 M KCl_{aq} (previously purged with nitrogen for 1 hour) was tested at different rotation speeds (***Figure 4.13A)***). Levich elaboration was performed and it is displayed in ***Figure 4.13B)***.

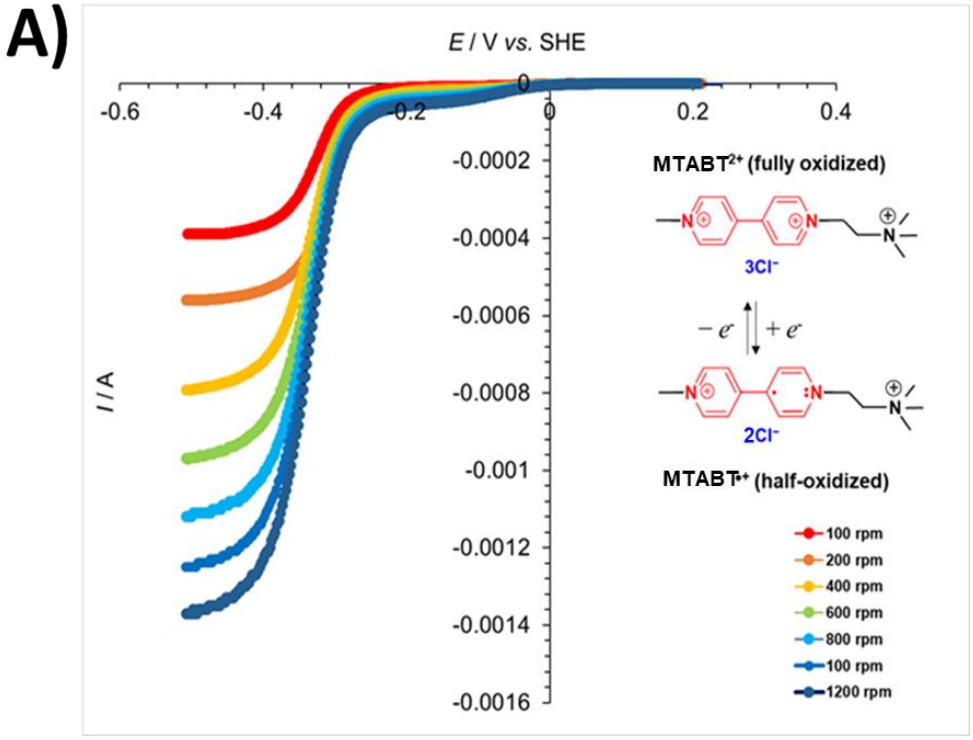

Figure 4.13 A) RDE voltammograms of 10 mM MTABT in 0.1 M KCl_{aq} on GCE (5 mm diameter). The solution was purged by nitrogen for 1 hour before the measurement.

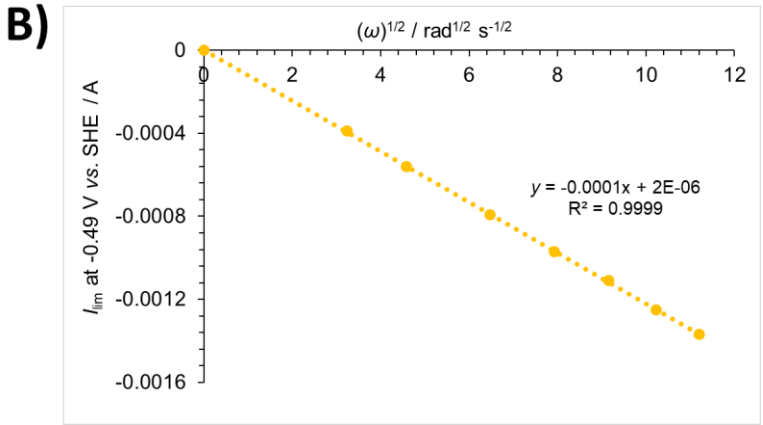

Figure 4.13 B) Levich plot of the RDE voltammogram in Figure 4.13A). Limiting current was taken at -0.49 V vs SHE for the various rotation speeds.

At the surface of the electrode the viologen reacted and exchanged one electron to generate the radical-cation. Despite this viologen is a two-electron storage material,[175] the second reduction reaction was not studied since it is known for being quite unstable[120]; in fact, this form of viologen likely precipitates in the solution.[178] For this reason, in the entire work just the first electron transfer reaction is targeted. Accordingly, for the elaboration of the Levich plot limiting currents at -0.49 V *vs*. SHE were taken (***Figure 4.13B)***).

From the Levich equation (expression in ***i)***), the diffusion coefficient (*D*) was found as $1.53 \cdot 10^{-5}$ $cm^2\ s^{-1}$. This value is slightly bigger than what Janoschka *et al*.[125] reported for the MV ($5.7\ 10^{-6}\ cm^2\ s^{-1}$, for a solution of 4.5 mM in 0.1 M KCl_{aq}),[125] and as well for that of the methyl propyl viologen chloride ($0.54\ 10^{-5}\ cm^2\ s^{-1}$).[175]

$$I_{\text{lim.}} = (0.620) n F A D^{2/3} \omega^{1/2} \nu^{-1/6} C \qquad \textbf{\textit{i)}}$$

Where, *n* is the number of electrons (1 in this case), *F* the Faraday constant (96485 C mol^{-1}), *D* the diffusion coefficient, ω the rotation speed (in radians per seconds), $\nu^{-1/6}$ is the kinematic viscosity ($cm^2\ s^{-1}$, which in the case of 1 M KCl_{aq} is equal to 1.043 $cm^2\ s^{-1}$, with a density of 1.2 g mL^{-1}) and *C* the concentration of the MTABT in solution ($1 \cdot 10^{-5}$ mol cm^{-3} in 0.1 M KCl_{aq}).

Later, for the same solution of 10 mM MTABT in 0.1 M KCl_{aq} (having an electrode geometric area of 0.196 cm^2), according to the Koutecky-Levich equation in ***ii***), the reaction rate constant k^0 for one electron exchanged can be determined by measuring the kinetic current (I_k) at a variety of different overpotential along the RDE voltammogram. In the present case k^0 is equal to $6.9\ 10^{-4}$ cm s^{-1}.

$$\frac{1}{I_L} = \frac{1}{I_k}\left(\frac{1}{0.620 n F A D^{2/3} \nu^{-1/6} c}\right) \qquad \textbf{\textit{ii)}}$$

MTABT does not show typical Koutecky-Levich trend, which should correspond to a linear plot of the reciprocal current against the reciprocal square root of the angular rotation rate ($\omega^{-1/2}$). The reason of this behavior is not fully clear yet and it needs further investigation. However, the k^0 for one electron exchanged in MTABT is quite close to that of MV found by Janoschka *et al*. [125] ($3.3\ 10^{-3}$ cm s^{-1}, for a solution of 4.5 mM in 0.1 M KCl_{aq}). [125]

4.3.2 Redox flow battery with MTABT and TEMPTMA

In this section some preliminary cycling experiments were undertaken to evaluate the stability of MTABT. In particular, cycling tests were performed first to study the possible decomposition mechanisms of both the electrolytes under the experimental conditions and second to check any "effect" of the electrolytes on specific cell components. Regarding the flow cell configuration, a complete schematic is reported in chapter 5, where all the components and relative materials are specified. An AORFB equipped with 10 mL of 50 mM in 1 M KCl_{aq} MTABT as negative-side electrolyte and 10 mL of 50 mM in 1 M KCl_{aq} TEMPTMA as positive-side, was assembled in a glovebag previously inflated by nitrogen. Importantly, the flow battery was configured as a three-electrode electrochemical cell, with an Ag/AgCl (in 3 M KCl_{aq}) reference electrode in the MTABT reservoir, but the TEMPTMA's potential was also actively recorded upon cycling. The electrochemical cell configuration was chosen most of all to constrain the viologen to the first electron transfer reaction, which leads to the formation of the radical-cation, since the second electron transfer reaction is known for being electrochemically not reversible.[127] Subsequently, charging polarization of a 0% SOC of the MTABT (***Figure 4.14A)***) in galvanostatic mode was performed prior effective cell cycling. During the polarization the viologen charged and the TEMPTMA discharged. Upon the polarization, MTABT reached a power of *ca*. 10 mW cm^{-2} at *ca*. 22 $mA \cdot cm^{-2}$, where the viologen reduced to the radical-cation form. Since the battery was totally discharged when this measurement was performed and the fact that only half of the storage capacity of the viologen was targeted, the power curve does not reach its maximum. However, the polarization curve of MTABT shows the three conventional regions in the relation between the potential and the current (or current density). In this case, from *ca*. 0 to −0.1 V *vs*. SHE there is the activation region, from *ca*. −0.1 V to *ca*. −0.25 V *vs*. SHE there is the region of the kinetic losses, from *ca*. -0.25 V to −0.40 V *vs*. SHE there is the ohmic region and finally from *ca*. -0.40 V to −0.50 V *vs*. SHE there is the mass transport region.

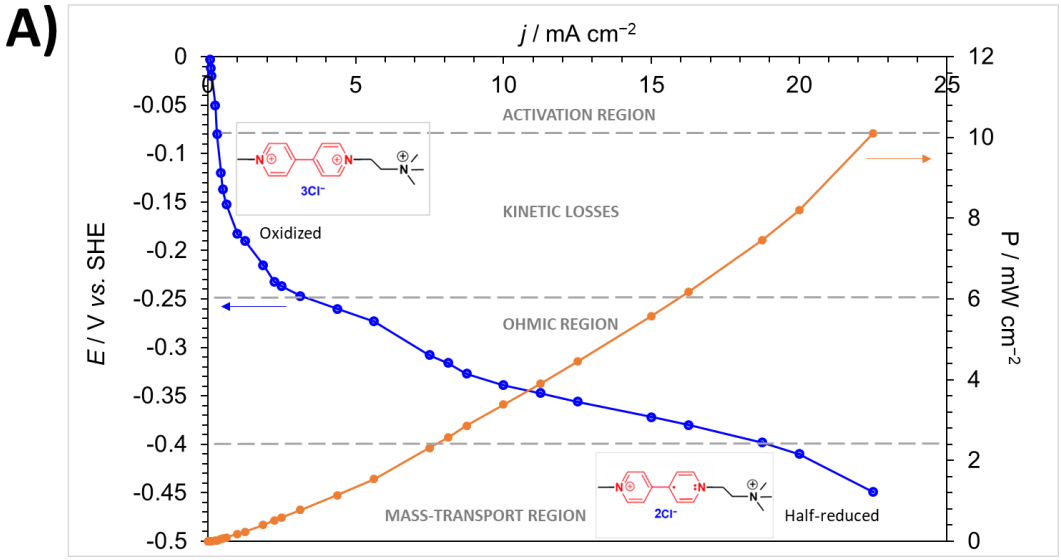

Figure 4.14 A) Charging polarization of 0% SOC MTABT (blue line and dots). In orange on the secondary y-axis, it is displayed the power in mW cm^{-2}. The porous felt electrodes had a geometric area of 8 cm^2. The polarization regions are depicted on the plot along with the fully oxidized and half-reduced forms of MTABT.

Subsequently, the flow cell was cycled galvanostatically at 25 mA of current (3.125 mA cm^{-2} current density), with upper cutoff potential of -0.10 V *vs*. SHE and -0.50 V *vs*. SHE as lower cutoff potential. The flow rate was 20 mL min^{-1}.

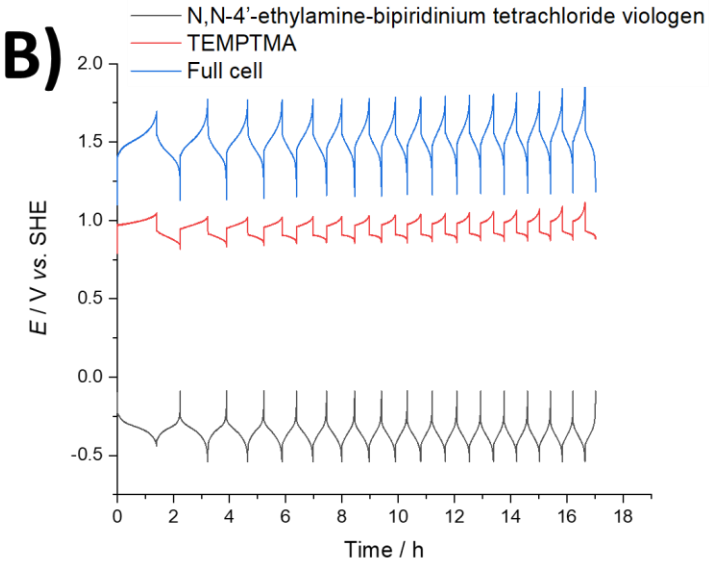

Figure 4.14 B) Potential vs. time ARFB configured with50 mM in 1 M KCl$_{aq}$. MTABT (black line) and 50 mM TEMPTMA in 1 M KCl$_{aq}$. (red line). The full cell is represented in blue line.

Figure 4.14B) shows the potential *versus* time of the electrolytes in the AORFB. It can be noticed almost at the second cycle the potential *vs*. time of the viologen electrolyte (dark line in ***Figure 4.14B)***) looks shorter and this trend is kept until at least the sixth cycle. After it seems stable. The same cycling behavior is observed at the TEMPTMA's side (red line in ***Figure 4.14B)***) and in the full cell (blue line in ***Figure 4.14B)***). This phenomenon could be due to decomposition of the electrolytes and most likely of the viologen. Interestingly, the capacity (for charge and discharge) follows a similar trend (***Figure 4.14C)***).

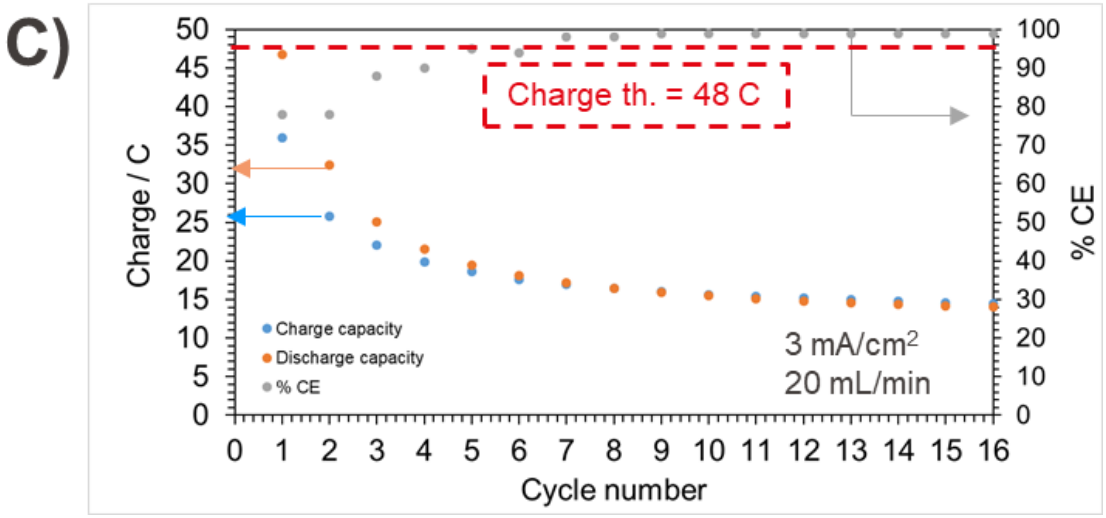

Figure 4.14 C) Charge and discharge vs. cycle number capacity of the AORFB equipped with 50 mM electrolytes. The charge capacity is represented as blue dots and the discharge capacity as orange dots. On the secondary y-axis the % CE is represented as grey dots.

The cell reached experimentally *ca*. 46 C of discharge capacity in the first cycle (96% of the theoretical charge, 48 C for 10 mL volume, 50 mM concentration and one electron transfer reaction), which decreased at the second cycle at *ca.* 26 C, corresponding to a loss of 54% as compared to the theoretical value. The discharge capacity decreased again at the third cycle, reaching *ca*. 23 C. At the last cycle (number sixteen) the discharge capacity reached *ca*. 16 C, which corresponds to three times less the theoretical value (48 C). However, despite the considerable initial capacity fade, the discharge capacity almost stabilizes around the fifth cycle until the end of the experiment. The % CE in ***Figure 4.14C)*** (on the secondary *y*-axis) shows a very similar trend to that of the discharge capacity.

A possible reason behind this significant capacity fade might be due to the fact that the radical-cation of the viologen can be readily oxidized back from molecular oxygen, decreasing the amount electrochemically active species in the reservoir which can react at the electrochemical cell. Importantly, despite this cycling experiment was performed in a nitrogen filled glovebag, it is not possible to completely exclude the presence oxygen from the working atmosphere. Once the reaction of the radical-cation with

molecular oxygen is completed, the remaining electrolyte continues to react regularly at the electrode surface and the equivalent cycling performances are stable over time.

Figure 4.14D) shows the efficiencies of the AORFB cycled with 10 mL of electrolytes at 50 mM. As for the capacity trend in ***Figure 4.14C)***, at the beginning of the cycling test the overall energy efficiency of the full system (blue line in ***Figure 4.14C)***) is around 35%; then after the 7th cycle (when any possible mechanism involving molecular oxygen is concluded) the energy efficiency rises up to ~80% and finally it reaches a constant value of 89% at the end of the experiment when probably all the oxygen in the system is consumed.

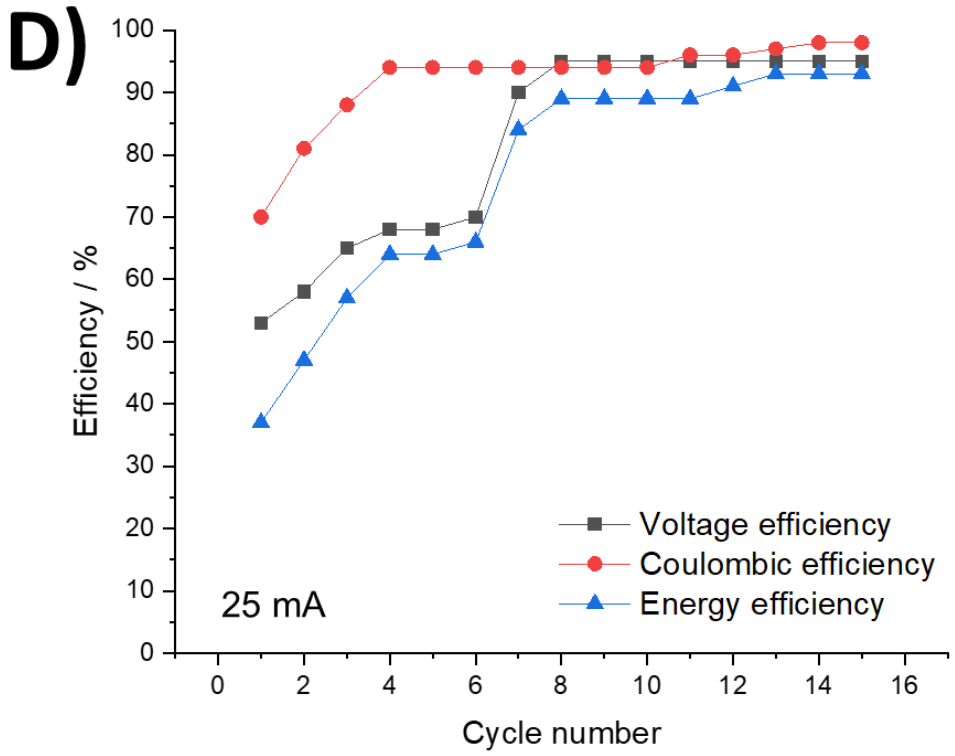

Figure 4.14 D) Efficiency plots (%VE in black, %CE in red and %EE in blue) of the AORFB having 50 mM in 1 M KCl_{aq} electrolytes at both sides.

<u>I) Preliminary investigation of O_2 permeation on the capacity fade and pH shift</u>

In order to explain such big capacity losses in the cycling test, an initial investigation of any possible decomposition mechanism in the electrolytes was performed. Primarily, the electrolytes pH was measured and interestingly it was found that TEMPTMA reached *ca*. pH 1 and the MTABT *ca*. pH 8.5.

In the case of TEMPTMA, acid-base equilibria in water were first considered as possible explanation to this pH behavior (***Figure 4.15A)***).

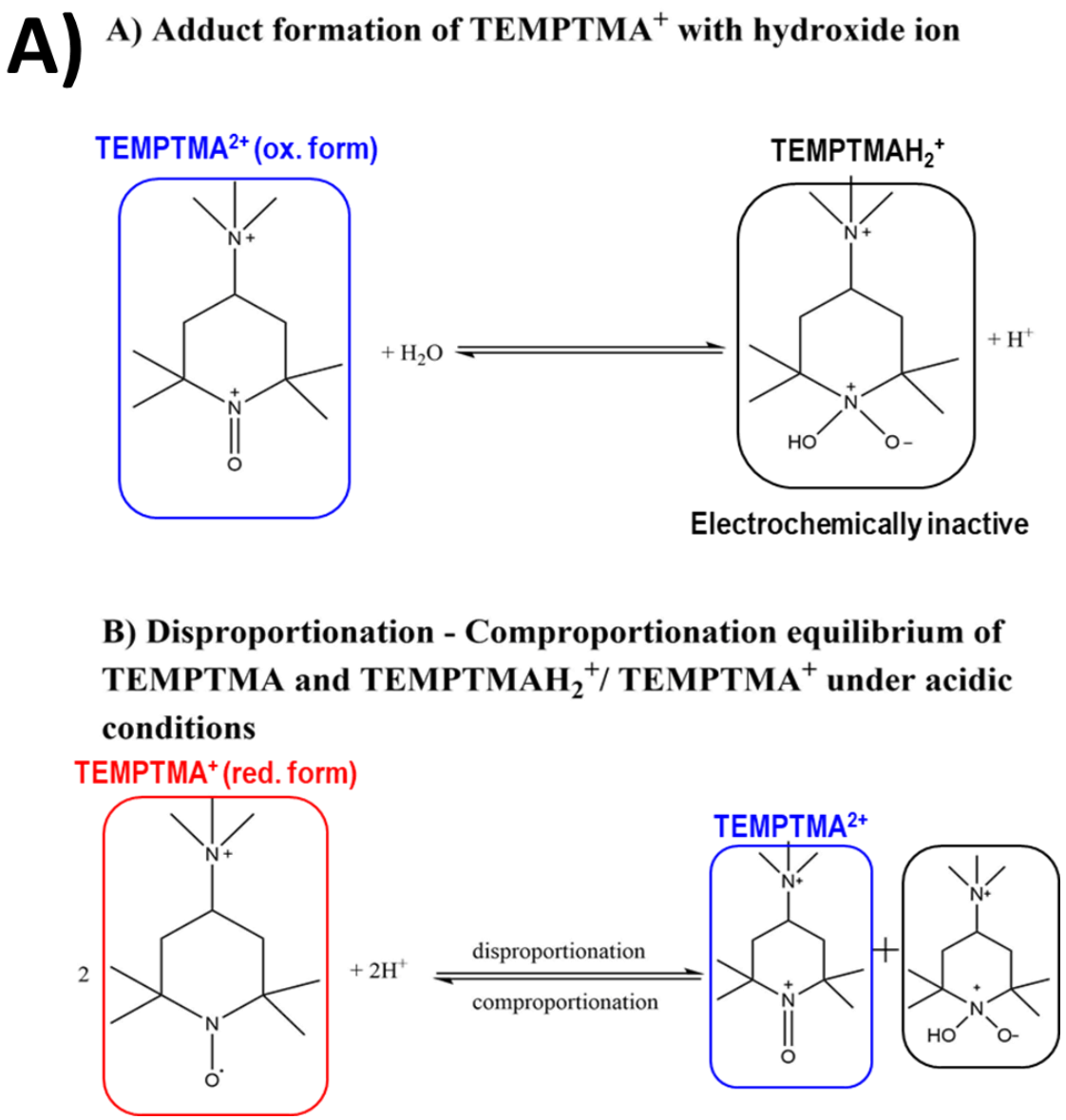

Figure 4.15 A) Schematic of possible acid-base equilibria of TEMPTMA in water and adduct formation under acidic conditions.

The schematic shows how the change in pH rises from protonation in water of the nitrogen atom of the N-oxyl group in TEMPTMA, generating an adduct TEMPTMAH-OH^+ that is electrochemically inactive (***step A in Figure 4.15A)***).[128] Then, under acidic condition the reduced form of TEMPTMA can undergo a disproportionation mechanism and form again the adduct TEMPTMAH-OH^+ along with the oxidized form $TEMPTMA^{2+\cdot}$((***step B in Figure 4.15A)***).[128] Subsequently, CV of the cycled TEMPTMA solution was recorded and compared with that of a fresh solution (***Figure 4.15B)***).

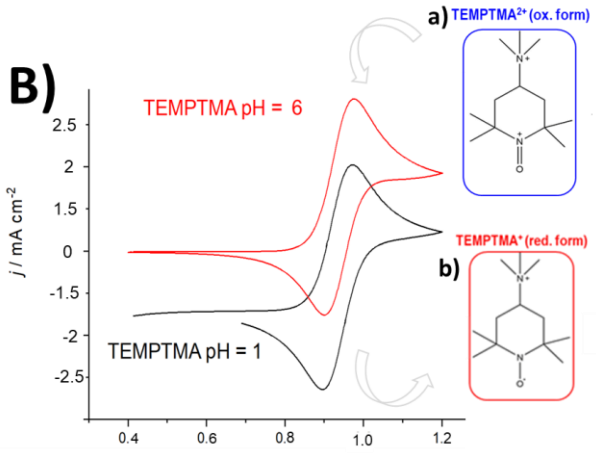

Figure 4.15 B) CV of TEMPTMA on GCE (0.071 cm^2) before (red line) and after (black line) the cell cycling. The concentration was 50 mM in 1 M KCl_{aq}. The CV were not iR drop compensated.

The voltammogram of TEMPTMA after cycling (black line in ***Figure 4.15B)***) shows a decrease in the anodic currents, reflecting a possible depletion of $TEMPMA^{2+}$ in the solution.[128] At pH 1 the cathodic current reaches a maximum value that is approximately half of the initial anodic current, indicating that the concentration of $TEMPMA^{2+}$ is half of the original $TEMPMA^+$ concentration. [128] In addition, it is possible to notice that the voltammogram does not start at zero, thus it could be possible that the electrolyte was unbalanced and more of the reduced form was in solution which needed to first be reduced. These results provide a possible correlation to the disproportionation of TEMPMA under acidic conditions shown in ***Figure 4.15A)***, since electrochemically inactive species could have been generated.

For the pH shift found in the MTABT's tank, it was supposed in agreement with Aziz and co-workers,[120] that the radical-cation in the solution can be readily oxidized back from molecular oxygen and contemporarily generate OH^- (see the mechanism proposed below, ***Figure 4.16***).

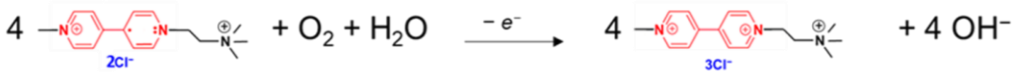

Figure 4.16 Possible mechanism of decomposition of MTABT responsible of shifting the pH to more alkaline values upon cell cycling.

II) Preliminary investigation of the capacity fade rate in absence of O_2

To investigate the cycling performance of the electrolytes when O_2 is strictly excluded, a preliminary test was performed in a H-cell battery placed in a nitrogen filled glove box and equipped with an anion exchange membrane and two graphite porous electrode felts. The battery was galvanostatically cycled at +1 mA of current (0.16 mA·cm^{-2} current density with 6.25 cm^2 graphite felt electrodes), with upper cutoff potential +1.10 V *vs*. SHE and lower cutoff potential +0.60 V *vs*. SHE. The battery was configured as three-electrochemical cell, with the reference electrode (Ag/AgCl in 3 M KCl_{aq}.), in the TEMPTMA's reservoir. The electrolytes were 50 mM in 1 M KCl_{aq}.in both sides with a volume of 6 mL *ca*. (the TEMPTMA's side had a little more to try to balance the number of Coulomb as compared to the 2 electron-storage of the viologen at the negative-side). Before any cell cycling, CV of the electrolytes were performed in the glove box (***Figure 4.17***), then the battery was cycled under constant stirring. The performances are reported in ***Figure 4.17*** and ***C)***. In this battery, the theoretical charge is 29 C (with 50 mM electrolytes and 6 mL volume in each tank), which was reached after 1 day of cycling at 1 mA of current. The overpotential for each redox reaction is *ca*. 50 mV, as depicted in ***Figure 4.17B)***, suggesting moderate ohmic resistance in the battery configuration.

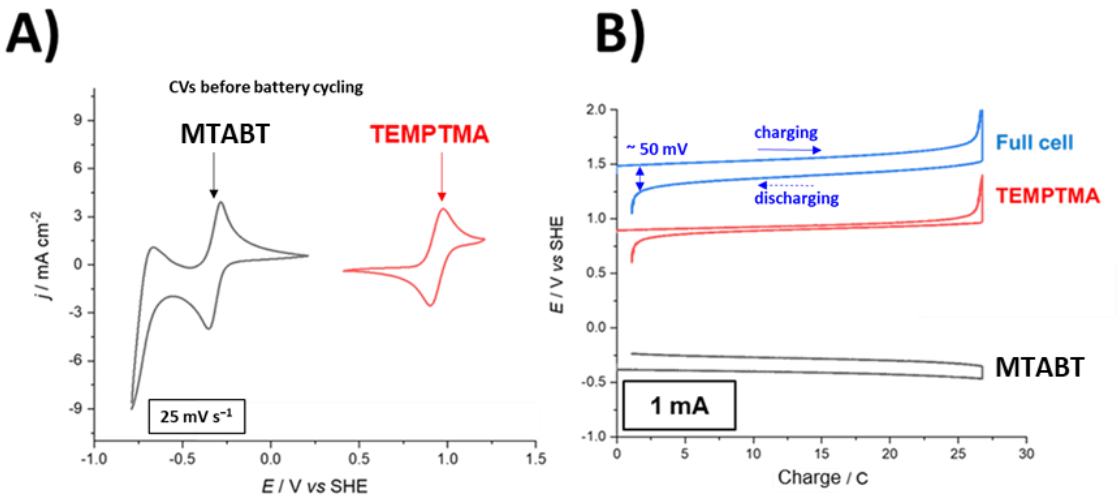

Figure 4.17 A) CV of the electrolytes at 50 mM in 1 M KCl_{aq} on GCE (0.071 cm^2), recorded in glove box before the battery cycling at 25 mV s^{-1} as sweep rate. The CVs were not iR drop compensated. B) Battery cycling (as H-cell configuration) at 1 mA of current: potential vs. charge of the full cell in blue, potential vs. charge of the TEMPTMA in red and potential vs. charge of the MTABT in black.

Then, CV of the cycled electrolytes after 1 day of cycling experiment were performed to check any change as compared to the fresh solutions (***Figure 4.18A)***). The measurements were recorded in the glove box as before the cycling test. ***Table 4.2*** summarizes the peak currents and peak potentials of these CV.

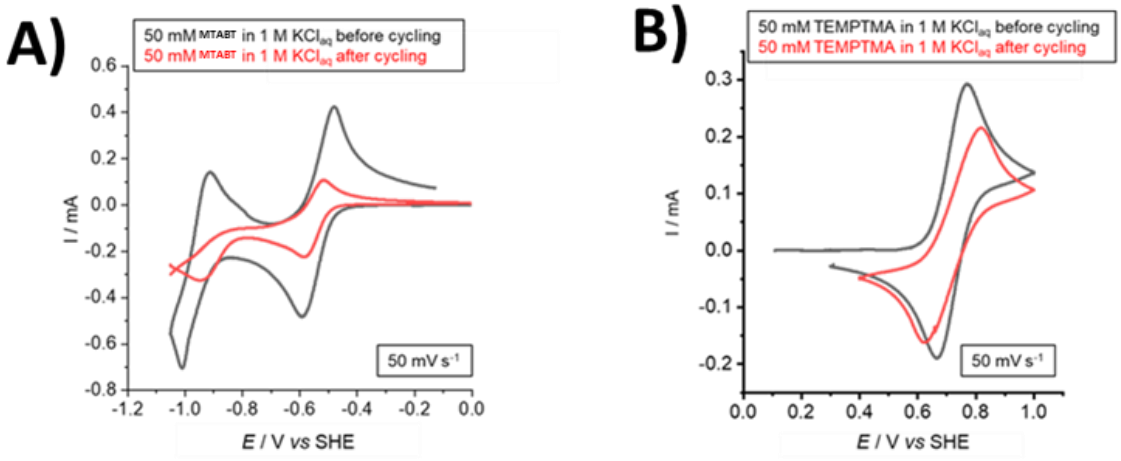

Figure 4.18 A) CV on GCE (0.071 cm^2) of 50 mM in 1 M KCl$_{aq}$ MTABT at 50 mV s^{-1} before (black line) and after (red line) battery cycling. B) CV on GCE of 50 mM in 1 M KCl$_{aq}$ TEMPTMA at 50 mV s^{-1} before (black line) and after (red line) battery cycling. The CV were not iR drop compensated.

Table 4.2 Peak currents (anodic and cathodic) and peak potentials (anodic and cathodic) for TEMPTMA and MTABT before and after battery cycling in glove box.

Electrolyte	$I_{p,a}$ / mA	$I_{p,c}$ / mA	$E_{p,a}$ / V *vs.* SHE	$E_{p,c}$ / V *vs.* SHE
TEMPTMA uncycled	0.27	-0.21	0.98	0.93
TEMPTMA cycled	0.21	-0.15	1.10	0.81
MTABT uncycled (1st wave)	0.40	-0.51	-0.41	-0.44
MTABT cycled (1st wave)	0.18	-0.23	-0.41	-0.44

It is interesting to see that despite the battery was operated in the glove box, where the presence of O_2 is strictly excluded, the electrolytes show signs of decomposition. Regarding the MTABT, the most probable decomposition mechanism is the dimerization reaction illustrated at the beginning of this chapter (see ***Figure 4.4***).

4.3.3 Conclusions on the investigation of the cycling performance of MTABT and TEMPTMA

In this section, a preliminary investigation of the cycling performance of the new viologen derivative (MTABT) along with TEMPTMA in an AORFB was accomplished. The full system (at a concentration of 50 mM in 1 M KCl_{aq} of both the electrolytes) placed in a nitrogen filled glovebag exhibited rather poor performances, with high capacity fading (*ca*. 54%) already at the second cycle. However, this cycling test was particularly inspiring to start an investigation (which is currently in progress) on the possible reasons behind the capacity fading in both the electrolytes. As first experimental proof, a considerable pH change of the electrolytes after the cell cycling was found. In particular, the TEMPTMA's solution reached very acidic pH (*ca*. = 1) and the viologen's slightly alkaline (pH = 8.5). In the case of TEMPTMA, acidic-base equilibria in water were considered, when either $TEMPTMA^{2+}$ or $TEMPTMA^{+}$ in presence of acids can generate an adduct ($TEMPTMAH\text{-}OH^{+}$) by disproportionation. This adduct is not electrochemically active. This mechanism was also supported by the comparison of the CV of TEMPTMA before and after the cell cycling, where a decrease of the anodic currents could have been a possible evidence of the fact that the concentration of $TEMPTMA^{2+}$ was less than the original $TEMPTMA^{+}$. [128]

In the case of the MTABT, the investigation was focused more on the role of molecular oxygen in the decomposition process. Indeed, despite the flow cell was cycled in a nitrogen filled glovebag, it is not possible to completely exclude the presence of O_2 from the working atmosphere, therefore, a possible interaction with the radical-cation which it is likely happening upon the cell charging. Interestingly, decomposition of MTABT was observed even in absence of O_2. In this case, the most probable mechanism of decomposition is a dimerization reaction, which suddenly leads to the fully oxidized and reduced species of the viologen. This mechanism is considered responsible of increasing capacity fade since the initial reactant concentration has changed. Finally, an investigation of the "effect" of the electrolytes on the porous graphite felt electrodes used in the battery cycling performed in glove box was evaluated. Unsurprisingly, both the electrolytes "stick" on the surface of the porous felts, and above all MTABT, probably because of the π-stacking interaction of the aromatic rings.

4.3.4 Future perspectives AORFB

As recently reported by Kwabi *et al*.[178], despite the numerous advantages (*e.g*. abundance of the raw materials, relatively low manufacturing costs, operation in cheap and safe supporting electrolytes, *etc*.), ROM are not fully chemically stable electrolytes at neutral pH. For the ROM presented in this work (TEMPTMA and MTABT), some strategies were matured to further proceed with the flow cycling tests. First, new experiments should be performed using a buffer in the supporting electrolyte, for example at pH 7 or 7.5, in order to mitigate the pH shift observed during cycling. Second, all new cycling tests should be performed in absence of O_2, for instance, in glove box. Importantly, this aspect should be carefully considered in the entire design of the RFB, choosing appropriate materials for the cell to avoid extra permeation. Third, the MTABT can be chemically modified to have a symmetric molecule in terms of N-alkyl substituents. More precisely, ethyl can be better than methyl to mitigate the dimerization mechanism (happening in absence of O_2), due to increased charge repulsion by two additional positively charged ethyl ammonium pendent arms.[179] Unfortunately, working at neutral pH limits the choice of electrolyte candidates for the negative-side of the RFB. Although, a couple of alternatives can be proposed:

i) Polymer electrolytes, such as in the work proposed by Janoschka *et al*.[50], where almost no capacity fade was observed (10 Wh L^{-1} energy density, current densities of up 100 mA cm^{-2} and stable long-term capability)[50]

ii) Modify the pH of the aqueous supporting electrolyte to be in the range of 9-12. This would require to reconsider the choice of the viologen (and derivatives) in the electrolyte.

In this case, Aziz and co-workers[180] again proposed an interesting work, where a highly stable phosphonate-functionalized anthraquinone was introduced as the negative-side electrolyte.[180] They authors successfully demonstrated by pairing a phosphonate-functionalized anthraquinone with a potassium ferri/ferrocyanide at the positive-side, an AORFB with a cell voltage of 1.0 V and a capacity fade rate of 0.00036% per cycle and 0.014% per day, which is the lowest ever reported for any flow battery in the absence of rebalancing processes. [180]

4.4 Research of candidate solid boosters for the MTABT electrolyte

As for the positive-side with TEMPTMA and CuHCF, the aim for the negative-side is to find a solid booster candidate to couple. Indeed, the ultimate goal is to propose a full "redox-mediated flow battery" made of ROM capable of reaching enhanced capacities and operating in mild chemical conditions (*e.g.* safe supporting electrolytes such as KCl_{aq} or $NaCl_{aq}$ at neutral pH). Consequently, the search of the solid booster was done following these motivations. In addition, the idea is to keep the electrolyte cost rather low, with the perspective of scale-up. In good agreement with this statement, once again organics make potential access to low cost and greener chemistry possible because they are mainly composed of C, H, O, N, and S, which are naturally abundant elements as well as the main constituents of biomass.[181] Material made of such elements are for instance polymers, as also seen in the second chapter of this manuscript discussing about PANI and others.

Poizot *et al.* [181] have recently made a very interesting review of safe materials for sustainable storage applications. In this work, several naturally occurring polyphenols (*e.g.*, ellagic acid[182], purpurin[183]) were electrochemically assessed in Li/Na half cells; but, the proof of concept of realizing a "renewable" all-organic LIB was first demonstrated with oxocarbon derivatives as active electrode materials almost ten years ago. [181] Importantly, PPy, PANI and polyimides have attracted considerable attention in this context too.[184] Indeed, they are frequently used for their facile synthesis and redox properties, showing redox potentials around −0.8 to +0.3 V *vs*. SHE.[184] According to Kim *et al.*,[184] one of the first aqueous rechargeable LIB was demonstrated using PPy at the negative-side and $LiMn_2O_4$ at the positive-side, in a saturated solution of Li_2SO_4 at pH 7.[184] In this system, lithium ions were released in and out of the PPy *via* a "doping" and "de-doping" mechanism at an average potential of −0.026 V *vs*. SHE.[184] The study revealed that cycling performances of polymers might be better than those of polyanionic materials (*e.g.* TiP_2O_7). [184] Wang *et al.* [185], discuss the cycling performances of TiP_2O_7 in a LIB system and they show that the material exhibits irreversible capacity losses of 20 $mAh{\cdot}g^{-1}$ since the first cycle.[185] TiP_2O_7 intercalates/de-intercalates lithium ions in a potential range of +0.30 V and −0.70 V *vs*. SHE[185] (at neutral pH), which is very close to hydrogen evolution reaction (*ca.* −0.70 V *vs*. SHE)[185]

4.5 Polyimides

Among negative-side materials and polymers frequently employed in aqueous rechargeable solid-state batteries[185], polyimides are considered promising candidates, since they are mechanically strong and thermally stable. [186] [187] Song *et al.*,[186] have made an interesting review of polyimides as energy storage materials for building "sustainable batteries", as also discussed by Tarascon and co-workers.[188]

Redox activity in polyimides foresees that during the charging process in the presence of *mono*-cations (*e.g.* K^+, Na^+ [187], Li^+)[184] [189] an enolate group is generated through electrostatic attraction with simultaneous charge redistribution throughout the conjugated polymeric structure (***Figure 4.19***).[184] Then, upon discharging, intercalated *mono*-cations dissociate from the carbonyl group rebuilding the ketone for another cycle.

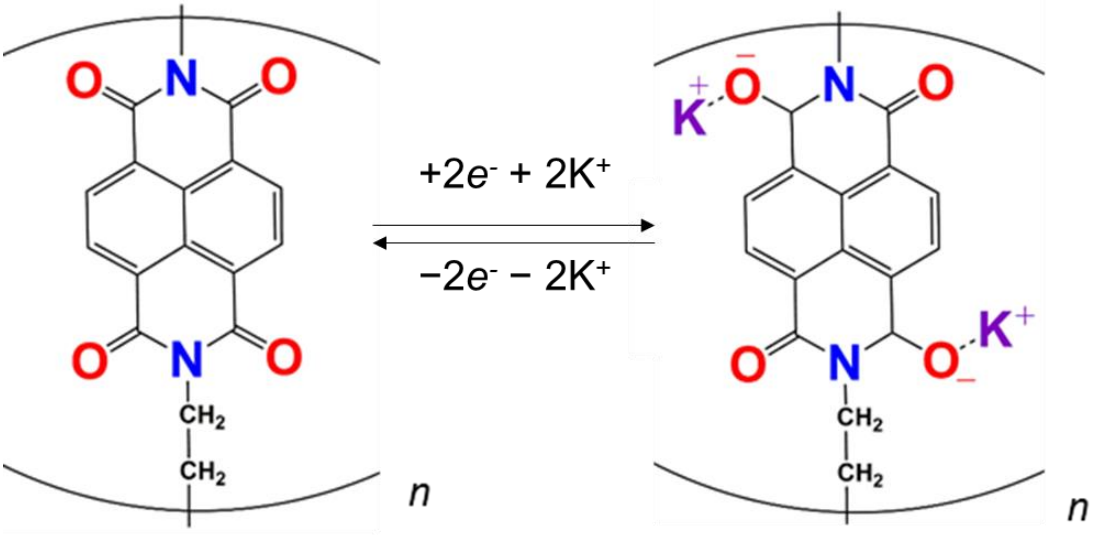

Figure 4.19 Enolisation mechanism in polyimide PNTCDA in presence of K^+ ions.

In polyimides, enolisation on a flexible polymer backbone can ensure better structural stability over repetitive cycles, since the charge can be re-distributed all over the aromatic ring on the polymer structure.[184] Ideally polyimides should allocate four cations (accompanied by four electrons) during the enolisation reaction (reduction or charging), through two steps mechanism,[186] however, they likely undergo a two-electron and two-cation redox process, to minimize either the steric hindrance or the charge repulsion in the molecular structure. [186]

Recently, Wang *et al.*[189] proposed an interesting work on the characterization of polyimide (PNTCDA) and evaluation of its structural properties. In particular, the authors used first-principles calculations to study the adsorption, diffusion and storage capacity of cation ions in the PNTCDA chain and bulk crystal, as well as the modification of the geometric structure and electronic properties induced by

the ion insertion. [189] The authors found optimized lattice parameters of bulk PNTCDA (in this case, it was considered as if the polymer has a crystalline structure in order to compute the simulations) of AA stacking type (***Figure 4.20***, a) = 10.623 Å, b) = 9.497 Å, c) = 9.293 Å, α = 120.37°, β = 84.16°, and γ = 55.33°),[189] and additionally, that the enolisation mechanism leads to small lattice contraction ratios of only −1.68% for Li, −0.37% for Na, and −0.56% for K, during charge/discharge processes. [189]

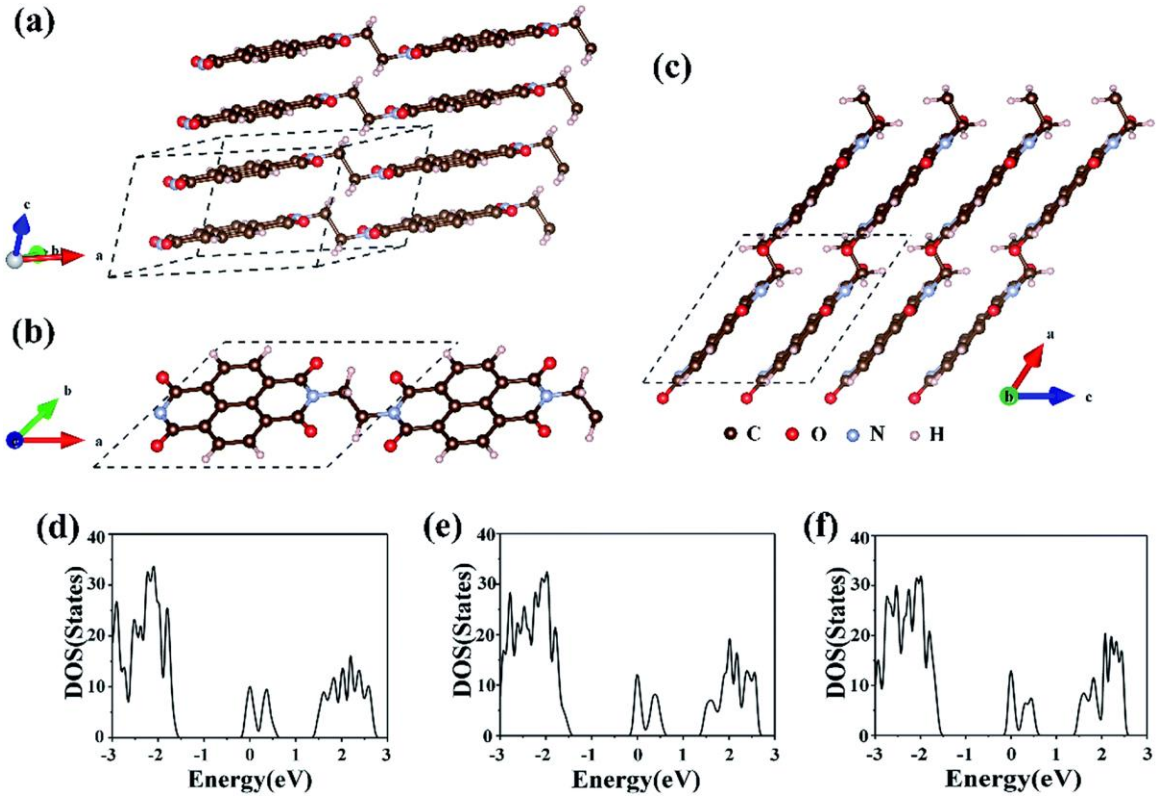

Figure 4.20 a) The three-dimensional structure of bulk PNTCDA, and b) top and c) side views in bulk PNTCDA. The electron density of states (DOS) for a d) Li, e) Na, f) K atom inserting into the bulk PNTCDA. The energy at the Fermi level is set to zero. This image is reproduced with permission from the work of Wang* et al.*[189]. Copyright 2020, Royal Society of Chemistry.

Furthermore, the same authors[189] claim storage capacities of 366 mA h g^{-1} (Li), 366 mAh·g^{-1} (Na), and 183 mAh·g^{-1} (K) of PNTCDA, rather comparable to those of inorganic materials. Polyimides are generally synthesized by a facile method, which consists of a polymerization reaction from the monomer precursor in organic solvent under inert atmosphere. This can be considered as another advantage to scale-up the manufacturing process of these materials for safe grid-level energy storage installations.

In the present work, a polyimide from the 1,4,5,8-naphthalenetetracarboxylic dianhydride (PNTCDA) was synthesized as candidate solid booster to be paired with the MTABT as RM, at the negative-side the neutral pH AORFB. Pristine PNTCDA was electrochemically characterized confirming the storage mechanism with enolisation mechanism observed in the literature and later to mitigate its electronic insulation an *ex-situ* composite with CNTs was synthesized, showing encouraging electrochemical performances. Finally, the viability of pristine PNTCDA solid booster in presence MTABT as RM was preliminarily assessed by scanning electrochemical microscopy (SECM).

4.5.1 PNTCDA in the present approach with MTABT as RM

Polyimide from the 1,4,5,8-naphthalenetetracarboxylic dianhydride was selected among other polyimides because of its facile synthetic route, robustness and most of all since it shows two redox potentials which nicely match those in the MTABT. The following ***Table 4.3*** summarizes the values of the half-wave redox potentials of PNTCDA and of MTABT for the first redox reaction only, which corresponds to the studied reaction.

Table 3.3 Comparison of the half-wave redox potentials of the solid booster PNTCDA and of the RM MTABT, according to the "redox-mediated" approach of the charge transfer.

Redox materials	$E_{1/2}$ **/ V *vs.* SHE**	***Condition***
MTABT (RM) (first electron transfer reaction)	-0.33	1 M KCl_{aq} at pH 6
PNTCDA (SB) (first electron transfer reaction)	-0.18	1 M KCl_{aq} at pH 6

Despite PNTCDA is a two-electron storage compound[175], it will be used in this work just as one to target the first electrochemical potential of the MTABT. The reason behind this choice is because the second electron transfer mechanism of the viologen is not electrochemically reversible,[127] as it leads to a neutral state that likely precipitates in the solution.

The alignment of the half-wave potential for this candidate pair of materials looks quite good, the small overpotential difference (15 mV) should guarantee the charge transfer process with no particular issues. ***Figure 4.21A)*** and ***B)*** show a graphical representation of the role of PNTCDA solid booster coupled with MTABT in the aqueous electrolyte of "redox-mediated flow battery".

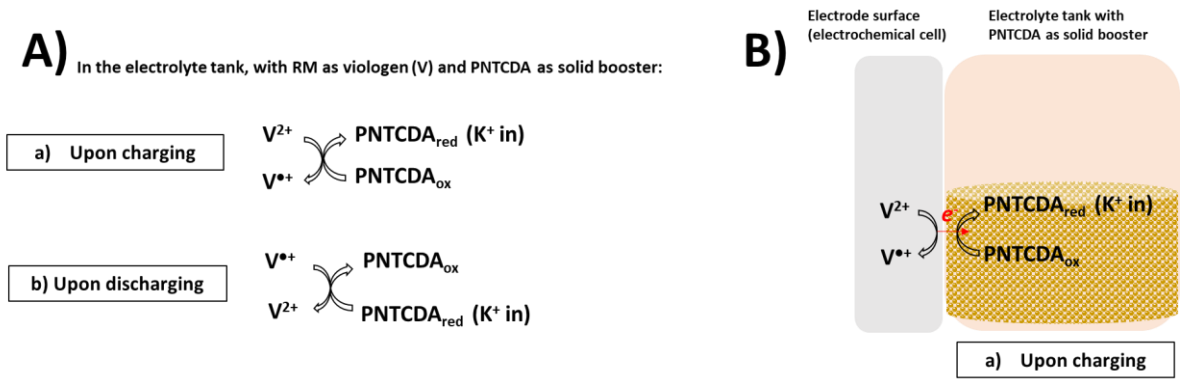

Figure 4.21 A) and B) redox reactions of viologen and PNTCDA solid booster in the electrolyte according to the "redox-mediated" charge transfer approach.

In addition, in order to show the viability of the PNTCDA as solid booster in the MTABT solution, a brief calculation can be done knowing the theoretical capacity of the materials.

Assuming an initial MTABT solution of 1 M, the equivalent volumetric capacity is 26.8 Ah L^{-1} (for one electron transfer reaction). Then, knowing the theoretical capacity of PNTCDA as 183 mAh g^{-1} [189] and its density (1.3 g mL^{-1}, experimentally measured), the volumetric capacity is 237.9 Ah L^{-1}, which is almost 9 times the volumetric capacity of the MTABT electrolyte alone.

Then, assuming a system made 50% from the PNTCDA booster and 50% from the viologen electrolyte, the final volumetric capacity will be 132.3 Ah L^{-1}, which corresponds to 5 times the volumetric capacity of the MTABT electrolyte alone. This simple calculation shows the potential of this approach once again, considering PNTCDA as solid booster.

4.6 Results and Discussion about PNTCDA solid booster

4.6.1 Characterization of pristine synthesized PNTCDA

Polymer of 1,4,5,8-naphtalenetetracarboxilicdianhydride (PNTCDA), was synthesized *via* a facile method described in the experimental section of this work (chapter 5). The pristine powder was first characterized by ^{1}H NMR (***Figure 4.22A)***) and ^{13}C solid-state NMR (***Figure 4.22B)***).

^{1}H NMR spectrum confirmed the molecular structure of the synthesized PNTCDA: at ~ 1 ppm the chemical shift of the protons belonging to the –NH_2 groups can be found; from ~ 2 to ~ 2.7 ppm the chemical shift of the protons in the ethyl bonds connected to the aromatic N atom, and finally at *ca*. 8.8 ppm the chemical shift of the protons in the aromatic ring. The chemical structure of the molecule on the spectrum confirms the exact correlation between each proton and each chemical shifts.

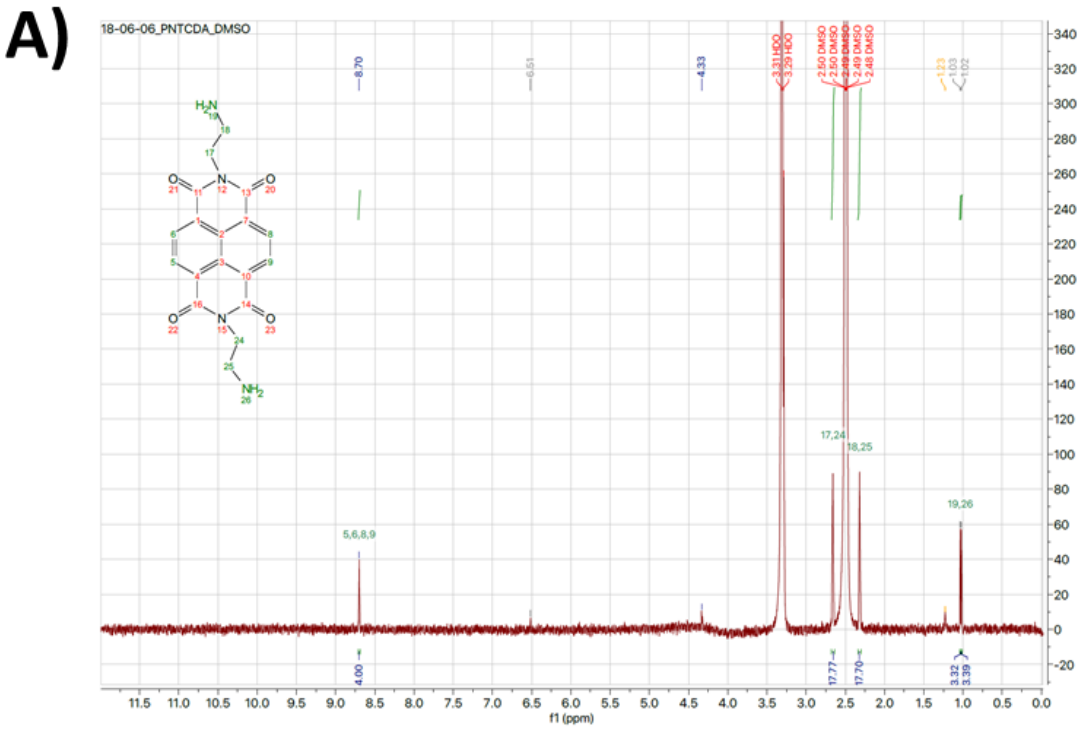

Figure 4.22 A) ^{1}H NMR spectrum of the synthesized PNTCDA powder. The NMR solvent is DMSO, 400 MHz): δ (ppm) = 1.02, (s, 3 H), 2.4 (s, 17 H), 2.6 (s, 17 H), 8.70 (s, 4 H).

Subsequently, solid-state ^{13}C NMR of the synthesized PNTCDA confirmed again the molecular structure; the chemical shifts at high field (40 ppm) belongs to C atoms of the alkane chains in between the monomer unit. Then, the chemical shift at low field (120-180 ppm) corresponds to the C atoms on the aromatic rings.

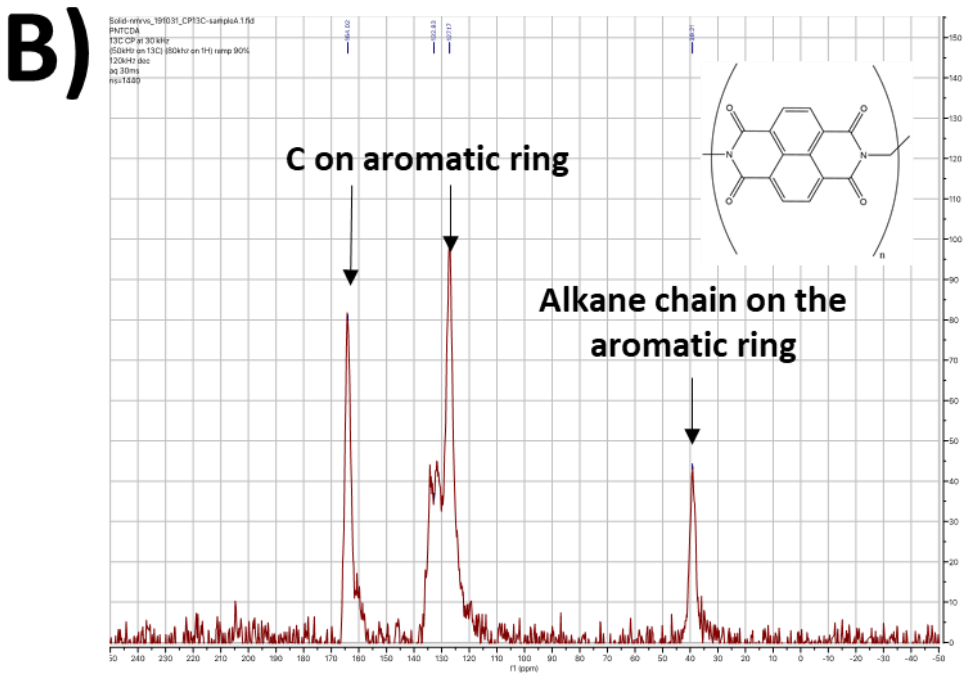

Figure 4.22 B) ^{13}C solid-state NMR spectrum of the synthesized PNTCDA powder at 30 kHz.

Then, PNTCDA was also characterized by FTIR (***Figure 4.22C)***) and SEM (***Figure 4.22D)***). The attribution of the peaks is depicted on the spectrum directly in this case.

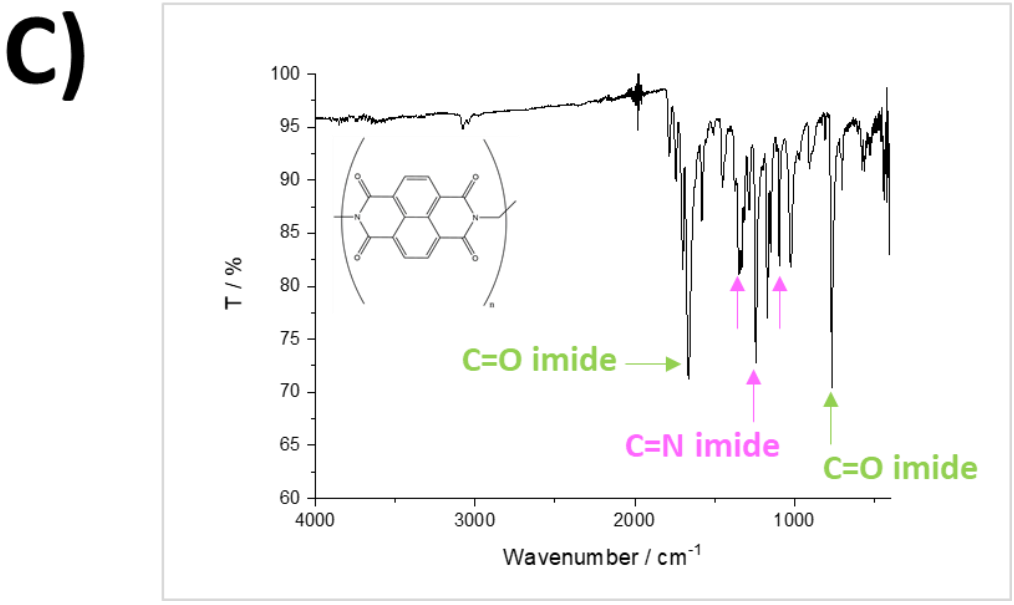

Figure 4.22 C) FTIR spectrum of the synthesized PNTCDA.

Finally, SEM images of pristine PNTCDA powder was recorded using in-lens detector, (***Figure 4.22D)***). The polymer looks as an agglomeration of amorphous clusters.

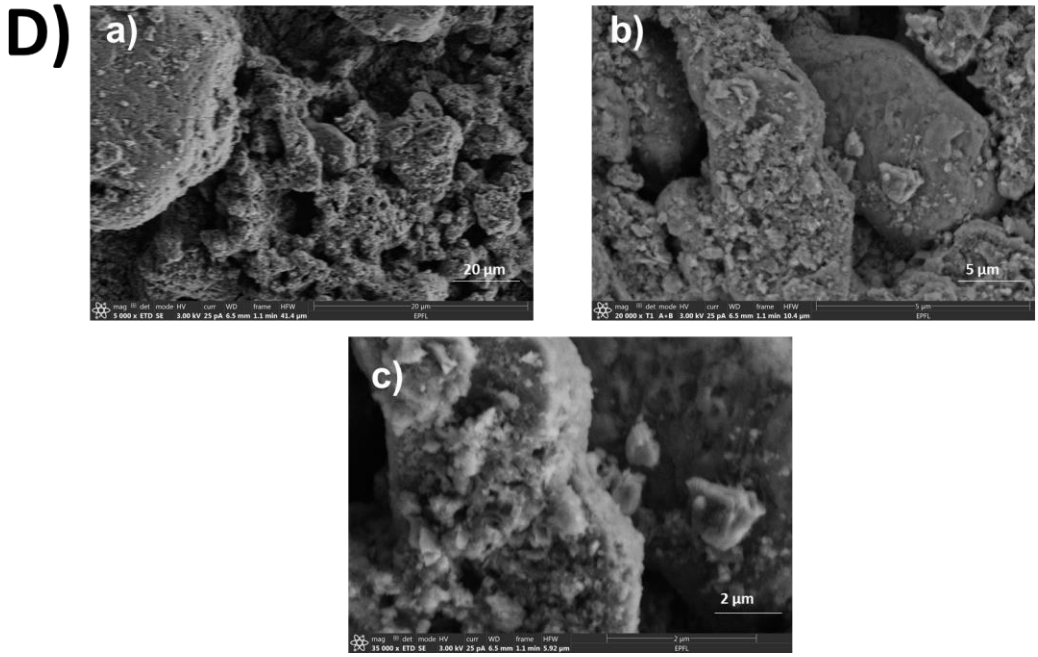

Figure 4.22 D) SEM images of pristine PNTCDA powder recorded using in-lens detectors: a) (20 µm, 3 kV, 25 pA), b) (5 µm, 3 kV, 25 pA), c) (2 µm, 3 kV, 25 pA).

4.6.2 Electrochemical characterization of pristine PNTCDA in 1 M KCl_{aq}

CV of pristine PNTCDA film drop-casted on GCE was recorded in 1 M KCl_{aq} in anaerobic conditions (***Figure 4.23A)***). The CV of pristine PNTCDA shows two main redox pairs at $E^{1/2}$ −0.18 V and −0.49 V *vs*. SHE. The experimental section dedicated to this chapter explains how the PNTCDA film was prepared on the surface of the GCE.

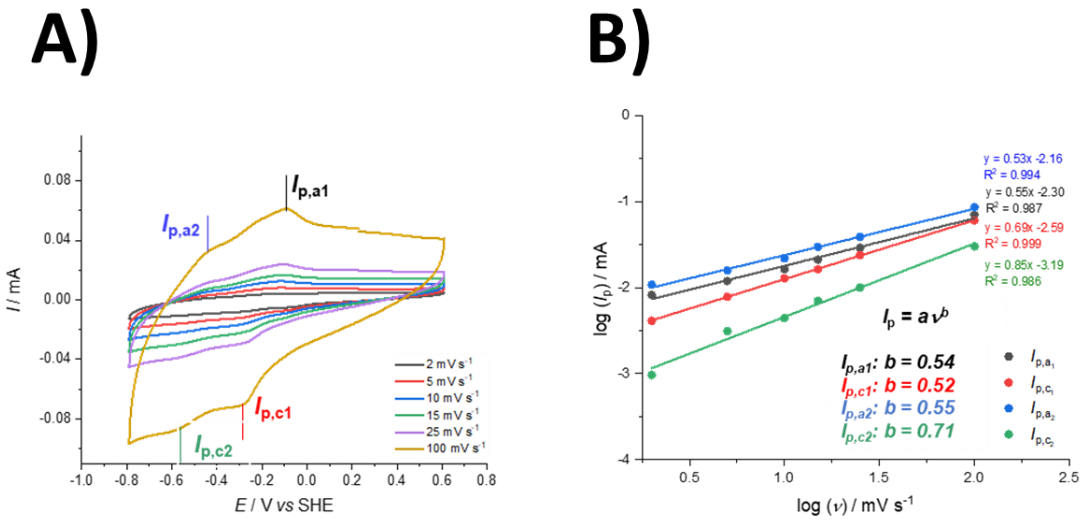

Figure 4.23 A) CV in 1 M KCl_{aq} of PNTCDA film drop-casted on GCE at 2, 5, 10, 15, 25 and 100 mV s^{-1}, respectively. The CV were recorded after purging the solution for 1 hour with nitrogen and they were not iR drop compensated. The anodic and cathodic peak currents for the two redox waves are marked on the plot as Ip_{a1}, Ip_{c1} and I_{pa2} and Ip_{a2}, Ip_{c2}, respectively. B) Logarithm of the sweep rate vs. logarithm of the peak currents for the CV in A). The relation $I_p = a \cdot \nu^b$ allowed to find the parameter b for all the peak currents (0.54 for Ip_{a1}, 0.52 for Ip_{c1}, 0.55 for Ip_{c2} and 0.77 for Ip_{c2}, respectively).

The peak currents and the sweep rates in the CV of PNTCDA (***Figure 4.25A)***) follow a linear fit according to the power-law relationship ($I = a \bullet \nu^b$). Dong *et al.*[190] explained that for a redox reaction limited by semi-infinite diffusion, the peak-current varies with ν (which means b = 0.5); then, for a capacitive process $\nu^{\frac{1}{2}}$ varies with ν (which means b = 1).[190] For the present case, the values of b suggest a diffusion-limited process of K^+ ions through the PNTCDA film on the GCE surface from the bulk of the solution.

4.6.3 Galvanostatic cycling of pristine PNTCDA in 1 M KCl_{aq}.

In the present case, pristine PNTCDA film on GCE in 1 M KCl_{aq} exhibited an experimental gravimetric capacity of 35.25 $mAh \cdot g^{-1}$ at 140 $\mu A \cdot cm^{-2}$ (10 µA) with a CE equal to 79%, obtained after 10 cycles (***Figure 4.24***). This experimental gravimetric capacity was calculated taking into account the whole amount of PNTCDA mass (24 µg) deposited onto the geometric area of the GCE (0.071 cm^2) from the initial concentration of the ink. Such low gravimetric capacity as compared to the theoretical value (183 $mAh \cdot g^{-1}$)[189], can be justified considering the rather small surface coverage, calculated from the integration of the anodic faradaic currents obtained from the CV recorded before this cycling test (0.039 µmol cm^{-2}).

In addition, a possible lack in the electronic conductivity[184] of the pristine PNTCDA film might be another issue of such low capacity value.

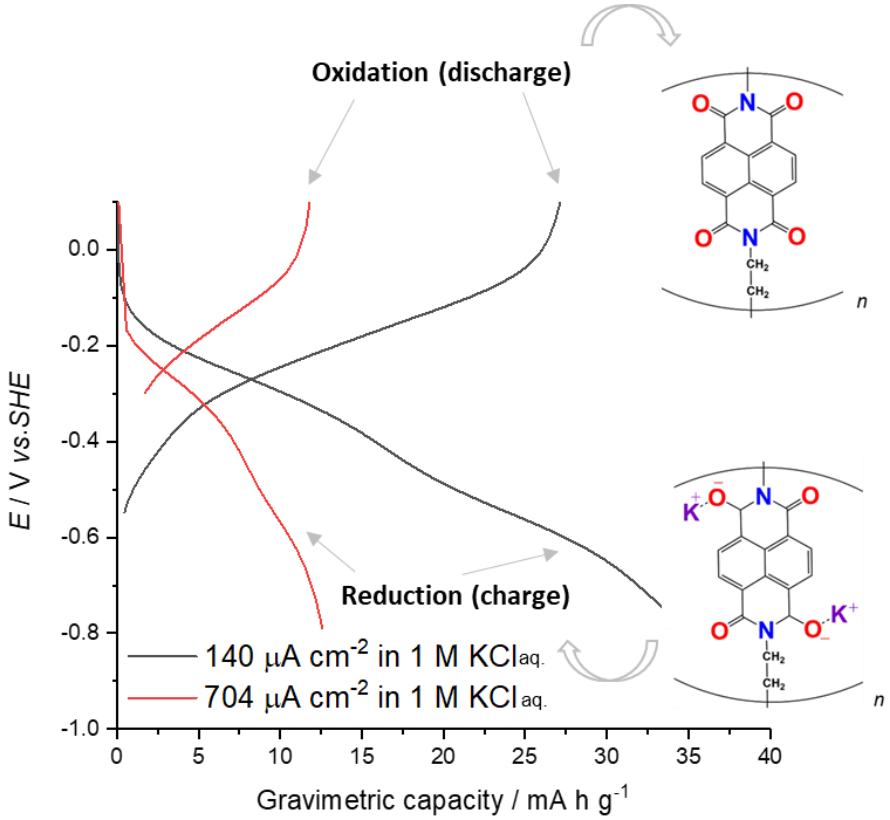

Figure 4.24 Galvanostatic cycling of PNTCDA film drop-casted on GCE in 1 M KCl_{aq} purged solution at 10 µA (140 µA cm^{-2}) and 50 µA (704 µA cm^{-2}) of currents (and of current densities). The gravimetric capacity on the y-axis was found knowing the mass of pristine PNTCDA drop-casted on the geometric area of the GCE ($2.4 \cdot 10^{-5}$ g). The corresponded oxidized and reduced PNTCDA species are reported on the plot for the respective charging (reduction) and discharging (oxidation) process.

Interestingly, from both the galvanostatic cycling in ***Figure 4.26***, in the reduction reaction (charge) of the polymer two plateaus can be spotted (around -0.25 V *vs*. SHE and -0.50 V *vs*. SHE), but this is not evident in the oxidation (discharge) reactions. This might suggest different kinetics in the two mechanisms. Indeed, upon charging, we could imagine the bonding of the two potassium ions as two consecutive separate steps (one after the other), which could explain the two plateaus. Then, upon discharging the re-organization of the molecular structure might be just one step mechanism. Interestingly, this type of behavior isn't in agreement with similar cycling performances of PNTCDA in aqueous solution containing K ions. In particular, Wang *et al*.[191] develop a negative-side PNTCDA battery material and they electrochemically tested its performances in a saturated solution of KNO_3. The cycling test shows two plateaus in the charging and discharging process. Therefore, considering this last work proposed by Wang *et al*.[191], another possible explanation to the experimental results obtained from the galvanostatic cycling, could be that supporting electrolyte solution was not enough concentrated.

Notably, performing the same type of electrochemical characterization (CV) and galvanostatic cycling in a solution of saturated KCl, very different results were obtained (***Figure 4.25A)*** and ***B)***). Interestingly, the mass of the PNTCDA on the GCE was as before equal to 24 μg, but this time the experimental gravimetric capacity is *ca*. two times as compared to the values obtained in 1 M KCl_{aq}.(35 $mAh \cdot g^{-1}$). These last results can confirm that the amount of K^+ ions in the supporting electrolyte solution is significant on the practical amount of gravimetric capacity achievable upon galvanostatic cycling tests. For the present work, the goal is to develop the booster in an aqueous solution, thus, the saturated KCl is not used in further experiments.

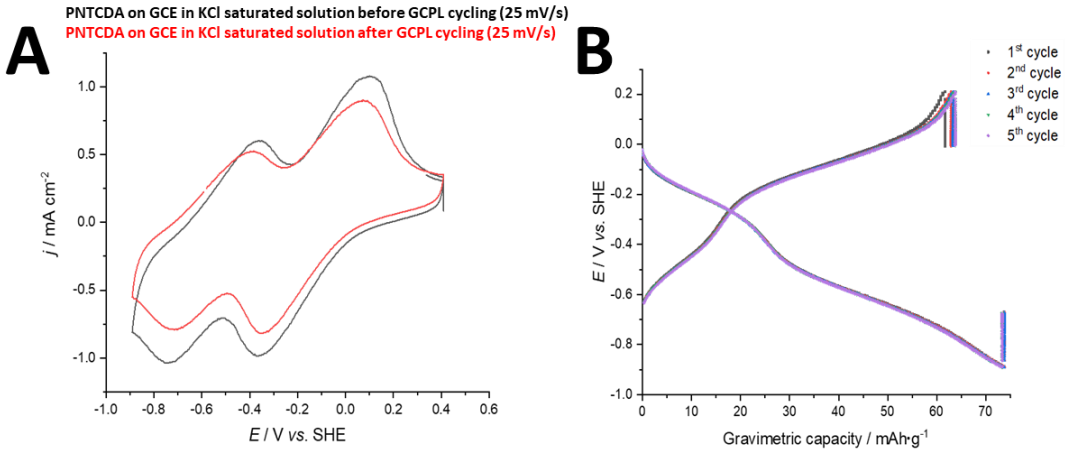

Figure 4.25 A) CV on GCE (0.071 cm^2) in a saturated solution of KCl at 25 mV/s. The measurements were performed after purging the solution for 1 hour with nitrogen. The CV were recorded without iR drop compensation. B) Galvanostatic

cycling of PNTCDA film drop-casted on GCE in a saturated solution of KCl, at 10 μA (140 μA·cm^{-2}). The mass of the active PNTCDA material was in this case 24 μg and it is used to normalize the gravimetric capacity on the x-axis.

To see whether the PNTCDA capacity behavior was affected also by any lack in the electronic conductivity, an *ex-situ* composite with CNTs was easily synthesized and characterized electrochemically. The goal was to use CNTs as conducting addictive to interconnect particles of PNTCDA to enhance the whole cycling performances in the aqueous KCl solution.

4.7 Ex-situ composite of PNTCDA with CNTs

Composite materials of PNTCDA with CNTs are largely investigated in the literature[192] [193] [194] [195] [196], and one interesting example is proposed by Manuel *et al*.[192] (***Figure 4.26***).

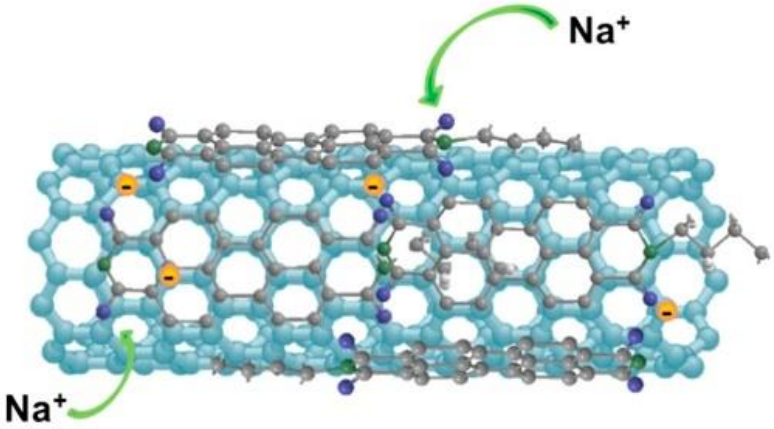

Figure 4.26 Representation of the structure of the composite PNTCDA with CNTs from the work of Manuel et al. at ref [192]. This image is reproduced with permission from the work of Manuel et al. at ref. [192]. Copyright 2020, American Chemical Society (ACS).

In this work, the authors suggest the synthesis of the composite of PNTCDA with CNTs by a two-step imidization process. [192] The cycling performance of this composite are really remarkable, in particular, the rate capability of the cell with the PNTCDA/CNTs nanocomposite electrode was examined at 0.1, 0.2, 0.5, 1, 2, 5, and 10 C-rates consecutively, and high initial discharge capacities of 125, 123, 120.8, 115.6, 112, 108.5, and 98.3 mAh·g^{-1} were obtained, respectively in 1 M $NaClO_4$ in EC/PC/DME (1:1:1 volume ratio). [192] Undoubtedly, the use of CNTs as a conductive and high strength filler into polymer hosts has attracted great attention[193], however, in order to achieve a final composite with the polymer where the conductivity is higher than in the pristine form and the structure mechanically more stable, the integration of the CNTs has to be effective. [193] Indeed, the ultimate goal is to produce a highly conductive thin film at low CNT's loading and reach a level of electrical conductivity high enough for electromagnetic interference shielding and to prevent electrostatic charge. [193] Importantly, also according to the type of application,

Thuau[193] discusses that it is desirable to have very low percolation thresholds of CNTs into the polymer structure; indeed, the lowest filler concentration required (*i.e*. connected network that provide mechanical backbone and a conductive pathway through the polymer) for electrical conductivity and mechanical strength increases. [193] In agreement with this idea, Thuau[193] proposes a composite of polyimide with CNTs, where the mechanical and electrical properties of the polymer are enhanced with the addition of 5% wt. CNTs. [193] The resulting electrical conductivity of the composite increased 12 order of magnitudes as compared to the pristine form of the polymer. [193] In the author's opinion, the conductivity follows a percolation-like power-law relation, with a percolation threshold of 0.15 wt. % CNTs for the composite. [193]

4.7.1 Characterization of the ex-situ composite of PNTCDA with CNTs

An *ex-situ* composite of PNTCDA with MWCNTs was synthesized as described in the experimental section of this work (chapter 5). The optimized weight ratio was 25% for CNTs and 75% for PNTCDA. SEM images (***Figure 4.27***) show the interlacing network of the CNT into the amorphous structure of the PNTCDA.

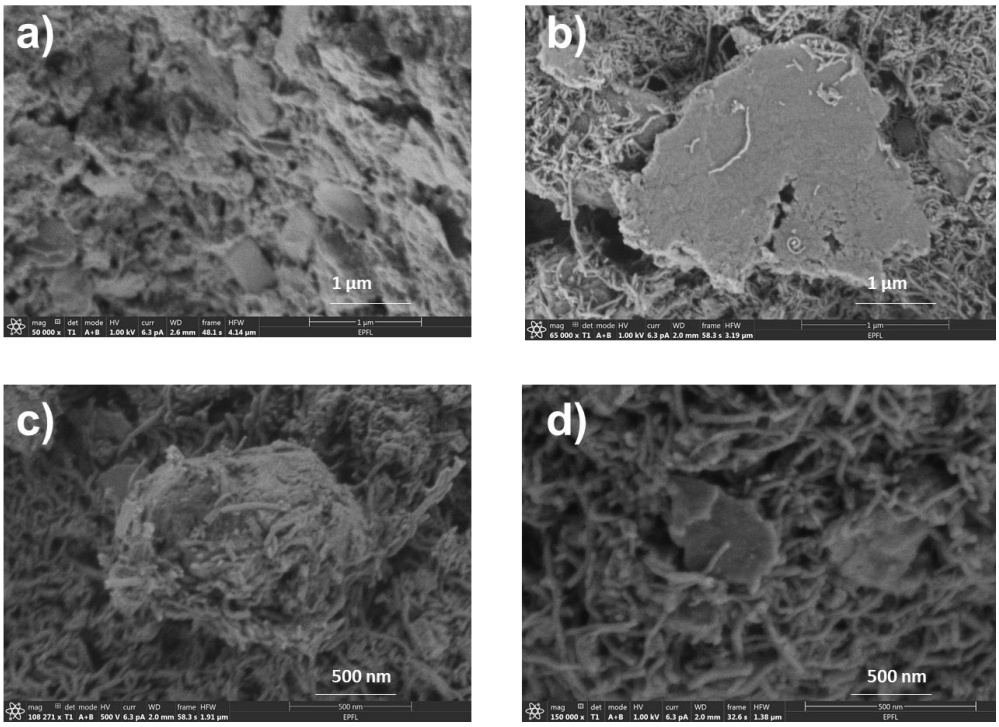

Figure 4.27 SEM images of the composite of PNTCDA with CNTs (75-25) wt.%. recorded using in-lens detectors: a) (1 µm, 1 kV, 6.3 pA), b) (1 µm, 1 kV, 6.3 pA), c) (500 nm, 500 V, 6.3 pA) and d) (500 nm, 1 kV, 6.3 pA).

As in the case of pristine PNTCDA, the CV of the *ex situ* composite exhibits two consecutive redox waves ($E_{½}$ = -0.18 V and $E_{½}$ = -0.53 V *vs.* SHE). In the composite PNTCDA with CNTs film, oxidative and reductive peak current densities exhibits two kinetics (***Figure 4.28B)***). Plotting the scan rates *vs*. the

square root of the peak current densities, shows two apparent linear trends: at slow scan rates (<50 $mV \cdot s^{-1}$) and at higher scan rates (from 50 to 150 $mV \cdot s^{-1}$). This might be due to the fact that the mechanism changes from a surface controlled process to a solution diffusion-limited process.

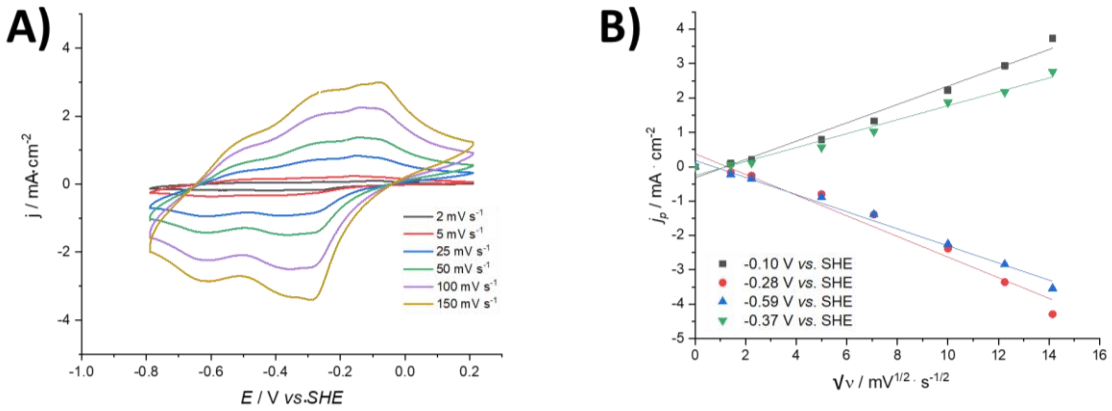

Figure 4.28 A) CV of the ex-situ composite of PNTCDA with CNTs in the ratio (75-25) wt. % . The CV was recorded as film of the active material drop-casted on the geometric area (0.071 cm^2) of a GCE in 1 M KCl_{aq} at 2, 5, 25, 50, 100 and 150 $mV\ s^{-1}$ as scan rates. The CV were recorded without iR drop compensation. B) Peak current densities vs. the square root of the scan rates for the CV in A). The equations of the plots are depicted on the graph directly.

Later, galvanostatic cycling with potential limitation of the *ex-situ* composite in 1 M KCl aqueous solution on GCE were performed, showing a gravimetric capacity of 78 mA h g^{-1} at 352 µA cm^{-2} (25 µA), with a CE equal to 79% after 10 cycles (***Figure 4.28C)***).

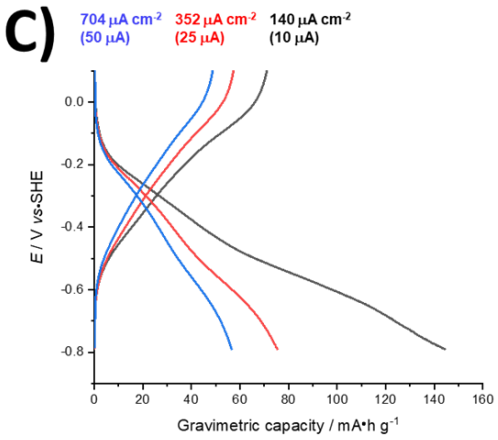

Figure 4.28 C) Galvanostatic cycling of the ex-situ composite of PNTCDA with CNTs, at three different current densities (the last cycle is shown).

Such experimental gravimetric capacity was calculated taking into account the whole amount of composite deposited onto the GCE (25 µg, which is comparable to the amount previously reported for the

pristine PNTCDA), knowing the concentration of the material dispersion and the volume drop-casted. In this case, the integration of the faradaic currents on the cyclic voltammetry is equal to 0.83 μmol cm^{-2}, which is 20 times higher than the value found for the pristine PNTCDA (0.039 μmol cm^{-2}). The presence of CNTs results in a considerable capacity enhancement, which is due to the improvement in intraparticle electron conductivity and K^+ transport in the overall electrode surface.[197] The gravimetric capacity of CNTs alone was also measured separately, and it was found equal to 14.03 $mAh \cdot g^{-1}$. The latter values shows that most of the gravimetric capacity is brought from PNTCDA, while CNTs enhance the electronic conductivity interconnecting polymer chains at long distance.[198] [199] Imbedding active electrode materials into CNTs network helps in improving conductivity, reduce electrode weight, provide high tensile strength and enhanced kinetics.[200] [201]

CNTs allow the transport of the electrons to and from the polyimide during enolisation mechanisms. Polyimide deposited on the outside and inside of the surfaces of CNTs can capture K^+ without impeding the charging mechanism of CNTs occurring outside the walls.

Interestingly, the *ex-situ* composite can be a promising booster especially for the battery cycling. As it can be observed from the comparison of either the CV or the galvanostatic cycling, it shows more enhanced performances (***Figure 4.29A)*** and ***B)***). In particular, looking at the galvanostatic cycling the specific capacity (calculated just taking into account the mass of the PNTCDA on the electrode) is roughly 5 times higher.

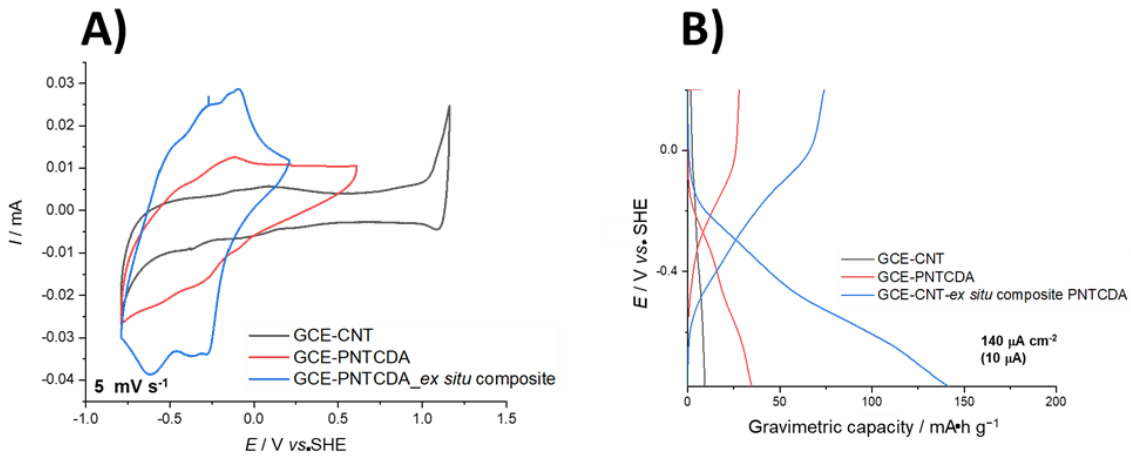

Figure 4.29 A) CVs comparison at 5 mVs^{-1} as scan rate in 1 M KCl_{aq}. recorded on GCE coated with one layer of CNTs (black line), with one layer of pristine PNTCDA (red line) and with one layer of ex-situ composite (blue line). The CV were recorded without iR drop compensation. B) Galvanostatic cycling at 10 μA of current of the CVs in A).

Later, the viability of pristine PNTCDA booster was initially tested in presence of MTABT as RM by SECM. The main objective of this preliminary characterization is to investigate the regeneration mechanism of the RM at the solid/liquid interface and the kinetics of the charge transfer, accordingly.

4.8 Preliminary investigation of the charge transfer mechanism at the liquid-solid interface of MTABT/PNTCDA by SECM

As initial characterization of the system MTABT/PNTCDA, SECM with feedback mode was employed to investigate the charge transfer mechanism at the liquid/solid interface with regeneration of the MTABT as RM. The feedback mode of the SECM involves diffusion-controlled oxidation/reduction of the RM at the electrode tip and the reverse process at the substrate surface at a rate determined by interfacial charge transfer.[202] For the present system a general scheme of the working principle is provided in ***Figure 4.30***.

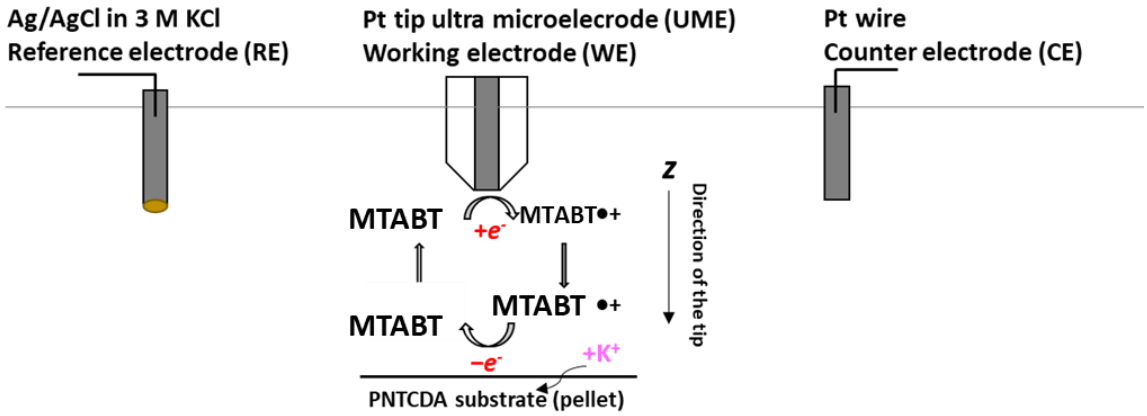

Figure 4.30 Schematic of the system booster/mediator (PNTCDA/MTABT) studied by SECM with feedback mode. The scheme depicts the reaction studied which starts with the generation of the radical-cation of MTABT at the tip of the UME, then, as soon as the tip approaches the substrate (PNTCDA) moving along the z-axis, the regeneration of the mediator happens at the interface liquid/solid. At this step the booster which is originally fully oxidized reduces itself (with enolisation mechanism and K^+ bonding) and the mediator gets oxidized again.

Before discussing the experimental results of this characterization, a brief theoretical background of SECM needs to be provided to understand better the results later displayed. In particular, two aspects will be treated: *i*) the theory of the linear and hemispherical diffusion and *ii*) the theory of the feedback mode.

4.8.1 Brief theoretical background of SECM

i) Linear and hemispherical diffusion

If the reversible oxidation reaction: $\mathrm{Red} - ne^- \uparrow \mathrm{Ox}$ is studied with macroscopic electrodes of classical dimensions (*e.g.* a few mm diameter disk), we have a semi-infinite linear diffusion propagating in one dimension, perpendicular to the electrode surface.[203] The scheme in ***Figure 4.33A)*** shows a representation.

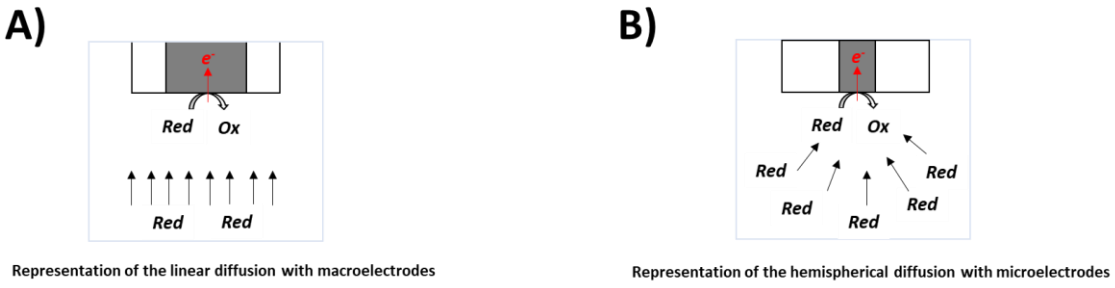

Figure 4.31 A) Representation of the linear diffusion of redox mediator Red towards the surface of the electrode where the electrochemical reduction of species Red to Ox occurs. B) Representation of the hemispherical diffusion of the same mechanism. These figures are inspired from the thesis of D. Momotenko at ref [203].

In this case, the faradaic current upon application of a potential step is given by Cottrell equation (***eqn. 4.1***)[203]

Eqn. 4.1

$$I = nFAc_0\sqrt{\frac{D}{\pi t}}$$

Where, n is the number of electrons, F is the Faraday constant (96485 C mol^{-1}), D is the diffusion coefficient (in $cm^2\ s^{-1}$), t the time (s), A the electrode area and c_0 the starting concentration of the reactant. On the other hand, the diffusion process at an ultramicroelectrode (UME) proceeds in a different way (***Figure 4.31B)***). The mass- transport regime changes from linear (that is related to one dimensional propagation of diffusion layer away from the electrode surface)[203] into spherical type, with two dimensional (hemi)spherical structure of finite size.[203] In this case, the Fick's law of diffusion represents the model (***eqn. 4.2***).[203]

Eqn. 4.2

$$I_{T,\infty} = 4nFDr_Tc_0$$

Where, n is the number of electrons, F the Faraday constant (90485 C mol^{-1}), D the diffusion coefficient (in $cm^2\ s^{-1}$), r_T the radius of the tip of the UME, and c_0 the starting concentration of the reactant.

As explained by Momotenko *et al*.,[203] UMEs are usually advantageous than macroelectrodes due to a relatively fast steady-state response, small capacitive currents and the sensing capabilities as the currents are in the range nA or pA.[203] In UME tip there are two important parts: *i)* the insulating glass sheath (which as a finite size) and *ii)* the radius (r_T). The ratio between the r_T and the insulating glass sheath is usually defined as dimensionless parameter *RG* ($RG = \frac{r_T}{R_{ins}}$).

Therefore, the diffusion-limited current at a microdisc electrode can be defined as in ***eqn. 4.3***.

Eqn. 4.3

$$I_{T,\infty} = 4nFDr_T c_0 \beta(RG)$$

Where, *n* is the number of electrons, *F* the Faraday constant (96485 C mol^{-1}), *D* the diffusion coefficient (in $cm^2\ s^{-1}$), r_T the radius of the tip of the UME, c_0 the starting concentration of the reactant and $\beta(RG)$ a dimensionless coefficient. According to Lefrou *et al*.[204], the value of this parameter varies from 1.43 (for *RG* = 1.1) to 1 (for *RG* = 100).[204] Additionally, the correction compared to infinite *RG* values achieves 43% for very small *RG* and it is already 2% for *RG* = 10.[204]

ii) Feedback mode of SECM

The second theoretical part of this section is dedicated to the feedback mode of the SECM. According to Momotenko *et al*.[203], when a UME is placed close to a substrate, the Faradaic response is related to the local electrochemical reactivity of the substrate towards the mediating redox couple.[203]

In case of an (electro) chemically inert substrate, the diffusion of the redox mediator to the active area of the UME can be blocked, resulting in a drop of the amperometric signal.[203] In this scenario the smallest the tip-substrate distance the more effective the hindered diffusion effect, leading eventually the I_T to drop to zero. [203] This is called "negative feedback".

The opposite scenario occurs when a recycling of the redox mediator at a reactive interface under diffusion control leads to an increase of the current of I_T ($I_T > I_\infty$). This is called "positive feedback mode". The following schematics in ***Figure 4.32A)*** and ***B)*** represent these two cases.

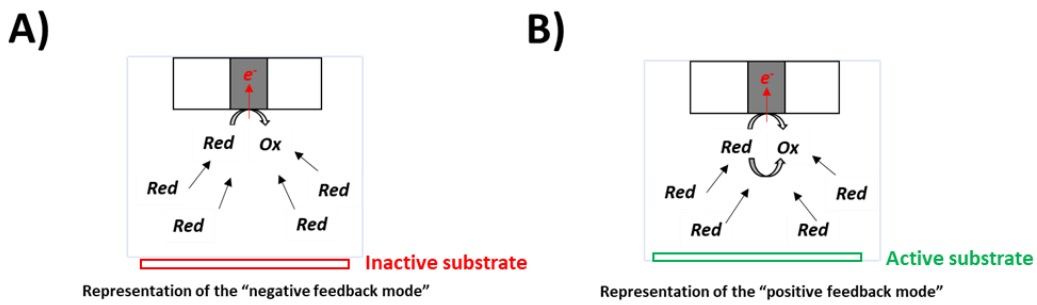

Figure 4.32 SECM feedback mode: A) "negative feedback mode" and B) "positive feedback mode". These images are inspired from the work of D. Momotenko et al. at ref [203].

Cornut and Lefrou[204] have performed finite element modeling and derived numerical approximations for these current-distance behavior. These numerical approximations were used for the data treatment in the case of the present work, thus it is important to describe them to understand better the elaboration. In their modeling Cornut and Lefrou[204] took into account different parameters such as *RG* and the first-order heterogeneous rate constant *k* at the substrate.[203] The summarized expressions are reported below (***eqn. 4.4-4.9***)[204 203]

General expression for the negative feedback (from Cornut and Lefrou)[204]:

Eqn. 4.4

$$I^{ins}{}_T \approx \left[\frac{2.08}{RG^{0.358}}\left(L-\frac{0.145}{RG}\right)+1.585\right]\times\left[\frac{2.08}{RG^{0.358}}\left(L+0.0023RG\right)+1.57+\frac{\ln RG}{L}+\frac{2}{\pi RG}\ln\left(1+\frac{\pi RG}{2L}\right)\right]^{-1}$$

Accuracy better than 1% for all *L* values if *RG*<200. [204] In ***eqn. 4.4***, *L* is defined as $L=\frac{d}{r_T}$, which is the normalized form for the tip-substrate distance. *RG* was defined already as $RG=\frac{r_T}{R_{ins}}$ and $I_T=\frac{I_T}{I_\infty}$.

General expression for the positive feedback (from Cornut and Lefrou)[204] (with accuracy better than 2% and valid for any *L* and *RG* values).

Eqn. 4.5-6-7

$$I^{cond}{}_T \approx \alpha(RG)+\frac{1}{\beta(RG)}\frac{\pi}{4\,\mathrm{Arc\,Tan}\,L}+\left(1-\alpha(RG)-\frac{1}{2\beta(RG)}\right)\frac{2}{\pi}\mathrm{Arc\,Tan}\,L$$

$$\alpha=\ln 2+\ln 2\left(1-\frac{2}{\pi}\mathrm{Arc\,Cos}\frac{1}{RG}\right)-\ln 2\left[1-\left(\frac{2}{\pi}\mathrm{Arc\,Cos}\frac{1}{RG}\right)^2\right]$$

$$\beta=1+0.639\left(1-\frac{2}{\pi}\mathrm{Arc\,Cos}\frac{1}{RG}\right)-0.186\left[1-\left(\frac{2}{\pi}\mathrm{Arc\,Cos}\frac{1}{RG}\right)^2\right]$$

Then, there is another expression (shorter than ***eqn. 4.5***) for the positive feedback (from Cornut and Lefrou)[204] valid for large *RG* values >10.

Eqn. 4.8

$$I^{cond}{}_T \approx \ln 2 + \frac{\pi}{4\,\mathrm{Arc\,Tan}\,L} + \left(\frac{1}{2} - \ln 2\right)\frac{2}{\pi}\,\mathrm{Arc\,Tan}\,L$$

Finally, Cornut and Lefrou[204] have proposed a numerical model for the first order substrate kinetics (***eqn. 4.9***).[204] This expression is valid above all for any *RG* <20 (*L*>0.1 and any κ), while the previous just for *RG*=10.[204]

Eqn. 4.9

$$I_T(L,RG,\kappa) \approx I^{cond}{}_T\left(L + \frac{1}{\kappa}, RG\right) + \frac{I^{ins}{}_T(L,RG) - 1}{(1 + 2.47RG^{0.31}L\kappa)\,(1 + L^{0.006RG+0.113}\kappa^{-0.0236RG+0.91})}$$

In conclusion the heterogeneous rate constant for the redox mediator regeneration is given in normalized form: $\Lambda = \frac{kr_T}{D}$, where *D* is the diffusion coefficient.

4.8.2 "Redox-mediated" charge transfer at the liquid electrolyte /solid booster interface

The present section outlines the first experimental results obtained from the investigation of the "redox-mediated" charge transfer at the liquid/solid interface, with regeneration of the mediator. For clearness, in the present system the RM is represented by the MTABT viologen synthesized as negative-side electrolyte candidate for the AORFB at neutral pH and the substrate (or sample) by the solid booster PNTCDA. The goal is to observe whether approaching with a UME tip the surface of the PNTCDA booster any regeneration process of the RM would occur and what is the respective interfacial charge transfer rate constant. Each electrochemical measurement was carried out in a plastic cell arranged in a three-electrode setup (Pt UME, 25 µm diameter as working electrode, an Ag/AgCl in 3 M KCl_{aq}. as reference electrode and a Pt wire (1.0 cm length) as counter electrode, respectively). The MTABT aqueous solution (3 mM in 1 M KCl_{aq}) was purged with argon over 1 hour before each test. All the measurements were recorded using a homemade SECM setup, running under SECMx software (G. Wittstock, University of Oldenburg) and comprising an Ivium Compactstat (Ivium Technologies).

The first measurement was a steady-state cyclic voltammetry of the MTABT in the bulk of the solution (***Figure 4.33***), which allowed obtaining I_{inf} from which the diffusion coefficient of the mediator could be computed using ***eqn. 4.2***.

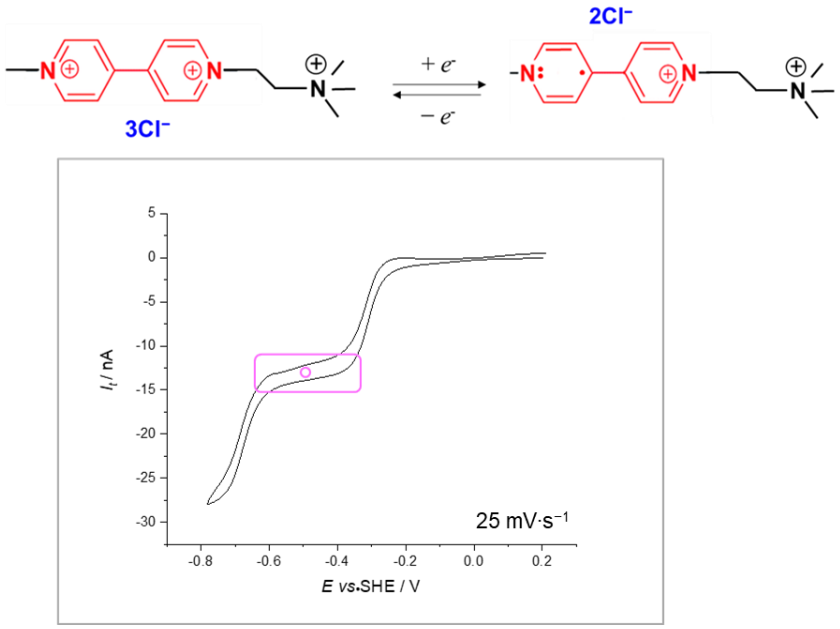

Figure 4.33 Steady-state CV of 3 mM MTABT recorded at 25 mV·s^{-1} as sweep rate using a Pt 25 µm UME. The region in violet represents the plateau potential region for the studied electron transfer reaction involving the formation of the radical-cation.

Importantly, effective tip radius (11.1 μm) was determined from the CV of FcMeOH (1.5 mM in 0.1 M KCl_{aq}.) whose diffusion coefficient can be set equal to literature value.[205] The diffusion coefficient of the MTABT was then computed form the limiting current I_{inf} of the steady-state voltammetry (***Figure 4.33***) as calibrated with the diffusion coefficient of FcMeOH. For the present case ***Table 4.3*** summarizes the results:

Table 4.3 Determination of the diffusion coefficient for the system 3 mM MTABT in 0.1 M KClaq. The radius of the tip was determined before from the calibration in FcMeOH where the diffusion coefficient is known from the literature.

Redox mediator	$\lvert I_{inf} \rvert$ / **nA**	r_T / *cm*	***F / C mol^{-1}***	c_0 / *mol cm^{-3}*	D / *cm^2 s^{-1}*
MTABT	12.50	$1.11 \cdot 10^{-3}$	96485	$3.00 \cdot 10^{-6}$	$9.80 \cdot 10^{-5}$

Subsequently, approach curves where performed. The tip was moved in the *z*-axis direction, towards the substrate. Each measurement was recorded with an initial resting time of 20 s, after which the tip was moved towards the substrate at a speed rate of 5 μm s^{-1} with 1 μm step. In each experiment a potential of -0.5 V *vs*. SHE was applied (according to the steady state voltammogram registered of RM in the bulk of the solution, ***Figure 4.33***).

The UME tip was placed above an insulating substrate (glass) and as soon as it approaches the surface, a negative feedback mode was observed ($L \approx 0$ and $I_T \approx 0$). The theoretical model of this approach curve was defined before in ***eqn.4.4***, from Cornut and Lefrou (light green dots and line in ***Figure 4.34***).[204] The fitting of the experimental data (yellow dots and line ***in Figure 4.34***) was computed with the software MIRA (G. Wittstock, University of Oldenburg). The fitting model in the software called "insulator from Lefrou" was used to calibrate *RG* (found as equal to 2) with the effective tip radius (1.11 10^{-3} cm), the current at the bulk (*ca*. -3 nA) and the current at the approach point.

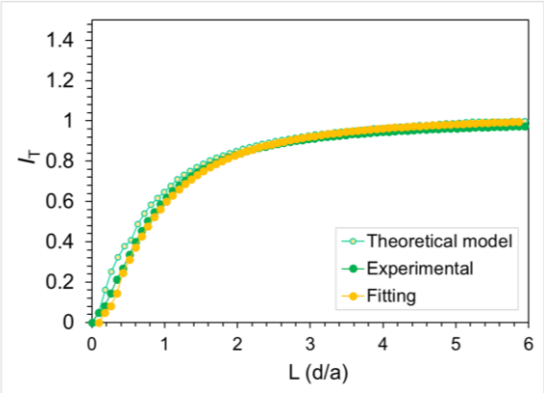

Figure 4.36 Normalized feedback approach curves (negative feedback mode) for a 11.1 μm Pt disk UME towards a piece of microscope glass slide (0.5x1.0) cm. The green dots represent the experimental dataset, the yellow dots the fitting and the light green dots the theoretical model "insulator from Lefrou". (RG=2)

This experimental trend is consistent with the fact that in presence of an inert substrate (*i.e.* the glass), the diffusion of the redox mediator MTABT to the active area of the UME is blocked, resulting in a drop of the amperometric signal.[203]

Subsequently, approach curves were done towards an active substrate, the PNTCDA solid booster. In this case, a pellet of PNTCDA (4 mm diameter and *ca.* 1 mm thickness) was fabricated from the pristine powder and placed on top of the glass substrate. The Pt UME tip was not mechanically polished from the previous approach curves against the glass, but just rinsed properly with milli-Q water and with one/two drops of isopropanol to remove possible traces of the MTABT and checked with an optical microscope before each new measurement. Prior new approach curves, steady-state voltammetry was recorded to check the electrochemical response of the mediator at the tip of the UME. For this second series of measurements a fresh solution was employed, carefully purged over 1 hour with argon. The scenario is graphically described in ***Figure 4.37A)***.

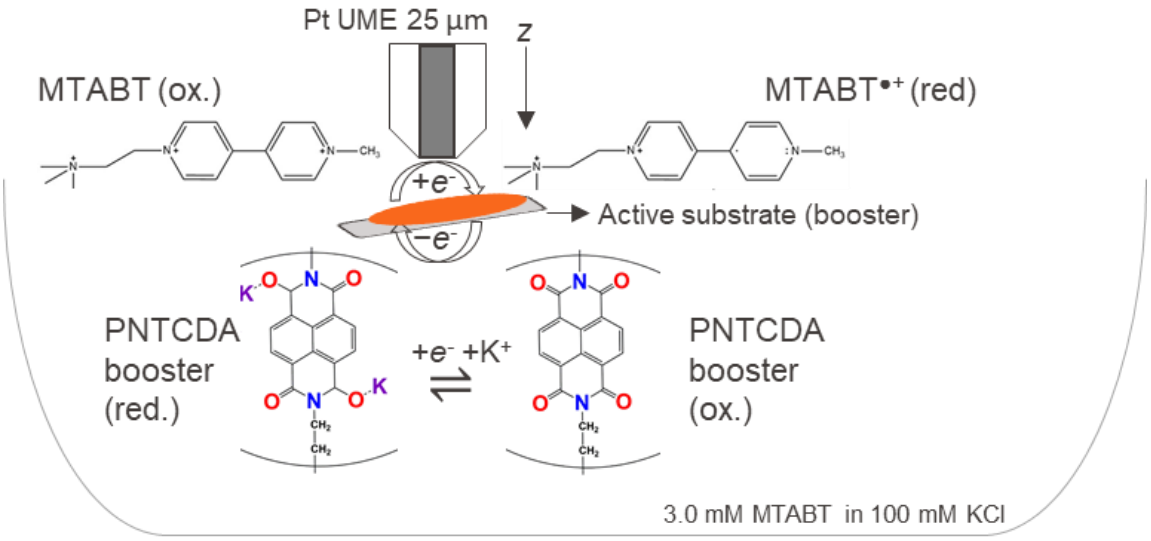

Figure 4.37A) Schematic representing the approach curve of the Pt UME tip towards the electrochemically active PNTCDA pellet.

As before, the Pt UME tip moves in the *z*-axis towards the PNTCDA pellet and at the moment it reaches the interface, a regeneration of the mediator is expected at the interface. This scenario is known as positive feedback mode of SECM. In particular, when the UME tip approaches the PNTCDA, the radical-cation of the viologen at the tip will be re-oxidized at the solid/liquid interface along with booster reduction, thanks to the "mediated" charge transfer. Therefore, even in this case, the redox reactions have to be considered *in tandem*, in good agreement with the "redox-mediated" charge transfer approach of this work.

Approach curves towards the PNTCDA pellet were performed in two different positions, in order to see any difference in the electrochemical response.

Both measurements were recorded using the same experimental conditions of the previous measurements towards the inactive substrate (*i.e.* glass), meaning with an initial resting time of 20 s, after which the tip was moved towards the substrate at a speed rate of 5 μm s^{-1} with 1 μm step. ***Figure 4.37B)*** shows the approach curves recorded of the Pt UME tip moving in the *z*-axis towards the first position of the PNTCDA pellet ("named position 1" in the plot).

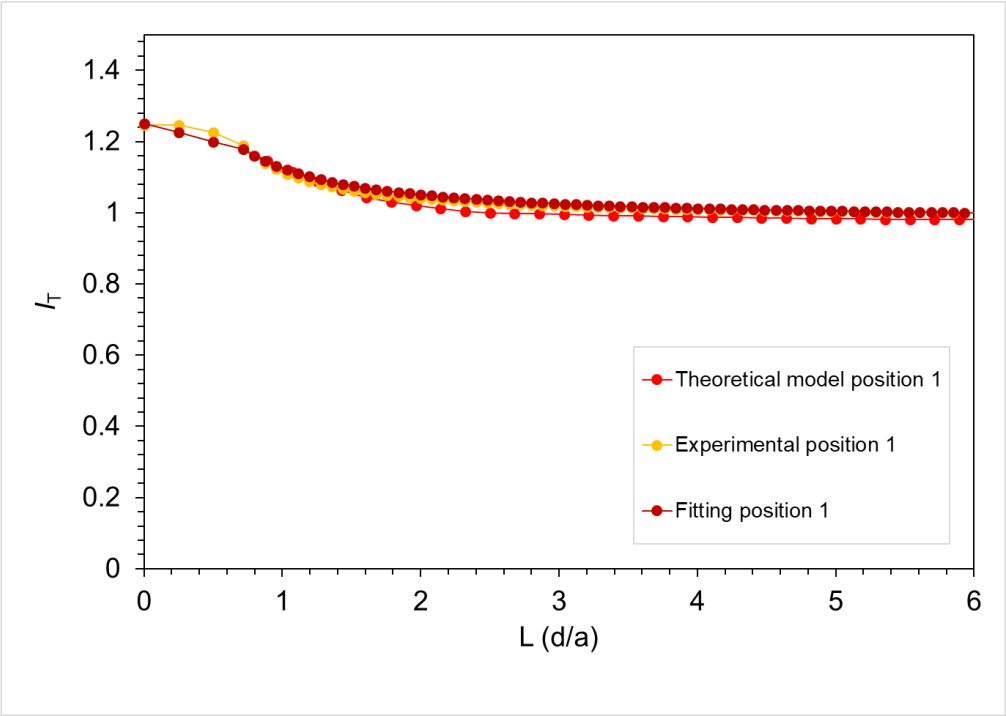

Figure 4.37 B) Normalized feedback approach curves (positive feedback mode) for a 5.60 μm Pt disk UME towards a pellet of PNTCDA solid booster (4 mm diameter and ca. 1 mm thickness). The yellow dots represent the experimental dataset, the brown dots the fitting and the red dots the theoretical model "conductor from Lefrou". (RG=2)

Figure 4.37C) represents the second approach curve of the Pt UME in 3 mM MTABT solution towards the second position of the PNTCDA pellet. In this case, the solution was not changed from the previously recorded approach curve. The second position (named "position 2" in the plot of ***Figure 4.37C)***), is 100 μm distant from the position "1" on the *x*-axis (positive direction).

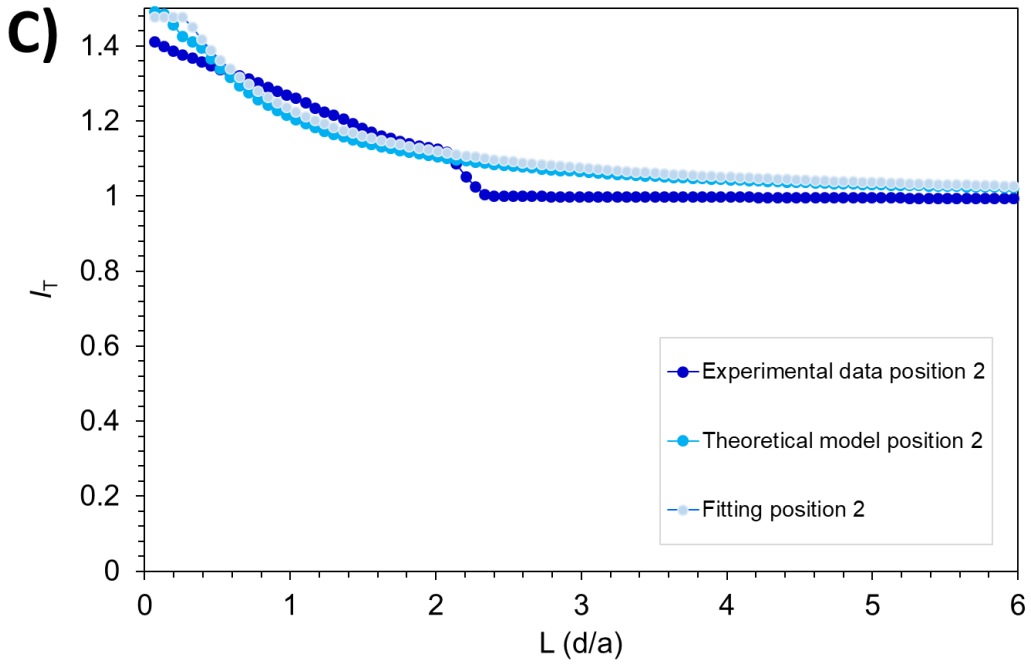

Figure 4.378 C) Normalized feedback approach curves (positive feedback mode) for a 4.24 µm Pt disk UME towards a pellet of PNTCDA solid booster (4 mm diameter and ca. 1 mm thickness). The dark blue dots represent the experimental dataset, the grey dots the fitting and the light blue dots the theoretical model "conductor from Lefrou". (RG=2)

As it can be observed from the plot in ***Figure 4.37C)***, the approach of the Pt UME tip to the PNTCDA pellet in this position is quite irregular, a sort of "step" can be spotted on the curve around 2 *L (d/a)*. The reason behind this behavior is not fully clear, however, this could be either related to experimental condition of the sample, or to a not perfect alignment of the UME as respect to the sample. The first assumption is actually confirmed from the fact that during the measurements a thin layer of bubbles was covering the exterior of the pellet surface, therefore, presumably when the UME arrived in touch with the pellet to approach, it had to first "break" this thin layer before reaching the actual sample.

Subsequently, for first order substrate kinetics the ***eqn. 4.9***,[204] valid above all for any *RG* <20 (*L*>0.1) and any κ allows calculating the factor $\kappa = \frac{k_{eff} \bullet a}{D}$, which then leads to the kinetic constant for the charge transfer reaction. ***Table 4.4*** summarizes the results for the two position on the PNTCDA pellets.

Table 4.4 Determination of the kinetic constant for the system PNTCDA/ N,N-4'-ethylamine-bipiridinium tetrachloride viologen . The fitted parameters for kappa are reported accordingly.

PNTCDA	r_T ***/ cm***	***D / cm² s⁻¹***	***κ (fitted)***	k_{eff} ***/ cm s⁻¹***
Position 1	$1.11 \cdot 10^{-3}$	$9.80 \cdot 10^{-5}$	0.016	$1.42 \cdot 10^{-3}$
Position 2	$1.11 \cdot 10^{-3}$	$9.80 \cdot 10^{-5}$	0.088	$7.84 \cdot 10^{-4}$

In another study recently proposed by Wang and co-workers[202], a similar work was done investigating the charge transfer reaction (lithiation/de-lithiation) of $LiFePO_4$ with two pair of redox shuttle molecules, $FcBr_2^+$ and Fc. The effective rate constant, k_{eff}, was determined to be around 3.70–6.57 10^{-3} cm s^{-1} for the two-way pseudo-first-order reactions, which feature a linear dependence on the composition of $LiFePO_4$.[202] Importantly, the entire system was operating in organic solvents.

This preliminary study confirms that MTABT can be regenerated only because of a "mediated" charge transfer reaction with the solid booster PNTCDA, in agreement with the fact the Fermi level of the booster has to be aligned with the standard redox potential of the mediator. Nevertheless, an additional characterization of this system was planned to further validate the "mediated-charge tranfer" concept. The working electrode in the electrochemical system would have been replaced by another one known as soft SECM probe. Soft probes are completely different electrodes as compared to the Pt UME tip, much more flexible and versatile. They are used for different applications, and for instance an interesting work has been recently proposed by Lesch and co-workers[206], where soft probes are employed in the electrochemical detection of melanoma. One of the main advantages of soft probes is that they allow approaching or scanning the sample by gentle "brushing" the exterior of the surface. Therefore, even if the sample presents any irregularity, roughness, height or particular morphology, the electrochemical measurement will not be affected. The soft probe will be used as working electrode to linearly scan (in contact mode) a pellet of PNTCDA booster, placed securely on top of a glass inactive substrate. The main goal will be to detect the activity of the booster in presence of the mediator solution, which should correspond to an increase of the amperometric electrochemical signal. All these measurements were planned already as well as the setup, but unfortunately, due to the current situation of the COVID-19, the laboratory was closed before their actual realization.

4.9 Conclusion and future perspectives

This chapter presented a dissertation on the chemical stability of MTABT, synthesized as new negative-side electrolyte for the AORFB at neutral pH. A preliminary assessment of this molecule in presence of the commonly employed TEMPTMA at the positive-side was performed in an ARFB positioned in a nitrogen filled glovebag and after in a glove box. When the electrolytes were first cycled in the glovebag they showed major capacity fading upon time (*ca*. 54%). The reasons for this fading were preliminary investigated on each electrolyte and a few aspects were particularly identified: *i*) the electrolyte pH and *ii*) the effect of O_2. The shift pH was interestingly discovered by a simple measurement in each electrolyte tank after the cycling test. The TEMPTMA's tank reached an acidic pH and the MTABT a slightly alkaline (*ca*. 8.5). For the TEMPTMA, the pH shift was attributed to acidic-base equilibria of this nitroxyl radical in water. On the other hand, in the case of the MTABT, the pH change was probably due to the formation of an adduct (due to the presence of molecular oxygen), which suddenly led to the release of OH^- into the solution.[62] Subsequently, any decomposition mechanism in absence of O_2 was considered. In particular, for the MTABT it was assumed a dimerization process. [62]

Despite the limited chemical stability of MTABT, the goal was to find a solid booster to pair and preliminarily demonstrate the "mediated-charge" transfer mechanism. In this case, polyimides were found as promising candidate materials, because they show a facile synthetic route, a solid backbone and relatively low chemical risk, being made of C, N and O atoms. Among polyimides, PNTCDA was selected for its redox potential matching that of the mediator with just 15 mV of difference, and also for the relatively high theoretical gravimetric capacity in aqueous systems (183 mAh g^{-1})[189].

Pristine PNTCDA was easily synthesized and electrochemically characterized by CV. Then, galvanostatic cycling showed a modest gravimetric capacity in 1 M KCl_{aq} (35 mAh g^{-1}) due to the rather small surface coverage (0.039 μmol cm^{-2}) and probably from the insulating character of the polymer.[184] Interestingly, testing the pristine PNTCDA in a saturated solution of KCl gave more enhanced performances, showing a gravimetric capacity of *ca*. 70 mAh g^{-1}, confirming that the amount of K^+ ions in the solution is a significant factor in the cycling performance of the polymer. To mitigate the insulation of the pristine polymer, an *ex-situ* composite of PNTCDA with CNTs was synthesized and electrochemically tested. It exhibited almost 5 times the gravimetric capacity of the pristine polymer (*ca*. 145 mAh g^{-1} *vs*. 35 mAh g^{-1}), at the same current (10 μA). The CNTs helped making a more conducting network of PNTCDA particles, interlacing polymer chains.

Finally, as preliminary characterization of the system pristine PNTCDA/MTABT, SECM was employed to study the charge transfer mechanism at the solid/liquid interface. The investigation was performed using a Pt UME as working electrode and approach curves in SECM feedback mode were

recorded of the electrode moving in the *z*-axis towards an insulating and then an active surface. In the case of an insulating substrate, a negative feedback mode of the SECM was obtained, while in the presence of active substrate a positive feedback mode, confirming a regeneration process of the RM at the interface with the PNTCDA booster. The kinetic constant for the interfacial charge transfer reactions was found for two position of the same PNTCDA sample, distant *ca*. 100 μm on the *x*-axis ($1.42 \cdot 10^{-3}$ and $7.84 \cdot 10^{-4}$ cm s^{-1}), according to a first order kinetic.[202]

This chapter opens different future perspectives for both the topics discussed: the electrolyte stability and the viability of the booster in presence of the electrolyte. First, regarding the electrolyte stability, further cycling tests have to be performed in a glove box, utilizing a buffer in the supporting electrolyte to minimize the pH shift. In addition, a pH probe could also be installed in the reservoir to monitor the pH upon cycling. Then, beside electrochemical characterization such as CV before and after the cycling tests, it can be interesting to perform other measurements, such as 2D nuclear magnetic resonance, including correlation spectroscopy (COSY), since more specific information on any eventual change in the molecular structure can be detected as compared to 1D NMR. Regarding the second topic, SECM characterization on the pristine sample has to be performed more accurately to have a bigger dataset for the evaluation of the interfacial kinetic constant. The *ex-situ* composite of PNTCDA with CNTs can be tested to compare to the pristine PNTCDA.

Chapter 5 *Materials and Methods*

Section 1: Materials and Methods of Chapter 2: "Redox-mediated" flow battery at acidic pH using polyaniline as solid booster

5.1.1 Chemicals and solutions

Electrolyte solutions were prepared using hydrochloric acid (HCl, 32 %, Carlo Erba) and sulfuric acid (H_2SO_4, 95-97%). Aniline (C_6H_7N, 99% Reagent Plus) and ammonium peroxydisulfate ($(NH_4)_2S_2O_8$, 99 %) were employed for the chemical synthesis of polyaniline and purchased from Sigma Aldrich. For the synthesis of the composite of polyaniline with carbon black, carbon acetylene black (CB, 99.99%, 50% compressed, average particles size 0.042 μm) was purchased from Strem Chemicals.

Iron electrolyte solutions were prepared from either ferric (III) sulfate heptahydrate (99% Sigma Aldrich) or ferrous (II) sulfate heptahydrate (99% Sigma Aldrich). For vanadium electrolyte solutions, a commercial electrolyte is used as-received (Gildemeister Energy Solutions, Germany). The composition of this electrolyte was, according to the supplier's information, assumed to be 1.6 M vanadium, 2 M H_2SO_4, 0.05 M H_3PO_4. A Millipore filtration system (Merck Millipore, Billerica, MA) was used to generate ultrapure water (18.2 MΩ·cm^{-1}), from which all aqueous solutions were made. All reagents were employed without further purification.

5.1.2 Synthesis

5.1.2.1 Chemical synthesis of polyaniline (PANI)

The bulk synthesis of polyaniline powder was performed at room temperature (RT), in a regular fume hood and under vigorous stirring. In particular, 0.77 M aniline (C_6H_7N) was dissolved in 1 M HCl solution and subsequently oxidized by adding an equimolar amount of ammonium persulfate ($(NH_4)_2S_2O_8$). This step lasted *ca*. 2 h at RT under vigorous stirring. The resulting blue precipitate was filtered on Büchner filtration system equipped with a Whatman filter paper (Durapore membrane filter 0.45 μm) and washed with Milli-Q water until the filtrate became colorless. The collected precipitate was dried under vacuum at 50°C to facilitate water evaporation. A final yield of 90% was obtained. ***Figure 5.1.1*** depicts the schematic of the synthetic route.

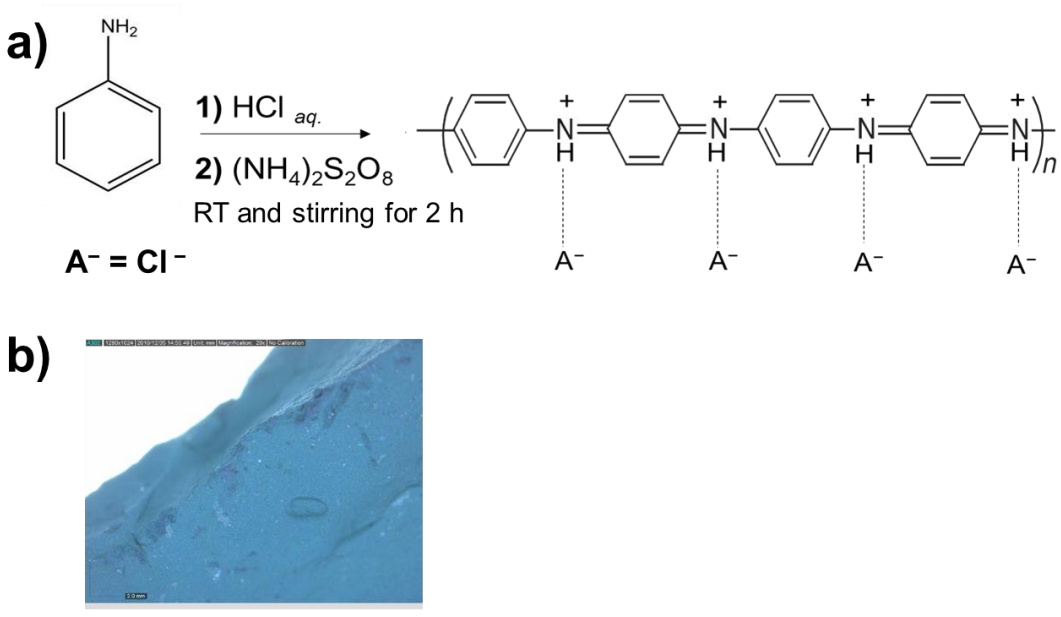

Figure 5.1.1 a) Schematic of the chemical polymerization of PANI from aniline monomer in presence of hydrochloric acid (HCl) and ammonium persulfate ($(NH_4)_2S_2O_8$). The chemical synthesis was performed in a regular fume hood at room temperature and in a regular fume under vigorous stirring. b) Image of the PANI salt obtained as blue powder (2 mm particle size) after the filtration step of the synthesis.

5.1.2.2 Chemical synthesis of PANI composite with carbon acetylene black (CB) (PANI/CB)

The bulk synthesis of the composite of PANI powder with carbon acetylene black (CB) was a 80-20 wt. % ratio. CB powder was dispersed in the aniline solution (0.77 M) before the addition of the oxidant ammonium persulfate, stirring vigorously for 1 hour at RT. Later, ammonium persulfate was added to the solution and the overall mix was kept for 2 more hours at RT under vigorous stirring. At this time, a blue solid precipitate was formed and then filtered on Buckner filtration system equipped with Whatman filter paper (Durapore membrane filter 0.45 μm). Finally, the precipitate was rinsed with Milli-Q water until colorless. The solid precipitate was collected and dry under vacuum at 50°C to facilitate water evaporation. ***Figure 5.1.2*** depicts the schematic of the synthetic route.

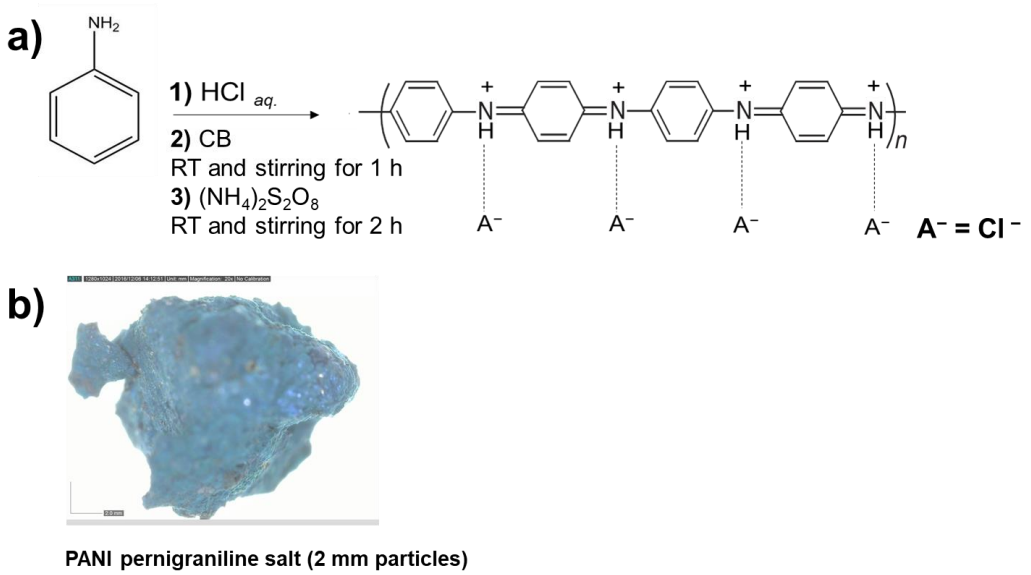

Figure 5.1.2 a) Schematic of the chemical polymerization of PANI/CB composite from aniline monomer in presence of hydrochloric acid and ammonium persulfate. The chemical synthesis was performed in a regular fume hood at RT under vigorous stirring. b) Image of the PANI/CB pernigraniline salt obtained as blue powder (2 mm particle size) after the filtration step of the synthesis.

5.1.3 Electrochemical methods and characterization techniques

5.1.3.1 Electrodeposition of PANI on carbon paper (CP) (PANI/CP) and other electrodes

The electrochemical synthesis of polyaniline was conducted using a PGSTAT 12 potentiostat (Metrohm, CH). Carbon paper (SGL Sigracet 10 AA, 36.75 cm^2 geometric area) was used as a porous and conductive support for PANI electrochemical deposition. A 6 cm coiled platinum wire was employed as counter electrode, and an Ag/AgCl in 3 M potassium chloride (KCl) as reference electrode (+0.21 V *vs.* standard hydrogen electrode, SHE). The electrolyte solution contained 0.2 M aniline monomer in 1 M hydrochloric acid (HCl). The electrochemical deposition was performed under galvanostatic conditions, applying 10 mA (270 $\mu A \cdot cm^{-2}$) for 2 hours (***Figure 5.1.3a)***). All the experiments were performed at room temperature in air in a regular fume hood. In addition, as seen in the results discussion in chapter 2, PANI can be easily electrodeposited on other electrode materials, such as fluorine tin doped oxide electrode (FTO). This electrodeposition was accomplished for completeness of this work and ***Figure 5.1.3b)*** shows a photo of the electrochemical setup.

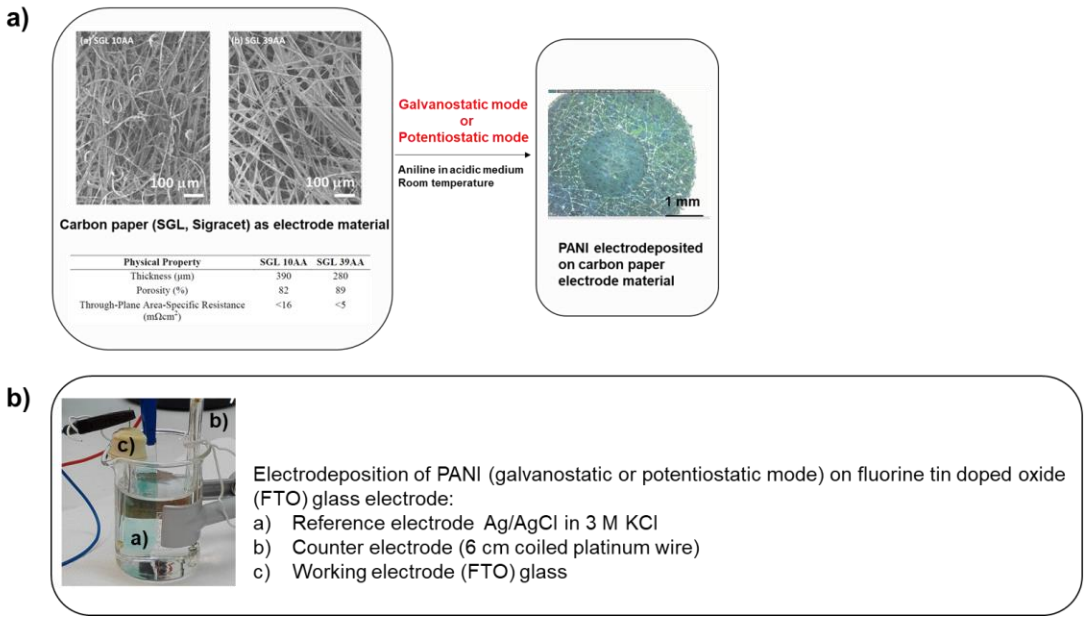

Figure 5.1.3 a) Schematic of the electrodeposition of PANI on carbon paper electrode materials. As example common carbon papers (10AA and 39AA SGL Sigracet, microscopy images from the work of Wong et al.[207] Copyright 2020 Electrochemical Society) usually employed in RFB applications. The PANI sample shown is an experimental result of this thesis work and later it will be better discussed. b) Schematic of the electrodeposition of PANI on fluorine tin doped oxide glass electrode material. The photo is an experimental result done for this this work to provide an example of electrodeposition techniques. The legend beside the image details the experimental conditions employed for performing that experimental measurement.

5.1.3.2 Cyclic voltammetry (CV) of PANI on carbon paper (CP) (PANI/CP)

CV was performed in 1 M HCl aqueous solution in a regular fume hood in air. The working electrode was an 8 mm diameter disk of PANI electrodeposited on carbon paper (here denoted as PANI/CP), placed together in a polyetheretherketone (PEEK) plastic holder with a titanium current collector (8 mm diameter disk). A 6 cm coiled platinum wire was used as a counter electrode and an Ag/AgCl in 3 M KCl as the reference electrode.

5.1.3.3 Electrochemical cycling of PANI on carbon paper (CP)

Pristine PANI in 1 M HCl was oxidized/reduced potentiostatically at +0.90/ +0.66 V and +0.47/ 0.23 V *vs.* SHE to determine the intrinsic gravimetric capacity within the potential windows of $Fe^{3+/2+}$ and $V^{4+/3+}$, respectively. The applied potentials were determined by the Nernst equation, assuming a ratio of (99:1) and (1:99) of oxidized/ reduced species, for the two electrolytes. Each of the potentiostatic charge/

discharge steps were applied for 10 minutes, and a total of 5 charge/ discharge cycles were performed for each sample.

5.1.3.4 "Indirect" chemical cycling of polyaniline via robotic positioning system

Chemically-driven oxidation/ reduction of polyaniline on carbon paper was performed using a *ROBO Pro* (Fischer Techniques Robotics) robotic positioning system (***Figure 5.1.4***), synchronized with an Ivium Compactstat potentiostat in a two-electrode configuration.

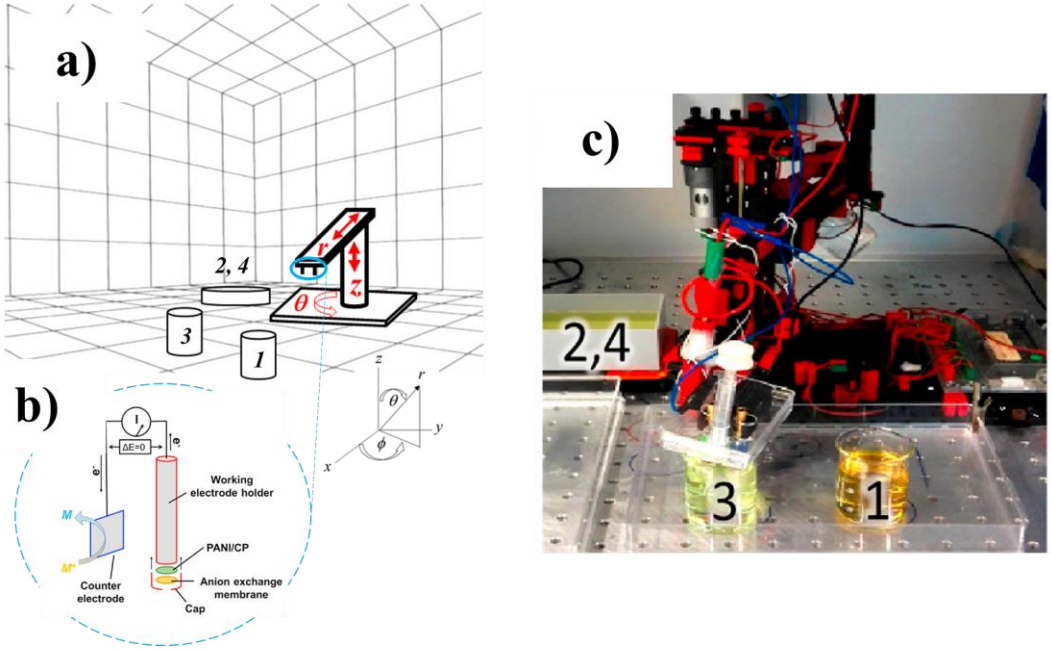

Figure 5.1.4 a) b) schematic and C) photograph of the experimental setup used to simulate the 'indirect' cycling of PANI in presence of actual solutions of $Fe^{3+/2+}$ and $V^{4+/3+}$. A computer controlled positioning system was used to alternately submerge electrodes into beakers containing solutions of the oxidizing species (either Fe^{3+} or V^{4+}, position "1") or a solution of the reducing species (either Fe^{2+} or V^{3+}, position "3"), with washing steps in between (position "2" and "4"). During each cycle, the potential difference between the two electrodes was fixed to 0 V and the current is measured.

The working electrode assembly, shown in ***Figure 5.1.4b)***, consisted of an 8 mm PANI on CP disk immersed in 1 M HCl and protected by an anion exchange membrane (Fumasep® FAP-375 PP, Fuma-Tech, thickness 70-80 µm), to prevent the redox mediator from directly oxidizing/reducing PANI. The counter electrode consisted of a 2 cm coiled platinum wire for tests involving iron or a 8 cm^2 piece of graphite felt (SGL Sigracet), for tests involving vanadium. The working and counter electrodes were both fixed to the arm of the positioning system. The positioning system moved the electrodes between three beakers containing:

i) 0.3 M oxidizing solution (Fe^{3+} or V^{4+}, position "1" in ***Figure 5.1.4a)*** and ***c)***)

ii) 0.3 M reducing solution (Fe^{2+} or V^{3+} position "3" in ***Figure 5.1.4a)*** and ***c)***)

iii) 1 M HCl (washing solution, position "2" and "4" in ***Figure 5.1.4a)*** and ***c)***)

First, the electrodes were immersed in the oxidizing solution for 30 minutes, and a potential difference of 0 V was imposed between the counter and working electrodes. In this configuration, the PANI/CP attempted to reach thermodynamic equilibrium with the solution. Thus, the oxidant was reduced at the counter electrode, while polyaniline was correspondingly oxidized at the working electrode (simulating "indirect" charging). The current passing between the two electrodes (named "chemical current") was measured with the potentiostat. The working electrode was washed in 1 M HCl for 80 seconds, and then immersed in the reducing solution. Again, a potential difference of 0 V was imposed for 30 minutes between the working and counter electrodes, causing the reductant to be oxidized at the counter electrode and polyaniline to be reduced at the working electrode surface (simulating "indirect" discharging). Overall, 25 cycles of chemical "indirect" charging/discharging were registered. All experiments were performed in a humidified chamber to minimize evaporation of the various solutions.

5.1.3.5 Conductivity measurements of solid PANI and PANI/CB

Conductivity measurements were performed using a four-point probe with a 1 mm probe spacing (Jandel Engineering LTD., UK). Samples of PANI and PANI composite with CAB synthesized as reported in paragraphs 5.2.1 and 5.2.2, were submerged in solutions of Fe^{2+} and Fe^{3+} to obtain the leucoemeraldine (fully reduced) and pernigraniline (fully oxidized) forms of the polymer, respectively. A schematic of the conductivity measurements of PANI and PANI/CB with four-point probe is reported in ***Figure 5.1.5a)*** along with PANI and PANI/CB synthesized samples (***Figure 5.1.5b***)).

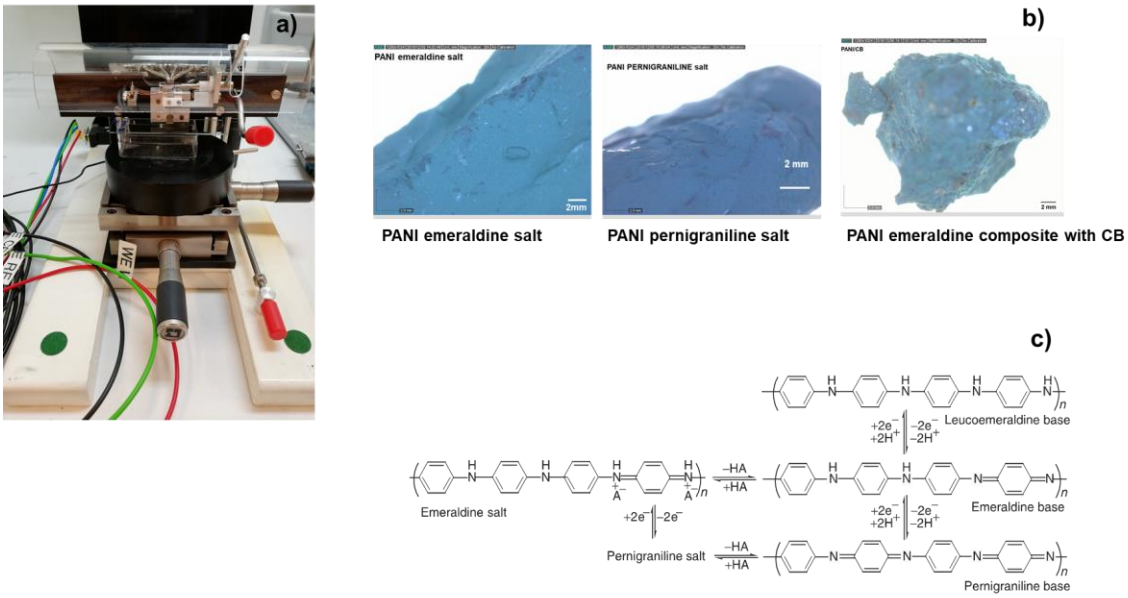

Figure 5.1.5 a) Four-point probe used in the conductivity measurement of the synthesized PANI and PANI/CB. The probe spacing is 1 mm and the electrode connections (working electrode (WE), reference electrode (RE), counter electrode (CE) and the ground) are displayed. b) Sample of PANI and PANI/CB powder synthesized for the conductivity measurement and then for the flow cell cycling. c) Schematic of the redox reactions of the three forms of PANI with deprotonation and protonation, reported for completeness.

All samples were then washed with 1 M sulfuric acid (H_2SO_4) solution and dried thoroughly before analysis. Samples were contacted with the measurement head and cyclic amperometry from −1 mA to +1 mA was applied using a PGSTAT 12 potentiostat (Autolab, Metrohm). A linear fit was applied to the current/potential data to obtain the sample conductance, from which conductivity was calculated by assuming semi-infinite volume.

5.1.4 RFB and "redox-mediated" flow battery setup

5.1.4.1 Design of a Fe-V RFB and of a "redox-mediated" flow battery

For the flow cell tests, a cell consisting of a titanium (Bibus Metals Ag) and graphite current collectors (negative and positive-side, respectively), carbon felt electrodes (SGL Sigracet, 13 cm^2 active area, employed without pre-treatment), anion exchange membrane (Fumasep® FAP-375 PP, FuMA-Tech, 13 cm^2 active area, employed without pre-treatment) and silicone gaskets (2 and 3 mm thickness, respectively) was assembled (***Figure 5.1.6A) B)*** and ***C***)).

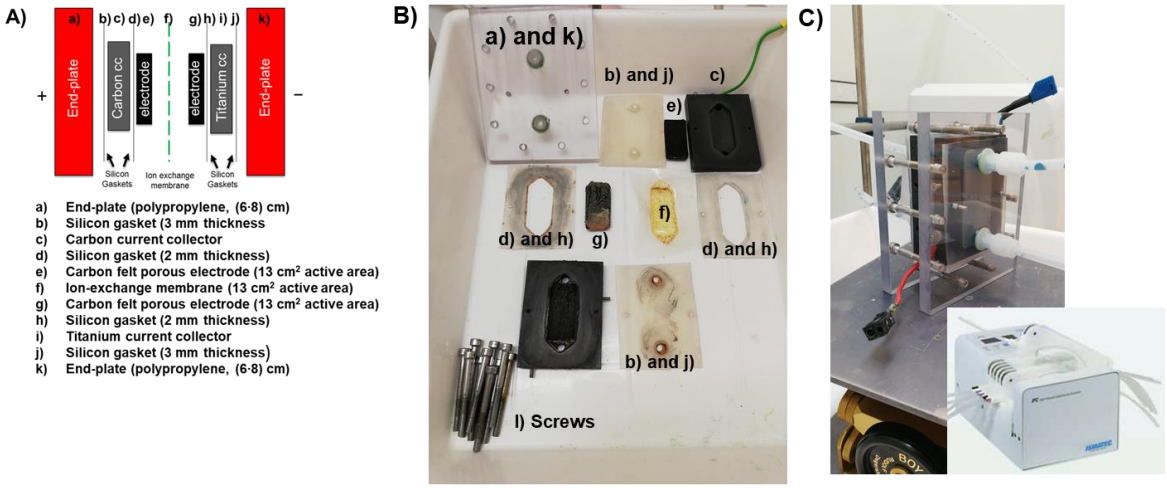

B) Images of the components of the electrochemical cell of a RFB setup with electrode. C) Images of the electrochemical cell connected either to the potentiostat or to the peristaltic pump (Ismatech).

Figure 5.1.6 A) Schematic of the electrochemical cell with explanation of all single components. B) Image of all components used in the actual electrochemical cell configuration. The letters refer to the legend in A). C) Image of the electrochemical cell mounted for cycling test in a regular fume hood.

The electrolyte solutions Fe and V (contained in glass bottles of 100 mL each, sealed with caps equipped by holes for the pipes) were pumped through the cell at a flow rate of 20 $mL \cdot min^{-1}$ (0.45 $cm \cdot s^{-1}$ mean linear flow velocity), using a multichannel peristaltic pump (Ismatech). The pipeline system was realized using Ismatech pump tubing, 3-stops, PVC, 2.06 mm inner diameter (ID). A Biologic SP-300 potentiostat was used in a *3-electrode* configuration to control the potential at the positive electrode. The potential of the negative electrode was also actively recorded. Flow cell tests were performed at 200 mA and 500 mA (15.4 and 38.5 $mA \cdot cm^{-2}$, respectively).

For experiments involving PANI or PANI/CB, the electrolyte tanks were configured as a *vertical-flow-packed-bed* reactor. Electrolyte returning from the flow cell was injected at the bottom of the tank, below the bed of particles, forcing it to flow upward through the particle bed, ensuring good percolation. A piece of carbon felt was used to prevent the particles from passing through the flow cell and the electrolyte.

Section 2: Materials and Methods of Chapter 3: Copper hexacyanoferrate as redox solid booster for aqueous batteries at neutral pH

5.2.1 Chemicals and Solutions

Copper nitrate trihydrate ($(Cu(NO_3)_2 \cdot 3H_2O$, puriss. p.a. 99%), 1-Methyl-2-Pyrrolidone, (NMP, reag. grade 99%), Acetone (CH_3COCH_3, puriss. p.a. ACS, reag, reag ISO, reag. Ph. Eur ≥ 99.5%) Potassium chloride (KCl, ACS reagent, 99-100%), 4-dimethylamino-2,2,6,6 tetraethyl piperidine (96%), methyl iodide (CH_3I, contains copper as stabilizer, Reagent Plus, 99%) were purchased from Sigma-Aldrich. Potassium ferrocyanide trihydrate ($K_3Fe(CN)_6$, $\cdot 3H_2O$, 99+% for analysis), N,N-dimethylfornamide (DMF, ≥ 99.5%) were purchased from Acros Organics. Multi-walled carbon nanotubes (MWCNT, purity > 98%, Outer Diameter 20-30 nm, length 0.5-2 µm) were purchased from Carbon Nanotubes Plus. Carbon black acetylene (CB, 99.99%, 50% compressed, average particles size 0.042 µm) was purchased from Strem Chemicals. Polyvinylidene fluoride (PVDF) was purchased from ABCR. Anion exchange resin (analytical grade anion exchange resin, AG ® I-X8, 50-100 mesh, chloride form, Bio-Rad laboratories, Dowex) was purchased from Dow Chemical Co. All solvents and reactants were utilized without any further purification.

Potassium chloride (KCl, ACS reagent, 99-100%, Sigma Aldrich) aqueous solutions were used as electrolyte and prepared at different concentrations using Milli-Q water. A Millipore filtration system (Merck Millipore, Billerica, MA) was used to generate ultrapure water (18.2 MΩ cm^{-1}), from which all aqueous solutions were prepared. The pH was measured with a 744 pH meter Ω (Metrohm, Switzerland) and found to be 5.55 at 23.5 °C. For the electrochemical characterizations, a SP-300.101 potentiostat from Bio-Logic (France) in a three-electrode setup was employed. The working electrode was a glassy carbon electrode (GCE glassy carbon electrode OD: 6 mm ID: 3 mm, BAS Inc., Japan). A platinum wire (2 cm of length) was used as counter electrode and Ag/AgCl in 3 M KCl as reference electrode. PXRD pattern of as-synthesized CuHCF sample was recorded by Bruker diffractometer with Cu K_α non-monochromic irradiation (λ = 1.5406 Å), operated at 40 kV and 40 mA. Scanning electron microscopy (FEI SEM Teneo) was performed at 1-5kV, 0.12-1pA with lower in-lens and in-column detectors. X-ray photoelectron spectroscopy (VersaProbe II from Physical Electronics) was used to characterized the ex-situ composite.

5.2.2 Synthesis

5.2.2.1 Synthesis of copper hexacyanoferrate Prussian blue analogue

Copper hexacyanoferrate pristine powder was synthesized by simultaneous addition of 120 mL of 0.1 M copper (II) nitrate trihydrate and 120 mL of 0.05 M potassium ferrocyanide trihydrate to 60 mL of Milli-Q water upon vigorous and constant stirring.[155] The so-obtained solution was centrifuged for 30

minutes for three times and then the obtained suspension was allowed to rest for six hours. Then, the formed precipitate was filtered, washed with Milli-Q water and finally dried under vacuum at room temperature overnight. The yield of this synthesis is 90%.

5.2.2.2. Synthesis of N,N,N-2,2,6,6-heptamethylpiperidinyl oxy-4-ammonium chloride (TEMPTMA)

The synthesis of TEMPTMA was done by suspending 4.96 g (29 mmol) of 4-dimethylamino-2,2,6,6 tetraethyl piperidine in a first aliquot of 20 mL of acetone under vigorous agitation. 10 mL of methyl iodide was added into the mix followed by a second aliquot of 20 mL of acetone.[170] The reaction mixture was stirred at 60 °C for 20 hours to form *N,N,N*-2,2,6,6-heptamethylpiperidinyl oxy-4-ammonium iodide **(1)**. The resulting mix was cooled down to room temperature and the suspended solid was collected by vacuum filtration. The solid was rinsed three times with 100 mL of acetone and then dried in the oven for two hours at 80 °C. Yield **(1)**: 2.08 g (42%) of fine yellow powder. This material was treated with an anion exchange resin to exchange iodide into chloride by stirring an aqueous solution of **(1)** (2.08 g of **(1)** in 30 mL of Milli-Q water with an ion-exchange resin (*ca*. 10 g) for 24 hours at room temperature. The resulting solution was filtered to remove the ion exchange resin, which was then rinsed 2 times with 5 mL of Milli-Q water. The yellow aqueous filtered solution was collected and evaporated *in vacuo* to give pure *N,N,N*-2,2,6,6-heptamethylpiperidinyl oxy-4-ammonium chloride **(2)**. The collected yellow powder was dried in the oven at 80 °C overnight. Yield **(2)**: 90%. The absence of iodide was confirmed by cyclic voltammetry.

Chemical synthesis of N,N,N-2,2,6,6-heptamethylpiperdinyl oxy-4-ammionium chloride (TEMPTMA)

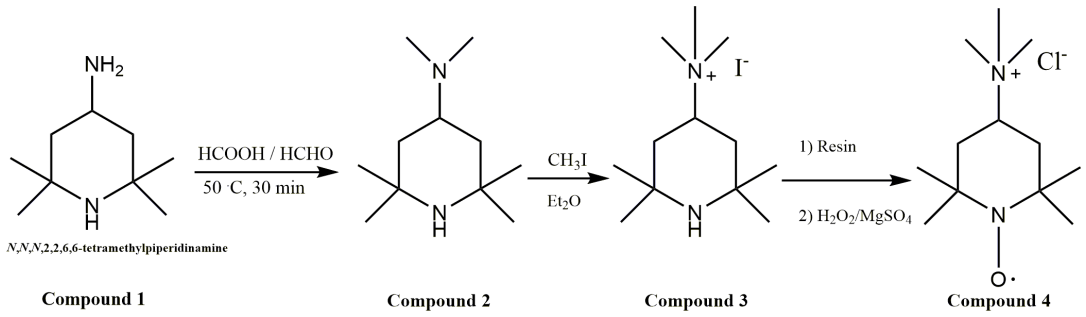

Figure 5.2.1 Synthetic route of N,N,N-2,2,6,6-heptamethylpiperidinyl oxy-4-ammonium chloride (TEMPTMA).

5.2.2.3 Ex-situ synthesis of the MWCNT-CuHCF composite for drop-casting onto glassy carbon electrode

An *ex-situ* composite of MWCNT-CuHCF was synthesized by first sonicating 70 mg of MWCNT for 1 h in 150 mL of DMF in order to obtain a homogeneous black suspension. Then, 30 mg of CuHCF was added to the MWCNT dispersion. The dark suspension was stirred for 24 hours at 80 °C under nitrogen and then filtered onto polytetrafluoroethylene filters (PTFE, Omnipore membrane filters, 0.45 µm JH, Merck Millipore Ltd). The obtained black powder was then dried under vacuum in order to remove any traces of DMF.

5.2.2.4 Ex-situ synthesis of the MWCNT-CuHCF composite for redox battery cycling

An *ex-situ* composite of MWCNT-CuHCF for battery cycling was synthesized by sonicating 10 mg of MWCNT for 1 h in 70 mL of DMF in order to obtain a homogeneous black suspension. Then, 90 mg of CuHCF was added to the MWCNT dispersion. The dark suspension was stirred for 24 hours at 80°C under nitrogen and then filtered onto polytetrafluoroethylene filters (PTFE, Omnipore membrane filters, 0.45 µm JH, Merck Millipore Ltd). The obtained black powder was finally dried under vacuum. The yield of this synthesis is 90%.

5.2.2.5 Ink formulations for the electrochemical characterizations

Table 5.2.1 summarizes the ink formulations used in the electrochemical characterization. All the inks were sonicated for 30 minutes in NMP as solvent. 8µL of the final dispersion was then drop-casted onto a glassy carbon electrode (GCE glassy carbon electrode OD: 6 mm ID: 3 mm, BAS Inc., Japan) and allowed to dry under vacuum for 30 minutes in order to obtain a homogeneous film.

Table 5.2.1: Inks formulation used for the electrochemical characterizations.

Inks	***MWCNT (mg)***	***Carbon Black (mg)***	***CuHCF (mg)***	***NMP (mL)***
MWCNT	5.3	-	-	0.1
Carbon black	-	5.3	-	1
CuHCF	-	-	3	1
CB-CuHCF (30-70) wt%	-	0.9	2.1	1
CNT-CuHCF (30-70) wt%	0.9	-	2.1	1

Ex-situ CNT-CuHCF composite	3	-	-	1
CNT-CuHCF – different amounts of CuHCF	5.3 5.3 5.3	/	0.9 2.1 3.4	1 1 1

5.2.3 Electrochemical characterization

Cyclic voltammetry (CV) was performed in 1 M KCl aqueous solution as supporting electrolyte in the presence of nitrogen, in a regular fume hood. Galvanostatic cycling was performed in 1 M KCl as supporting electrolyte solution in the presence of nitrogen at different current values. Cutoff potentials of +1.10 and +0.41V *vs.* SHE were applied for the charge and discharge processes, respectively. For both electrochemical characterization techniques, a glassy carbon electrode (GCE glassy carbon electrode OD: 6 mm ID: 3 mm, BAS Inc., Japan), with geometric area covered by an ink of solid booster was used as working electrode, an Ag/AgCl in 3 M KCl as reference electrode and a 6 cm coiled platinum wire as auxiliary electrode.

5.2.4 Aqueous organic redox battery

Chronoamperometry was performed in an electrochemical H-cell equipped by a porous glass frit of 2 cm^2 (***Figure 5.2.1a) and b)***). Reticulated vitreous carbon (RVC, 1 cm × 1 cm × 2 cm, 45 pores per inch) was used as a working electrode. The battery experiments were performed using a three-electrochemical cell setup. The working electrode was connected onto the positive side, the counter electrode onto the negative side and an Ag/AgCl (KCl 3M) was used as reference electrode and used to control the electrochemical reaction at the positive side. The electrolyte reservoirs were continuously purged with nitrogen. 10 mM TEMPTMA solution in 1 M KCl was used on the positive side and 0.5 M $ZnCl_2$ solution in 1 M KCl_{aq} was used on the negative side.

The electrolyte volume was fixed at 25 mL on both sides. For the battery test, the positive solution was electrochemically charged at + 1.10 V *vs.* SHE as upper cutoff potential for 12 hours and discharged at + 0.41 V *vs.* SHE for the same amount of time.

The same experiment was then performed in the presence of the solid electrochemical energy storage materials, *e.g.* 100 mg of pristine CuHCF or CNT-CuHCF composite. Once the mediated-electron

transfer was demonstrated, galvanostatic cycling at 2.5 mA cm^{-2} was performed for 25 cycles within the same potential window.

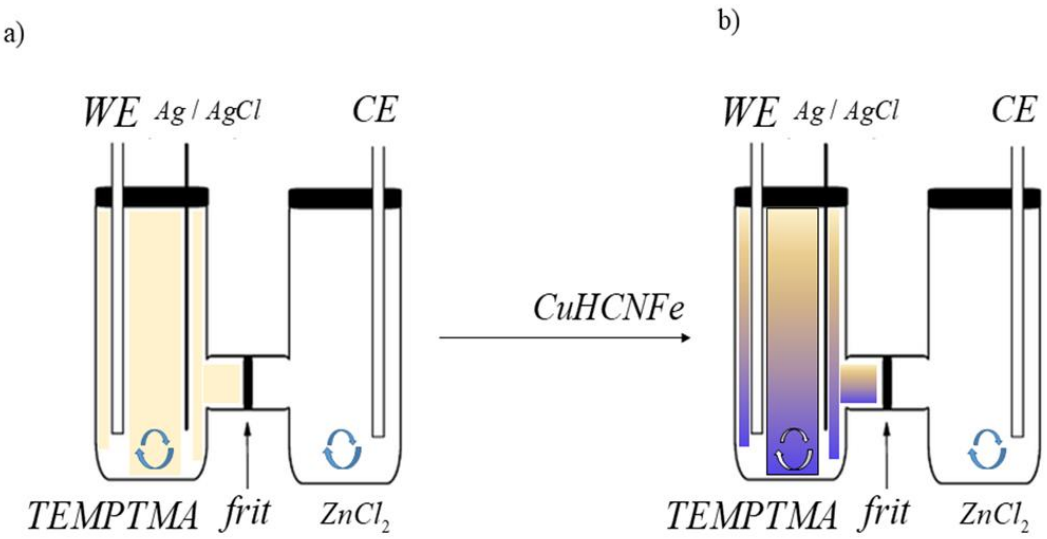

Figure 5.2.2 a) H-cell for electrochemical cycling of TEMPTMA and ZnCl2. b) H-cell configuration after the addition of the booster in the TEMPTMA's tank.

5.2.5 Scanning electron microscopy (SEM) and X-ray photoelectron spectroscopy (XPS)

Scanning electron microscopy (FEI SEM Teneo) images were performed at 1-5 kV, 0.12-1 pA with lower in-lens and in-column detectors. Different samples were imaged after drop-casting on a gold foil. The *ex-situ* composite of CuHCF with MWCNT composition was acquired by XPS. A drop of 20 µL composite or pristine MWCNT was deposited onto glassy carbon electrode and allowed to dry under vacuum. The spectra were calibrated with the C-C bound of the adventitious carbon contamination at 284.8 eV.

5.2.6 Ex-situ Powder X-ray diffraction (PXRD)

PXRD pattern of as-synthesized CuHCF sample was recorded by a Bruker diffractometer with Cu K_α non-monochromic irradiation (λ = 1.5406 Å), operated at 40 kV and 40 mA. Crystal structure with space group Fm-3m was confirmed and diffraction patterns were recorded between 10° and 90° 2θ with a step of 0.01° and 1s of acquisition time per point. Lattice parameter (a = 10.03 ± 0.005 Å) was determined using a Rietveld refinement in TOPAS5 package.

5.2.7 Computational methods

5.2.7.1 Density Functional Theory (DFT)

All calculations where done by Quantum Espresso 6.1.[208] The electrons where described in the formalism of the DFT+U, using projector augmented waves pseudo-potentials and the PBE-Sol exchange and correlation functional. The Hubbard parameter was set to 1 for the iron atoms and 3 for the copper atoms. An energy cut-off of 950 eV was used and a Monkhorst-Pack grid of 4 × 4 × 4 k points (12 × 12 × 12 for the calculations of the electronic properties, *i.e.* density of states and conductivity). A Gaussian smearing of 0.01 Ry was used in every calculation. The geometry of each structure was first optimized (cell and atoms) prior to the calculation of the electronic properties (band structure, density of state, conductivity). The electrical conductivity of the compounds was calculated using the Kubo-Greenwood formula with the help of the KGEC code.[209]

5.2.7.2 COMSOL Simulation

Finite element simulations were performed on COMSOL 5.4. The model based was adapted from the example ”1D Isothermal Nickel-Metal Hydride Battery”,[210] and modified accordingly to study the scan rate dependency of the cyclic voltammetry on the CuHCF composite electrodes.

Section 3: Materials and Methods of Chapter 4: Booster based-negative side electrolyte: a viologen derivative as redox mediator and a polyimide as solid booster

5.3.1 Chemicals and solutions

1,4,5,8-naphtalenetetracarboxilicdianhydride (NTCDA, 97% HPLC, TCI), *N*-methyl-2-pyrrolidone (NMP, 99%, Reagent Grade, Sigma Aldrich), ethylene diamine (EDA, 99.5% GC, TCI), Whatman 597 filter papers (55 mm diameter) and ethanol (99% Reagent Grade, Sigma Aldrich) were utilized for the synthesis of polyamide 1,4,5,8-naphtalenetetracarboxilicdianhydride. The redox-mediator MTABT, was obtained from 4,4'-bipyridinium (BP, TCI), (2-bromoethyl) trimethylammonium bromide (BETMAB, Toronto), acetonitrile (ACN, ACS Reagent Ph. Eur., Merck) and iodomethane (CH_3I, Sigma Aldrich). Potassium chloride (KCl, ACS Reagent, 99-100%) was purchased from Sigma Aldrich. *N*,*N*-dimethylformamid (DMF, ≥ 99.5%) was obtained from Acros Organics. Multi-walled carbon nanotubes (MWCNT, purity ≥ 98%, outer diameter 20-30 nm, length 0.5-2 μm) were purchased from Carbon Nanotubes Plus. Ferrocene methanol ($C_{11}H_{12}FeO$, 97%, Sigma Aldrich). All solvents and reactants were utilized without any further purification. A Millipore filtration system (Merck Millipore, Billerica MA) was used to generate ultrapure water (18.2 MΩ cm^{-1}), from which all aqueous solutions were further prepared. The pH of each aqueous solution was measured with a 744 pH meter probe (Metrohm, Switzerland) and found to be equal to 6.0 at 23°C.

5.3.2 Synthesis

5.3.2.1 Synthesis of MTABT

The synthesis of *MTABT* is elucidated in ***Figure 5.3.2***:

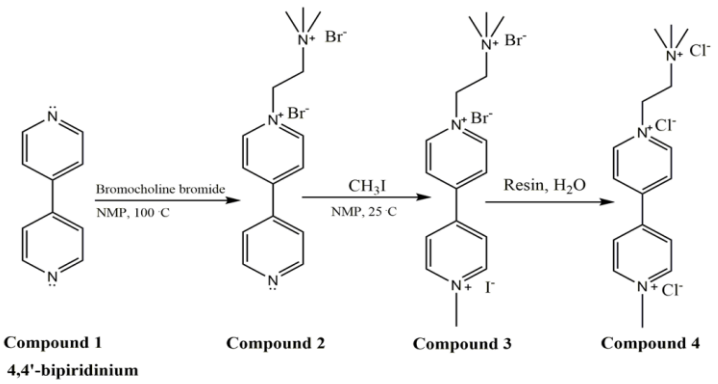

Figure 5.3.1 Synthetic route of MTABT.

The *compound 2* (***Figure 5.3.2***) was synthesized starting from 4,4'-bipyridinium (*compound 1* in ***Figure 5.3.2***), (3 eq.). In a small reactor equipped with magnetic stirrer, 4,4'-bipyridinium was suspended with bromocholine bromide (1 eq.) in *N*-methyl-2-pyrrolidone (NMP) (1 mM). The reaction mix was stirred at 100 °C over 20 h. The reaction was followed by ^{1}H NMR in D_2O. Once bromocholine was entirely consumed, the reaction mix was cooled down and the precipitate was filtered and then washed with 5 mL of NMP and the 5 mL of acetonitrile. The yield of this step is equal to 65%. The filtrate containing *compound 1* (***Figure 5.3.1***) was transferred in a rotavapor in order to eliminate the acetonitrile. Then, 1 eq. of bromocholine bromide was added and the reaction mix was heated up again at 100 °C over 20 h. The yield of this synthesis step is 65%. Later, in a small reactor equipped with magnetic stirrer, the *compound 2* (***Figure 5.3.1***), was suspended in NMP (1 mM) and then in CH_3I is added (2 eq.). The reaction mix became red and a new precipitate formed. The mix was left reacting under vigorous stirring over 2 h at room temperature and the reaction was followed by ^{1}H NMR in D_2O. Once *compound 2* was fully consumed, the precipitate was filtered, washed with NMP (5 mL) and then with acetonitrile (5 mL). The *compound 3* (***Figure 5.3.1***) was finally obtained as a brown solid with a yield of 90%, after dried *in vacuo*.

5.3.2.2 Synthesis of 1,4,5,8-naphthalenetetracarboxylic dianhydride (NTCDA)-derived polyimide (PNTCDA)

A previous procedure involving simple polycondensation was adopted for the synthesis of PNTCDA. Anhydrous N-Methyl-2-pyrrolidone (NMP) (20 mL) was added to the flask and N_2 was poured into it for 30 min, then, 1, 4, 5, 8-napthalenetetracarboxylic dianhydride (1.98 g, 7.383 mmol) and ethylenediamine (0.5 mL, 7.479 mmol) were added into the NMP and mixed with stirring under inert atmosphere. The mixture was heated to reflux at 140 °C overnight followed by filtration and rinsed with ethanol and NMP several times in a turn. The product was dried at 150 °C in an oven for 12 h (~1.52 g). After that, the intermediate polyamic acid was calcined in a tubular furnace at 300 °C for 8 h under nitrogen atmosphere at a ramp rate of 6.5 °C/min to form PNTCDA (~0.53 g).

5.3.2.3 Ex-situ synthesis of the PNTCDA composite

An *ex-situ* composite of \PNTCDA with CNTs was synthesized by sonicating 12.5 mg of MWCNT for 1 h in 70 mL of DMF in order to obtain a homogeneous black suspension. Then, 50 mg of CuHCF was added to the MWCNT dispersion. The dark suspension was stirred for 24 hours at 80°C under nitrogen and then filtered onto polytetrafluoroethylene filters (PTFE, Omnipore membrane filters, 0.45 µm JH, Merck Millipore Ltd). The obtained black powder was finally dried under vacuum. The yield of this synthesis is 90%.

5.3.2.4 Ex-situ synthesis of the PNTCDA composite for drop-casting onto glassy carbon electrode

An *ex-situ* composite of PNTCDA with CNTs was synthesized by first sonicating 70 mg of MWCNT for 1 h in 150 mL of DMF in order to obtain a homogeneous black suspension. Then, 30 mg of CuHCF was added to the MWCNT dispersion. The dark suspension was stirred for 24 hours at 80 °C under nitrogen and then filtered onto polytetrafluoroethylene filters (PTFE, Omnipore membrane filters, 0.45 µm JH, Merck Millipore Ltd). The obtained black powder was then dried under vacuum in order to remove any traces of DMF.

5.3.2.5 Ink formulation of solid boosters on glassy carbon electrode

Table 1 summarizes the composition of each ink. All inks were sonicated for 30 minutes in *N*-methyl-2-pyrrolidone (NMP, 99%, Reagent Grade, Sigma Aldrich) or in *N*,*N*-dimethylformamid (DMF, ≥ 99.5%, Merck). All inks were drop-casted onto glassy carbon electrodes (GCE, OD 6 mm ID 3 mm, BAS Inc., Japan) and allowed to dry under vacuum for 30 minutes in order to obtain a homogeneous film. The modified-GCE were characterized by electrochemistry.

Table 5.3.1: Inks formulation used for the electrochemical characterizations.

Inks	***MWCNT (mg)***	***Polymer (mg)***	***Solvent (mL)***	***Volume drop-casted (µL)***
PNTCDA pristine		6	DMF, 1	4
PNTCDA-CNT composite (*)		5*	DMF, 1	5
CNT blank	5	/	NMP, 0.5	5

(*) The *ex-situ* composite is (25-75) wt. % CNT-polymers.

5.3.2.6 Electrochemical characterization of boosters on glassy carbon electrode

Electrochemical characterizations were recorded with a SP-300°101 potentiostat from Bio-Logic (France) in a three-electrode configuration. The working electrode was a glassy carbon electrode (GCE, glassy carbon electrode, OD 6 mm ID 3 mm, BAS Inc. Japan). A platinum coiled wire (length 2 cm) was used as counter electrode and Ag/AgCl (in KCl 3 M) as reference electrode. The electrochemical characterization was performed in 1 M $KCl_{aq,}$ which was always purged for 1 hour sometimes with nitrogen and sometimes with argon to mitigate oxygen.

5.3.2.7 Galvanostatic cycling of boosters on glassy carbon electrode

Galvanostatic cycling tests with potential limitation (GCPL) were recorded in 1 M KCl aqueous solution only (the solution was always purged as in the case of the CV). In the case of pristine and *ex-situ* composite of PNTCDA, cutoff potentials of 0 and -0.8 V *vs.* SHE were applied for the discharge and the charge processes.

5.3.2.8 Other characterization techniques

i) Scanning electron microscopy (SEM)

Scanning electron microscopy (FEI SEM Teneo) was performed at 1-5 kV, current with lower in-lens and in-column detectors, as well as with ET (Everhart-Thornley) detector. Different samples were imaged as powders immobilized on graphite tape or as homogeneous films drop-casted on gold foils. In these cases, films were obtained by drop casting on gold inks that were dried *in vacuo* to eliminate the solvent.

ii) Fourier-transform infrared spectroscopy (FTIR) and solid-state nuclear magnetic resonance (^{13}C NMR)

Fourier transform infrared spectra were performed using Nicolet 6700 from ThermoFisher Scientific for all the materials.

iii) UV/Visible spectroscopy for solubility determination

The experiment was performed using a UV/Visible spectrometer (Agilent Cary 8545 UV-Vis Diode Array system spectrometer (Agilent Technologies, USA)) preparing four standard solutions of the fully oxidized form of the viologen in 1 M KCl_{aq} supporting electrolyte. The absorbance of each was recorded. These absorbance values allowed building up a calibration curve. Subsequently, a saturated solution of viologen (*i.e.* sample) in 1 M KCl_{aq} was prepared and centrifuged to recover the supernatant. Finally, the supernatant was removed and diluted to fit in the calibration curve of the standard solutions. The initial concentration of the solution was determined using the dilution factors.

5.3.2.9 SECM with UME tip

Scanning electrochemical microscopy (SECM) measurements were carried out on a custom-built SECM set-up comprising a Märzhäuser three-axes positioning system (Märzhäuser GmbH & Co. KG, Wetzlar, Germany), connected to an Ivium Compactstat potentiostat (Ivium Technologies, Eindhoven, The Netherlands).

A homemade Pt UME (Pt 25 µm diameter) was used as working electrode. Electrode diameter was calibrated by studying the steady-state current of 1.5 mM ferrocene methanol in 0.1 mM KCl_{aq} solution. The reference electrode was Ag/AgCl in 3 M KCl and the auxiliary electrode a platinum wire (0.5 mm in diameter, 1 cm length). A homemade electrochemical plastic cell was used for all the experiments. At the bottom of the homemade cell an insulating and then a conducting substrate were placed to record approach curves in feedback mode.

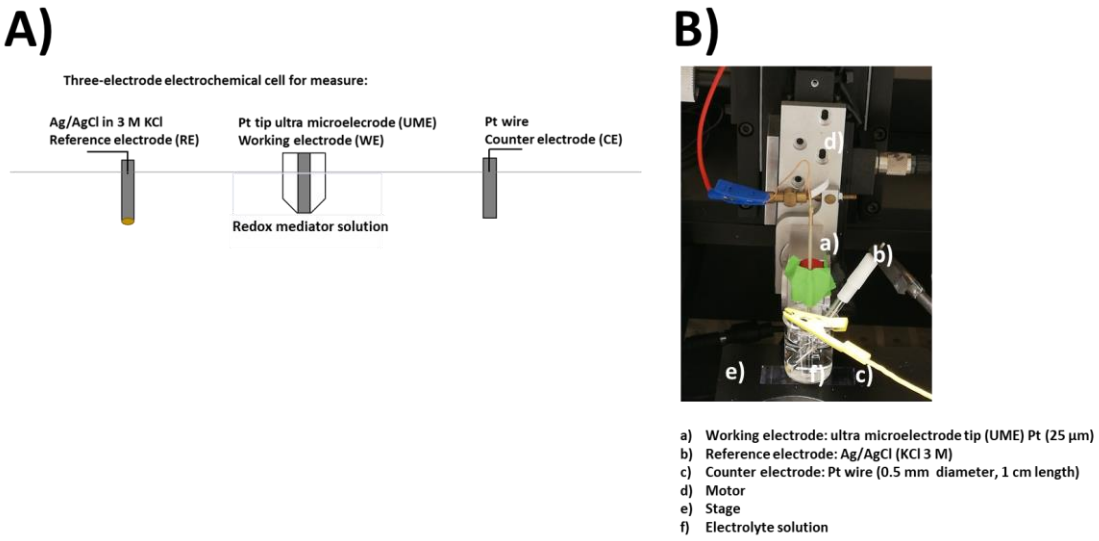

Figure 5.3.2 A) Schematic of the configuration used for the SECM measurements. B) Image of the setup. All the components are detailed in the legend.

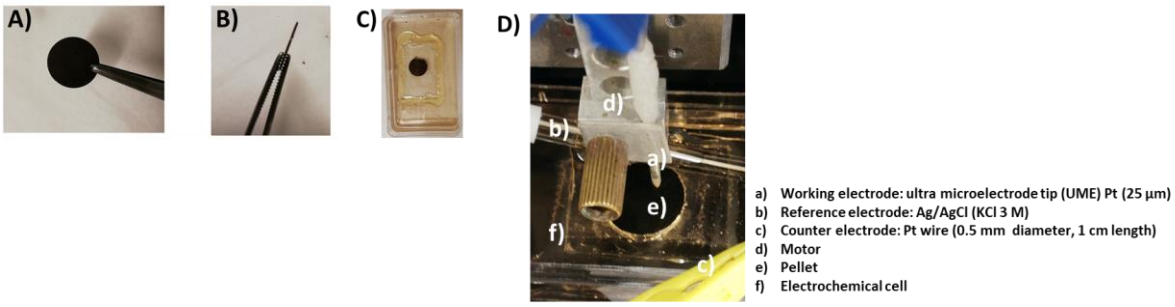

Figure 5.3.3 A) B) Pellets of solid booster PNTCDA (4 mm diameter). The thickness was ca. 1 mm. C) Electrochemical cell for SECM. The pellet sample was secured on a piece of microscope slide glass. D) Real measurement of approach curve with Pt UME towards the pellet of PNTCDA. All the single components are detailed in the legend.

5.3.2.10 Redox flow battery design

The redox flow battery was charged and discharged galvanostatically with potential limitation. The upper cutoff potential was -0.10 V *vs*. SHE and the lowest cutoff potential was -0.50 V *vs*. SHE (the viologen electrolyte was kept as working side along with a reference electrode Ag/AgCl in 3 M KCl with double junction). The flow cell was cycled with 50 mM in 1 M KCl aqueous solution in a glove bag inflated with nitrogen. The electrochemical cell was equipped with polypropylene end plates, silicon gaskets (2 mm thickness), polytetrafluoroethylene gaskets (2 mm thickness), graphite (sometimes changed with titanium at the negative-side) current collectors, graphite felt porous electrodes (3 mm thickness, 8 cm^2 geometric area, pre-treated at 400°C for 4 hours) and an anion-exchange membrane (Selemion, pre-treated in 300 mM aqueous solution since its arrival). The electrochemical cell was equipped with polytetrafluoroethylene tubing (1.5 mm inner diameter) and it was run at 20 $mL \cdot min^{-1}$ with a peristaltic pump (multichannel Ismatech).

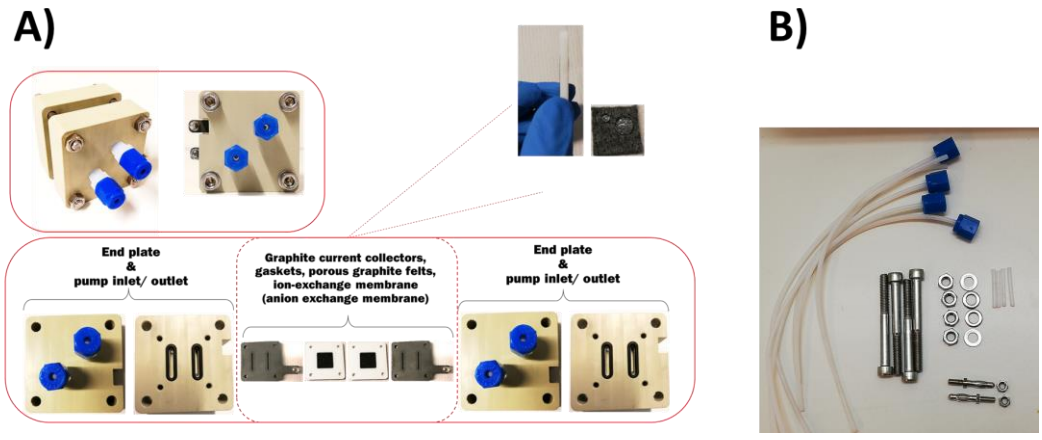

Figure 5.3.4 A) Electrochemical cell components. B) Tubing, nuts and bolts for closing the electrochemical cell and electrode connectors.

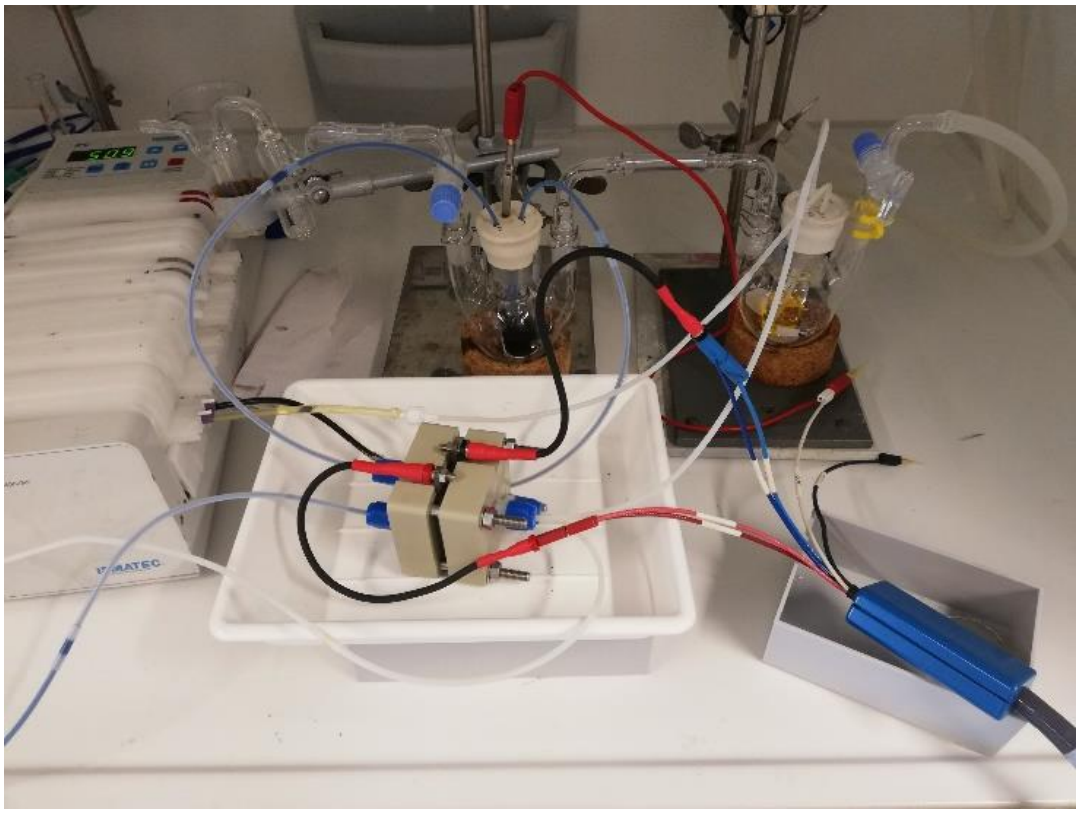

Figure 5.3.5 Photo of the redox flow battery equipped with the peristaltic pump.

Chapter 6

General conclusions and future perspectives

This thesis outlines a promising method to enhance the charge storage in ARFB, which is a fundamental aspect considering further a development of these devices and their outbreak in the energy market. Indeed, ARFB suffer from rather low energy storage density (10-40 Wh L^{-1}) constrained from the solubility limit of the electroactive species dissolved in the electrolytes. The concept developed and demonstrated in this thesis for enhancing the storage capacity in ARFB is based on utilizing solid-phase charge storage materials (herein solid boosters) alongside redox liquid electrolytes (herein redox mediators) in the reservoir. Solid boosters are judiciously chosen and paired to the redox mediators according to the Fermi level position. This promising concept was investigated essentially in two flow batteries, first in an AIRFB and second in an AORFB.

In the AIRFB, the system operated under acidic condition with redox couples ($Fe^{3+/2+}$ at the positive-side and $V^{4+/3+}$ at the negative side), dissolved in 2 M H_2SO_4. This system was cycled at 200 mA and a total charge of 3467 C was obtained (90% of the theoretical value of 3859 C). The $V^{4+/3+}$ redox couple at the negative-side was deemed unsuitable, probably due to sluggish kinetics. Subsequently, in the same system, the viability of pristine PANI as solid booster was tested: *ca*. 7 g of synthesized powder (2 mm in size) was stationary placed at the bottom of a "vertical-bed-packed-reactor". Initially, cycling tests at 200 mA resulted in a 12.8% charge decrease, as compared to the electrolyte alone. This result was attributed to the change in the electronic conductivity of the polymer upon the flow cell cycling, switching from the emeraldine salt to the fully oxidized and reduced forms, which are insulating. In order to mitigate this issue, a new solid booster was synthesized as composite of PANI with CAB in (80-20) wt.%. Cycling tests in the same experimental conditions were performed and this time the electrolyte in presence of the composite PANI-CB booster at 500 mA of current showed a 3-fold charge improvement (84.2 Ah·L^{-1} *vs*. 26.8 Ah·L^{-1}) in the volumetric capacity, as compared to the electrolyte alone. This last cycling test was encouraging and it enhanced the motivation to apply the same approach to an AORFB at neutral pH. Indeed, ARFBs using ROM have been recently attracting considerable attention, especially as good alternative to the VRFB, since they are cost-competitive and earth abundant.

In particular, ROM operating at neutral pH have been investigated in the last five years and they exhibit interesting and promising performances when used in ARFBs, especially because of the possibility of reaching high solubility and redox potentials by synthesis modification with different functional groups. In addition, the operating environment with safe supporting electrolytes such as KCl_{aq}, makes them highly preferable for grid-scale installations.

In this work, TEMPTMA (a derivative of the nitroxyl radical TEMPO), was used at the positive-side and a new synthesized derivative of the MV, the MTABT, at the negative-side of an AORFB at neutral pH. The equivalent system was cycled at 25 mA to preliminarily check the chemical stability of both the electrolytes. The cycling performance was rather poor exhibiting charge fading of *ca*. 54% immediately at the second cycle. In the early stage investigation of the possible electrolyte decomposition mechanisms, the role of O_2 and of the pH were particularly investigated, suggesting that for further cycling tests a fully inert atmosphere and a buffer in the supporting electrolyte solution are required. Nevertheless, in good agreement with the approach of charge storage developed in this thesis to enhance the volumetric capacity of ARFBs, a couple of solid boosters were judiciously found and paired with both these ROM in the electrolyte.

In particular, at the positive-side, CuHCF a Prussian blue analogue, was paired with TEMPTMA and the alignment of the redox potentials was showing just less than 50 mV of difference. The viability of pristine CuHCF as solid booster was evaluated in presence of a rather diluted solution of TEMPTMA, but most importantly, an *ex-situ* composite with CNTs (90-10) wt.% delivered a very stable performance over 25 hours (95% CE and 350 C mL^{-1}), which represent a 10^4 factor of increase , taking into account that the electrolyte concentration was rather small (only 10 mM). At the negative-side of the AORFB at neutral pH, a polyimide (PNTCDA) was chosen because of its robust chemical structure, facile synthetic route and respectable gravimetric capacity in aqueous medium (183 $mAh \cdot g^{-1}$)[189]. In addition, when paired to the candidate viologen (MTABT), only 15 mV of potential difference is observed (considering the first redox wave of the electrolyte), making this couple of material a promising contender for ARFBs. Furthermore, the PNTCDA was electrochemically characterized, confirming an enolisation mechanism in presence of K^+, at two carbonyl positions of the molecule, in good agreement with the literature.[184] Even in this case, an ex-situ composite with CNTs was synthesized and electrochemically tested to mitigate the insulating character of the pristine polymer and it showed enhanced cycling performances (*ca*. 145 $mAh \cdot g^{-1}$ *vs*. *ca*. 35 $mAh \cdot g^{-1}$). Finally, still at early stage, an investigation of the charge transfer mechanism at the solid/liquid interface (booster/mediator) was accomplished by SECM by feedback mode, using a Pt UME. This characterization allowed founding the kinetic constants for the charge transfer at the interface solid/liquid, which for two positions on the PNTCDA sample are equal to ($1.42 \cdot 10^{-3}$ and $7.84 \cdot 10^{-4}$ $cm \cdot s^{-1}$), according to a first order kinetic.[202]

This work opens up to many future perspectives, in particular regarding the choice of the electrolytes for the RFB. It was quite challenging to find a good candidate for the negative-side at neutral pH, thus a possible solution could be to switch to more alkaline pH. In particular, Aziz and co-workers[122] recently proposed a negative-side electrolyte material working at pH 9 (1,1'-bis(3-phosphonopropyl)-[4,4'-bypyridine]-1,1'-diium dibromide). This molecule is highly soluble in the supporting electrolyte at pH 9 and it shows a reasonably good potential for the negative-side of the RFB (−0.42 V *vs*. SHE). Nevertheless, working in 1 M KOH could help to increase the number of candidate electrolytes for both positive and negative-side. In particular, coupling anthraflavic acid (negative-side electrolyte) with a quinone (positive-side electrolyte) could give an ARFB with ~ 0.85 V as cell voltage and ~ 23 Wh/L as volumetric energy density.

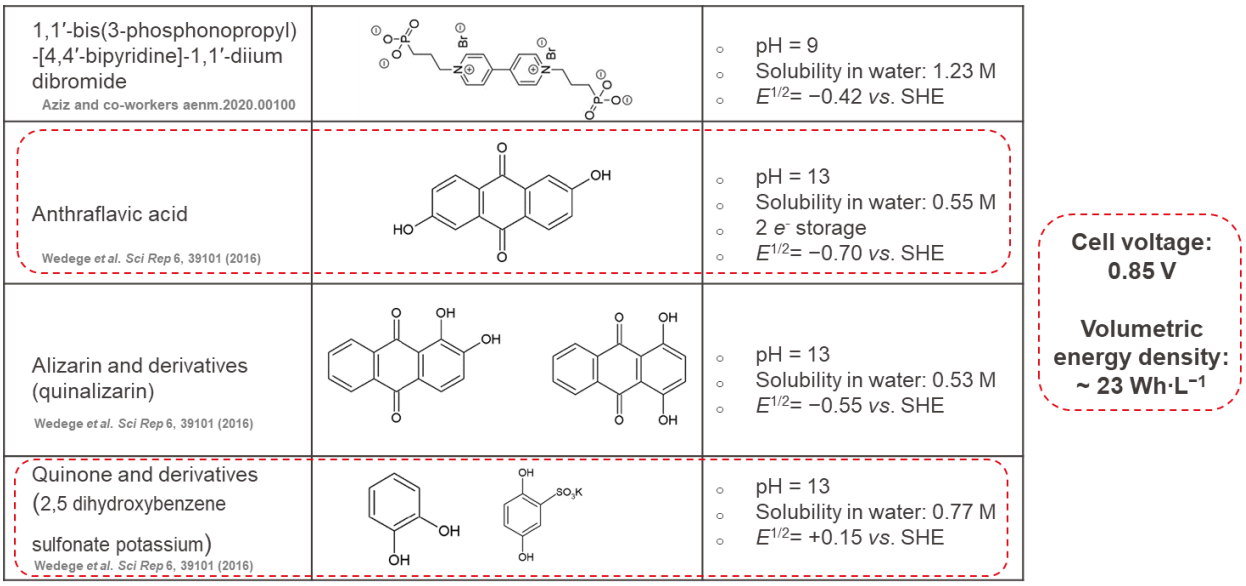

The proposed AORFB with anthraflavic acid and quinone at alkaline pH does still not have a very high energy density, thus it will be interesting to include solid boosters to enhance it. In this regard, PBAs could be a promising option since they are not pH dependent. In particular, it will be interesting to explore other synthesis procedures rather than the quite simple co-precipitation method in order to improve structural and morphological properties of the material, as well as to include multiple center-metals. On the other hand, coating steps in the material preparation will be needed to ensure always good electronic conductivity; therefore CNTs are valid option as demonstrated in this thesis. In addition, polymers can be good coaters to increase the flexibility of the structure.

References

(1) World Energy Outlook 2019 International Energy Agency.
(2) IEA. OECD Total Electricity Statistics International Energy Agency.
(3) IEA. World Transition Indicators International Energy Agency 2019.
(4) Amstutz, V. Redox Flow Battery and Indirect Water Electrolysis. **2015**.
(5) Ibrahim, H.; Ilinca, A.; Perron, J. Energy Storage Systems—Characteristics and Comparisons. *Renew. Sustain. Energy Rev.* **2008**, *12* (5), 1221–1250.
(6) Suberu, M. Y.; Mustafa, M. W.; Bashir, N. Energy Storage Systems for Renewable Energy Power Sector Integration and Mitigation of Intermittency. *Renew. Sustain. Energy Rev.* **2014**, *35*, 499–514.
(7) Reynard, D.; Dennison, C.; Battistel, A.; Girault, H. H. Efficiency Improvement of an All-Vanadium Redox Flow Battery by Harvesting Low-Grade Heat. *J. Power Sources* **2018**, *390*, 30–37.
(8) Schmidt, O.; Melchior, S.; Hawkes, A.; Staffell, I. Projecting the Future Levelized Cost of Electricity Storage Technologies. *Joule* **2019**, *3* (1), 81–100.
(9) Pires, V. F.; Romero-Cadaval, E.; Vinnikov, D.; Roasto, I.; Martins, J. Power Converter Interfaces for Electrochemical Energy Storage Systems–A Review. *Energy Convers. Manag.* **2014**, *86*, 453–475.
(10) Leadbetter, J.; Swan, L. Battery Storage System for Residential Electricity Peak Demand Shaving. *Energy Build.* **2012**, *55*, 685–692.
(11) Cowie, I. All About Batteries, Part 3: Lead-Acid Batteries. *EE Times Httpswww Eetimes Comauthor Asp* **2014**.
(12) Breeze, P. *Power System Energy Storage Technologies*; Academic Press, 2018.
(13) Huff, G. *DOE Global Energy Storage Database.*; Sandia National Lab.(SNL-NM), Albuquerque, NM (United States), 2015.
(14) Baxter, R. *Energy Storage: A Nontechnical Guide*; PennWell Books, 2006.
(15) Zubi, G.; Dufo-López, R.; Carvalho, M.; Pasaoglu, G. The Lithium-Ion Battery: State of the Art and Future Perspectives. *Renew. Sustain. Energy Rev.* **2018**, *89*, 292–308.
(16) An, S. J.; Li, J.; Daniel, C.; Mohanty, D.; Nagpure, S.; Wood III, D. L. The State of Understanding of the Lithium-Ion-Battery Graphite Solid Electrolyte Interphase (SEI) and Its Relationship to Formation Cycling. *Carbon* **2016**, *105*, 52–76.
(17) Wen, J.; Yu, Y.; Chen, C. A Review on Lithium-Ion Batteries Safety Issues: Existing Problems and Possible Solutions. *Mater. Express* **2012**, *2* (3), 197–212.
(18) Stevens, D.; Dahn, J. High Capacity Anode Materials for Rechargeable Sodium-ion Batteries. *J. Electrochem. Soc.* **2000**, *147* (4), 1271.
(19) Senguttuvan, P.; Rousse, G.; Seznec, V.; Tarascon, J.-M.; Palacin, M. R. Na2Ti3O7: Lowest Voltage Ever Reported Oxide Insertion Electrode for Sodium Ion Batteries. *Chem. Mater.* **2011**, *23* (18), 4109–4111.
(20) Wu, D.; Li, X.; Xu, B.; Twu, N.; Liu, L.; Ceder, G. NaTiO 2: A Layered Anode Material for Sodium-Ion Batteries. *Energy Environ. Sci.* **2015**, *8* (1), 195–202.
(21) Keller, M.; Buchholz, D.; Passerini, S. Layered Na-Ion Cathodes with Outstanding Performance Resulting from the Synergetic Effect of Mixed P-and O-Type Phases. *Adv. Energy Mater.* **2016**, *6* (3), 1501555.

(22) Lu, Y.; Wang, L.; Cheng, J.; Goodenough, J. B. Prussian Blue: A New Framework of Electrode Materials for Sodium Batteries. *Chem. Commun.* **2012**, *48* (52), 6544–6546.
(23) Song, J.; Wang, L.; Lu, Y.; Liu, J.; Guo, B.; Xiao, P.; Lee, J.-J.; Yang, X.-Q.; Henkelman, G.; Goodenough, J. B. Removal of Interstitial H2O in Hexacyanometallates for a Superior Cathode of a Sodium-Ion Battery. *J. Am. Chem. Soc.* **2015**, *137* (7), 2658–2664.
(24) Bauer, A.; Song, J.; Vail, S.; Pan, W.; Barker, J.; Lu, Y. The Scale-up and Commercialization of Nonaqueous Na-Ion Battery Technologies. *Adv. Energy Mater.* **2018**, *8* (17), 1702869.
(25) Kwabi, D. G.; Ji, Y.; Aziz, M. J. Electrolyte Lifetime in Aqueous Organic Redox Flow Batteries: A Critical Review. *Chem. Rev.* **2020**.
(26) Skyllas-Kazacos, M. Electro-Chemical Energy Storage Technologies for Wind Energy Systems. In *Stand-alone and hybrid wind energy systems*; Elsevier, 2010; pp 323–365.
(27) Skyllas-Kazacos, M.; Menictas, C.; Lim, T. Redox Flow Batteries for Medium-to Large-Scale Energy Storage. In *Electricity transmission, distribution and storage systems*; Elsevier, 2013; pp 398–441.
(28) Jalan, V.; Stark, H.; Giner, J. Requirements for Optimization of Electrodes and Electrolyte for the Iron/Chromium Redox Flow Cell. **1981**.
(29) Bard, A. J.; Faulkner, L. R.; Leddy, J.; Zoski, C. G. *Electrochemical Methods: Fundamentals and Applications*; Wiley New York, 1980; Vol. 2.
(30) Girault, H. H. *Electrochimie Physique et Analytique*; PPUR presses polytechniques, 2007.
(31) Park, M.; Ryu, J.; Wang, W.; Cho, J. Material Design and Engineering of Next-Generation Flow-Battery Technologies. *Nat. Rev. Mater.* **2016**, *2* (1), 1–18.
(32) Forner-Cuenca, A.; Brushetta, F. R. Engineering Porous Electrodes for Next-Generation Redox Flow Batteries: Recent Progress and Opportunities. *Curr. Opin. Electrochem.* **2019**.
(33) Rychcik, M.; Skyllas-Kazacos, M. Evaluation of Electrode Materials for Vanadium Redox Cell. *J. Power Sources* **1987**, *19* (1), 45–54.
(34) Li, X.; Zhang, H.; Mai, Z.; Zhang, H.; Vankelecom, I. Ion Exchange Membranes for Vanadium Redox Flow Battery (VRB) Applications. *Energy Environ. Sci.* **2011**, *4* (4), 1147–1160.
(35) Sillanpää, M.; Shestakova, M. *Electrochemical Water Treatment Methods: Fundamentals, Methods and Full Scale Applications*; Butterworth-Heinemann, 2017.
(36) Schwenzer, B.; Zhang, J.; Kim, S.; Li, L.; Liu, J.; Yang, Z. Membrane Development for Vanadium Redox Flow Batteries. *ChemSusChem* **2011**, *4* (10), 1388–1406.
(37) Larminie, J.; Dicks, A.; McDonald, M. S. *Fuel Cell Systems Explained*; J. Wiley Chichester, UK, 2003; Vol. 2.
(38) Shi, W.; Baker, L. A. Imaging Heterogeneity and Transport of Degraded Nafion Membranes. *Rsc Adv.* **2015**, *5* (120), 99284–99290.
(39) Ran, J.; Wu, L.; Ru, Y.; Hu, M.; Din, L.; Xu, T. Anion Exchange Membranes (AEMs) Based on Poly (2, 6-Dimethyl-1, 4-Phenylene Oxide)(PPO) and Its Derivatives. *Polym. Chem.* **2015**, *6* (32), 5809–5826.
(40) Amstutz, V. *Redox Flow Battery and Indirect Water Electrolysis*; EPFL, 2015.
(41) Yang, Z.; Zhang, J.; Kintner-Meyer, M. C.; Lu, X.; Choi, D.; Lemmon, J. P.; Liu, J. Electrochemical Energy Storage for Green Grid. *Chem. Rev.* **2011**, *111* (5), 3577–3613.
(42) Kim, K. J.; Park, M.-S.; Kim, Y.-J.; Kim, J. H.; Dou, S. X.; Skyllas-Kazacos, M. A Technology Review of Electrodes and Reaction Mechanisms in Vanadium Redox Flow Batteries. *J. Mater. Chem. A* **2015**, *3* (33), 16913–16933.

(43) Piwek, J.; Dennison, C.; Frackowiak, E.; Girault, H.; Battistel, A. Vanadium-Oxygen Cell for Positive Electrolyte Discharge in Dual-Circuit Vanadium Redox Flow Battery. *J. Power Sources* **2019**, *439*, 227075.
(44) Amstutz, V.; Toghill, K. E.; Powlesland, F.; Vrubel, H.; Comninellis, C.; Hu, X.; Girault, H. H. Renewable Hydrogen Generation from a Dual-Circuit Redox Flow Battery. *Energy Environ. Sci.* **2014**, *7* (7), 2350–2358.
(45) Janoschka, T.; Morgenstern, S.; Hiller, H.; Friebe, C.; Wolkersdörfer, K.; Häupler, B.; Hager, M.; Schubert, U. Synthesis and Characterization of TEMPO-and Viologen-Polymers for Water-Based Redox-Flow Batteries. *Polym. Chem.* **2015**, *6* (45), 7801–7811.
(46) Winsberg, J.; Janoschka, T.; Morgenstern, S.; Hagemann, T.; Muench, S.; Hauffman, G.; Gohy, J.; Hager, M. D.; Schubert, U. S. Poly (TEMPO)/Zinc Hybrid-Flow Battery: A Novel,"Green," High Voltage, and Safe Energy Storage System. *Adv. Mater.* **2016**, *28* (11), 2238–2243.
(47) Gentil, S.; Reynard, D.; Girault, H. H. Aqueous Organic and Redox-Mediated Redox Flow Batteries: A Review. *Curr. Opin. Electrochem.* **2020**.
(48) Janoschka, T.; Martin, N.; Martin, U.; Friebe, C.; Morgenstern, S.; Hiller, H.; Hager, M. D.; Schubert, U. S. An Aqueous, Polymer-Based Redox-Flow Battery Using Non-Corrosive, Safe, and Low-Cost Materials. *Nature* **2015**, *527* (7576), 78–81.
(49) Winsberg, J.; Hagemann, T.; Janoschka, T.; Hager, M. D.; Schubert, U. S. Redox-flow Batteries: From Metals to Organic Redox-active Materials. *Angew. Chem. Int. Ed.* **2017**, *56* (3), 686–711.
(50) Janoschka, T.; Martin, N.; Martin, U.; Friebe, C.; Morgenstern, S.; Hiller, H.; Hager, M. D.; Schubert, U. S. An Aqueous, Polymer-Based Redox-Flow Battery Using Non-Corrosive, Safe, and Low-Cost Materials. *Nature* **2015**, *527* (7576), 78–81.
(51) Janoschka, T.; Martin, N.; Hager, M. D.; Schubert, U. S. An Aqueous Redox-flow Battery with High Capacity and Power: The TEMPTMA/MV System. *Angew. Chem. Int. Ed.* **2016**, *55* (46), 14427–14430.
(52) Hu, B.; DeBruler, C.; Rhodes, Z.; Liu, T. L. Long-Cycling Aqueous Organic Redox Flow Battery (AORFB) toward Sustainable and Safe Energy Storage. *J. Am. Chem. Soc.* **2017**, *139* (3), 1207–1214.
(53) Zanzola, E.; Dennison, C. R.; Battistel, A.; Peljo, P.; Vrubel, H.; Amstutz, V.; Girault, H. H. Redox Solid Energy Boosters for Flow Batteries: Polyaniline as a Case Study. *Electrochimica Acta* **2017**, *235*, 664–671.
(54) Singh, V.; Kim, S.; Kang, J.; Byon, H. R. Aqueous Organic Redox Flow Batteries. *Nano Res.* **2019**, 1–14.
(55) Gerhardt, M. R.; Tong, L.; Gómez-Bombarelli, R.; Chen, Q.; Marshak, M. P.; Galvin, C. J.; Aspuru-Guzik, A.; Gordon, R. G.; Aziz, M. J. Anthraquinone Derivatives in Aqueous Flow Batteries. *Adv. Energy Mater.* **2017**, *7* (8), 1601488.
(56) Kwabi, D. G.; Lin, K.; Ji, Y.; Kerr, E. F.; Goulet, M.-A.; De Porcellinis, D.; Tabor, D. P.; Pollack, D. A.; Aspuru-Guzik, A.; Gordon, R. G. Alkaline Quinone Flow Battery with Long Lifetime at PH 12. *Joule* **2018**, *2* (9), 1894–1906.
(57) Beh, E. S.; De Porcellinis, D.; Gracia, R. L.; Xia, K. T.; Gordon, R. G.; Aziz, M. J. A Neutral PH Aqueous Organic–Organometallic Redox Flow Battery with Extremely High Capacity Retention. *ACS Energy Lett.* **2017**, *2* (3), 639–644.

(58) Huang, J.; Yang, Z.; Murugesan, V.; Walter, E.; Hollas, A.; Pan, B.; Assary, R. S.; Shkrob, I. A.; Wei, X.; Zhang, Z. Spatially Constrained Organic Diquat Anolyte for Stable Aqueous Flow Batteries. *ACS Energy Lett.* **2018**, *3* (10), 2533–2538.
(59) Zanzola, E.; Gentil, S.; Gschwend, G.; Reynard, D.; Smirnov, E.; Dennison, C.; Girault, H. H.; Peljo, P. Solid Electrochemical Energy Storage for Aqueous Redox Flow Batteries: The Case of Copper Hexacyanoferrate. *Electrochimica Acta* **2019**, *321*, 134704.
(60) Striepe, L.; Baumgartner, T. Viologens and Their Application as Functional Materials. *Chem. Eur. J.* **2017**, *23* (67), 16924–16940.
(61) Ding, J.; Zheng, C.; Wang, L.; Lu, C.; Zhang, B.; Chen, Y.; Li, M.; Zhai, G.; Zhuang, X. Viologen-Inspired Functional Materials: Synthetic Strategies and Applications. *J. Mater. Chem. A* **2019**, *7* (41), 23337–23360.
(62) Pande, G. K.; Kim, N.; Choi, J. H.; Balamurugan, G.; Moon, H. C.; Park, J. S. Effects of Counter Ions on Electrochromic Behaviors of Asymmetrically Substituted Viologens. *Sol. Energy Mater. Sol. Cells* **2019**, *197*, 25–31.
(63) Savin, K. A. *Writing Reaction Mechanisms in Organic Chemistry*; Academic Press, 2014.
(64) Smith, P.; Heath, D.; Fishman, A. P. Paraquat. *CRC Crit. Rev. Toxicol.* **1976**, *4* (4), 411–445.
(65) Tsai, W.-T. A Review on Environmental Exposure and Health Risks of Herbicide Paraquat. *Toxicol. Environ. Chem.* **2013**, *95* (2), 197–206.
(66) Zielonka, J.; Rybak, M.; Celińska, J.; Adamus, J.; Marcinek, A.; Gebicki, J. Effect of Heparin on Viologen-Stimulated Enzymatic NADH Depletion. *Chem. Res. Toxicol.* **2006**, *19* (5), 668–673.
(67) Hayyan, M.; Hashim, M. A.; AlNashef, I. M. Superoxide Ion: Generation and Chemical Implications. *Chem. Rev.* **2016**, *116* (5), 3029–3085.
(68) Keyer, K.; Imlay, J. A. Superoxide Accelerates DNA Damage by Elevating Free-Iron Levels. *Proc. Natl. Acad. Sci.* **1996**, *93* (24), 13635–13640.
(69) Dennison, C. R.; Vrubel, H.; Amstutz, V.; Peljoa, P.; Toghill, K. E.; Girault, H. H. Redox Flow Batteries, Hydrogen and Distributed Storage. *Chim. Int. J. Chem.* **2015**, *69* (12), 753–758.
(70) Vijayakumar, M.; Wang, W.; Nie, Z.; Sprenkle, V.; Hu, J. Elucidating the Higher Stability of Vanadium (V) Cations in Mixed Acid Based Redox Flow Battery Electrolytes. *J. Power Sources* **2013**, *241*, 173–177.
(71) Wen, Y.; Xu, Y.; Cheng, J.; Cao, G.; Yang, Y. Investigation on the Stability of Electrolyte in Vanadium Flow Batteries. *Electrochimica Acta* **2013**, *96*, 268–273.
(72) Wuu, Y.; Fan, F. F.; Bard, A. J. High Resolution Deposition of Polyaniline on Pt with the Scanning Electrochemical Microscope. *J. Electrochem. Soc.* **1989**, *136* (3), 885–886.
(73) Skyllas-Kazacos, M.; Peng, C.; Cheng, M. Evaluation of Precipitation Inhibitors for Supersaturated Vanadyl Electrolytes for the Vanadium Redox Battery. *Electrochem. Solid-State Lett.* **1999**, *2* (3), 121–122.
(74) Lei, Y.; Liu, S.; Gao, C.; Liang, X.; He, Z.; Deng, Y.; He, Z. Effect of Amino Acid Additives on the Positive Electrolyte of Vanadium Redox Flow Batteries. *J. Electrochem. Soc.* **2013**, *160* (4), A722–A727.
(75) Wang, W.; Li, L.; Nie, Z.; Chen, B.; Luo, Q.; Shao, Y.; Wei, X.; Chen, F.; Xia, G.-G.; Yang, Z. A New Hybrid Redox Flow Battery with Multiple Redox Couples. *J. Power Sources* **2012**, *216*, 99–103.

(76) Huskinson, B.; Marshak, M. P.; Suh, C.; Er, S.; Gerhardt, M. R.; Galvin, C. J.; Chen, X.; Aspuru-Guzik, A.; Gordon, R. G.; Aziz, M. J. A Metal-Free Organic-Inorganic Aqueous Flow Battery. *Nature* **2014**, *505* (7482), 195–198.
(77) Pratt, H. D.; Hudak, N. S.; Fang, X.; Anderson, T. M. A Polyoxometalate Flow Battery. *J. Power Sources* **2013**, *236*, 259–264.
(78) Colli, A. N.; Peljo, P.; Girault, H. H. High Energy Density MnO 4−/MnO 4 2− Redox Couple for Alkaline Redox Flow Batteries. *Chem. Commun.* **2016**, *52* (97), 14039–14042.
(79) Duduta, M.; Ho, B.; Wood, V. C.; Limthongkul, P.; Brunini, V. E.; Carter, W. C.; Chiang, Y. Semi-Solid Lithium Rechargeable Flow Battery. *Adv. Energy Mater.* **2011**, *1* (4), 511–516.
(80) Dennison, C. R.; Gogotsi, Y.; Kumbur, E. C. In Situ Distributed Diagnostics of Flowable Electrode Systems: Resolving Spatial and Temporal Limitations. *Phys. Chem. Chem. Phys.* **2014**, *16* (34), 18241–18252.
(81) Wang, Q.; Zakeeruddin, S. M.; Wang, D.; Exnar, I.; Grätzel, M. Redox Targeting of Insulating Electrode Materials: A New Approach to High-Energy-Density Batteries. *Angew. Chem.* **2006**, *118* (48), 8377–8380.
(82) Zhao, Y.; Ding, Y.; Li, Y.; Peng, L.; Byon, H. R.; Goodenough, J. B.; Yu, G. A Chemistry and Material Perspective on Lithium Redox Flow Batteries towards High-Density Electrical Energy Storage. *Chem. Soc. Rev.* **2015**, *44* (22), 7968–7996.
(83) Jia, C.; Pan, F.; Zhu, Y. G.; Huang, Q.; Lu, L.; Wang, Q. High–Energy Density Nonaqueous All Redox Flow Lithium Battery Enabled with a Polymeric Membrane. *Sci. Adv.* **2015**, *1* (10), e1500886.
(84) Peljo, P.; Vrubel, H.; Amstutz, V.; Pandard, J.; Morgado, J.; Santasalo-Aarnio, A.; Lloyd, D.; Gumy, F.; Dennison, C. R.; Toghill, K. E. All-Vanadium Dual Circuit Redox Flow Battery for Renewable Hydrogen Generation and Desulfurisation. *Green Chem.* **2016**, *18* (6), 1785–1797.
(85) Leung, P.; Li, X.; De León, C. P.; Berlouis, L.; Low, C. T. J.; Walsh, F. C. Progress in Redox Flow Batteries, Remaining Challenges and Their Applications in Energy Storage. *Rsc Adv.* **2012**, *2* (27), 10125–10156.
(86) Scanlon, M. D.; Peljo, P.; Méndez, M. A.; Smirnov, E.; Girault, H. H. Charging and Discharging at the Nanoscale: Fermi Level Equilibration of Metallic Nanoparticles. *Chem. Sci.* **2015**, *6* (5), 2705–2720.
(87) Peljo, P.; Girault, H. H. Electrochemical Potential Window of Battery Electrolytes: The HOMO–LUMO Misconception. *Energy Environ. Sci.* **2018**, *11* (9), 2306–2309.
(88) Horie, K.; Barón, M.; Fox, R.; He, J.; Hess, M.; Kahovec, J.; Kitayama, T.; Kubisa, P.; Maréchal, E.; Mormann, W. Definitions of Terms Relating to Reactions of Polymers and to Functional Polymeric Materials (IUPAC Recommendations 2003). *Pure Appl. Chem.* **2004**, *76* (4), 889–906.
(89) Casado, N.; Hernandez, G.; Sardon, H.; Mecerreyes, D. Current Trends in Redox Polymers for Energy and Medicine. *Prog. Polym. Sci.* **2016**, *52*, 107–135.
(90) Kim, J.; Kim, J. H.; Ariga, K. Redox-Active Polymers for Energy Storage Nanoarchitectonics. *Joule* **2017**, *1* (4), 739–768.
(91) Yurash, B.; Cao, D. X.; Brus, V. V.; Leifert, D.; Wang, M.; Dixon, A.; Seifrid, M.; Mansour, A. E.; Lungwitz, D.; Liu, T. Towards Understanding the Doping Mechanism of Organic Semiconductors by Lewis Acids. *Nat. Mater.* **2019**, *18* (12), 1327–1334.

(92) Su, C.; Wang, L.; Xu, L.; Zhang, C. Synthesis of a Novel Ferrocene-Contained Polypyrrole Derivative and Its Performance as a Cathode Material for Li-Ion Batteries. *Electrochimica Acta* **2013**, *104*, 302–307.
(93) Luo, Y.; Guo, R.; Li, T.; Li, F.; Liu, Z.; Zheng, M.; Wang, B.; Yang, Z.; Luo, H.; Wan, Y. Application of Polyaniline for Li-Ion Batteries, Lithium–Sulfur Batteries, and Supercapacitors. *ChemSusChem* **2019**, *12* (8), 1591–1611.
(94) Hu, J.; Jia, F.; Song, Y.-F. Engineering High-Performance Polyoxometalate/PANI/MWNTs Nanocomposite Anode Materials for Lithium Ion Batteries. *Chem. Eng. J.* **2017**, *326*, 273–280.
(95) Ge, D.; Yang, L.; Honglawan, A.; Li, J.; Yang, S. In Situ Synthesis of Hybrid Aerogels from Single-Walled Carbon Nanotubes and Polyaniline Nanoribbons as Free-Standing, Flexible Energy Storage Electrodes. *Chem. Mater.* **2014**, *26* (4), 1678–1685.
(96) Mohanty, S.; Nayak, S. K.; Kaith, B.; Kalia, S. *Polymer Nanocomposites Based on Inorganic and Organic Nanomaterials*; John Wiley & Sons, 2015.
(97) Shimizu, A.; Kuramoto, H.; Tsujii, Y.; Nokami, T.; Inatomi, Y.; Hojo, N.; Suzuki, H.; Yoshida, J. Introduction of Two Lithiooxycarbonyl Groups Enhances Cyclability of Lithium Batteries with Organic Cathode Materials. *J. Power Sources* **2014**, *260*, 211–217.
(98) Lu, Y.; Zhao, Q.; Miao, L.; Tao, Z.; Niu, Z.; Chen, J. Flexible and Free-Standing Organic/Carbon Nanotubes Hybrid Films as Cathode for Rechargeable Lithium-Ion Batteries. *J. Phys. Chem. C* **2017**, *121* (27), 14498–14506.
(99) Schon, T. B.; McAllister, B. T.; Li, P.-F.; Seferos, D. S. The Rise of Organic Electrode Materials for Energy Storage. *Chem. Soc. Rev.* **2016**, *45* (22), 6345–6404.
(100) Lai, Y. Y.; Li, X.; Zhu, Y. Polymeric Active Materials for Redox Flow Battery Application. *ACS Appl. Polym. Mater.* **2020**.
(101) Sukegawa, T.; Masuko, I.; Oyaizu, K.; Nishide, H. Expanding the Dimensionality of Polymers Populated with Organic Robust Radicals toward Flow Cell Application: Synthesis of TEMPO-Crowded Bottlebrush Polymers Using Anionic Polymerization and ROMP. *Macromolecules* **2014**, *47* (24), 8611–8617.
(102) Nagarjuna, G.; Hui, J.; Cheng, K. J.; Lichtenstein, T.; Shen, M.; Moore, J. S.; Rodríguez-López, J. Impact of Redox-Active Polymer Molecular Weight on the Electrochemical Properties and Transport across Porous Separators in Nonaqueous Solvents. *J. Am. Chem. Soc.* **2014**, *136* (46), 16309–16316.
(103) Molapo, K. M.; Ndangili, P. M.; Ajayi, R. F.; Mbambisa, G.; Mailu, S. M.; Njomo, N.; Masikini, M.; Baker, P.; Iwuoha, E. I. Electronics of Conjugated Polymers (I): Polyaniline. **2012**.
(104) Stafström, S.; Bredas, J.; Epstein, A.; Woo, H.; Tanner, D.; Huang, W.; MacDiarmid, A. Polaron Lattice in Highly Conducting Polyaniline: Theoretical and Optical Studies. *Phys. Rev. Lett.* **1987**, *59* (13), 1464.
(105) López-Palacios, J.; Muñoz, E.; Heras, M. A.; Colina, Á.; Ruiz, V. Study of Polyaniline Films Degradation by Thin-Layer Bidimensional Spectroelectrochemistry. *Electrochimica Acta* **2006**, *52* (1), 234–239.
(106) Bhadra, S.; Khastgir, D.; Singha, N. K.; Lee, J. H. Progress in Preparation, Processing and Applications of Polyaniline. *Prog. Polym. Sci.* **2009**, *34* (8), 783–810.
(107) Gao, M.; Yang, Y.; Diao, M.; Wang, S.; Wang, X.; Zhang, G.; Zhang, G. Exceptional Ion-Exchange Selectivity for Perchlorate Based on Polyaniline Films. *Electrochimica Acta* **2011**, *56* (22), 7644–7650.

(108) Tanguy, N. R.; Thompson, M.; Yan, N. A Review on Advances in Application of Polyaniline for Ammonia Detection. *Sens. Actuators B Chem.* **2018**, *257*, 1044–1064.
(109) Choi, H. J.; Cho, M. S.; To, K. Electrorheological and Dielectric Characteristics of Semiconductive Polyaniline-Silicone Oil Suspensions. *Phys. Stat. Mech. Its Appl.* **1998**, *254* (1), 272–279.
(110) Al-Dulaimi, A.; Hashim, S.; Abdulrazak, L. F.; Husham, M. Electrical Conductive Polyaniline in Various Nanostructures for Corrosion Inhibition of Carbon Steel. *J Mech Eng Sci* **2018**, *12* (2), 3738–3749.
(111) Thyssen, A.; Borgerding, A.; W Schultze, J. Formation and Electronic Conductivity of Polyaniline. In *Makromolekulare Chemie. Macromolecular Symposia*; Wiley Online Library, 1987; Vol. 8, pp 143–157.
(112) Wei, Y.; Jang, G. W.; Chan, C. C.; Hsueh, K. F.; Hariharan, R.; Patel, S. A.; Whitecar, C. K. Polymerization of Aniline and Alkyl Ring-Substituted Anilines in the Presence of Aromatic Additives. *J. Phys. Chem.* **1990**, *94* (19), 7716–7721.
(113) Lippe, J.; Holze, R. The Anion-Specific Effect in the Overoxidation of Polyaniline and Polyindoline. *J. Electroanal. Chem.* **1992**, *339* (1–2), 411–422.
(114) Stilwell, D. E.; Park, S. Electrochemistry of Conductive Polymers: VI. Degradation Reaction Kinetics of Polyaniline Studied by Rotating Ring-disk Electrode Techniques. *J. Electrochem. Soc.* **1989**, *136* (3), 688.
(115) Tang, H.; Kitani, A.; Shiotani, M. Effects of Anions on Electrochemical Formation and Overoxidation of Polyaniline. *Electrochimica Acta* **1996**, *41* (9), 1561–1567.
(116) Focke, W. W.; Wnek, G. E.; Wei, Y. Influence of Oxidation State, PH, and Counterion on the Conductivity of Polyaniline. *J. Phys. Chem.* **1987**, *91* (22), 5813–5818.
(117) Angelopoulos, M.; Ray, A.; Macdiarmid, A. G.; Epstein, A. J. Polyaniline: Processability from Aqueous Solutions and Effect of Water Vapor on Conductivity. *Synth. Met.* **1987**, *21* (1–3), 21–30.
(118) McManus, P. M.; Yang, S. C.; Cushman, R. J. Electrochemical Doping of Polyaniline: Effects on Conductivity and Optical Spectra. *J. Chem. Soc. Chem. Commun.* **1985**, No. 22, 1556–1557.
(119) MacDiarmid, A. G.; Epstein, A. J. Polyanilines: A Novel Class of Conducting Polymers. *Faraday Discuss. Chem. Soc.* **1989**, *88*, 317–332.
(120) Beh, E. S.; De Porcellinis, D.; Gracia, R. L.; Xia, K. T.; Gordon, R. G.; Aziz, M. J. A Neutral PH Aqueous Organic–Organometallic Redox Flow Battery with Extremely High Capacity Retention. *ACS Energy Lett.* **2017**, *2* (3), 639–644.
(121) Huskinson, B.; Marshak, M. P.; Suh, C.; Er, S.; Gerhardt, M. R.; Galvin, C. J.; Chen, X.; Aspuru-Guzik, A.; Gordon, R. G.; Aziz, M. J. A Metal-Free Organic–Inorganic Aqueous Flow Battery. *Nature* **2014**, *505* (7482), 195–198.
(122) Ji, Y.; Goulet, M.; Pollack, D. A.; Kwabi, D. G.; Jin, S.; De Porcellinis, D.; Kerr, E. F.; Gordon, R. G.; Aziz, M. J. A Phosphonate-Functionalized Quinone Redox Flow Battery at Near-Neutral PH with Record Capacity Retention Rate. *Adv. Energy Mater.* **2019**, *9* (12), 1900039.
(123) Lin, K.; Chen, Q.; Gerhardt, M. R.; Tong, L.; Kim, S. B.; Eisenach, L.; Valle, A. W.; Hardee, D.; Gordon, R. G.; Aziz, M. J. Alkaline Quinone Flow Battery. *Science* **2015**, *349* (6255), 1529–1532.

(124) Lin, K.; Gómez-Bombarelli, R.; Beh, E. S.; Tong, L.; Chen, Q.; Valle, A.; Aspuru-Guzik, A.; Aziz, M. J.; Gordon, R. G. A Redox-Flow Battery with an Alloxazine-Based Organic Electrolyte. *Nat. Energy* **2016**, *1* (9), 1–8.
(125) Janoschka, T.; Martin, N.; Hager, M. D.; Schubert, U. S. An Aqueous Redox-Flow Battery with High Capacity and Power: The TEMPTMA/MV System. *Angew. Chem. Int. Ed.* **2016**, *55* (46), 14427–14430.
(126) Liu, T.; Wei, X.; Nie, Z.; Sprenkle, V.; Wang, W. A Total Organic Aqueous Redox Flow Battery Employing a Low Cost and Sustainable Methyl Viologen Anolyte and 4-HO-TEMPO Catholyte. *Adv. Energy Mater.* **2016**, *6* (3), 1501449.
(127) Liu, Y.; Goulet, M.-A.; Tong, L.; Liu, Y.; Ji, Y.; Wu, L.; Gordon, R. G.; Aziz, M. J.; Yang, Z.; Xu, T. A Long-Lifetime All-Organic Aqueous Flow Battery Utilizing TMAP-TEMPO Radical. *Chem* **2019**, *5* (7), 1861–1870.
(128) Nutting, J. E.; Rafiee, M.; Stahl, S. S. Tetramethylpiperidine N-Oxyl (TEMPO), Phthalimide N-Oxyl (PINO), and Related N-Oxyl Species: Electrochemical Properties and Their Use in Electrocatalytic Reactions. *Chem. Rev.* **2018**, *118* (9), 4834–4885.
(129) Pasta, M.; Wessells, C. D.; Liu, N.; Nelson, J.; McDowell, M. T.; Huggins, R. A.; Toney, M. F.; Cui, Y. Full Open-Framework Batteries for Stationary Energy Storage. *Nat. Commun.* **2014**, *5*, 3007.
(130) Pasta, M.; Wessells, C. D.; Huggins, R. A.; Cui, Y. A High-Rate and Long Cycle Life Aqueous Electrolyte Battery for Grid-Scale Energy Storage. *Nat. Commun.* **2012**, *3*, 1149.
(131) Kraft, A. *On the Discovery and History of Prussian Blue*, Bulletin for the history of chemistry.; 2; Division of the History of Chemistry of the American Chemical Society, 2008; Vol. 33.
(132) Ma, F.; Li, Q.; Wang, T.; Zhang, H.; Wu, G. Energy Storage Materials Derived from Prussian Blue Analogues. *Sci. Bull.* **2017**, *62* (5), 358–368. https://doi.org/10.1016/j.scib.2017.01.030.
(133) Xu, Y.; Zheng, S.; Tang, H.; Guo, X.; Xue, H.; Pang, H. Prussian Blue and Its Derivatives as Electrode Materials for Electrochemical Energy Storage. *Energy Storage Mater.* **2017**, *9*, 11–30. https://doi.org/10.1016/j.ensm.2017.06.002.
(134) Neff D., V. Electrochemical Oxidation and Reduction of Thin Films of Prussian Blue. *J. Electrochem. Sci. Technol.* **1978**, *125* (6).
(135) Wang, B.; Han, Y.; Wang, X.; Bahlawane, N.; Pan, H.; Yan, M.; Jiang, Y. Prussian Blue Analogs for Rechargeable Batteries. *Iscience* **2018**, *3*, 110–133.
(136) Xu, Y.; Zheng, S.; Tang, H.; Guo, X.; Xue, H.; Pang, H. Prussian Blue and Its Derivatives as Electrode Materials for Electrochemical Energy Storage. *Energy Storage Mater.* **2017**, *9*, 11–30.
(137) Karyakin, A. A.; Gitelmacher, O. V.; Karyakina, E. E. Prussian Blue-Based First-Generation Biosensor. A Sensitive Amperometric Electrode for Glucose. *Anal. Chem.* **1995**, *67* (14), 2419–2423.
(138) Jia, X.; Cai, X.; Chen, Y.; Wang, S.; Xu, H.; Zhang, K.; Ma, M.; Wu, H.; Shi, J.; Chen, H. Perfluoropentane-Encapsulated Hollow Mesoporous Prussian Blue Nanocubes for Activated Ultrasound Imaging and Photothermal Therapy of Cancer. *ACS Appl. Mater. Interfaces* **2015**, *7* (8), 4579–4588.
(139) Vipin, A. K.; Hu, B.; Fugetsu, B. Prussian Blue Caged in Alginate/Calcium Beads as Adsorbents for Removal of Cesium Ions from Contaminated Water. *J. Hazard. Mater.* **2013**, *258*, 93–101.

(140) Wu, X.; Shao, M.; Wu, C.; Qian, J.; Cao, Y.; Ai, X.; Yang, H. Low Defect FeFe (CN) 6 Framework as Stable Host Material for High Performance Li-Ion Batteries. *ACS Appl. Mater. Interfaces* **2016**, *8* (36), 23706–23712.
(141) Hurlbutt, K.; Wheeler, S.; Capone, I.; Pasta, M. Prussian Blue Analogs as Battery Materials. *Joule* **2018**, *2* (10), 1950–1960.
(142) Wessells, C. D.; Huggins, R. A.; Cui, Y. Copper Hexacyanoferrate Battery Electrodes with Long Cycle Life and High Power. *Nat. Commun.* **2011**, *2* (1). https://doi.org/10.1038/ncomms1563.
(143) Huang, B.; Shao, Y.; Liu, Y.; Lu, Z.; Lu, X.; Liao, S. Improving Potassium-Ion Batteries by Optimizing the Composition of Prussian Blue Cathode. *ACS Appl. Energy Mater.* **2019**, *2* (9), 6528–6535.
(144) Li, W.; Han, C.; Cheng, G.; Chou, S.; Liu, H.; Dou, S. Chemical Properties, Structural Properties, and Energy Storage Applications of Prussian Blue Analogues. *Small* **2019**, *15* (32), 1900470.
(145) Yang, J.; Zhang, X.; Xu, Z.; Huang, J.; Chen, J. Synthesis of Mesoporous Co (OH) 2 Nanocubes Derived from Prussian Blue Analogue and Their Electrocapacitive Properties. *J. Electroanal. Chem.* **2017**, *788*, 54–60.
(146) Kumar, A.; Bhattacharyya, S. Porous NiFe-Oxide Nanocubes as Bifunctional Electrocatalysts for Efficient Water-Splitting. *ACS Appl. Mater. Interfaces* **2017**, *9* (48), 41906–41915.
(147) Durand, P.; Fornasieri, G.; Baumier, C.; Beaunier, P.; Durand, D.; Rivière, E.; Bleuzen, A. Control of Stoichiometry, Size and Morphology of Inorganic Polymers by Template Assisted Coordination Chemistry. *J. Mater. Chem.* **2010**, *20* (42), 9348–9354.
(148) Zakaria, M. B.; Malgras, V.; Takei, T.; Li, C.; Yamauchi, Y. Layer-by-Layer Motif Hybridization: Nanoporous Nickel Oxide Flakes Wrapped into Graphene Oxide Sheets toward Enhanced Oxygen Reduction Reaction. *Chem. Commun.* **2015**, *51* (91), 16409–16412.
(149) Zhang, K.; Guo, C.; Zhao, Q.; Niu, Z.; Chen, J. High-Performance Organic Lithium Batteries with an Ether-Based Electrolyte and 9, 10-Anthraquinone (AQ)/CMK-3 Cathode. *Adv. Sci.* **2015**, *2* (5), 1500018.
(150) Zheng, X.-J.; Kuang, Q.; Xu, T.; Jiang, Z.-Y.; Zhang, S.-H.; Xie, Z.-X.; Huang, R.-B.; Zheng, L.-S. Growth of Prussian Blue Microcubes under a Hydrothermal Condition: Possible Nonclassical Crystallization by a Mesoscale Self-Assembly. *J. Phys. Chem. C* **2007**, *111* (12), 4499–4502.
(151) Song, J.; Wang, L.; Lu, Y.; Liu, J.; Guo, B.; Xiao, P.; Lee, J.-J.; Yang, X.-Q.; Henkelman, G.; Goodenough, J. B. Removal of Interstitial H2O in Hexacyanometallates for a Superior Cathode of a Sodium-Ion Battery. *J. Am. Chem. Soc.* **2015**, *137* (7), 2658–2664.
(152) Silva, W. O.; Costa Bassetto, V.; Baster, D.; Mensi, M.; Oveisi, E.; Girault, H. H. Oxidative Print-Light-Synthesis Thin Film Deposition of Prussian Blue. *ACS Appl. Electron. Mater.* **2020**.
(153) Zhang, F.; Huang, S.; Wang, X.; Jia, C.; Du, Y.; Wang, Q. Redox-Targeted Catalysis for Vanadium Redox-Flow Batteries. *Nano Energy* **2018**, *52*, 292–299.
(154) Fan, L.; Jia, C.; Zhu, Y. G.; Wang, Q. Redox Targeting of Prussian Blue: Toward Low-Cost and High Energy Density Redox Flow Battery and Solar Rechargeable Battery. *ACS Energy Lett.* **2017**, *2* (3), 615–621.

(155) Barnhart, C. J.; Dale, M.; Brandt, A. R.; Benson, S. M. The Energetic Implications of Curtailing versus Storing Solar- and Wind-Generated Electricity. *Energy Environ. Sci.* **2013**, *6* (10), 2804. https://doi.org/10.1039/c3ee41973h.

(156) Renman, V.; Ojwang, D. O.; Valvo, M.; Gómez, C. P.; Gustafsson, T.; Svensson, G. Structural-Electrochemical Relations in the Aqueous Copper Hexacyanoferrate-Zinc System Examined by Synchrotron X-Ray Diffraction. *J. Power Sources* **2017**, *369*, 146–153. https://doi.org/10.1016/j.jpowsour.2017.09.079.

(157) Engel, D.; Grabner, E. W. Copper Hexacyanoferrate-Modified Glassy Carbon: A Novel Type of Potassium-Selective Electrode. *Berichte Bunsenges. Für Phys. Chem.* **1985**, *89* (9), 982–986. https://doi.org/10.1002/bbpc.19850890911.

(158) Kahlert, H.; Retter, U.; Lohse, H.; Siegler, K.; Scholz, F. On the Determination of the Diffusion Coefficients of Electrons and of Potassium Ions in Copper(II) Hexacyanoferrate(II) Composite Electrodes. *J. Phys. Chem. B* **1998**, *102* (44), 8757–8765. https://doi.org/10.1021/jp981623q.

(159) Majidi, M. R.; Asadpour-Zeynali, K.; Shahmoradi, K.; Shivaeefar, Y. Electrochemical Characteristics of a Copper Hexacyanoferrate (CuHCNF) Modified Composite Carbon Electrode and Its Application toward Sulfite Oxidation. *J. Chin. Chem. Soc.* **2010**, *57* (3A), 391–398. https://doi.org/10.1002/jccs.201000058.

(160) Makowski, O.; Stroka, J.; Kulesza, P. J.; Malik, M. A.; Galus, Z. Electrochemical Identity of Copper Hexacyanoferrate in the Solid-State: Evidence for the Presence and Redox Activity of Both Iron and Copper Ionic Sites. *J. Electroanal. Chem.* **2002**, *532* (1–2), 157–164. https://doi.org/10.1016/S0022-0728(02)00965-8.

(161) Du, D.; Wang, M.; Qin, Y.; Lin, Y. One-Step Electrochemical Deposition of Prussian Blue–Multiwalled Carbon Nanotube Nanocomposite Thin-Film: Preparation, Characterization and Evaluation for H_2O_2 Sensing. *J Mater Chem* **2010**, *20* (8), 1532–1537. https://doi.org/10.1039/B919500A.

(162) Smith, D. A.; Heeg, M.; Heineman, W. R.; Elder, R. Direct Determination of Fe-C Bond Lengths in Iron (II) and Iron (III) Cyanide Solutions Using EXAFS Spectroelectrochemistry. *J. Am. Chem. Soc.* **1984**, *106* (10), 3053–3054.

(163) Targholi, E.; Mousavi-Khoshdel, S. M.; Rahmanifara, M.; Yahya, M. Cu-and Fe-Hexacyanoferrate as Cathode Materials for Potassium Ion Battery: A First-Principles Study. *Chem. Phys. Lett.* **2017**, *687*, 244–249.

(164) Thouless, D. Relation between the Kubo-Greenwood Formula and the Boltzmann Equation for Electrical Conductivity. *Philos. Mag.* **1975**, *32* (4), 877–879.

(165) Feng, C.; Chen, Y.; Liu, D.; Zhang, P. Conductivity and Electrochemical Performance of $LiFePO_4$ Slurry in the Lithium Slurry Battery. *IOP Conf. Ser. Mater. Sci. Eng.* **2017**, *207*, 012076. https://doi.org/10.1088/1757-899X/207/1/012076.

(166) Wen, M.; Sun, X.; Su, L.; Shen, J.; Li, J.; Guo, S. The Electrical Conductivity of Carbon Nanotube/Carbon Black/Polypropylene Composites Prepared through Multistage Stretching Extrusion. *Polymer* **2012**, *53* (7), 1602–1610.

(167) Guan, L.; Yu, L.; Chen, G. Z. Capacitive and Non-Capacitive Faradaic Charge Storage. *Electrochimica Acta* **2016**, *206*, 464–478. https://doi.org/10.1016/j.electacta.2016.01.213.

(168) Sathiya, M.; Prakash, A. S.; Ramesha, K.; Tarascon, J.; Shukla, A. K. V_2O_5 -Anchored Carbon Nanotubes for Enhanced Electrochemical Energy Storage. *J. Am. Chem. Soc.* **2011**, *133* (40), 16291–16299. https://doi.org/10.1021/ja207285b.

(169) Ardizzone, S.; Fregonara, G.; Trasatti, S. “Inner” and “Outer” Active Surface of RuO2 Electrodes. *Electrochimica Acta* **1990**, *35* (1), 263–267. https://doi.org/10.1016/0013-4686(90)85068-X.
(170) Janoschka, T.; Martin, N.; Hager, M. D.; Schubert, U. S. An Aqueous Redox-Flow Battery with High Capacity and Power: The TEMPTMA/MV System. *Angew. Chem. Int. Ed.* **2016**, *55* (46), 14427–14430. https://doi.org/10.1002/anie.201606472.
(171) Streeter, I.; Wildgoose, G. G.; Shao, L.; Compton, R. G. Cyclic Voltammetry on Electrode Surfaces Covered with Porous Layers: An Analysis of Electron Transfer Kinetics at Single-Walled Carbon Nanotube Modified Electrodes. *Sens. Actuators B Chem.* **2008**, *133* (2), 462–466. https://doi.org/10.1016/j.snb.2008.03.015.
(172) Pandolfo, A. G.; Hollenkamp, A. F. Carbon Properties and Their Role in Supercapacitors. *J. Power Sources* **2006**, *157* (1), 11–27.
(173) Lee, H.-W.; Wang, R. Y.; Pasta, M.; Lee, S. W.; Liu, N.; Cui, Y. Manganese Hexacyanomanganate Open Framework as a High-Capacity Positive Electrode Material for Sodium-Ion Batteries. *Nat. Commun.* **2014**, *5*, 5280.
(174) Hu, B.; DeBruler, C.; Rhodes, Z.; Liu, T. L. Long-Cycling Aqueous Organic Redox Flow Battery (AORFB) toward Sustainable and Safe Energy Storage. *J. Am. Chem. Soc.* **2017**, *139* (3), 1207–1214.
(175) DeBruler, C.; Hu, B.; Moss, J.; Liu, X.; Luo, J.; Sun, Y.; Liu, T. L. Designer Two-Electron Storage Viologen Anolyte Materials for Neutral Aqueous Organic Redox Flow Batteries. *Chem* **2017**, *3* (6), 961–978.
(176) DeBruler, C.; Hu, B.; Moss, J.; Luo, J.; Liu, T. L. A Sulfonate-Functionalized Viologen Enabling Neutral Cation Exchange, Aqueous Organic Redox Flow Batteries toward Renewable Energy Storage. *ACS Energy Lett.* **2018**, *3* (3), 663–668.
(177) Luo, J.; Hu, B.; Debruler, C.; Liu, T. L. A Π-Conjugation Extended Viologen as a Two-Electron Storage Anolyte for Total Organic Aqueous Redox Flow Batteries. *Angew. Chem. Int. Ed.* **2018**, *57* (1), 231–235.
(178) Kwabi, D. G.; Ji, Y.; Aziz, M. J. Electrolyte Lifetime in Aqueous Organic Redox Flow Batteries: A Critical Review. *Chem. Rev.* **2020**.
(179) Hu, B.; Tang, Y.; Luo, J.; Grove, G.; Guo, Y.; Liu, T. L. Improved Radical Stability of Viologen Anolytes in Aqueous Organic Redox Flow Batteries. *Chem. Commun.* **2018**, *54* (50), 6871–6874.
(180) Ji, Y.; Goulet, M.; Pollack, D. A.; Kwabi, D. G.; Jin, S.; De Porcellinis, D.; Kerr, E. F.; Gordon, R. G.; Aziz, M. J. A Phosphonate-Functionalized Quinone Redox Flow Battery at Near-Neutral PH with Record Capacity Retention Rate. *Adv. Energy Mater.* **2019**, *9* (12), 1900039.
(181) Poizot, P.; Gaubicher, J.; Renault, S.; Dubois, L.; Liang, Y.; Yao, Y. Opportunities and Challenges for Organic Electrodes in Electrochemical Energy Storage. *Chem. Rev.* **2020**.
(182) Goriparti, S.; Harish, M.; Sampath, S. Ellagic Acid–a Novel Organic Electrode Material for High Capacity Lithium Ion Batteries. *Chem. Commun.* **2013**, *49* (65), 7234–7236.
(183) Reddy, A. L. M.; Nagarajan, S.; Chumyim, P.; Gowda, S. R.; Pradhan, P.; Jadhav, S. R.; Dubey, M.; John, G.; Ajayan, P. M. Lithium Storage Mechanisms in Purpurin Based Organic Lithium Ion Battery Electrodes. *Sci. Rep.* **2012**, *2*, 960.
(184) Kim, H.; Hong, J.; Park, K.-Y.; Kim, H.; Kim, S.-W.; Kang, K. Aqueous Rechargeable Li and Na Ion Batteries. *Chem. Rev.* **2014**, *114* (23), 11788–11827.

(185) Wang, H.; Huang, K.; Zeng, Y.; Yang, S.; Chen, L. Electrochemical Properties of TiP2O7 and LiTi2 (PO4) 3 as Anode Material for Lithium Ion Battery with Aqueous Solution Electrolyte. *Electrochimica Acta* **2007**, *52* (9), 3280–3285.
(186) Song, Z.; Zhan, H.; Zhou, Y. Polyimides: Promising Energy-storage Materials. *Angew. Chem. Int. Ed.* **2010**, *49* (45), 8444–8448.
(187) Chen, L.; Li, W.; Wang, Y.; Wang, C.; Xia, Y. Polyimide as Anode Electrode Material for Rechargeable Sodium Batteries. *RSC Adv.* **2014**, *4* (48), 25369–25373.
(188) Armand, M.; Tarascon, J.-M. Building Better Batteries. *nature* **2008**, *451* (7179), 652–657.
(189) Wang, J.; Li, F.; Qu, Y.; Liu, Y.; Yang, Y.; Li, W.; Zhao, M. PNTCDA: A Promising Versatile Organic Electrode Material for Alkali-Metal Ion Batteries. *J. Mater. Chem. A* **2018**, *6* (48), 24869–24876.
(190) Dong, X.; Chen, L.; Liu, J.; Haller, S.; Wang, Y.; Xia, Y. Environmentally-Friendly Aqueous Li (or Na)-Ion Battery with Fast Electrode Kinetics and Super-Long Life. *Sci. Adv.* **2016**, *2* (1), e1501038.
(191) Wang, M.; Wang, H.; Zhang, H.; Li, X. Aqueous K-Ion Battery Incorporating Environment-Friendly Organic Compound and Berlin Green. *J. Energy Chem.* **2020**, *48*, 14–20.
(192) Manuel, J.; Zhao, X.; Cho, K.-K.; Kim, J.-K.; Ahn, J.-H. Ultralong Life Organic Sodium Ion Batteries Using a Polyimide/Multiwalled Carbon Nanotubes Nanocomposite and Gel Polymer Electrolyte. *ACS Sustain. Chem. Eng.* **2018**, *6* (7), 8159–8166.
(193) Thuau, D.; Koutsos, V.; Cheung, R. Electrical and Mechanical Properties of Carbon Nanotube-Polyimide Composites. *J. Vac. Sci. Technol. B Microelectron. Nanometer Struct. Process. Meas. Phenom.* **2009**, *27* (6), 3139–3144.
(194) Jiang, X.; Bin, Y.; Matsuo, M. Electrical and Mechanical Properties of Polyimide–Carbon Nanotubes Composites Fabricated by in Situ Polymerization. *Polymer* **2005**, *46* (18), 7418–7424.
(195) Deshmukh, S.; Call, C.; Ounaies, Z.; Park, C.; Harrison, J. S. Effect of Single Walled Carbon Nanotubes (SWNTs) on the Electromechanical Response of a Polyimide Nanocomposite; International Society for Optics and Photonics, 2006; Vol. 6168, p 61680Y.
(196) Ogasawara, T.; Ishida, Y.; Ishikawa, T.; Yokota, R. Characterization of Multi-Walled Carbon Nanotube/Phenylethynyl Terminated Polyimide Composites. *Compos. Part Appl. Sci. Manuf.* **2004**, *35* (1), 67–74.
(197) Xie, F.; Zhang, L.; Su, D.; Jaroniec, M.; Qiao, S. Na2Ti3O7@ N-Doped Carbon Hollow Spheres for Sodium-Ion Batteries with Excellent Rate Performance. *Adv. Mater.* **2017**, *29* (24), 1700989.
(198) Song, Z.; Xu, T.; Gordin, M. L.; Jiang, Y.-B.; Bae, I.-T.; Xiao, Q.; Zhan, H.; Liu, J.; Wang, D. Polymer–Graphene Nanocomposites as Ultrafast-Charge and-Discharge Cathodes for Rechargeable Lithium Batteries. *Nano Lett.* **2012**, *12* (5), 2205–2211.
(199) Chen, B.; Lu, H.; Zhou, J.; Ye, C.; Shi, C.; Zhao, N.; Qiao, S. Porous MoS2/Carbon Spheres Anchored on 3D Interconnected Multiwall Carbon Nanotube Networks for Ultrafast Na Storage. *Adv. Energy Mater.* **2018**, *8* (15), 1702909.
(200) Que, L.; Yu, F.; Wang, Z.; Gu, D. Pseudocapacitance of TiO2− x/CNT Anodes for High-Performance Quasi-Solid-State Li-Ion and Na-Ion Capacitors. *Small* **2018**, *14* (17), 1704508.

(201) Chen, K.-S.; Xu, R.; Luu, N. S.; Secor, E. B.; Hamamoto, K.; Li, Q.; Kim, S.; Sangwan, V. K.; Balla, I.; Guiney, L. M. Comprehensive Enhancement of Nanostructured Lithium-Ion Battery Cathode Materials via Conformal Graphene Dispersion. *Nano Lett.* **2017**, *17* (4), 2539–2546.
(202) Yan, R.; Ghilane, J.; Phuah, K. C.; Pham Truong, T. N.; Adams, S.; Randriamahazaka, H.; Wang, Q. Determining Li+-Coupled Redox Targeting Reaction Kinetics of Battery Materials with Scanning Electrochemical Microscopy. *J. Phys. Chem. Lett.* **2018**, *9* (3), 491–496.
(203) Momotenko, D. *Scanning Electrochemical Microscopy and Finite Element Modeling of Structural and Transport Properties of Electrochemical Systems*; EPFL, 2013.
(204) Lefrou, C.; Cornut, R. Analytical Expressions for Quantitative Scanning Electrochemical Microscopy (SECM). *ChemPhysChem* **2010**, *11* (3), 547–556.
(205) Cannes, C.; Kanoufi, F.; Bard, A. J. Cyclic Voltammetry and Scanning Electrochemical Microscopy of Ferrocenemethanol at Monolayer and Bilayer-Modified Gold Electrodes. *J. Electroanal. Chem.* **2003**, *547* (1), 83–91.
(206) Darvishi, S.; Pick, H.; Lin, T.-E.; Zhu, Y.; Li, X.; Ho, P.-C.; Girault, H. H.; Lesch, A. Tape-Stripping Electrochemical Detection of Melanoma. *Anal. Chem.* **2019**, *91* (20), 12900–12908.
(207) Wong, A. A.; Aziz, M. J.; Rubinstein, S. Direct Visualization of Electrochemical Reactions and Comparison of Commercial Carbon Papers in Operando by Fluorescence Microscopy Using a Quinone-Based Flow Cell. *ECS Trans.* **2017**, *77* (11), 153.
(208) Giannozzi, P.; Baroni, S.; Bonini, N.; Calandra, M.; Car, R.; Cavazzoni, C.; Ceresoli, D.; Chiarotti, G. L.; Cococcioni, M.; Dabo, I. QUANTUM ESPRESSO: A Modular and Open-Source Software Project for Quantum Simulations of Materials. *J. Phys. Condens. Matter* **2009**, *21* (39), 395502.
(209) Calderín, L.; Karasiev, V. V.; Trickey, S. B. Kubo–Greenwood Electrical Conductivity Formulation and Implementation for Projector Augmented Wave Datasets. *Comput. Phys. Commun.* **2017**, *221*, 118–142. https://doi.org/10.1016/j.cpc.2017.08.008.
(210) *COMSOL, 1D Isothermal Nickel-Metal Hydride Battery*.

ELENA ZANZOLA

Contact +41 786741257 *elena.zanzola@gmail.com*

PROFESSIONAL PROFILE

Passionate researcher in energy technologies and material science with extroverted temper and strong communication skills.

Excellent attitude to work in team. Problem solving and results-oriented mind-set. Calm behavior under pressure and within challenging circumstances.

Able to adapt easily to foreign environments and changing situations.

WORK EXPERIENCES

May 2016-present — **Ph.D. in Chemistry and Chemical Engineering** — **Sion, Switzerland**

École polytechnique fédérale de Lausanne (EPFL)

Project contest

- The Ph.D research is focused on the development of a new and innovative energy storage approach.
- The technology studied during the Ph.D is called redox flow battery.

Key achievements

- Study to overcome low capability of energy storage in redox flow batteries.
- Synthesis and development of new materials at laboratory scale for enhanced and safe redox flow batteries.
- Design and installation at laboratory scale of advanced flow battery systems with improved performances compared to commercial solutions.
- Benefit assessment of the present study within the current energy market.

Jan 2012-Jan 2013 — **Sales promoter** — **Milan, Italy**

WALA Italia and Dr. Hauschka

Outline

- WALA is a well-established company of natural products for health care.
- Within WALA, Dr. Hauschka is known for being one of the finest brand in natural skin care.
- Dr. Hauschka promotes fair farming activities for its products all over the world.

Key responsibilities

- Customers' careful assistance to move towards natural skin care.
- Customers' personal consultancy towards the most suitable solution of Dr. Hauschka skin care.

Key achievements

- Solid establishment of Dr. Hauschka into new shops of natural products.

EDUCATION

2013-2016 — **Master of Science in Chemistry** — **GPA 3.9/4.0**

University of Milan — **Milan, Italy**

Project contest

- Investigation and development of new materials to catalyze oxygen reduction reaction (ORR) in fuel cells.

Key achievements

- Synthesis of new carbon-based nanomaterials.
- Performances assessment of candidate materials in fuel cells simulating environment and comparison with metal-based catalysts.
- Benefits estimation in terms of chemical safety and low costs.

This work was presented and evaluated as best in the field of electrochemistry at the Italian Electrochemistry Days (2016).

2010-2013 — **Bachelor of Science in Chemistry** — **GPA 3.7/4.0**

University of Milan (*collaboration with University Bicocca*) — **Milan, Italy**

Project contest

- Investigation of heavy metals distribution in water samples coming from Valtellina region (north of Italy).

Key features

- Development of innovative analytical methodology to quantify the content of heavy metals in water samples from Valtellina region.

Key achievements

- Chemical analysis of 30 different water samples.
- Quantification of heavy metals.
- Quantification of arsenic content and correlation with the particular configuration of Valtellina territory.

LANGUAGES

Italian (native), **English** (fluent), **French** (fluent), **German** (Intermediate)

SKILLS

Tools

Software		Software (engineering and science)	
Microsoft Office package	Matlab Origin	Chem draw Chem draw 3D	EC Lab (Biologic Instruments) NOVA (Autolab, Metrohm Instruments)

Industry knowledges

Chemical engineering	Chemistry	Materials	Materials' characterization techniques	Others
Redox flow batteries Fuel cells Hydrogen	Electrochemistry Physical chemistry Analytical chemistry Instrumental analytical chemistry Organic chemistry	Carbon-based Carbon nanomaterials Polymers Insulating Additives	Microscopy	Work expertise in inert environments

ACHIEVEMENTS

International awards

- Best paper reviewed from the committee of the international flow battery forum (IFBF). 2019th edition of IFBF, Lyon, France
  This paper is evaluated for its innovative approach to make safe and performant redox flow batteries with high energy density.
- Best work reviewed from the committee of the international flow battery forum (IFBF). 2018th edition of IFBF, Lausanne, Switzerland
  This work is awarded for proposing new advanced candidate materials for safe redox flow battery installations.

Key publications (international journals)

- Redox electrochemical energy storage for aqueous redox flow batteries: the case of copper hexacyanoferrate (**https://doi.org/10.1016/j.electacta.2019.134704**)
- Redox solid energy boosters for flow batteries: polyaniline as a case study (**https://doi.org/10.1016/j.electacta.2017.03.084**)

Both works are published in Electrochimica Acta, the journal of the International Society of Electrochemistry.

Other scientific contributions (international symposia)

- Enhanced aqueous organic redox flow batteries by solid boosters (2019, International Flow Battery Forum, Lyon, France)
- Electrochemical investigation on the behavior of ferroin as redox mediator for flow batteries (2018, International Flow Battery Forum, Lausanne, Switzerland)
- Enhanced aqueous flow batteries (1st Swiss battery days, Baden, Switzerland)
- Enhanced aqueous organic flow batteries (International Society of Electrochemistry meeting, Bologna, Italy)
- Redox flow batteries for fast EV charging and for hydrogen production for FCEVs (Electrochemistry Society, Seattle, USA)

ADDITIONAL INFORMATION

Sports: Artistic gymnastics (Italian National champion in 2003), fencing, skiing.